# Production, Manipulation and Spectroscopy of Cold Trapped Molecular Ions

Habilitationsschrift

**Dr. rer. nat. Bernhard Roth**

Institut für Experimentalphysik
Heinrich-Heine Universität Düsseldorf

März 2007

# Contents

# Chapter 1

# Introduction

The enormous success in the field of laser cooling of neutral and charged atoms, has lead, among others, to the first demonstration of Bose-Einstein condensation in dilute alkali gases, see e.g. [1], to new insights in the physics of many-body systems and the observation of a variety of quantum mechanical effects [2, 3, 4], as well as to significant advances in frequency metrology [5, 6, 7]. In the last years, the development of techniques for the production of translationally cold neutral and charged molecules with sub-Kelvin or even sub-Millikelvin temperatures has moved into focus [8, 9]. By common convention, the cold temperature regime is reached at temperatures $T<1\,K$, whereas we denote it as ultracold when temperatures $<1\,mK$ are reached.

The techniques developed for the laser-cooling of neutral and charged atoms cannot be directly applied to molecules, due to the lack of closed optical transitions or the lack of suitable laser sources, see, e.g., [10]. Therefore, new methods for the production of cold molecules are required. One challenge is to develop universal methods which do not depend on the internal nature of the particles, such as their magnetic or electric moments or their energy level structure, so that they can be applied to a large variety of molecular species, ranging from the from the simplest of all molecules, e.g. the hydrogen molecules and their isotopomers, to massive and complex molecules, such as proteins and polymers.

Strong efforts are currently under way towards first applications of cold and ultracold molecular systems. Cold molecules are interesting systems for fundamental physics and offer the possibility to study light-molecule and molecule-molecule interactions in a new temperature regime, previously not accessible. The availability of cold molecular samples holds great promise for the discovery of new phases of matter, for the study of the properties of cold neutral and non-neutral plasmas, or the demonstration of schemes for molecular quantum computers [11, 12].

The availability of techniques to produce molecules at translational temperatures down to unprecedented limits makes such systems interesting for performing rotational and vibrational spectroscopy with highest resolution [13]. In atomic physics, the combination of laser cooling and modern laser technology has paved the way to an enormous increase

in the spectral resolution, leading, for example, to the most precise measurement of a fundamental constant in nature (the Rydberg constant) [14] or to precise microwave and optical clocks, see, e.g., [15] and references therein. A comparable increase in spectral resolution is also expected for molecular systems at low temperatures, where line broadening effects due to, e.g., the Doppler effect, high thermal velocities, or finite transit times can be strongly reduced or even eliminated. In particular, due to the relatively long lifetime of vibrational levels of molecules (∼ms to s), the potential line resolution can be huge, with Q-factors $> 10^{14}$. The low translational temperature can also increase the absorption rate significantly, and efficient excitation is possible even on weak overtone transitions. Since methods for trapping and confinement of molecules are also available or have been developed, these systems are more and more attractive for precision studies of even weakest interactions in a controlled environment, taking advantage of long storage and interrogation times.

High-resolution spectroscopic measurements of transition frequencies in molecules are especially interesting for fundamental tests of physics, such as a precise determination of the electron-to-proton mass ratio, its possible time-independence, and of its Local Position Invariance, and for a test of the isotropy of space, for example. Furthermore, cold molecules allow to test quantum chemical calculations of rovibrational energy levels, which could stimulate the development of more accurate theoretical models for the description not only of simple, but also of larger, polyatomic molecules.

An exciting new direction is the investigation of collisions at very low temperatures, possibly at the quantum level [16, 17]. This temperature regime represents a unique environment to study the quantum mechanical details of collisional processes. For example, elastic and inelastic collision cross sections can be very large and details of chemical reactions could be observed which do not, or only partially, become manifest at higher temperatures. Thus, processes which take place, e.g., in white dwarfs or neutron stars might be accessible to laboratory experiments. Finally, one far-reaching goal is to use cold molecular systems in well-prepared single quantum states, for studying internal coherences or slow internal processes.

In this work, contributions to the above fields of research are presented. The contributions originate from research carried out in the Institute of Experimental Physics at the Heinrich-Heine University of Düsseldorf (Germany), starting from January 2002. The work is a summary of my scientific achievements to fulfil the requirements to apply for the "Habilitation" in physics according to the "Habilitationsordnung der Mathematisch-Naturwissenschaftlichen Fakultät der Heinrich-Heine-Universität Düsseldorf".

In detail, the present work describes the development of a novel, universal cooling method for charged particles, sympathetic cooling using laser-cooled atomic ions, suitable for the production of cold (millikelvin temperatures) atomic and molecular ions trapped in radio frequency ion traps. The method was applied in experiment to a large variety of particle species, covering the mass range from 1 to 470 amu so far. Furthermore, experimental and computational methods were developed, in order to reliably

identify the particles involved and to study the properties of the non-neutral one- and multi-component plasmas formed. These techniques are essential not only from the plasma physics point of view, in order to study and better understand the properties of cold, trapped non-neutral plasmas, but also for the controlled production of cold mixed-species ion ensembles, tailored to meet specific requirements regarding particle numbers, plasma shape or translational temperature for applications in fundamental physics studies. The techniques developed could be verified on a number of cold model systems, thus demonstrating their general applicability. Systematic investigations include the investigation of collective many-body effects in coupled Coulomb systems at low temperatures, as a function of the (tunable) coupling strength.

Based on these results, first applications of cold pure and mixed-species ion plasmas containing atomic and molecular ions were demonstrated. In particular, cold atomic and molecular ions were used in order to study ion-neutral chemical reactions and photodissociation of molecules in a new environment, whereas cold trapped hydrogen molecular ions were used to perform high-resolution rovibrational overtone spectroscopy, for the first time, with unprecedented spectral resolution. For this purpose, a generally applicable spectroscopic technique was developed and implemented, which was also used to measure the internal (rotational) temperature of molecular ions, and thus, the temperature of the blackbody radiation environment. The potential of this technique, e.g., for precise spectroscopic measurements on other simple molecular systems or the implementation of molecular thermometry (for applications in frequency metrology) were demonstrated.

This work is organized as follows: in Chapter 2, the method of sympathetic cooling of atomic and molecular ions by laser-cooled atomic ions is described, together with the two independent ion trap projects developed. The potential of the cooling method was demonstrated (see Chapter 2 for an overview of the atomic and molecular species cooled to date). The results obtained in this work (atomic and molecular species produced by sympathetic cooling and translational temperatures achieved) are compared to the results obtained by different groups using the same cooling method or alternative techniques. The techniques developed to analyze and characterize the various cold non-neutral ions plasmas are described in Chapter 3. Systematic studies of plasma properties and techniques for the manipulation and the control of the shape and the content of many-body Coulomb systems are explained. This Chapter also points out that besides experimental techniques for the identification of sympathetically cooled particles and the measurement of their translational temperature, numerical diagnostics tools, molecular dynamics (MD) simulations, are essential for reliable interpretation of the experimental results, in particular for the analysis of strongly coupled multi-species Coulomb systems containing many thousands of particles. The applications of cold non-neutral plasmas for studies of ion-neutral chemical reactions and photo fragmentation of polyatomic dye molecules are given in Chapter 4. The control of ion-neutral chemical reactions is also used to actually produce cold molecular ions efficiently. In

Chapter 5, the method developed for high-resolution rovibrational spectroscopy of cold, trapped molecular hydrogen ($HD^+$) ions, resonance enhanced multi-photon dissociation (REMPD), is described. The frequency of selected rovibrational transitions was measured and the results achieved are presented and compared to previous measurements on hydrogen molecular ions as well as theoretical calculations. Furthermore, the measurement of the internal temperature of the hydrogen molecular ions is presented. Chapter 6 briefly summarizes the results achieved and gives an outlook to the next steps and future goals.

# Chapter 2

# Production of Cold Molecules - Sympathetic Cooling in Ion Traps

## 2.1 Molecular Cooling Methods

Since the advent of cold atomic gases in the laboratory approximately twenty years ago, intense efforts are under way to develop methods for the production of neutral and charged molecules at low temperatures. In the meantime, the field comprises $\sim$ one hundred researchers in laboratories around the world.

Direct laser-cooling methods, applied with great success to atomic gases, cannot easily be applied to molecules and are probably limited to a few diatomic molecular species, such as BeH and CaH [10] (not yet demonstrated). The lack of closed optical transitions in molecules makes this method impractical for efficient cooling of most molecular species, due to the large number of lasers required.

Therefore, different methods for the cooling of neutral and charged molecules were developed during the last years, see Table 2.3 (Section 2.3) for an overview. For example, starting from cold atomic gases, neutral di-, tri- and tetra-atomic molecules can be produced by atom-to-molecule conversion methods, such as cold collisions of atoms assisted by light (photoassociation), or by driving an atom pair into a bound molecular state using Feshbach resonances, see, e.g., [8]. The methods rely on the availability of cold atomic gases, usually created by laser-cooling, and on the internal level structure of the atoms, i.e. the availability of suitable laser sources required for the photo-association process and the further stabilization of the molecules or the tunability of the scattering length of cold atoms using external magnetic fields.

In another approach, cold magnetic few-atom molecules have been produced by buffer gas cooling in a magnetic trap [18], relying on the magnetic properties of the particles. Furthermore, slow molecules with electric dipole moments have been created by Stark deceleration [19] and by cold particle selection, and trapped in electrostatic traps [20]. More general approaches rely on implanting molecules into superfluid droplets of $^3$He and $^4$He, acquiring the droplet temperature ($T\approx 0.38\,K$) [21], cooling by collisions in crossed

beams [22], mechanical cooling by rotation nozzles [23], or optical Stark deceleration of molecules in travelling optical lattices [24]. More recently, external-feedback laser cooling of particles based on coherent scattering was proposed [25].

A powerful method for the (indirect) cooling of a wide variety of particles is sympathetic cooling [26, 27]. The basic idea is simple: when two or more different species are trapped simultaneously in a trap and one of them is directly cooled by lasers, the other species will eventually also cool down through interaction. While sympathetic cooling was first observed in laser cooling experiments of atomic ions in Penning traps [27, 28] and later in radio frequency traps [29, 30, 31], it is not restricted to cooling of charged particles, but can also be applied to neutrals. As an example, Bose-Einstein condensation of potassium atoms via sympathetic cooling in an ultracold cloud of rubidium atoms was achieved [32].

One important advantage of sympathetic cooling is that it does not depend on the internal level structure of the particles or their electric and magnetic moments. The method is therefore applicable to a large number of molecular species, which makes it attractive for several fields of physics and chemistry, where cold ensembles of atomic and molecular species are interesting for precision experiments. The properties of cold ion plasmas produced using sympathetic cooling are summarized in Table 2.2 (Section 2.3).

At the beginning of this work, sympathetic cooling of molecular ions in Penning traps or in radio frequency traps had not been explored thoroughly. Open questions were related to the coolable mass range of the particles, the required atomic coolant species, as well as the achievable final translational temperatures and particle numbers. Numerical simulations of the cooling process showed that sympathetic cooling in an ion trap down to a mass ratio of 0.2 should be possible [33, 34]. However, simulations were either limited to small ion numbers when taking into account the full motion of the ions in a radio frequency trap, or were carried out in a time-averaged harmonic potential neglecting heating effects completely.

Most previous results on sympathetic cooling were on atomic species. Coolants were laser-cooled $^{9}Be^{+}$ [35], $^{24}Mg^{+}$ [36, 37, 38], $^{40}Ca^{+}$ [39], $^{114}Cd^{+}$ [40], and $^{138}Ba^{+}$ [41], in both electrostatic and electrodynamic ion traps. All sympathetically cooled species were singly charged medium-sized atoms, in one experiment highly charged xenon atoms from a special ion source, an EBIT, were trapped and cooled [35]. On the molecular side, cold molecular ions ($MgH^{+}$) have been formed by reactions of $H_2$ with optically excited trapped $Mg^{+}$, and were subsequently sympathetically cooled [42, 43]. Furthermore, using the same coolant, cold $H_3O^{+}$, $NH_4^{+}$, $O_2^{+}$, and $C_2H_5^{+}$ ions were formed, see [44] and references therein.

In the present work, sympathetic cooling is used to cool the translational temperature of atomic and molecular ions in the wide mass range from 1-470 amu, via their mutual interaction with laser-cooled beryllium and barium ions. Beryllium ions were used to sympathetically cool the mass range from 1-200 amu, in particular light hydrogen

molecular ions and other simple molecules, whereas barium ions were required to extend the coolable mass range up to 470 amu to date, with the potential to cool even heavier and more complex molecular ions, such as proteins and polymers. All species are stored in linear (Paul) radio frequency traps. Translational temperatures as low as a few mK to several tens of mK were achieved. The cold one-component and multi-component ion plasmas were analyzed experimentally and are in good agreement with results from numerical simulations, the latter being essential for a reliable analysis of the experiment.

## 2.2 Experimental Setups

In this work two independent ion trap setups were developed. In both setups, laser-cooled (LC) and sympathetically cooled (SC) particles are stored in a linear radio frequency trap, enclosed in an ultra-high vacuum chamber ($\approx 1 \times 10^{-10}$ mbar). Radio frequency ion traps were developed by W. Paul et al. (Bonn) and R.F. Wuerker et al. (Los Angeles) [45, 46, 47] after W. Paul invented the non-magnetic quadrupole mass filter in 1953, thus revolutionizing the field of mass-spectrometry. Since then, Paul traps and their various derivatives, among them linear Paul traps, were used in many applications in atomic physics, physical chemistry, and particle and high-energy physics [48].
Charged particles can be trapped by a combination of static electric and magnetic fields. However, the Laplace-equation,

$$\nabla^2 \Phi = 0, \tag{2.1}$$

shows that there is no electrostatic field which has a potential minimum in all three directions. Consequently, any electrostatic field $\Phi$ is always attractive in at least one direction and thus cannot give electrostatic confinement in three directions.
Confinement of charged particles in all three directions can be realized in a four-electrode configuration, by applying a combination of electrostatic fields and radio frequency fields to the electrodes. The traps used in this work are linear Paul traps, a special derivative of a radio frequency trap, consisting of four cylindrical electrodes, each sectioned longitudinally into three parts. Radial confinement of charged particles in such a configuration is achieved by applying a radio frequency voltage $\Phi_0 = U - V cos\Omega t$ to oppositely placed electrodes, whereas axial confinement along the symmetry axis of the trap is achieved by electrostatic voltages $V_{EC}$ applied to the 8 end sections (endcaps). Fig.2.1 displays a schematic of a linear radiofrequency trap used in one of the projects (top) together with a horizontal cross section of the UHV chamber where it is embedded (bottom). In Fig.2.2 an overview over both setups is given (for details, see [50, 49]).
The equations of motion of charged particles inside a linear Paul trap are differential equations of the Mathieu type, which lead to stable or unstable solutions depending on the trap parameters. A necessary condition for stable trapping of noninteracting ions is a (Mathieu) stability parameter, $q = 2QV_{RF}/m\Omega^2 r_0^2$, $< 0.9$. Here, $Q$ and $m$ are the charge and the mass of the trapped ions, $V_{RF}$ and $\Omega$ are the amplitude and

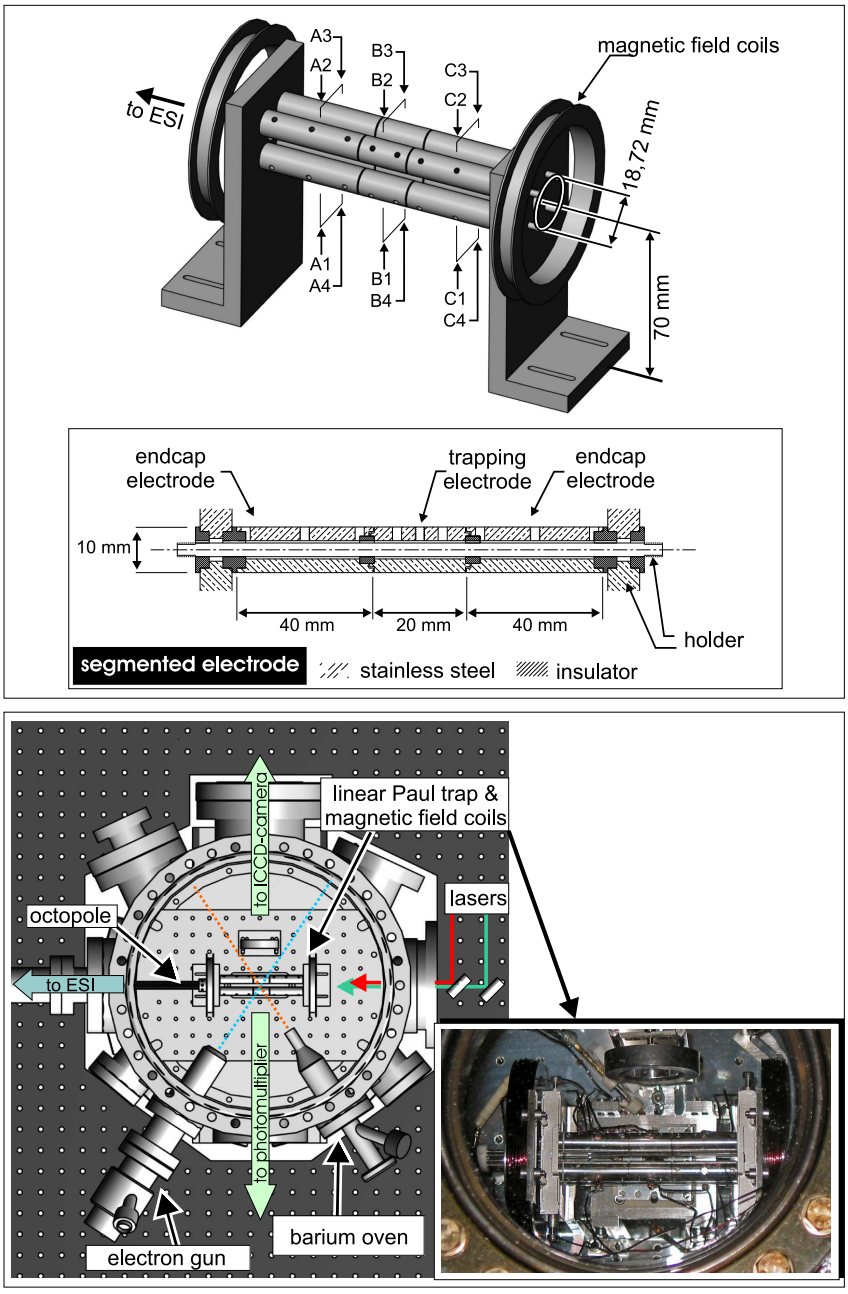


**Figure 2.1:**
The linear radiofrequency trap. Top: schematic of the ion trap used for sympathetic cooling of complex molecular ions by laser-cooled barium ions, see [49]. The trap used for sympathetic cooling of light molecular ions by laser-cooled beryllium ions is similar [50]. Bottom: UHV chamber (schematic and photograph) containing linear radiofrequency trap, electron gun, barium oven, octopole ion guide and imaging optics [49].

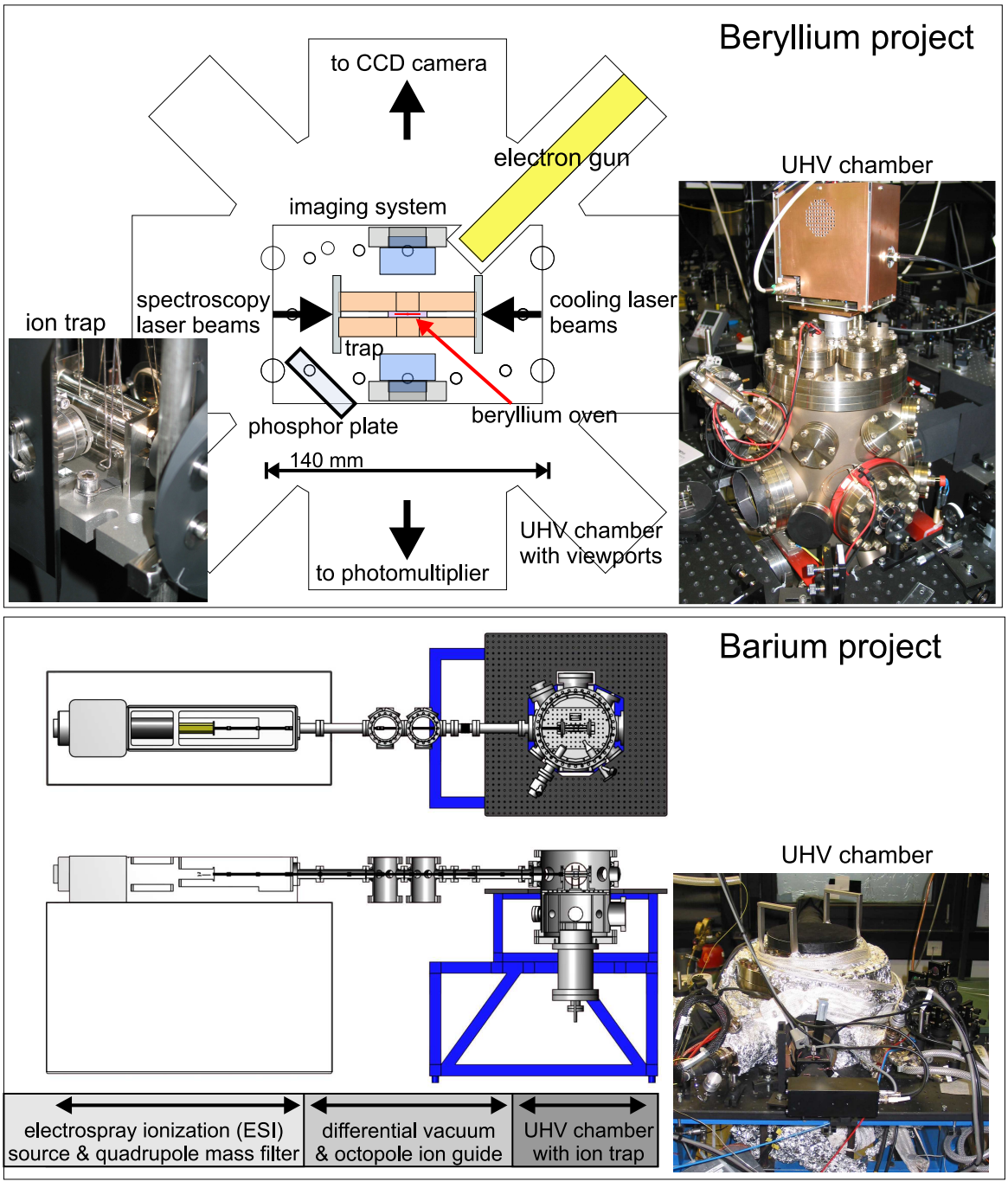


**Figure 2.2:**
The two ion trap projects. Experimental setup for sympathetic cooling of light (top) and complex (bottom) molecular ions [50, 49].

the frequency of the rf driving field and $r_0$ is the distance from the trap center to the electrodes. A small $q$ parameter implies that the amplitude of micromotion is small. When many ion are stored in the trap, trap operation at small $q$ parameters is favorable because heating effects induced by the radio frequency field are then less pronounced. Compared to other charged particle traps, linear Paul traps offer the possibility to store more particles close to the trap axis, where they are nearly at rest. In addition, they also ensure good optical access, which is favorable for the laser cooling and for spectroscopic measurements. An advantage compared to Penning ion traps [48] is the absence of magnetic fields, which would lead to Zeeman broadening and shifts.
For small Mathieu stability parameters $q$ one can approximate the interaction of the ions with the trap by an effective time-independent harmonic potential

$$U_{trap}(x, y, z) = \frac{m}{2}(\omega_r^2(x^2 + y^2) + \omega_z^2 z^2), \tag{2.2}$$

where the $z$-axis is the trap axis. The mass-specific motion of a single particle in such a potential is a superposition of harmonic motions with a transverse (to the $z$-axis) oscillation frequency $\omega_r = (\omega_0^2 - \omega_z^2/2)^{1/2}$, with $\omega_0 = QV_{RF}/\sqrt{2}m\Omega r_0^2$. The longitudinal frequency is $\omega_z = (2\kappa QV_{EC}/m)^{1/2}$, where $\kappa$ is a geometrical constant, $\kappa \approx 3 \times 10^{-3}\,\mathrm{mm}^{-2}$ for our traps.
The atomic coolants, beryllium and barium atoms, are produced by evaporating neutral atoms from an oven and ionizing them in-situ in the trap by an electron gun. For laser cooling of $Be^+$ ions light resonant with the $^2S_{1/2}(F = 2) \rightarrow {}^2P_{3/2}$ transition at 313 nm is produced [51]. Population losses by spontaneous emission to the metastable ground state $^2S_{1/2}(F = 1)$ are prevented by using repumping light red detuned by 1.250 GHz. $^{138}Ba^+$ ions are laser cooled on the $6^2S_{1/2} \rightarrow 6^2P_{1/2}$ transition at 493.4 nm [52]. A repumper laser at 649.8 nm prevents optical pumping to the metastable $5^2D_{3/2}$ state. In both setups absolute frequency stability is achieved by locking to hyperfine transitions in molecular iodine. The spontaneous atomic fluorescence can be recorded using photomultiplier tubes and charge-coupled device (CCD) cameras.
There are different ways to produce atoms and molecules to be sympathetically cooled. One way is to leak neutral gases into the vacuum chamber and ionize them *in situ* by an electron beam crossing the trap center [53, 54]. The loading rate is controlled by the partial pressure of neutral He gas and the electron beam intensity. However, this method is not very efficient for larger, polyatomic molecules, since a significant fraction is fragmented. As alternative, heavy polyatomic molecules with masses up to several thousand amu can be transferred into the gas-phase from solution, by electrospray ionization (ESI). There, charged droplets of the solvent are ejected by a needle and undergo rapid evaporation into smaller and smaller droplets until a final Coulomb explosion causes a significant fraction of single molecules to be created with varying numbers of protons attached. Molecules of a desired charge-to-mass ratio are then selected using a quadrupole mass filter. Fig.2.3 illustrates the principle of electrospray ionization and shows a mass-to-charge spectrum obtained for complex molecules. Since

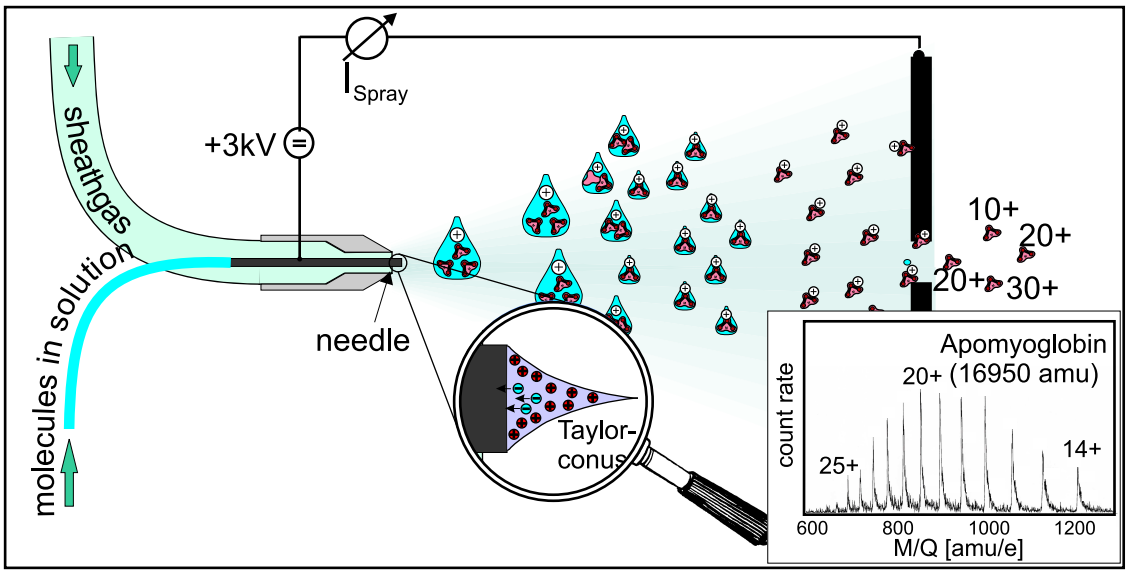


**Figure 2.3:**
Electrospray-ionization (ESI) method. ESI principle and mass-to-charge spectrum obtained for complex molecules (Apomyoglobin) [49].

the molecules are produced outside the ion trap, a radio frequency octopole ion guide has been developed and used for their transport and injection into the trap, see Fig.2.2 [49].

## 2.3 Cold trapped Coulomb clusters: one-component and multi-component non-neutral plasmas

A prerequisite for sympathetic cooling is the availability of cold atomic ions used as coolants. Using lasers, trapped atomic ions can be efficiently cooled to mK temperatures. Strong cooling results in phase transitions to a crystalline state, a Coulomb crystal, whose occurrence is described by the interaction parameter $\Gamma = Q^2/4\pi\epsilon_0 a k_B T$, the ratio between average nearest-neighbor Coulomb energy and thermal energy ($a$: average particle spacing, $Q$: particle charge) [55]. In this state the plasma exhibits strong spatial correlations. Typically, the phase transition to a crystalline state (onset of long-range order) for infinite one-component plasmas is predicted for $\Gamma > 170$ [56]. This corresponds to translational temperatures of the ions of $\approx$3 mK, at typical values $a \approx 30\,\mu$m. In finite systems, however, the phase transition occurs at higher temperatures, corresponding to smaller values for $\Gamma$, see Fig.2.4. For $\Gamma \geq 2$, the plasma becomes fluid-like (onset of short-range order), whereas for $\Gamma < 2$ it is called gaseous. Typical one component ion crystals containing beryllium and barium ions used for sympathetic cooling are shown in Fig.2.5. The images were observed using a CCD camera

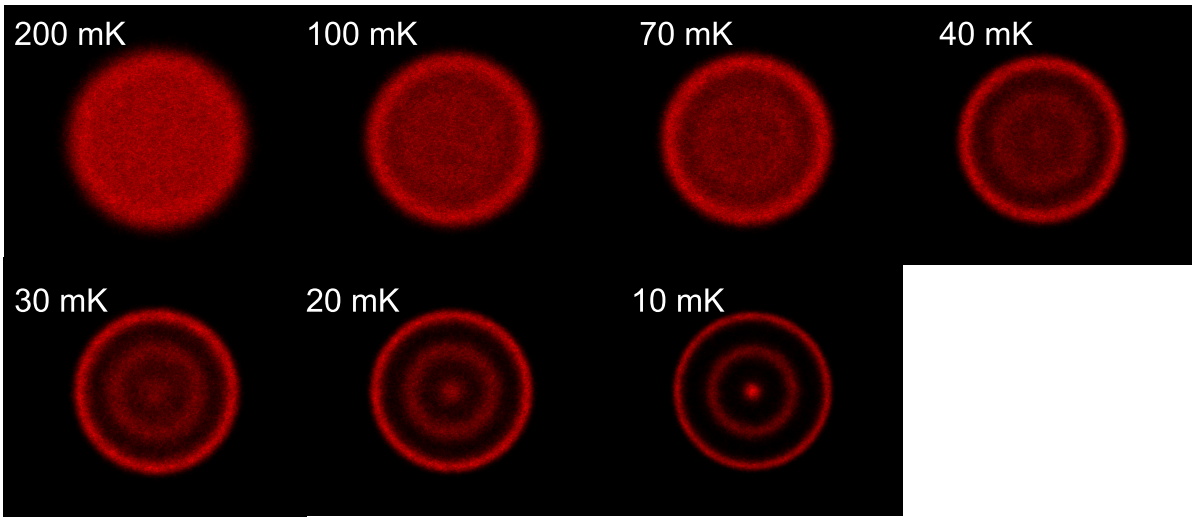


**Figure 2.4:**
Fluid-to-crystal phase transition. MD simulation of an one-component ion plasma containing 500 $Be^+$ ions for different translational temperatures. Particle trajectories were simulated for 1 ms. The view is in the $x$-$y$-plane of the trap. Only a short section along $z$ is shown. Clear separation between the ion shells is observed at temperatures $\leq$30 mK, while the plasma is fluid above $\approx$200 mK.

to observe the spontaneous fluorescence emission of the atomic ions when exposed to the cooling lasers. The direction of observation is perpendicular to the trap symmetry axis.

In the next step, atomic and molecular ions are added to the trap. Efficient sympathetic cooling is achieved, when all species are simultaneously trapped and, in addition, they exhibit a good spatial overlap. The condition for stable trapping is achieved, when the Mathieu stability parameters $q \sim Q/m$ of each species is smaller than 0.9. Furthermore, lower $q$-parameters are favorable, since the particles are located closer to the trap axis where heating effects are smaller. A good spatial overlap between the different species is obtained when the trap potentials $U_{trap,LC}$ and $U_{trap,SC}$ are similar in radial direction, or $Q^2/m_{LC} \approx Q^2/m_{SC}$, see Fig.2.6. Therefore, a good choice are (light) beryllium ions to sympathetically cool light and medium-sized atoms and molecules, whereas for heavy SC species a heavy atomic coolant (barium) is required.

Fig.2.7 shows beryllium and barium ions crystals after loading and sympathetic cooling of various atomic and molecular species. Due to their different mass-to-charge ratio, the SC particles are radially separated from the atomic coolants. For example, SC $HD^+$ ions (Fig.2.7 a) are located closer to the trap axis, due to their smaller mass-to-charge ratio (and consequently, the steeper trap potential) compared to the atomic coolants. This is obvious from the appearance of a dark (non-fluorescing) core in the initially pure ion crystal. Heavier SC ions with a larger mass-to-charge ratio are less tightly bound

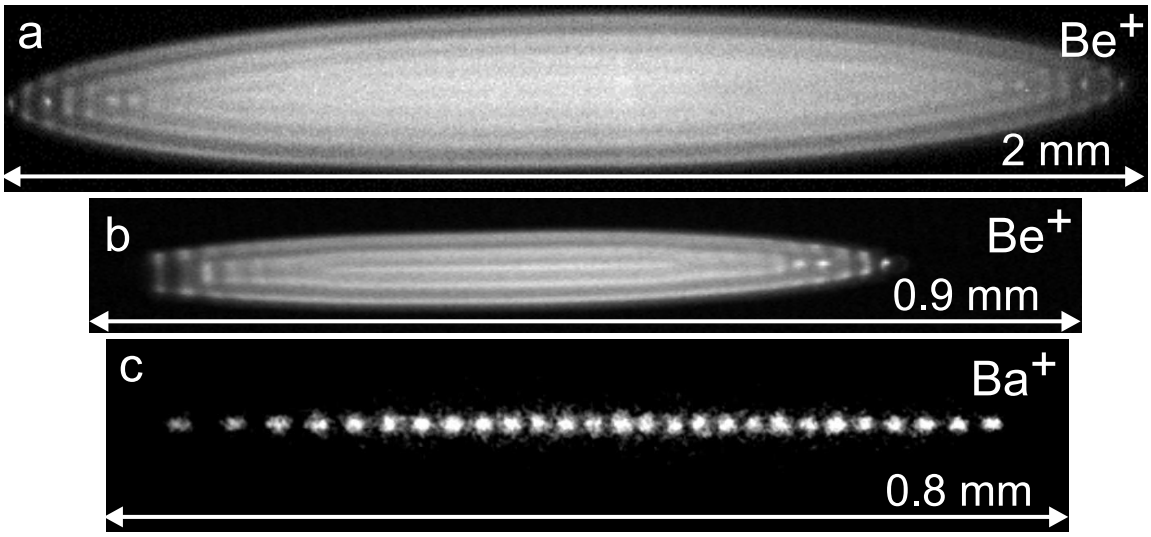


**Figure 2.5:**
Pure one-component Coulomb crystals. (a) Large ion crystal containing 2500 laser-cooled $^{9}Be^{+}$ at 20 mK translational temperature. (b) Medium-sized ion crystals containing 200 laser-cooled $^{9}Be^{+}$ at 10 mK. (c) Linear ion chain containing 27 laser-cooled $^{138}Ba^{+}$ ions at <5 mK. The trap axis $z$ is horizontal. The cooling laser beam direction is to the right. Ion numbers and temperatures were obtained from MD simulations, see Section 3.5. CCD camera integration time: 2 s.

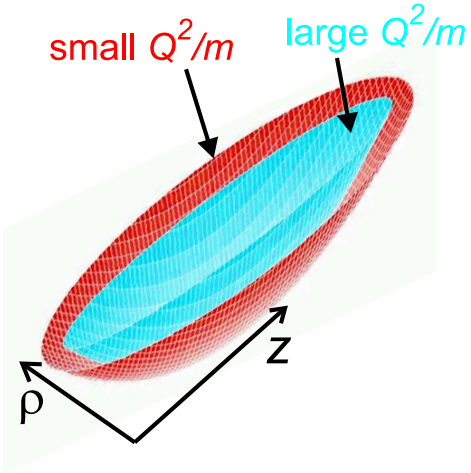


**Figure 2.6:**
The effective trap potential (for different values of $Q^2/m$). $\varrho = \sqrt{x^2 + y^2}$ and $z$ are the radial and axial trap coordinates, respectively. Efficient sympathetic cooling is achieved when $Q^2/m_{LC} \approx Q^2/m_{SC}$, i.e., when the LC and SC ion ensembles (assuming similar ion numbers) have good spatial overlap.

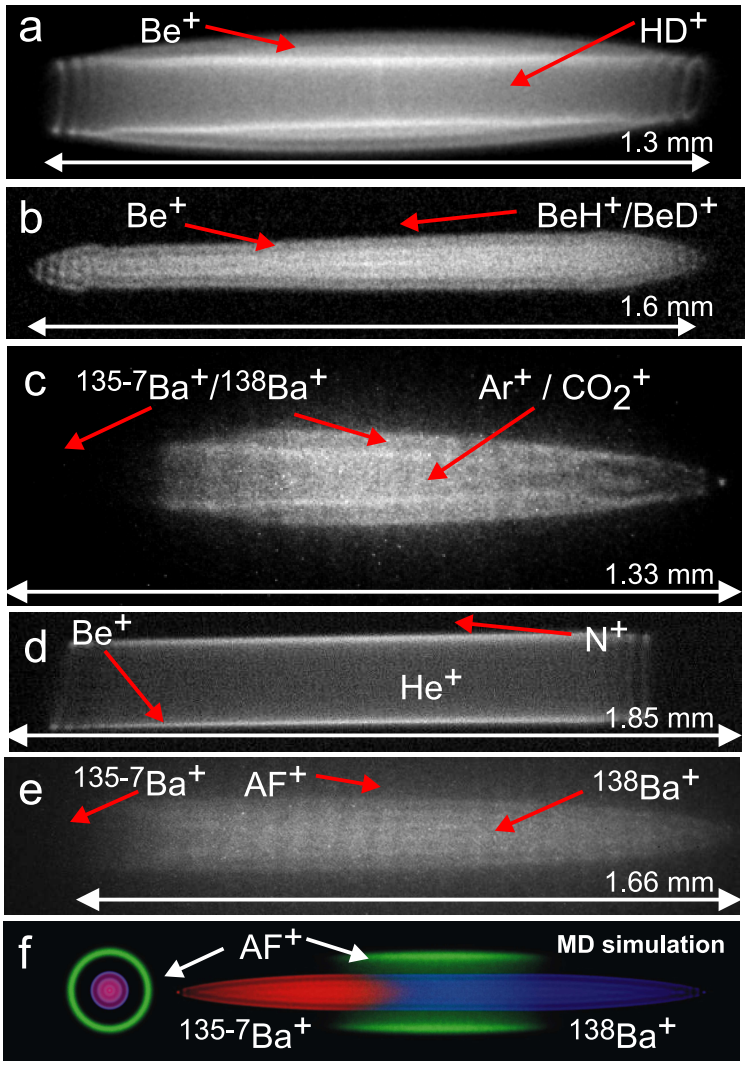


**Figure 2.7:**
Examples of mixed-species crystalline ion-plasmas. (a) 2000 LC $Be^+$ ions and 100 SC $HD^+$ ions at 30 mK, (b) 900 LC $Be^+$ ions, 1200 SC $BeH^+$ and $BeD^+$ ions (in equal amounts) at 15 mK [58]. (c) 300 LC $^{138}Ba^+$ ions, 150 SC $^{135-137}Ba^+$ isotopes, 240 SC $BaO^+$ ions, and ≈200 SC $Ar^+$ and $CO^+$ ions at ≈20 mK [52]. (d) 500 LC $Be^+$ ions, 1500 SC $He^+$, and 800 $N^+$ ions at ≈12 mK (e) 830 LC $^{138}Ba^+$ ions, 420 SC $^{135-137}Ba^+$ isotopes, and 200 SC $AF^+$ ions (mass 410 amu). The temperature of the barium ions including isotopes is at 25 mK, whereas the $AF^+$ ions are at ≈95 mK. (f) MD simulation of the crystal in (e) [57].

and are located outside the fluorescing crystal body (Fig.2.7 b,c,d). Fig.2.7 e shows a simulation of the crystal in (d), see also Chapter 3.
Certain molecular species, such as $H_2D^+$, $BeH^+$, $ArD^+$, or $BaO^+$ cannot be produced by loading and ionization of neutral gases or by using an ESI source. Here, controlled, sometimes multi-step, chemical reactions were used for their production, see,

| **Sympathetically cooled molecules** | | |
|---|---|---|
| | crystallization achieved | fluid state only |
| this work | $H_2^+$, $HD^+$, $D_2^+$, $H_3^+$, $D_3^+$, $H_2D^+$, $HD_2^+$, $BeH^+$, $BeD^+$, $NeH^+$, $NeD^+$, $N_2^+$, $OH^+$, $H_2O^+$, $O_2^+$, $O_2H^+$, $ArH^+$, $ArD^+$, $CO_2^+$, $KrH^+$, $KrD^+$, $BaO^+$, $C_4F_8^+$, $AF350^+$, $GA^+$, $R6G^+$ and fragments | |
| Aarhus Univ. | $MgH^+$, $O_2^+$, $MgO^+$, $CaO^+$ (see, e.g., [42, 60]) | |
| Hitachi Res. Center | | $NH_4^+$, $H_2O^+$, $H_3O^+$, $C_2H_5^+$, $COH^+$, $O_2^+$ (see, e.g., [41, 61]), |
| NIST (Boulder) | $BeH^+$ [62] | |
| Texas A & M Univ. | | $C_{60}^+$ [63] |
| **Sympathetically cooled atoms** | | |
| this work | $H^+$, $D^+$, $^3He^+$, $^4He^+$, $N^+$, $O^+$, $Ne^+$, $Ar^+$, $Ar^{2+}$, $Kr^+$, $Xe^+$, $^{135-137}Ba^+$ | |

**Table 2.1:**
Cold atomic and molecular ions produced by sympathetic cooling.

e.g, [52, 58, 59] and Chapter 4. Table 2.1 gives an overview of the molecular species sympathetically cooled and crystallized during this work. Among the largest molecules cooled and crystallized so far are $AF350^+$ (AlexaFluor350, 410 amu) and $R6G^+$ (Rhodamine 6G, 470 amu), common dye molecules, and $GA^+$ (glycerrhetinic acid, 480 amu). Typical temperatures achieved were in the range of 5-50 mK. Heavy molecules, such as $AF^+$ ions (mass 410 amu), were cooled to temperatures of 95 mK. The temperatures obtained are determined by the cooling and heating rates present in the trap and depend on the trap parameters and ion numbers involved. Using the cooling technique described here, it is expected that the achievable temperatures for LC and SC ions can be as low as the Doppler cooling limit ($\approx 0.5$ mK) for the atomic coolants. Lower temperatures could, in principle, be obtained using more sophisticated cooling techniques, such as sideband cooling or stochastic cooling (for example), see [64, 65].

Several atomic species were also sympathetically crystallized (Table 2.1), among them

| **Sympathetically crystallized molecular ions** |
|---|
| • have very low kinetic energies |
| • are confined in space in crystal-like structures |
| • are isolated to a large extent from perturbations by electric or magnetic fields |
| • are in a near collision-free regime |
| • are at large distances to the next neighbors in the crystal (between 10-30 $\mu$m) |
| • can be stored from several minutes up to several hours, thus eliminating transit-time broadening and allowing for long interrogation times by lasers |

**Table 2.2:**
Properties of sympathetically cooled molecular ions.

protons, helium isotope ions, and doubly-charged argon ions. Whereas cold protons could be interesting systems for the study of cold chemical reactions, the $^3He^+$ and $^4He^+$ isotopes are important systems because they are complementary to the hydrogen atom. For example, precision measurements of transition frequencies in helium ions could provide an independent determination of the Rydberg constant, of nuclear charge radii and the isotope shift, assuming QED calculations are correct, or a test of QED, using independent radius data as input [53]. Using techniques similar to this work, an experiment aimed at two-photon deep-UV $He^+$ spectroscopy is now under development at the Max-Planck-Institute in Munich (T. Udem et al.).
The cold and crystallized one-component and multi-component ion plasmas, produced via sympathetic cooling as described above, have several unique properties, summarized in Table 2.2. These features are essential for precision spectroscopic measurements, as described in Chapter 5. In particular, high-resolution rovibrational spectroscopy on a molecular system ($HD^+$) was demonstrated with unprecedented accuracy.
In Table 2.3 the sympathetic cooling method is compared to other techniques for the production of cold and ultracold molecules. The achievable temperatures and typical storage times for the different methods are given. Except for the first and the two last methods, additional electrostatic, magnetic or optical traps are required for further storage of the molecules. Typically, storage times from milliseconds to several seconds were reported so far.

| Method | Applicable to | Temperature | Groups |
|---|---|---|---|
| Buffer gas cooling & evaporation in magnetic quadrupole traps | paramagnetic molecules | ≈300 mK storage time <1 s | Harvard, Berlin,... |
| Supersonic expansion & Stark deceleration | polar molecules | ≈25 mK | Berlin, Hannover, Boulder, London |
| Cold particle selection | polar molecules | ≈500 mK | Garching |
| Photoassociation & Feshbach resonances | laser-cooled atoms | <50$\mu$K to several nK | Paris, Innsbruck,... |
| Collisional cooling | medium-sized molecules | ≈400 mK | Livermore [22] |
| Rotating nozzle & supersonic expansion | medium-sized molecules | several K to several ten K | Harvard, Bielefeld,... |
| Implantation into superfluid He droplets | neutral/charged atoms & molecules | ≈380 mK short observation times, due to high-speed of droplets | Göttingen, Chapel Hill, Freiburg, Graz, Bochum,... |
| Buffer gas cooling or cooling by cryogenic environment | charged atoms & molecules | several ten K storage time ∼ s | Chemnitz, Harvard, Köln, Lausanne,... |
| Sympathetic cooling (in ion traps) | charged atoms & molecules (also to neutrals) | ≈5 mK storage time ∼ minutes to several hours | Düsseldorf, Aarhus, NIST, College Station, Hitachi,... |

**Table 2.3:**
Overview of the methods used for cold and ultracold molecule production.

# Chapter 3

# Characterization and Manipulation of Cold Multi-Species Ion Plasmas

## 3.1 Properties of trapped non-neutral ion plasmas

One important property of cold non-neutral (pure or mixed-species) plasmas with a single sign of charge is, that they can be stored, for example, by using electric and magnetic fields. They also can reach a state of global thermal equilibrium. These properties make them interesting systems to study by both theory and experiment [55, 66].
Experimentally, such cold plasmas can be studied under a variety of conditions with a high degree of experimental control. For example, the relative fraction of particle constituents, the plasma temperature, or the shape and the symmetry of the trapping potential can easily be varied, allowing for detailed systematic studies. On the theoretical side, the analytic theory and numerical simulations of the plasma shape and the microscopic order, as well as the phase transition to the crystalline state being fundamentally different to the gas-fluid transition are of interest.
The spatial distribution of trapped one- and multi-component gaseous plasmas differs significantly from the fluid and crystalline state, as described by a global parameter, the Debye length $\lambda_D = (k_B T \epsilon_0 / nQ^2)^{1/2}$ ($n$ is the particle density of the plasma). This parameter describes the distance below which interactions between individual particles overcome collective effects, i.e. space charge effects become important [55]. Whereas warm non-neutral plasmas in ion traps display plasma oscillations and instabilities (weakly coupled regime), at low temperatures correlation effects become dominant (strongly coupled regime) and can be investigated.
Fig.3.1 shows a series of CCD images (a-d) of a pure one-component Coulomb crystal containing ≈250 $Be^+$ ions at 10 mK. By varying the static voltage on the endcap electrodes or the voltage of the rf amplitude the aspect ratio of the crystal was changed from prolate to round and oblate. For certain trap parameters, not only the microscopic order of the ions can change, but also the long-range order. One can observe a disk-

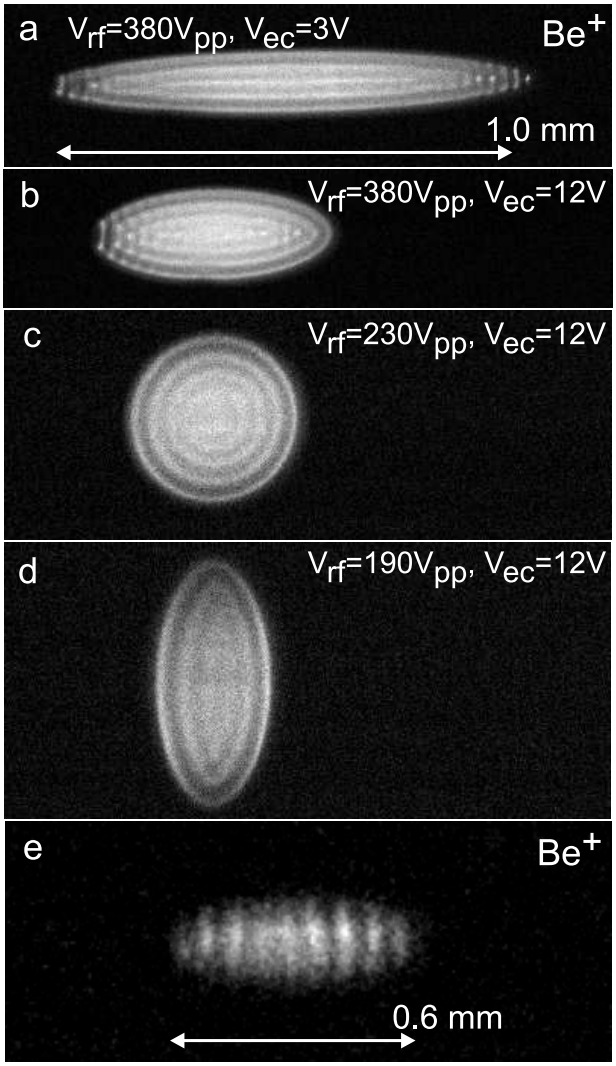


**Figure 3.1:**
Variation of Coulomb crystal shape with trap anisotropy. The static voltage on the endcap electrodes of the trap (yielding the axial confinement) was changed from 3 V (a) to 12 V (b), whereas the amplitude of the rf drive $V_{rf}$ (yielding the radial confinement) was changed from 380 $V_{pp}$ (peak-to-peak amplitude) (a,b) to 230 $V_{pp}$ (c) and 190 $V_{pp}$ (d). In this way, the aspect ratio of the cold plasma was changed over a wide range. The pictures are part of a sequence recorded over ≈2 minutes. The pure beryllium Coulomb crystal is at 10 mK. (e) Disk-shaped one-component Coulomb crystal, caused by rotation-like motion of the ions around the trap axis. The symmetry of the trap potential is cylindrical in all cases.

shaped configuration of the crystals, as shown in Fig.3.1 e, attributed to a rotation-like motion of the ions around trap symmetry axis, possibly due to a torque induced by the cooling laser or small anisotropies of the trapping potential. Detailed investigations of such structural transitions and of three-dimensional long-range orders in cold ion

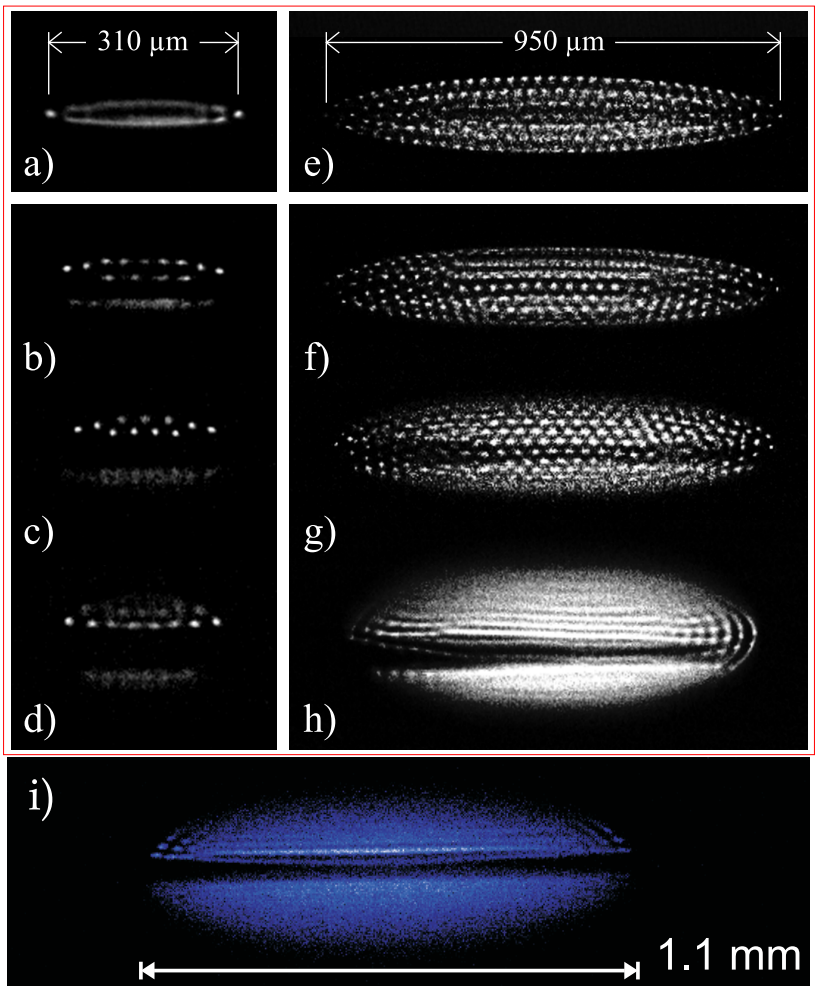


**Figure 3.2:**
Deformation of mixed-species crystals by a static quadrupole voltage $V_{DC}$ applied to the central electrodes. Left: small crystal containing $\simeq 20$ $Be^+$ and a smaller number of SC impurity ions at different values $V_{DC}$: 0 V (a), 2.8 V (b), 3.6 V (c), 4.2 V (d). Right: medium-sized crystal containing $\simeq 500$ $Be^+$ ions. $V_{DC}$ is set to 0 V (a), 1.4 V (b), 2.8 V (c), 4.0 V (d). Asymmetries in (b)-(d) and (f)-(h) are due to stray electric fields [72]. (i) Cold $Be^+$ ion crystal containing $HD^+$ ions in an asymmetric trap potential ($V_{DC} = 4.4$ V). For vanishing static voltage $V_{DC}$ the trap potential has cylindrical symmetry and the shape of the crystals is spheroidal, whereas for $V_{DC} \neq 0$ V the cylindrical symmetry is broken and the crystal shape is ellipsoidal.

crystals are reported by the group of M. Drewsen (Aarhus), see [67, 68] and references therein.

The properties of cold ion plasmas depend strongly on the symmetry of the trapping potential. For cylindrical trap potential symmetry, where the plasmas are spheroids, they were studied in both in linear radio frequency and Penning traps [60, 69]. In the absence of cylindrical symmetry the shape of the plasma has been predicted to be

that of an ellipsoid [70]. Ellipsoidal plasmas have already been observed and studied in Penning traps (see [71] and references therein). In this work, cold ellipsoidal plasmas in a linear Paul traps were produced and characterized, for the first time, by adding a static quadrupole potential to the effective trap potential and breaking its cylindrical symmetry. In particular, ellipsoidal crystals containing two ([72]) or more (up to 6) different ion species were obtained, see, e.g., Fig.3.2. The overall shape of Coulomb crystals in a fully anisotropic effective trap potential was studied and compared to theoretical predictions from a simple cold fluid plasma model. Deviations between experiment and theory, observed for larger anisotropy can be explained by the presence of some SC particles, indicating the relevance of space charge effects in this regime.
The ability to reversibly deform cold multi-component crystals by static quadrupole potentials, is interesting for several reasons. It allows for (i) a controlled ejection of heavier ion species from the trap (see below), (ii) for a complete radial separation of lower-mass SC ions from the LC ions, and (iii) opens up the possibility of studying trap modes of oscillation of ellipsoidal crystals, in particular of multi-species crystals. Conversely, a precise measurement of the trap modes of oscillation of cold ion crystals allows for the identification of even small anisotropies of the effective trap potential, which is important for precision measurement applications and the characterization of systematic effects, such as offset potentials [52].
Furthermore, by applying static offset potentials to individual trap electrodes a spatial manipulation of the ion crystals is possible. For example, by carefully aligning the atomic coolant ions around the dark core containing SC ions with a spatial accuracy $<20\,\mu$m, while observing the crystal using the CCD camera, trap imperfections can be minimized more efficiently compared to the commonly used fluorescence correlation measurements (Fig.3.2 i), see, e.g. [52, 73].

## 3.2 Particle Identification

Since fluorescence detection is not applicable to trapped and sympathetically cooled molecular ions in UHV [74], different techniques are required for their reliable identification. A commonly used destructive technique for molecular ions or after ionization of neutral molecules is time-of-flight mass spectroscopy. In this work, a slightly different, even simpler technique was developed. The trapped ions are extracted from the trap by reducing the radio frequency amplitude, which reduces the depth of the trap potential. Thus, for our experimental conditions, heavy and hot ions escape first. Upon leaving the trap, the ions are guided to and attracted by the cathode of a channel electron multiplier (CEM) and counted.
Fig.3.3 shows an example of a mass spectrum obtained. The ion count peaks occur at clearly separate radio frequency amplitudes, allowing for identification if LC and SC ions. Assuming equal detection efficiencies, the ion signal sizes allow determination of the ratio of the number of barium ions to $AF^+$ ions. In addition, the spectrum also

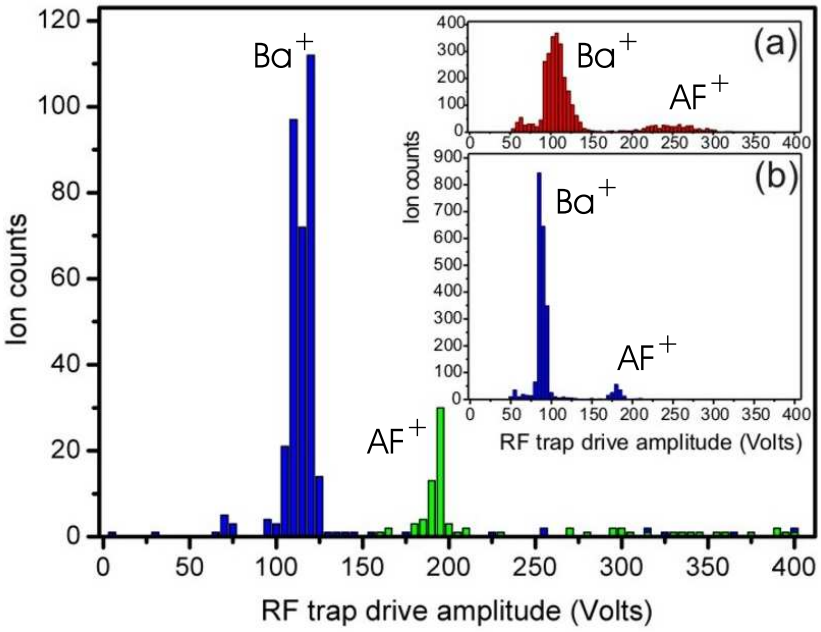


**Figure 3.3:**
Extraction of ions (of crystal in Fig. 2.7(e)) from the trap by reduction of the RF drive amplitude. $AF^+$ ions (mass 410 amu) are ejected first (green peak); inset (a): extraction of a different sample of non-laser-cooled barium and $AF^+$ ions at ~300 K; the small left-hand peak is due to SC $CO_2^+$ impurities; inset (b): extraction of a laser-cooled $Ba^+/AF^+$ ion cloud at a temperature of a few hundred mK (fluid state) [57].

provides evidence that the heavier molecules are sympathetically cooled by the barium ions, as can be seen by comparing the two insets in Fig. 3.3. Whereas the Fig. 3.3 a (inset) shows the extraction of both ion species when laser cooling is not applied, i.e. the ensemble is at room temperature, Fig. 3.3b (inset) shows the mass spectrum of an ensemble with similar ion numbers when the barium ions have been laser-cooled. For this case, the ion count peaks are narrower, indicating a narrowed energy distribution.

However, for a more accurate determination of the temperature of LC and SC ions as well as for an increased mass-to-charge resolution, nondestructive techniques are more favorable. One nondestructive technique is based on the excitation of mass-dependent motional resonances of trapped species. This technique has been used in the past for mass spectrometry of large ion clouds [41, 75]. For small systems containing a single molecular ion sympathetically cooled by a single atomic ion, the demonstrated mass resolution can be very high [43].

Here, excitation of motional resonances was used to identify atomic and molecular species embedded in large multi-species (beryllium and barium) ion crystals of various size, shape and symmetry [54, 57, 76]. No results were reported such ion plasmas before, neither were they accessible in experiment for systematic studies. In particular,

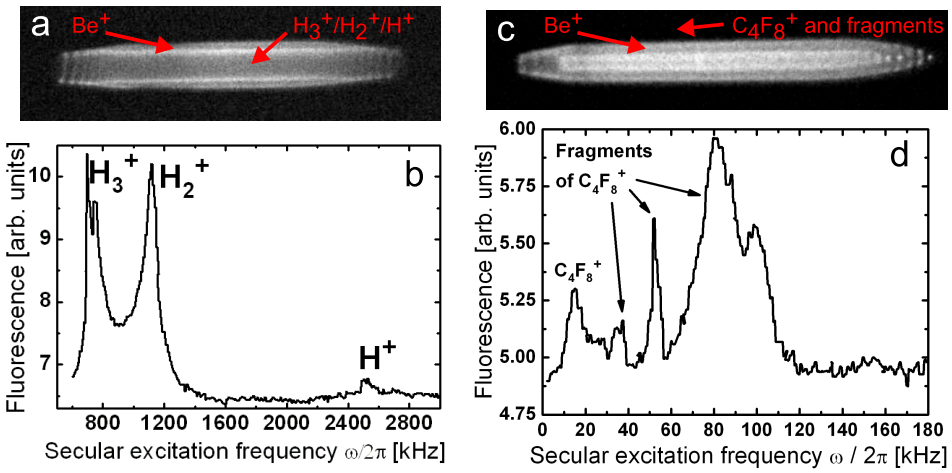


**Figure 3.4:**
Motional frequency spectra of mixed-species ion crystals. (a) Crystal containing $Be^+$, $H_3^+$, $H_2^+$, and $H^+$ ions at ≈15 mK. (b) Motional frequency spectrum (low-mass range) of the crystal in (a). The measured motional frequencies are shifted compared to the calculated single-particle frequencies (840 kHz for $H_3^+$, 1260 kHz for $H_2^+$, and 2520 kHz for H+; the $Be^+$ motional frequency is at 280 kHz), due to Coulomb coupling between LC and SC ions. (c) Crystal containing $Be^+$, $C_4F_8^+$, and various fragments of $C_4F_8^+$ ions at ≈20 mK. (d) $Be^+$ crystal after loading of $C_4F_8^+$ ions and fragments. (d) Motional frequency spectrum (high-mass range) of the crystal in (c). The calculated single-particle frequency for $C_4F_8^+$ (13 kHz) agrees well with the measured value (15 kHz), due to smaller Coulomb coupling to all other species. The fragment ions act as conducting layer and ensure efficient sympathetic cooling of the $C_4F_8^+$ ions [57].

cold ion plasmas containing several thousand ions and large fractions of SC ions were not studied previously.

The basic principle of the method is as follows: the radial motion of the ions in the trap is excited using an oscillating electric field of variable frequency applied either to an external plate electrode or to the central trap electrodes. When the excitation field is resonant with the oscillation mode of one species in the crystal, energy is pumped into the motion of that species. Some of this energy is distributed through the crystal as heat, via the Coulomb interaction. This, in turn, leads to an increased temperature of the atomic coolants and modifies their fluorescence intensity, which can be detected.

Fig.3.4 shows examples of multi-species ion crystals and their (radial) motional resonance spectra obtained. Fig.3.4 b shows the spectrum of a cold beryllium ions crystal containing $Be^+$, $H_3^+$, $H_2^+$, and $H^+$ ions at 15 mK. Even though the measured motional frequencies are shifted compared to their calculated single-particle frequencies, particle identification is possible. Fig.3.4 d shows a spectrum of a beryllium ion crystal containing $C_4F_8^+$ ions and various fragment ions (Fig.3.4 c). Due to the above coupling effects, reliable particle identification requires the use of MD simulations, see below.

## 3.3 Motional resonance coupling in cold multi-component ion crystals

In general, simple scaling laws apply for the radial oscillation frequencies of single trapped ions ($\omega_r \propto q/m$, see Eq.2.2) for the conditions chosen in traps used here [76]. Thus, simple ratios are expected between the motional frequencies of different trapped species, if the coupling between species is neglected. However, the interactions between the different ion species can perturb the observed motional frequencies by a significant amount (compared to the calculated single-particle frequencies). This complicates the analysis of the experimental spectra, in particular, for mixed-species ion crystals where the SC ions have comparable mass-to-charge ratios. Examples of spectra obtained for such an ion crystal are displayed in Fig.3.5.
A number of different line shifting effects were identified and studied systematically, for the first time, in this work. For example, the motional frequencies depend on the fractions of particles contained in the crystal. For strong coupling between the ion species, this can lead to a significant shift and broadening of individual features in the spectrum, so that they cannot be resolved in experiment (Fig.3.5 a). However, even for weaker coupling (Fig.3.5 b), various, sometimes more subtle, line shifting effects can be present, e.g., caused by space charge effects, trap anisotropies, or the finite amplitude of the excitation field. The observed frequency positions also depend on the sweep direction of the excitation field and the plasma temperature. Finally, the state of the ion plasma, crystalline or fluid, affects the motional resonances measured (see Fig.3.5 c).
Usually, the observed resonance frequencies are determined by a superposition of several, sometimes opposing line shifting effects. Therefore, an unambiguous identification of particles embedded in large, mixed-species ion crystals is not possible based on the experimental measurements only. In this work, the experimental data were compared to results from MD simulations (see Section 3.5), leading to an improved interpretation, and thus, to increased sensitivity for spectroscopic and chemical experiments on cold, trapped molecular ions.

## 3.4 Species-selective particle removal from Coulomb clusters

During loading and ionization of neutral gases in the trap center various impurity ions can be produced, along with the species under study, by chemical reactions between LC or SC ions and neutral gases. Such impurities can complicate precise measurements of motional resonances or systematic studies on pure or few-species ions plasmas. In particular, for the applications described in Chapters 4,5, crystals with a single species of SC particles are required. It is therefore favorable to remove unwanted species from

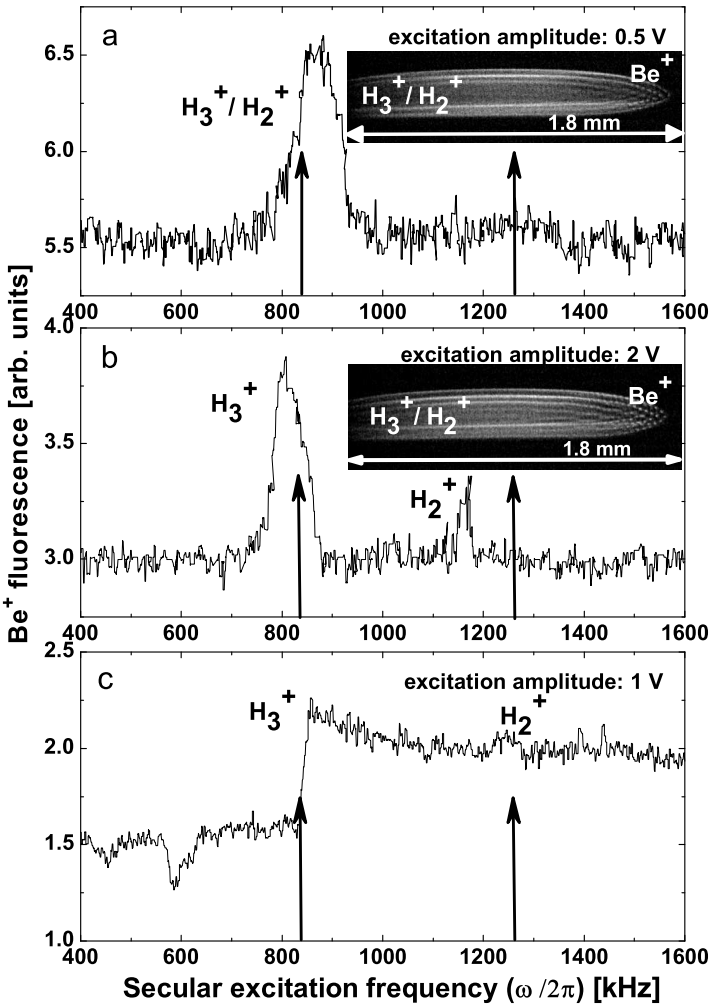


**Figure 3.5:**
Interaction-induced strong (a,b) and weak (b) coupling between radial modes. Motional frequency spectrum of (a) a $Be^+$ ion crystal following electron impact ionization of $H_2$. The crystal (inset) contains $\approx$ 1400 LC $Be^+$ and $\approx$ 1300 SC ions ($\approx$ 700 $H_2^+$ and $H_3^+$ in the crystal core, and $\approx$ 600 $BeH^+$ outside the $Be^+$, responsible for the slight asymmetry in the shape. Translational temperature $\approx$ 20 mK. (b) ion crystal in (a) after after partial removal of lighter SC ions (reduced size of the core), containing $\approx$ 1350 $Be^+$ and $\approx$ 1200 SC ions: $\approx$ 450 $H_3^+$, $\approx$ 100 $H_2^+$, and $\approx$ 650 $BeH^+$. (c) Spectrum following electron impact ionization of $H_2$ in the cloud state. Calculated single-particle secular frequencies (marked by arrows): 840 kHz ($H_3^+$) and 1260 kHz ($H_2^+$). The feature at $\approx$ 580 kHz is attributed to the second harmonic of the $Be^+$ trap mode (at 280 kHz) [76].

the crystal and leaving all other species undisturbed.

Particles with a mass-to-charge ratio **larger** than that of the atomic coolants, located outside the laser-cooled ion shells can be removed from the trap species-selectively by

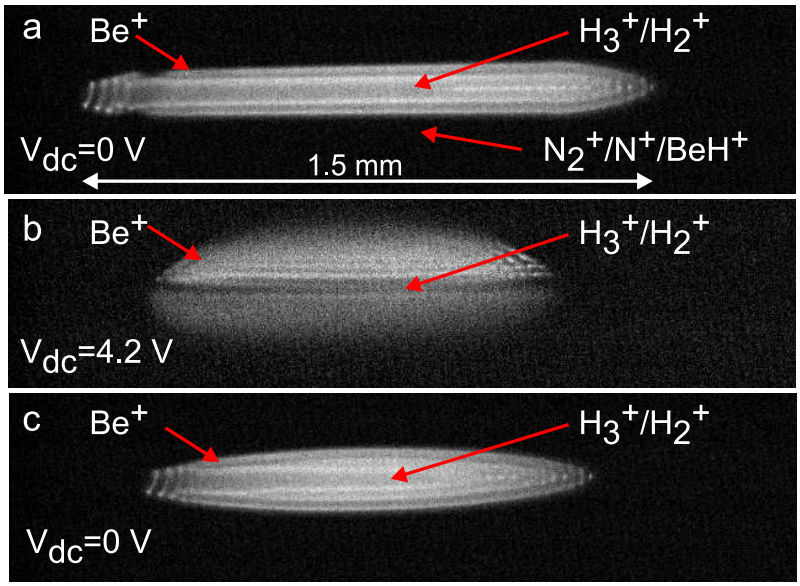


**Figure 3.6:**
Species-selective removal of heavy SC ions from a mixed-species ion crystal, by applying a static quadrupole potential $V_{DC}$ to the trap electrodes. CCD images are taken before (a) during (b) and after (c) removal of the particles. After removal a re-ordering of the beryllium ions shells is observed. The temperature of the crystal is slightly reduced, since heating effects for particles closer to the trap axis are smaller compared to those for particles at larger radial distances, leading to smaller equilibrium temperatures.

adding a static quadrupole potential to the trapping potential (and thus, breaking its cylindrical symmetry). For a sufficiently large quadrupole potential, the ion motion along one radial frequency becomes unstable, leading to the ejection of that particular species from the trap, see, e.g., [60, 72]. After switching off the quadrupole potential, again the absence of the removed species causes a change of shape of the crystal. This procedure is illustrated in Fig.3.6, where $N_2^+$, $N^+$, and $BeH^+$ ions were removed from a cold (≈20 mK) beryllium ion crystal. The dark core of the crystal containing lighter SC ions (hydrogen molecular ions, $H_3^+$ and $H_2^+$) was not affected.
Particles with a mass-to-charge ratio **smaller** than that of the atomic coolants, located closer to the trap axis, can be ejected from the crystal as follows (Fig.3.7). By detuning the cooling laser far from resonance, the ion crystal in Fig.3.7 a undergoes a phase transition to a disordered (fluid) state. In this situation, the coupling between different ion species is much weaker than in the crystalline state, and the secular motion of the unwanted species can be strongly excited, ejecting the ions from the trap, with almost negligible effect on other species. The remaining ions can then be re-crystallized by re-tuning the cooling laser back close to resonance (Fig.3.7 b). This procedure can be used to remove as many different species as required, producing highly pure two-component crystals.

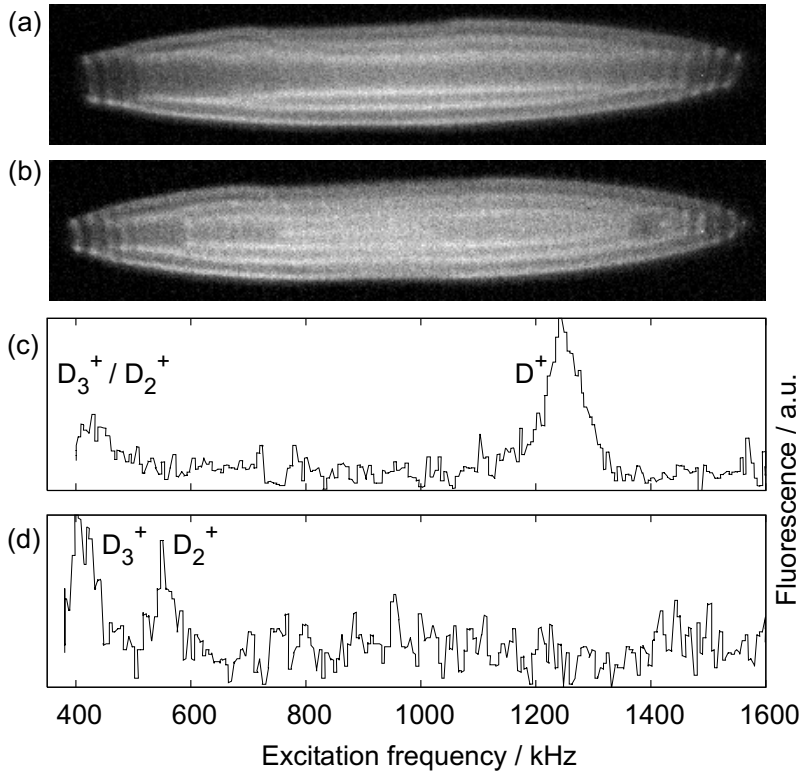


**Figure 3.7:**
Removal of light SC ions from a mixed-species ion crystal. CCD images (a) before and (b) after, and motional spectra (c) before and (d) after the ejection of mass 2 ions (deuterons) [54]. In the spectrum in (c), the individual contributions of $D_3^+$ and $D_2^+$ ions cannot be resolved, due to strong Coulomb coupling between the SC species (in contrast to the spectrum in (d)). Note that the spectra in (c),(d) were taken with different amplitudes of the excitation field, due to different ion numbers involved.

## 3.5 Molecular Dynamics simulations

### 3.5.1 Motivation

In the past, analytic calculations and numerical simulations of the dynamics of trapped charged particles were performed, in order to study the plasma properties and the spatial ordering of ion crystals, to obtain an upper limit for their translational temperature, or to investigate their eigenmodes. Usually, the models were limited to small or few-species systems, neglecting completely heating effects [55, 60, 77]. The sympathetic cooling process was simulated for small ion ensembles in a time-dependent trap potential [34]. More recently, molecular dynamics simulations of large few-species ensembles in time-dependent trap potentials were performed, in order to model radio frequency heating rates or the deceleration of highly-charged atomic ions [78, 79, 80].

Extensive numerical simulations were performed in this work in order to:

- model the three-dimensional shape and long-range order of Coulomb crystals,
- deduce ion numbers, translational temperatures, and spatial and velocity distributions of LC and SC species (see, e.g., [54, 57, 81]),
- study diffusion of ions inside Coulomb crystals,
- characterize the trap potential and determine small trap anisotropies and offset potentials,
- study properties of cold trapped ion plasmas in isotropic and anisotropic trap potentials,
- determine heating and cooling rates for LC and SC species [81],
- deduce light pressure forces (seen by the laser-cooled ions only),
- investigate micromotion heating processes and deduce rf heating rates [81],
- model motional resonance spectra of cold multi-species ion crystals,
- develop new detection methods for SC ions [58]
- analyze the extension of sympathetic cooling to complex molecules [57],
- study the coupling of the radial micromotion to the axial degrees of freedom of the ions.

### 3.5.2 Simulation model

In the simulations, Newton's equations of motions are solved for all ions in the linear Paul trap: $m_i\ddot{\mathbf{r}} = \mathbf{F}_i(\mathbf{r}_1, \ldots \mathbf{r}_{N_{LC}+N_{SC}}, \mathbf{v}_1, \ldots \mathbf{v}_{N_{LC}+N_{SC}}, t)$. Here, $i = 1, \ldots, N_{LC} + N_{SC}$ ($N_{LC}$ and $N_{SC}$ are the numbers of LC and SC ions, respectively). Masses and position vectors are $m_i$ and $\mathbf{r}_i$. The total force acting on each ion depends on ion positions, ion velocities and the time $t$ and can be written as:

$$m_i\ddot{\mathbf{r}} = \mathbf{F}_i^{trap} + \mathbf{F}_i^{Coulomb} + \mathbf{F}_i^{stochastic} + \mathbf{F}_i^{laser}, \tag{3.1}$$

Individual contributions are: the conservative trap force $\mathbf{F}_i^{trap}$, the Coulomb interaction force due to all other ions $\mathbf{F}_i^{Coulomb}$, the stochastic force $\mathbf{F}_i^{stochastic}$, due to interactions of ions with the environment, such as collisions with residual gas, scattered light, electric field noise, and the laser cooling force $\mathbf{F}_i^{laser}$, which acts on the laser-cooled ions only and also includes light pressure forces. In the simulations, individual photon absorption

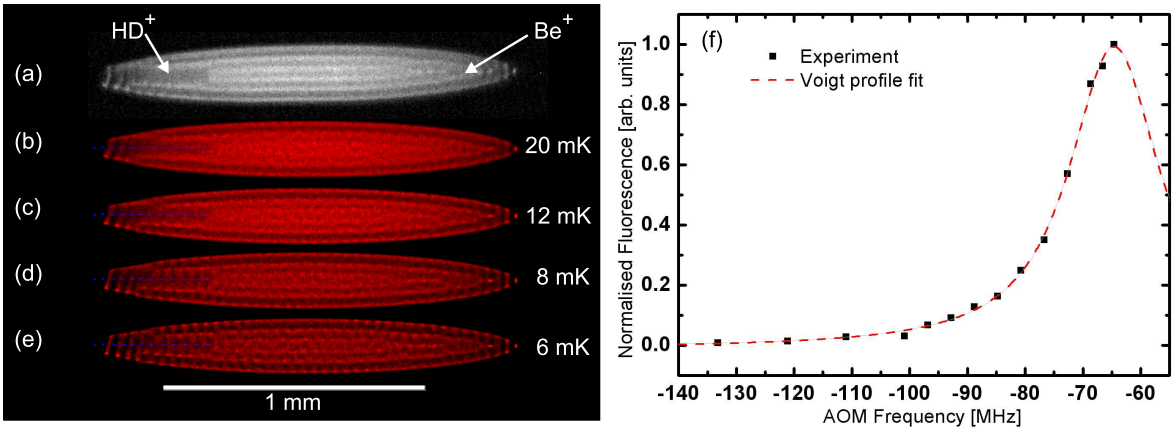


**Figure 3.8:**
Determination of translational temperatures of LC and SC ions. Left: CCD image (a) and simulated images (b-e) of a two-species ion crystal containing 690 $Be^+$ and 12 $HD^+$ ions. Ion numbers and translational temperatures for LC and SC ions are obtained by visual comparison between experiment and theory. The ions in this crystals are at around 10 mK [54]. The asymmetry of shape in axial direction is caused by light pressure forces (acting on LC ions only), included in the simulations [81]. Right: Determination of the translational temperature of a pure $Be^+$ ion crystal by fitting a Voigt profile to the fluorescence line shape yielding a temperature of $5 \pm 5$ mK. The fluorescence line shape was obtained by scanning the cooling laser over the $Be^+$ resonance using an acousto-optical modulator (AOM). Note, that the AOM frequency in the abscissa label has an arbitrary frequency offset compared to the atomic resonance. The method illustrated in (f) is not accurate enough to discriminate between a crystal at 1 mK and a crystal at 10 mK, for example.

and emission processes need not be taken into account, since the recoil energy of, for example, $Be^+$ is 11 $\mu$K, i.e. 1000 times less than typical temperatures.
In general, for the determination of ion numbers and translational temperatures, in particular, for large multi-species ion crystals, the equations of motion are solved in a time-averaged effective trap potential, see Section 2.2. This approach is less time-consuming compared to the more realistic case when rf micromotion is included, but the deviation between the results of the two approaches appear to be small for many properties of interest.

### 3.5.3 Simulation results

A comparison between observed and simulated ion crystals allows for an accurate determination of ion numbers, translational temperatures (Fig.3.8), and trap potentials [81], as well as for the investigation of diffusion dynamics and heating effects due to rf micromotion (Fig.3.9). The determination of ion numbers and temperatures via the

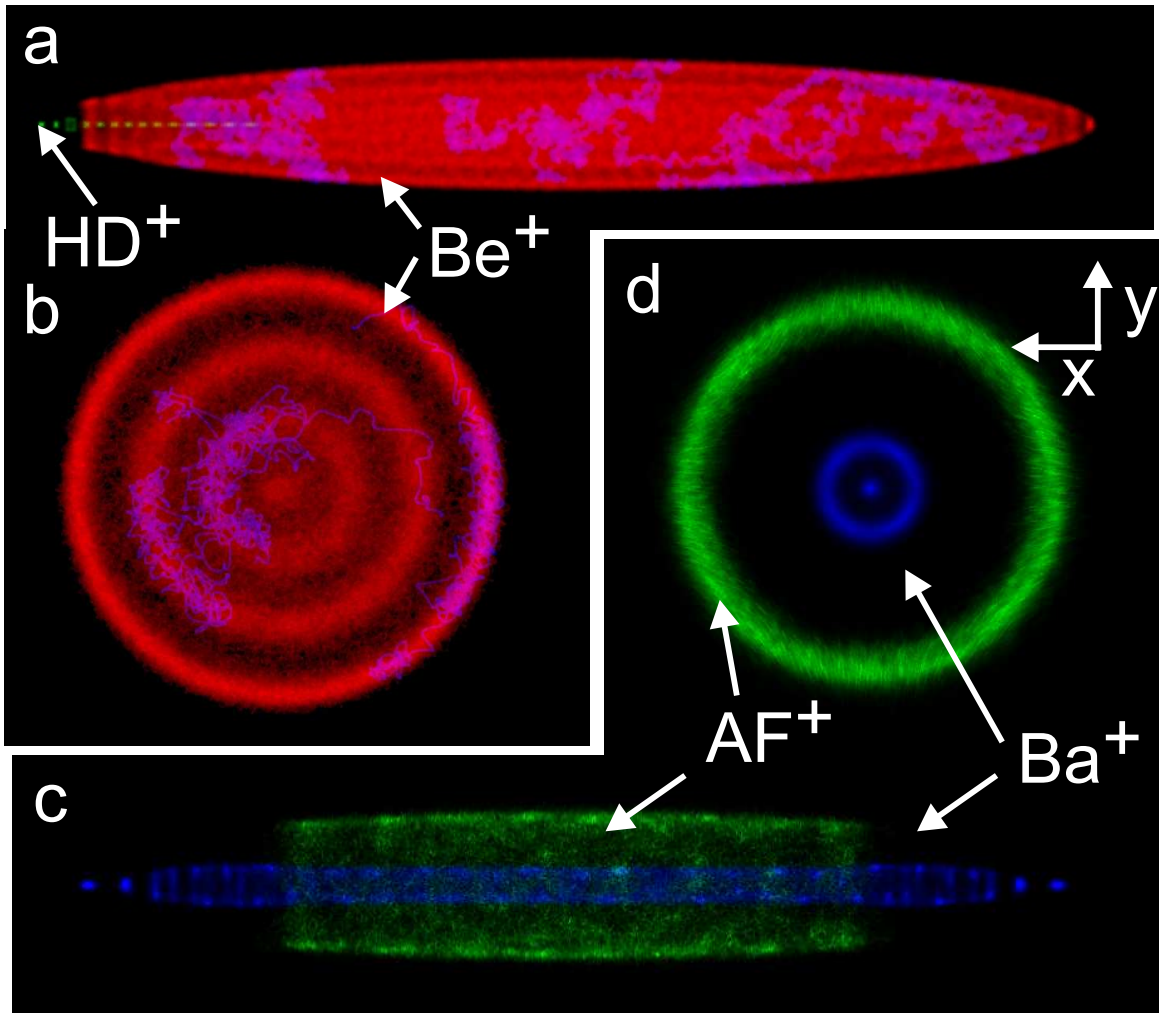


**Figure 3.9:**
Simulation of diffusion of ions in Coulomb crystals. (a) Trajectories of selected (marked) $Be^+$ ions in a cold (10 mK) $Be^+$-$HD^+$ ion crystal (time-averaged trap potential assumed; duration: 1 ms). Except for special sites, the bright spots are not the positions where a particular single ion is confined, but where the probability to find any ion is high. Simulations show that at temperatures > several mK the thermal motion is sufficiently strong that on ms timescales ions of the same species move in and out of "lattice sites". (b) Cross section of an axial section of the crystal in (a). (c) Simulation of an ion crystal containing 50 LC $Ba^+$ ions and 50 SC $AF^+$ ions at 15 mK and 18 mK, respectively. Here, rf micromotion is included. (d) Cross section of the crystal in (c). The (slight) additional blurring of the $AF^+$ ions in radial direction is due to driven micromotion directed towards the electrodes (located on the $x$ and $y$ axes). This additional blurring is not present when the simulations are performed in a time-averaged pseudopotential (see cross section in (b)), compare also [81].

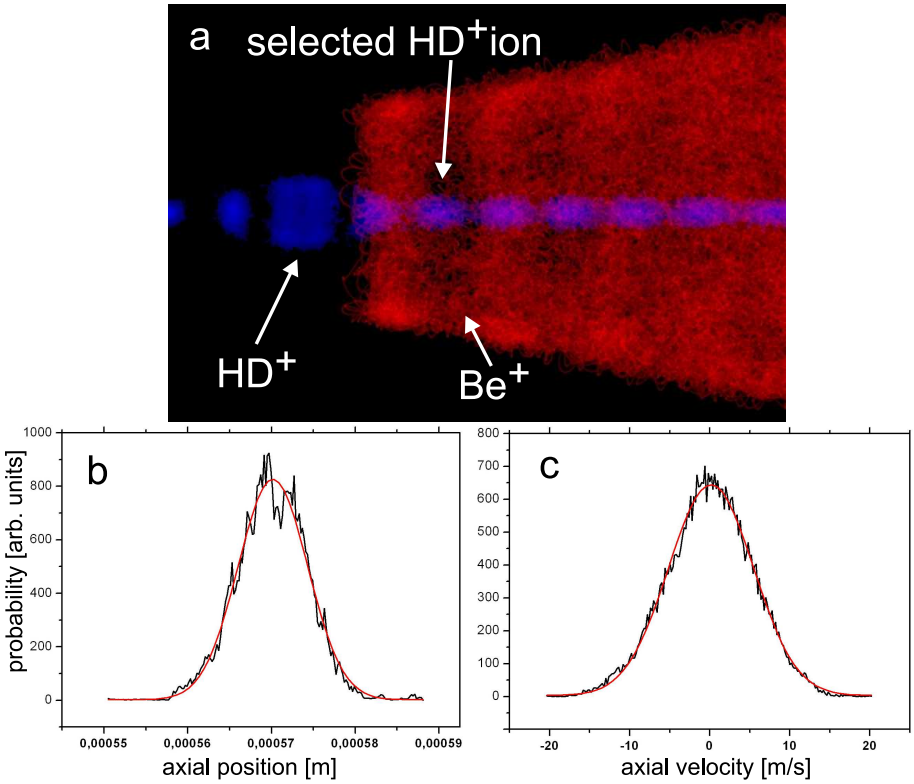


**Figure 3.10:**
Spatial and velocity distribution of an individual, localized $HD^+$ ion. The ion is embedded in a 10 mK beryllium ion crystal and is marked in (a). In the simulations, the particle trajectories were simulated for a time period of 1 ms. Distributions are along the $z$ axis of the trap.

simulations is more efficient compared to direct measurements based on extraction and counting of ions (Fig.3.3) or fluorescence line shape measurements (Fig.3.8 f). Furthermore, the method is relatively fast, even for large ion clusters, since is not so sensitive to the crystal temperature, therefore, simulations can be stopped before reaching thermal equilibrium.

In addition, using the simulations the spatial and velocity distribution of individual ions can be determined. Fig.3.10 shows the axial position and velocity histograms of an individual $HD^+$ ion. This is of interest for determination of the preferred laser propagation direction for spectroscopic studies of cold SC molecular ions, see Chapter 5, for an estimate of Doppler broadening, and for improvement of the confinement of the SC ions in our trap so that Doppler-free spectroscopy in the Lamb-Dicke regime becomes possible.

MD simulations are also required, in order to study the coupling between the radial micromotion to the axial degrees of freedom of the ions [81] and to better understand the mechanisms leading to the coupling between radial and axial modes of oscillation, as observed in experiment for special mixed-species plasmas [76].

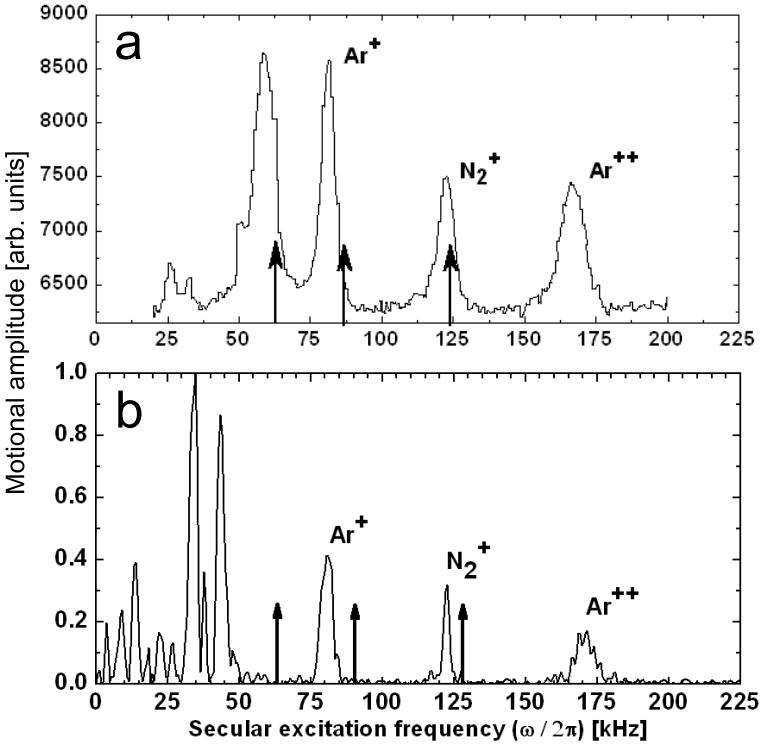


**Figure 3.11:**
Measured (a) and simulated (b) motional frequency spectrum of a cold (<20 mK) multi-species ion crystal. The crystal contains $Be^+$, $N_2^+$, $Ar^+$, and $Ar^{2+}$ ions. Only the high-mass range is shown [76].

As example, in Fig.3.11 the measured motional frequency spectrum for a mixed-species ion crystal is compared to the simulated spectrum. The measured spectrum shows a fairly complicated structure with features at 58 kHz, 82 kHz, 122 kHz, and 166 kHz. The feature at 82 kHz is due to sympathetically crystallized $Ar^+$, whereas the features at 122 kHz and 166 kHz are attributed to $N_2^+$ and $Ar^{++}$ ions, respectively. The calculated single-particle secular frequencies for $Ar^+$, $N_2^+$, and $Ar^{++}$ are 63 kHz, 90 kHz, and 126 kHz. Due to Coulomb coupling between the ions the measured and simulated frequencies deviate significantly from the calculated single-particle frequencies. Consequently, for assigning the resonances to the various species the MD simulations (b) are required. The feature at 58 kHz can be attributed to the excitation of the axial $\omega_z$ $Be^+$ mode, which appears to be split in frequency due to small anisotropies of the trap potential.

# Chapter 4

# Chemical Reactions using Cold Atomic and Molecular Ions

## 4.1 Ion-neutral chemical reactions

Cold trapped and well-confined atomic and molecular ions are well-suited to study chemical reactions with neutral gases. The neutral reactants can be either at room-temperature or at cryogenic temperatures. Having cold ions at disposal opens up the possibility to investigate reactive processes with a high degree of accuracy and control. Among the most challenging goals in this field is the investigation of chemical reactions at the quantum level. This implies the necessity to prepare the reactants in particular quantum states and with well-defined collision energy. Another far-reaching goal is to investigate ion-neutral reactions between cold trapped ions and ultracold atomic gases produced, e.g., in magneto-optical traps. Such cold atomic gases could perhaps be used as cold neutral buffer gas for achieving **internal** cooling of translationally cold molecules.

Many chemical reactions between ions and neutral reactants are of significant interest to astrochemistry. So far, studies of ion-neutral reactions at low temperatures are rare. For example, multipole ion traps using neutral buffer gas as coolant have been used and temperatures of $\approx$10 K were reached, see, e.g., [82]. Reaction rates and branching ratios of various chemical reactions could be deduced [16]. The study of such reactions at even lower temperatures could improve our understanding of important ion-neutral reactions occurring in interstellar clouds [17, 83, 84].

So far, the formation of cold trapped $CaO^+$ ions was observed [60]. Furthermore, ion-neutral reactions in which the molecular ions were sympathetically cooled to 10 K were studied [44]. The reaction was detected via mass spectroscopy based on the excitation of motional trap modes.

An astrophysically important chemical reaction [83] which was observed in this work is the reaction between sympathetically cooled $H_2^+$ ions and neutral $H_2$ gas:

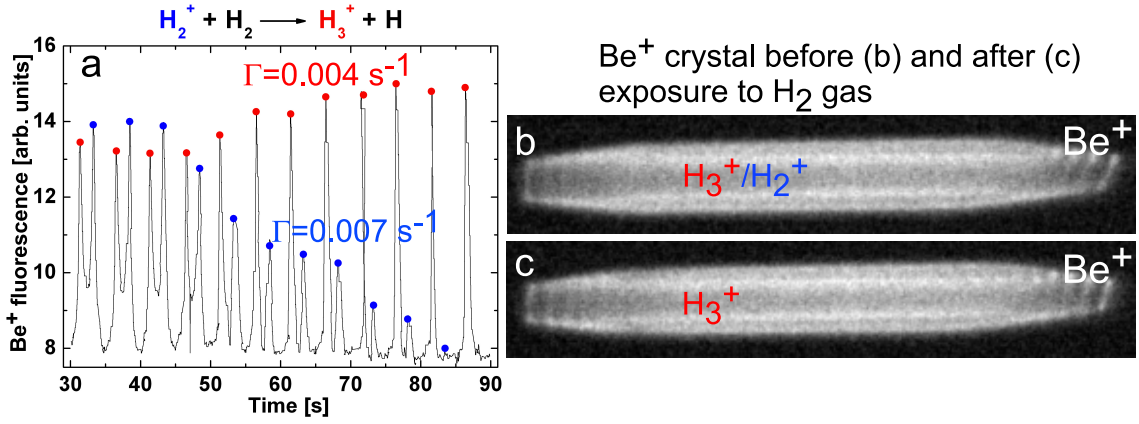


**Figure 4.1:**
Chemical reaction between cold $H_2^+$ and room-temperature $H_2$. (a) Motional frequency spectrum of a cold multi-species ion crystal containing $Be^+$, $H_3^+$, and $H_2^+$ ions, during exposure to neutral $H_2$ gas. CCD images are taken before (b) and after (c) exposure to $H_2$. No significant loss of $Be^+$ ions was observed. The difference between the loss rate of $H_2^+$, $\Gamma$ (blue), and the formation rate of $H_3^+$, $\Gamma$ (red), deduced is probably due to nonlinearities of the secular signal.

$$H_2^+ + H_2 \rightarrow H_3^+ + H \tag{4.1}$$

This is an example of an exothermic ion-neutral reaction involving two of the most fundamental molecular ions in the universe [85], and which proceeds without activation barrier. For such reactions, the Langevin theory predicts a temperature-independent rate coefficidnt, for suitably low temperatures [86, 87]:

$$k_L = Q\sqrt{\frac{\pi\alpha}{\epsilon_0\mu}}, \tag{4.2}$$

where $Q$ is the charge of the ion, $\alpha$ is the polarizability of the neutral reactant, and $\mu$ is the reduced mass of the particle pair.
The reaction was detected via secular excitation mass spectrometry, as shown in Fig.4.1. After exposure of the cold (≈10 mK) $H_2^+$ ions to room-temperature $H_2$ gas, in the motional resonance spectrum a decrease of the $H_2^+$ ion number is observed, while the $H_3^+$ ion number increases from an initially present amount. The heights of the peaks in the secular spectrum are, to a first approximation, a measure of the ion numbers of SC ions in the crystal. Exponential fitting to the peak maxima determines loss rates and formation rates ($\Gamma$) for both species. More exact rates can be deduced by using the MD simulations for an estimate of ion numbers and for the simulation of the motional spectra, since these are sensitive to the ion number fractions involved.
In this work, systematic studies of several chemical reactions were performed and reactions rates deduced:

- The reactions between trapped and laser-cooled $^{9}Be^{+}$ ions and room-temperature molecular hydrogen isotopomers were studied, see Fig.4.2 [58]. These reactions do not proceed with the beryllium ion in its ground electronic state. Therefore, the $Be^{+}$ ions are excited, e.g., to the $^{2}P_{3/2}$ state. The reaction products were determined by non-destructive mass spectrometry. Reaction rates were deduced from the time evolution of the $Be^{+}$ ion number (observed using a CCD camera) or from the observation of the spontaneous emission fluorescence rate (using a PMT). A resolution down to the single-particle level was achieved.

- The nearly thermoneutral ([88, 89]) reaction between SC triatomic hydrogen molecular ions, $H_3^+$, and room-temperature $O_2$ molecules was investigated, thus, demonstrating that it is possible to study certain reaction channels when neither one of the reactants nor the products can be directly detected. Reaction rates were deduced by determination of the $H_3^+$ loss rate as the rate of dark crystal core size reduction, using MD simulations as a tool. A similar sensitivity as above was achieved [58].

The measured rate coefficients for all reactions studied are in reasonable agreement with the values calculated from Langevin theory [58].
In summary, using the cold (mK-range) trapped atomic and molecular ions produced previous work on ion-neutral chemical reactions could be extended to:

- small ensembles, which are interesting for quantum state preparation of molecular ions, since the latter can be addressed individually using lasers,

- reactions with the simplest molecules in nature which are of importance for astrochemistry, and which are available, for the first time, at these low temperatures,

- reactions in which the laser-cooled and crystallized atomic ions are "spectators" only, opening up the possibility for studying a large variety of chemical reactions in ion trap laboratory experiments,

- using MD simulations (rather than mass spectrometry) for interpreting experimental results, e.g. determine reaction rates, which can lead to improved accuracy in ion-neutral reaction studies.

## 4.2 Production of cold trapped molecular ions by chemical reactions

Chemical reactions under controlled experimental conditions were also used to form certain molecular species, which cannot be produced in a different way, or to produce ion crystals containing only one SC species. For example, cold medium-sized $^{138}BaO^{+}$

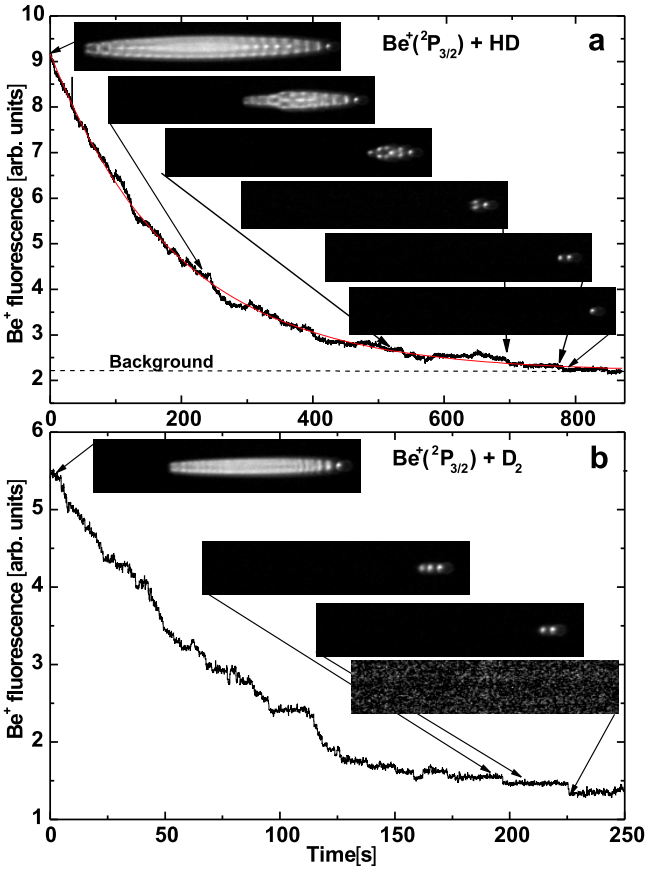


**Figure 4.2:**
Chemical reaction between laser-cooled $Be^+$ and room-temperature molecular hydrogen gases. Decay of a small $Be^+$ ion crystal (≈160 $Be^+$ at ≈5 mK) after exposure to HD gas. The line is an exponential fit to the data. The measured reaction coefficient k≈ $1.1 \cdot 10^{-9}$ $cm^3/s$. (b) Decay of a crystal (≈45 $Be^+$ ions) after exposure to $D_2$ gas. Discrete steps in the fluorescence towards the end of the run are due to the formation of a single $BeD^+$ and of two $BeD^+$ ions, respectively [58].

molecular ions were produced by chemical reactions with background $CO_2$ molecules (this reaction is exothermic by several eV) [52]:

$$Ba^+ + CO_2 \rightarrow BaO^+ + CO \tag{4.3}$$

In another example, sequential chemical reactions were used to form pure two-species ion crystals containing $Be^+$ and $H_3^+$ ions at low temperature. The two possible reaction paths for the production of cold $H_3^+$ ions are:

$$Ar^+ + H_2 \rightarrow Ar + H_2^+ \tag{4.4}$$

$$\Rightarrow H_2^+ + H_2 \rightarrow H_3^+ + H \tag{4.5}$$

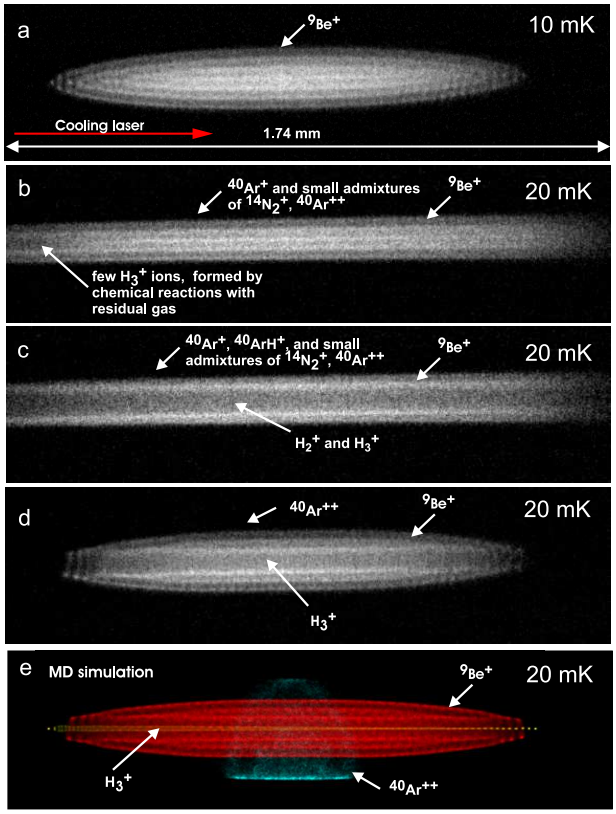


**Figure 4.3:**
Production of cold molecular ions using sequential chemical reactions. (a) CCD image of a pure $Be^{+}$ ion crystal, (b) after loading with $Ar^{+}$ ions, (c) after $H_2$ inlet, leading to the formation of (mainly) $H_3^{+}$ ions and a smaller fraction of $H_2^{+}$ ions (as found by secular excitation mass spectroscopy), (d) after removal of $Ar^{+}$, $ArH^{+}$, and heavier contaminants, and full conversion of $H_2^{+}$ ions into $H_3^{+}$. $Ar^{++}$ ions were deliberately not removed. (e) Ion numbers and temperatures for the crystal in (d) are obtained from MD simulations: $\approx 1150$ $Be^{+}$ ions, $\approx 100$ $H_3^{+}$ ions, and $\approx 30$ $Ar^{++}$ ions at $\approx 20\,\mathrm{mK}$ [59].

and

$$Ar^{+} + H_2 \rightarrow ArH^{+} + H \tag{4.6}$$

$$\Rightarrow ArH^{+} + H_2 \rightarrow H_3^{+} + Ar \tag{4.7}$$

For both paths (Eqs.(4.4), (4.5) and Eqs.(4.6), (4.7), respectively) all reactions are exothermic and are expected to proceed with a temperature independent Langevin reaction rate constant, see [59] and references therein for details. Pure ion crystals produced in this way, see Fig.4.3, could be useful systems for exploring the chemistry of $H_3^{+}$ ions in laboratory experiments. In particular, the study of state-specific reactions of $H_3^{+}$ via high-resolution infrared spectroscopy could provide valuable input for theories of ion-molecule gas-phase chemistry and precise calculations of molecular transition

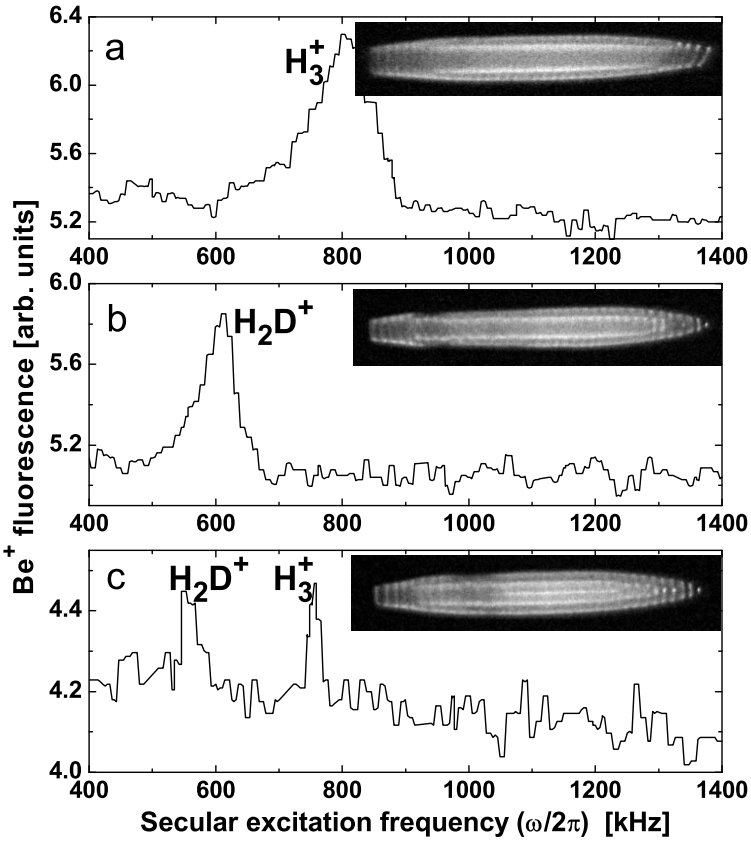


**Figure 4.4:**
Molecule-to-molecule conversion using SC molecular ions. (a) Motional (secular) frequency spectrum of a $Be^+$ ion crystal containing cold $H_3^+$ ions. After exposure to neutral HD gas, most $H_3^+$ ions are converted into $H_2D^+$ (c). Subsequent exposure to neutral $H_2$ gas leads to their back-conversion (c). According to the CCD images observed, losses of hydrogen molecular ions were mainly due to reactions with background gas present in the chamber. $Be^+$ losses are negligible, as confirmed by MD simulations.

frequencies.

Furthermore, heteronuclear diatomic ions, such as diatomic molecular hydrides, e.g., $ArH^+$ and $ArD^+$, were formed in a similar way [59]. These ions are promising systems for high-precision laser spectroscopy and fundamental studies, such as tests of time-independence of certain fundamental constants, since they have a relatively simple hyperfine structure of the ro-vibrational transitions [13, 90]. In addition, their large vibrational and rotational transition rates are still small enough for enabling ultra-high spectral resolution using state-of-the-art lasers, e.g. mid-infrared OPO's or quantum cascade lasers. The above diatomic molecules could also serve as model systems for the implementation of schemes for internal state manipulation, see, e.g., [90, 91] and references therein.

The ability to produce chemical reactions with a high degree of accuracy and control was used to implement a fast and efficient method for molecule-to-molecule conversion in multi-species ion crystals. In more detail, cold $H_3^+$ ions, see secular mass spectrum in Fig.4.4 a, were exposed to room-temperature HD gas, leading to the formation of $H_2D^+$ ions ($H_3^+ + HD \rightarrow H_2D^+ + H_2$), via chemical reactions (Fig.4.4 b). This reaction is exothermic by about 232 K [16]. After subsequent exposure to room-temperature $H_2$, the ions were converted back to $H_3^+$ ($H_2D^+ + H_2 \rightarrow H_3^+ + HD$). The barrier for this reaction pathway is surpassed by the thermal energy of the $H_2$ molecules or internal energy of the cold $H_2D^+$ ions. Depending on the exposure time to the neutral $H_2^+$ gas, conversion efficiencies close to maximum can be reached. Losses of hydrogen molecular ions are mainly due to reactions with nitrogen molecules present in the background gas, leading to the formation of heavier SC ions embedded outside the $Be^+$ [59]. The presence of the latter is obvious from the increasingly flattened shape of the ion crystal displayed in Fig.4.4 (going from (a) to (c)). Correspondingly, the decrease in size of the dark crystal core is due to the loss of hydrogen molecular ions via the above reaction channel. The technique described relies on the availability of suitable (exothermic) reaction channels, or their preparation using lasers, for example, and is, in principle, generally applicable to many molecular systems.

## 4.3 Photofragmentation of polyatomic molecules

Studies of laser-induced fragmentation of molecules are an important topic in chemical physics and can be useful, among others, for:

- the development of techniques to measure the internal state distribution of cold trapped molecules,
- the measurement and manipulation of branching ratios of dissociating channels in simple molecular systems,
- the development of theoretical photofragmentation models based on first principles in *ab initio* computational quantum chemistry, compare, e.g., [92],
- the study of photofragmentation and of conformational dynamics of complex polyatomic molecules, such as proteins and polymers, in the gas phase.

Studies of laser-induced fragmentation and determination of branching ratios are rare to date. So far, $MgH^+$ molecular ions cooled into Coulomb crystals were dissociated using a resonant two-photon dissociation scheme and the branching ratio of the two possible dissociation channels, $Mg + H^+$ and $Mg^+ + H$, was investigated [93]. In another experiment, singly charged AlexaFluor and Rhodamine ions were trapped in a hyperbolical Paul trap, cooled using cryogenic buffer gas to ≈140 K. Their photofragmentation rate

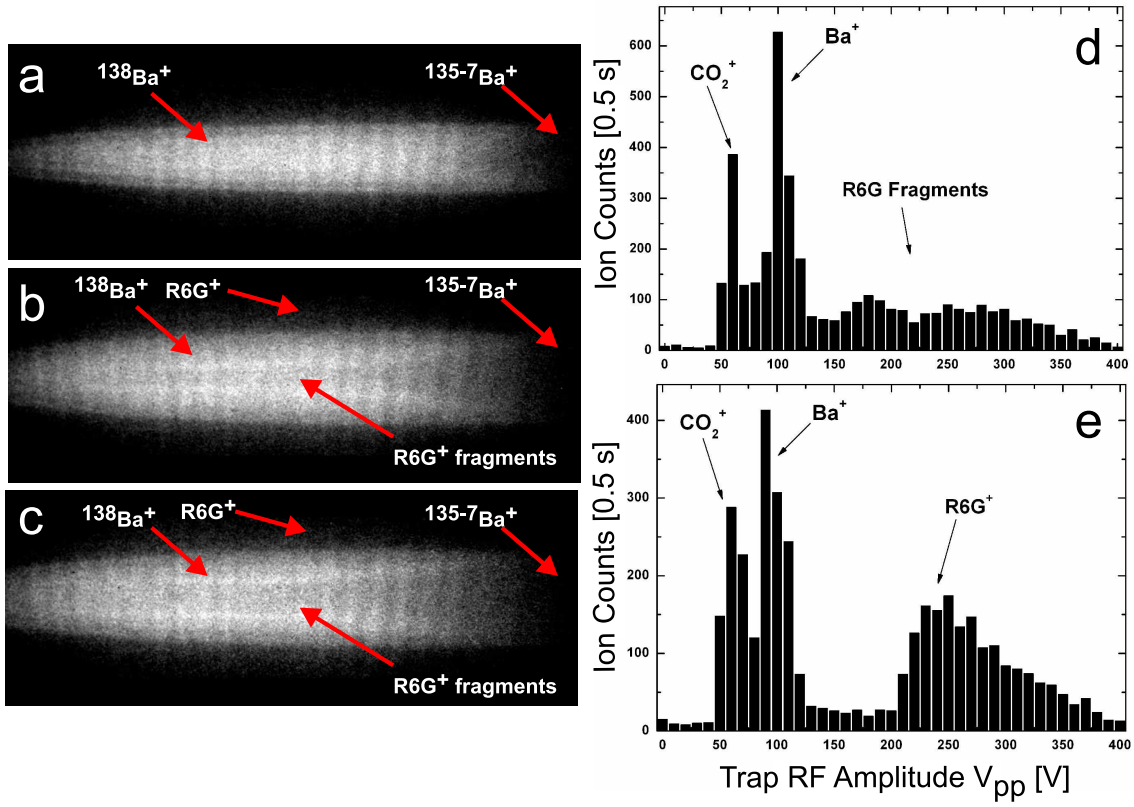


**Figure 4.5:**
Photodissociation of cold, singly charged Rhodamine 6G ions. Left: Cold $Ba^+$ ion crystal before (a) and after (b) loading of $R6G^+$. (c) CCD image taken after 60 s of exposure of the $R6G^+$ ions to the $Ba^+$ cooling laser at 493 nm. Right: (d) Mass spectrum of an ion crystal similar to the one in (c) containing cold $Ba^+$, $CO_2^+$ (narrow peaks), and various $R6G^+$ fragments (broad peak), after exposure to the 493 nm cooling laser. The spectrum was obtained by extraction and counting of the ions. (e) Mass spectrum for a ion cloud which was not laser-cooled. $R6G^+$ fragments were not formed. The broad peaks in (e) indicate translational temperatures around 300 K.

was measured via the decay of the fluorescence signal and by the parent ion number decay and compared to predictions of a photofragmentation model [94].

In the experiments described here, initial studies of the photofragmentation of cold (<0.1 K) polyatomic molecules, Rhodamine 6G ions ($R6G^+$) and Glycerrhetinic acid ions ($GA^+$, mass 470 amu), sympathetically cooled into Coulomb crystals using laser-cooled barium ions, were initiated (Figs.4.5, 4.6). One important difference compared to previous results is the possibility to use continuous-wave laser radiation. Three different detection techniques are possible: (i) by observation of the change of shape of the cold ion crystal containing cold $R6G^+$ ions, Figs.4.5 (a-c), or $GA^+$ ions, Figs.4.6 (a-d), upon exposure to continuous-wave 493 nm or 266 nm laser radiation, respectively, (ii) by ex-

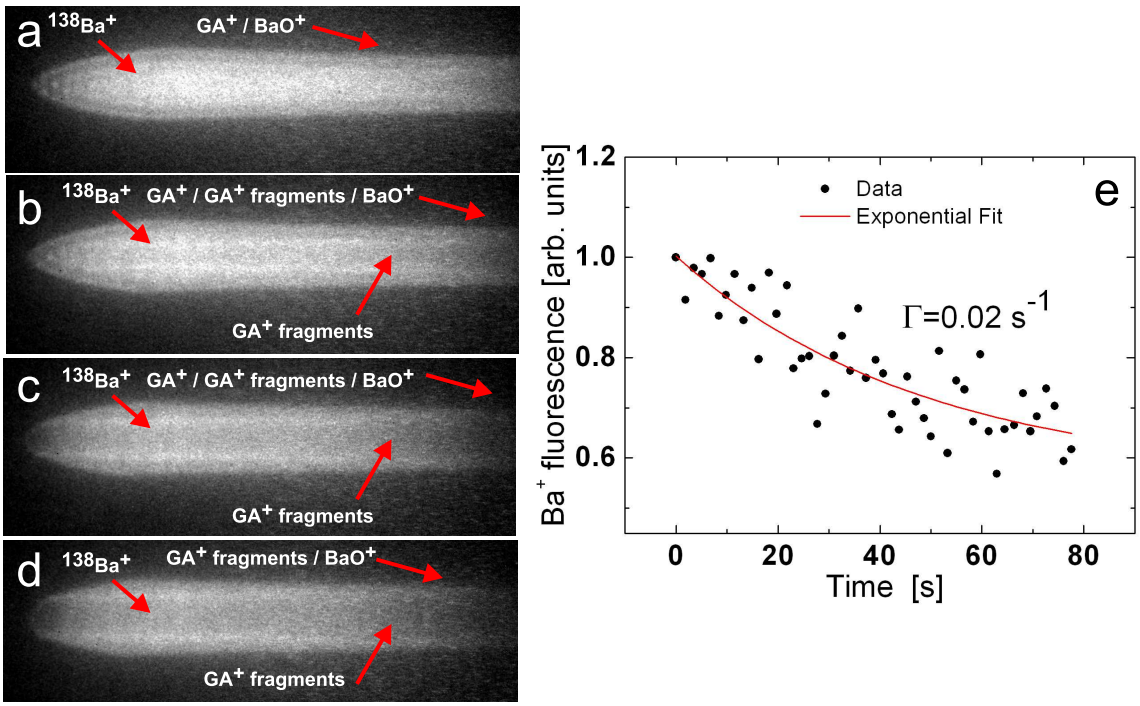


**Figure 4.6:**
Photodissociation rate of cold, singly charged Glycerrhetinic acid ions. Left: (a-d) Ion crystal containing $GA^+$ ions during exposure to 266 nm UV radiation. Laser-induced fragmentation of the cold (≈100 mK) $GA^+$ ions leads to the appearance of a dark crystal core containing $GA^+$ fragments. In addition, $GA^+$ fragments heavier than $Ba^+$ are likely to be formed. Right: (e) Decay of $GA^+$ ion number after switching on the 266 nm laser, observed via secular excitation mass spectroscopy. The dissociation rate $\Gamma$ was obtained by exponential fitting to the data. The measurement accuracy is limited mainly by electronic noise.

traction and counting of the parents ions and of fragmentation products Figs.4.5 (d,e), and (iii) by secular excitation mass spectroscopy, Fig.4.6 (e), as described in Section 3.2.

For the latter, there are no obvious limitations for improvement of the measurement accuracy (currently limited by technical noise, see Fig.4.6 (e)), other than the statistical uncertainty. Thus, it can be anticipated that the method is suitable for measurement of accurate photodissociation rates. In a similar way, trapped and sympathetically crystallized Rhodamine 101 ions were found to photodissociate in the presence of the cooling laser for the barium ions.

The ability to transfer a large variety of unsolvated molecules to the gas-phase, by electrospray ionization, holds great promise to study systematically photodissociation of more complex molecules, such as biomolecules, using one- or two-photon dissociation schemes and continuous-wave laser sources at relatively low intensities.

# Chapter 5

# High-Resolution Spectroscopy of Cold Trapped Hydrogen Molecules

Molecular hydrogen ions are the simplest molecules in nature, containing only two nuclei and a single electron. They are of fundamental importance in various aspects, e.g.:

- as benchmark systems for precise measurement of their energy levels and comparison with high-precision *ab initio* theory,
- for the study of collision processes and ion-neutral reactions (relevant for the chemistry in interstellar clouds),
- as model systems for the investigation of radiation-molecule reactions.

Several spectroscopic investigations on room-temperature molecular hydrogen ions or on ion beams were performed in the past, among them, radio frequency spectroscopy of the hyperfine structure of vibrational levels of $H_2^+$ ions trapped in an ion trap [95], laser spectroscopy of fundamental rovibrational transitions of $HD^+$ in an ion beam [96], and microwave and laser spectroscopy of rotational and rovibrational transitions of $H_2^+$, $HD^+$, and $D_2^+$ close to the dissociation, also in an ion beam [97, 98].
Experimentally, the highest spectroscopic accuracies reported so far were achieved in the experiments of Jefferts and of Wing et al. [96, 99], $\simeq 1 \times 10^{-6}$ and $4 \times 10^{-7}$ (in relative units), respectively. Furthermore, the dissociation energies were obtained by Zhang et al. with accuracies $\simeq 1 \times 10^{-6}$ [100]. On the theoretical side, *ab initio* calculations of dissociation energies of a multitude of rovibrational states in $H_2^+$ and $HD^+$ were reported by Moss [101, 102] with a relative accuracy of $5 \times 10^{-9}$, including leading order relativistic and radiative corrections. Using variational methods [103, 104], the nonrelativistic (i.e. Schrödinger) rovibrational transition frequencies were obtained with an uncertainty well below 1 kHz (relative accuracies are at $5 \times 10^{-24}$ and $8 \times 10^{-30}$, respectively). The full relativistic rovibrational energies have recently been calculated by V. Korobov *ab inito* with a precision better than $1 \times 10^{-9}$ (ppb) [105]. Precise *ab initio* calculations of the hyperfine structure of rovibrational states of the $HD^+$ were reported

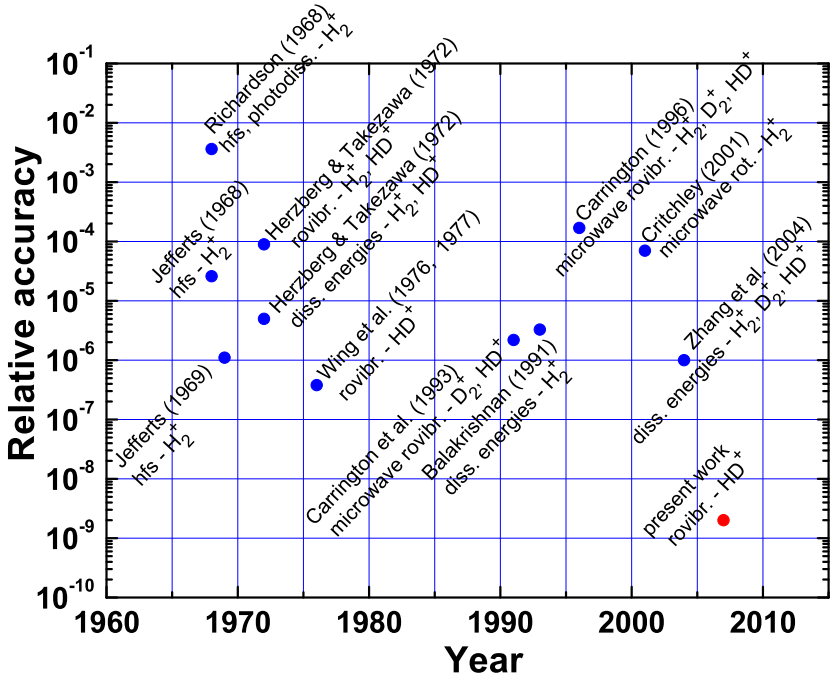


**Figure 5.1:**
Experimental accuracies for hyperfine (hfs), rotational, and rovibrational transitions in hydrogen molecular ions ($H_2^+$, $HD^+$, $D_2^+$).

recently by Bakalov et al. [106], with an estimated uncertainty of about 50 kHz. The experimental and theoretical accuracies achieved are summarized in Figs.5.1, 5.2, and 5.3. The different contributions to the calculated transition frequency for a particular rovibrational transition in $HD^+$, (v'=4, N'=3) $\leftarrow$ (v=0, N=2), are displayed in Fig.5.4. The experimental accuracies achieved in the past are far less compared to the theoretical ones reached in the meantime. In the cold molecular ion ensembles produced in this work [54], line-shifting and broadening effects due to collisions, high thermal velocities, and finite transit time can be strongly suppressed. On the side of the laser sources, novel narrow-band and highly stable laser systems based on diode lasers or optical parametric oscillators (OPO) are now available, allowing for measurement of fundamental transitions or overtone transitions in molecular systems. In addition, the advent of femtosecond frequency synthesizers enables absolute frequency measurement with high accuracy, see, e.g., [107].
There are several reasons for precise spectroscopic measurements of rovibrational transition frequencies in hydrogen molecular ions:

- test of advanced *ab initio* molecular calculations (in particular, QED contributions),

- measurement of fundamental constants, e.g., the electron-to-proton mass ratio

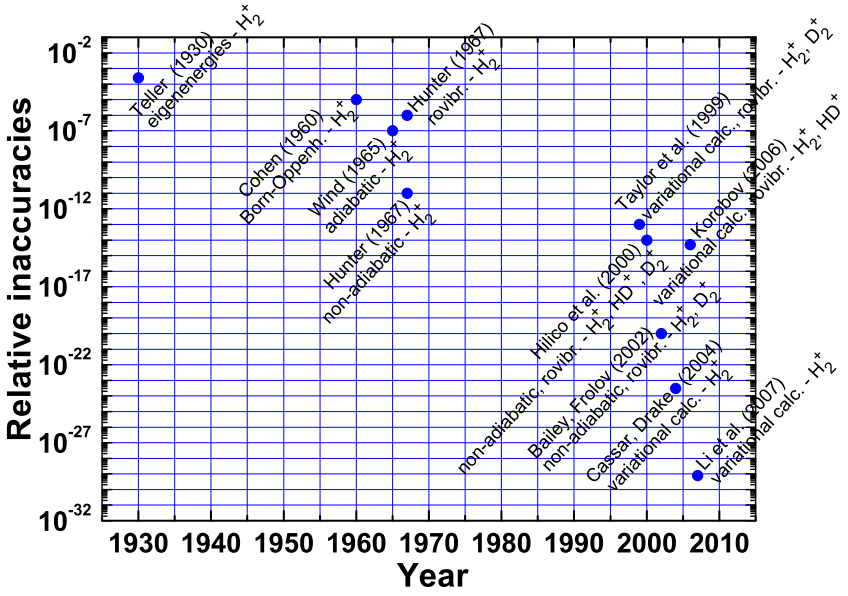


**Figure 5.2:**
Theoretical accuracies for Schrödinger problem eigenenergies in hydrogen molecular ions. Calculated quantities are given. Non-relativistic calculations using Born-Oppenheimer (adiabatic) or non-adiabatic approximations, or variational methods are indicated.

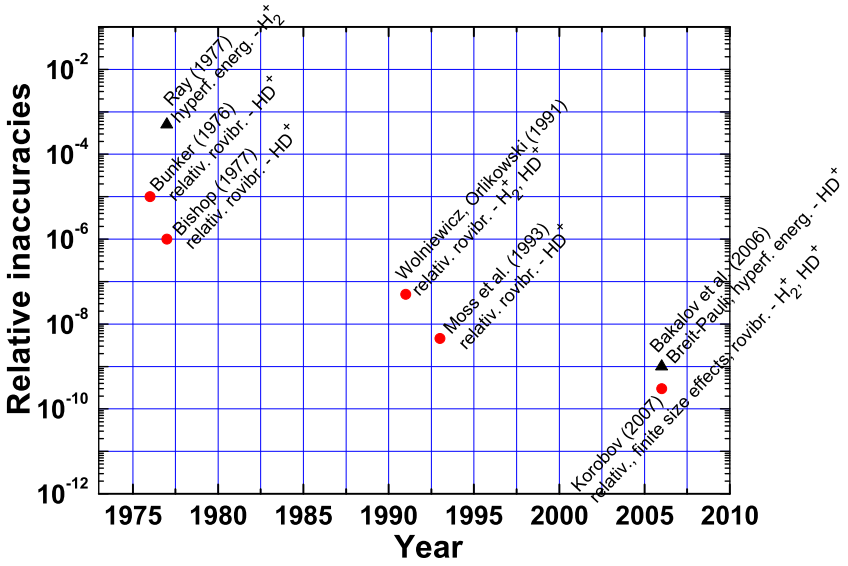


**Figure 5.3:**
Theoretical accuracies for the full ro-vibrational transition energies in hydrogen molecular ions. Calculated quantities and/or methods used are given. Results taking into account radiative and relativistic corrections as well as corrections due to the finite size of the proton and the deuteron are in red, whereas results for hyperfine levels are in black.

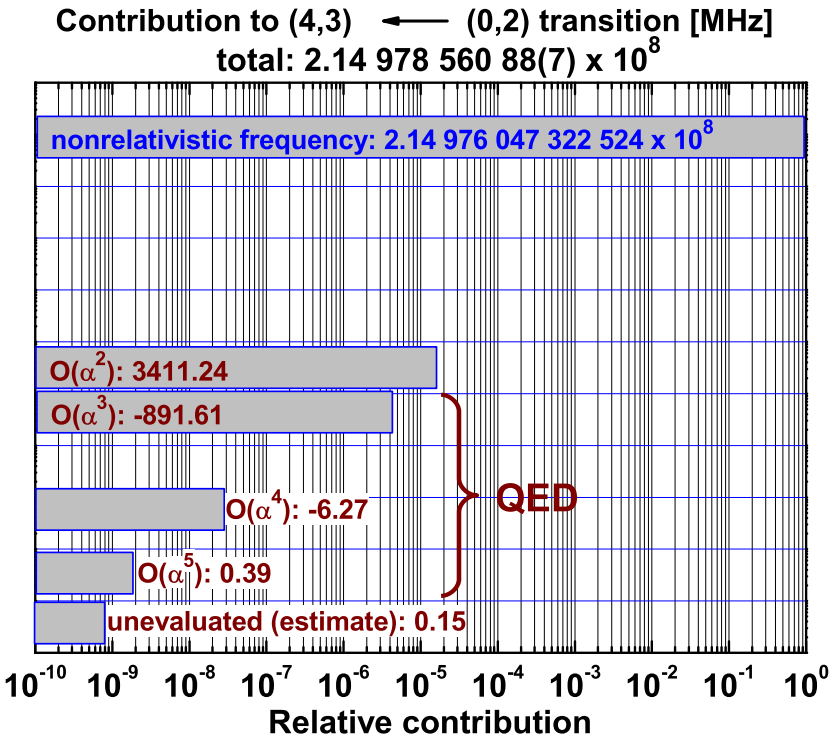


**Figure 5.4:**
Summary of the contributions to the (v'=4, N'=3) ← (v=0, N=2) rovibrational transition frequency in $HD^+$ molecular ions (in MHz).

$m_e/m_p$, the proton-to-deuteron mass ratio $m_p/m_d$, or the proton-to-triton mass ratio $m_p/m_t$,

- measurement of the deuteron quadrupole moment [108],
- tests of fundamental physics laws, e.g. Lorentz Invariance, time invariance of fundamental constants [109, 110],
- test of concepts for the internal state manipulation of molecules,
- blackbody thermometry [111].

One interesting aspect is the dependence of vibrational and rotational transition frequencies in hydrogen molecular ions on certain fundamental constants, e.g., $m_e/m_p$, $m_p/m_d$, or $m_p/m_t$. Fundamental vibrational and rotational transition frequencies scale approximately as:

$$\upsilon_{vib} \sim \sqrt{m_e/\mu} R_\infty, \tag{5.1}$$

$$\upsilon_{ro} \sim m_e/\mu R_\infty. \tag{5.2}$$

Here, where $\mu$ is the reduced mass of the two nuclei and $R_\infty$ is the Rydberg energy, see, e.g., [13, 112]. Currently, these constants are determined by Penning ion trap mass spectrometry. Their relative accuracies are $2 \times 10^{-10}$ for $m_p/m_d$ [113], $2 \times 10^{-10}$ for $m_p/m_t$, and $4.6 \times 10^{-10}$ for $m_e/m_p$ [113, 114], respectively. *Ab initio* calculations of energy levels in molecular ions are approaching the limits set by the uncertainties in the values of those fundamental constants entering the calculations, the largest contribution originating from the uncertainty in the value for the electron-to-proton mass ratio $m_e/m_p$. Therefore, provided that the accuracy of theoretical calculations of energy levels can be sufficiently increased (see below), a comparison between theoretical results and results from high-resolution spectroscopic measurements of rovibrational transition frequencies could lead to an improved value for $m_e/m_p$.
Furthermore, it has been suggested by Calmet, Fritsch and others that a possible variation of $m_e/m_p$ (and of the quark masses and the strong interaction constant) over time might be larger than a possible time variation of the electromagnetic interaction (fine structure) constant $\alpha$ [115, 116, 117], see also [118, 119, 120]. Recently, Reinhold et al. found indication of a variation of $m_e/m_p$ over Gyr timescales [121]. Their results are based on laboratory measurements of Lyman bands of neutral $H_2$ and were compared to $H_2$ spectral lines observed in quasars, indicating that $m_e/m_p$ could have decreased over the near age of the universe. High-resolution rovibrational spectroscopy on hydrogen molecular ions could enable laboratory based searches for a possible time variation of $m_e/m_p$.

## 5.1 Infrared spectroscopy of $HD^+$ ions with submegahertz accuracy

Rovibrational spectroscopy of homonuclear hydrogen molecular ions with no dipole moment like $H_2^+$ or $D_2^+$ is faced by the difficulty that electric-dipole transitions are forbidden. As a consequence, excitation rates of homonuclear molecules are about 8 orders of magnitude smaller than for heteronuclear molecules like $HD^+$. Doppler-free two-photon spectroscopy of $H_2^+$ ions, as pursued by Hilico and coworkers (see, e.g., [112]), requires special (high-power) infrared laser sources.
In this work, $HD^+$ molecular ions were chosen. The selection rule for electric dipole transitions in the electronic ground-state of $HD^+$ is $\Delta J = \pm 1$ ($J$ is the total angular momentum). This selection rule can be fulfilled for all rotational transitions $\Delta N = \pm 1$. The selection rule for vibrational levels is $\Delta v = \pm 1, \pm 2, \pm 3, \ldots$. Here, $N$ and $v$ are the rotational and the vibrational quantum numbers, respectively.
Rovibrational spectroscopy via fluorescence detection is not feasible in $HD^+$, due to the relatively low fluorescence rates which would require sophisticated photon counting systems in the mid to far infrared. Therefore, in this work, a destructive technique was implemented, namely (1+1') resonance enhanced multiphoton dissociation (REMPD).

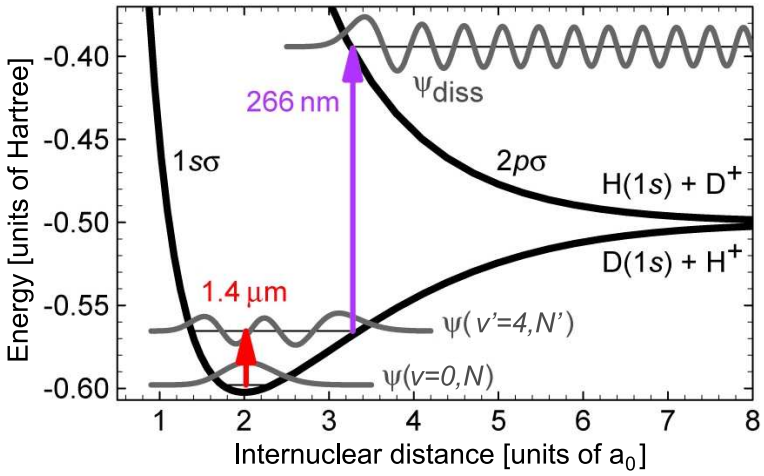


**Figure 5.5:**
Principle of (1+1') REMPD spectroscopy of $HD^+$ ions. A tunable IR diode laser excites a rovibrational overtone transition (v'=4, N') ← (v=0, N). The excited $HD^+$ ions are dissociated using a cw 266 nm laser: $HD^+$(v'=4) + h$\nu$ → H + $D^+$ or $H^+$ + D, see [123]. The calculated UV absorption cross section from the v'=4 level ($\sim 2.4 \times 10^{-17}$ cm$^2$) is about 7 orders of magnitude larger than from v=0 [122].

The molecules are excited by an infrared (IR) laser and then selectively photodissociated from the upper vibrational state by a second, fixed-wavelength ultraviolet (UV) laser, see Fig.5.5. The remaining number of molecular ions is measured as a function of the frequency of the excitation laser, as shown in Fig.5.6. The spectroscopic method has the following features:

- The molecular samples used are small (typically 40-100 ions). The spectroscopy requires the spectra to be obtained by repeated molecular ion production and interrogation cycles.
- The loss of $HD^+$ ions not only depends on the REMPD process, but also on transitions induced by blackbody radiation (BBR). Therefore, the loss of $HD^+$ ions was modelled by solving the rate equations for the populations of all (v,N) levels interacting with the IR and UV lasers, as well as with the BBR radiation at 300 K, see Fig.5.7.
- The methods used for trapping, cooling and detection are quite general, and are applicable to a host of other molecular ion species.
- Standard diode based laser systems at moderate intensities can be used.
- Compared to previous methods on warm molecular samples or on ion beams, an enhancement of about 10 was obtained for the excitation rate.

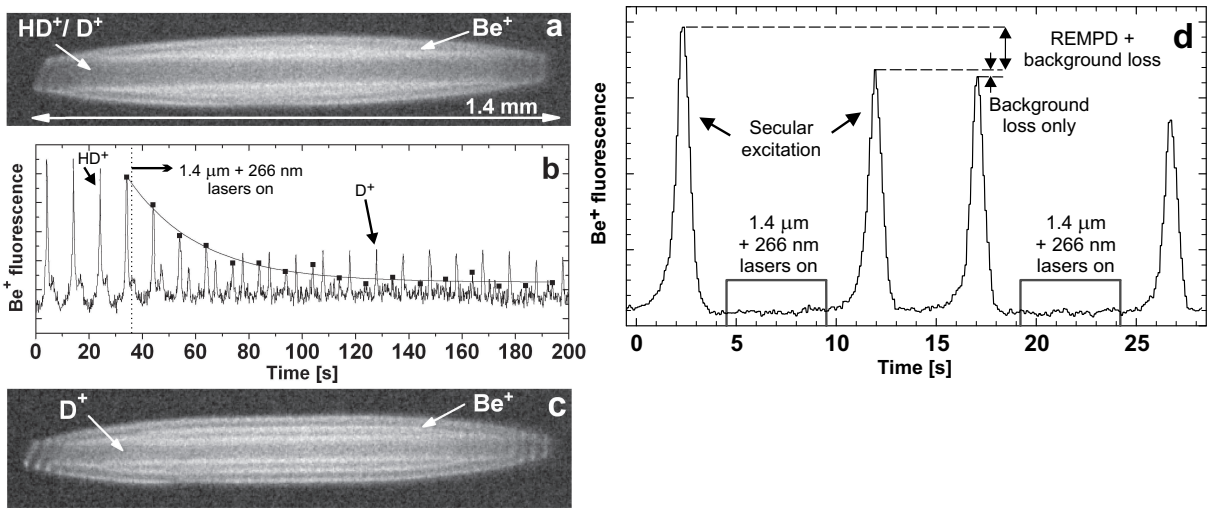


**Figure 5.6:**
(1+1') REMPD spectroscopy of $HD^+$ ions. (a) Initial ion crystal: ≈1100 $Be^+$, ≈100 $HD^+$, and ≈20 $D^+$ ions at ≈20 mK. The presence of cold $HD^+$ is obvious from the dark core. (b) Repeated secular excitation of the crystal in (a) at 3 V amplitude. The excitation frequency was swept between 500 and 1500 kHz. The IR laser is tuned to the maximum of the (v'=4, N'=1) ← (v=0, N=2) line. The curve is an exponential fit with a decay constant of 0.04 $s^{-1}$. (c) Ion crystal after dissociation of all $HD^+$ ions: ≈1100 $Be^+$ and ≈50 $D^+$ ions at ≈20 mK. (d) Measurement cycle consisting of repeated probing of the $HD^+$ number before and after exposure to the spectroscopy lasers [123].

The measured data (Fig.5.8) show partial resolution of the complicated hyperfine spectrum for individual rovibrational transitions, which are due to the coupling of four angular momenta (the spin of the electron, of the proton, and of the deuteron as well as the molecular rotation), assuming a broadening by ≈40 MHz [123]. This broadening is attributed to Doppler broadening, mainly due to the micromotion of the ions. Inhomogeneous broadening of the spectra is accounted for by convolving each line with a Gaussian lineshape of a given width. In total, 12 rovibrational transitions between 1391 nm and 1471 nm, from lower rotational levels N=0 to N=6, were observed.
Based on this method, the transition frequency for the rovibrational transition (v'=4, N'=3) ← (v=0, N=2) at 1395 nm was measured, using a novel narrowband grating-enhanced diode laser with resonant optical feedback locked to a femtosecond frequency synthesizer, developed and operated by A. Wicht and coworkers in our institute [125]. The synthesizer is stabilized to a maser which is referenced to the Global Positioning System (GPS) for longterm stability.
We achieved a relative accuracy of 2.3 ppb (corresponding to ≈0.5 MHz absolute accuracy), which is 165 times more accurate than previous results obtained by Wing et al. [96], see Fig.5.9. The value for the unperturbed transition frequency deduced agrees

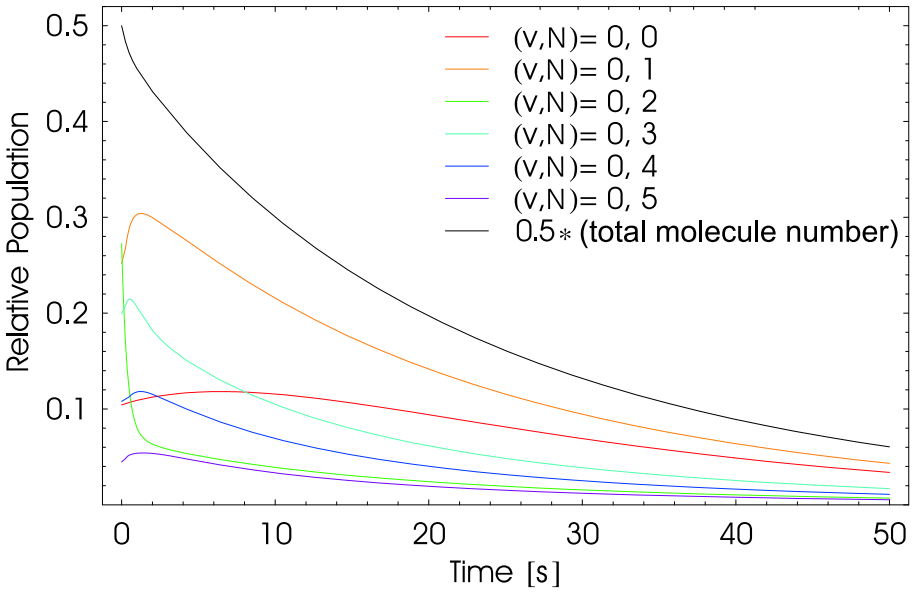


**Figure 5.7:**
Simulated population dynamics for a translationally cold (20 mK) collision-free ensemble of $HD^+$ ions. The IR laser is set to the maximum of the (v'=4, N'=1)←(v=0, J=N) transition (at around 1430 nm). The intensities of the lasers are $I(\nu_{IR}) = 0.32\,W/cm^2$, $I(266nm) = 0.57\,W/cm^2$. The time evolution of the population of lower rotational rotational levels from N=0 to N=6 is shown together with the time evolution of the total $HD^+$ number. The rate equation model reveals two different timescales at which the $HD^+$ number declines: a first, fast (<1 s) decay occurs when the IR laser selectively excites ions from a specific rovibrational level (here (v=0, N=2)) which are subsequently photodissociated. This process rapidly dissociates those (v=0, N) $HD^+$ ions which are in the hyperfine states probed by the IR laser. The remaining molecular fraction is dissociated significantly slower, at the rate at which the hyperfine levels of (v=0, N=2) are repopulated by BBR and spontaneous emission [124].

with the calculated value from V.I. Korobov [105] (theoretical uncertainty 0.3 ppb) to within measurement accuracy. The experimental uncertainty is due to measurement noise, Doppler broadening, and, to a lesser extent, due to systematic uncertainties associated with external fields in the ion trap, and uncertainties in the *ab initio* data used for the spectral fit. From the measured rovibrational frequency the electron-to-proton mass ratio $m_e/m_p$ could be deduced with an accuracy of 5 ppb accuracy. In order to obtain this value, the partial derivatives with respect to $m_e/m_p$ of the corresponding rovibrational levels were used. The value for $m_e/m_p$ deduced is in good agreement with the 2002 CODATA ([113]) recommended value (for comparison, the 2002 CODATA value itself has a relative uncertainty of 0.46 ppb).

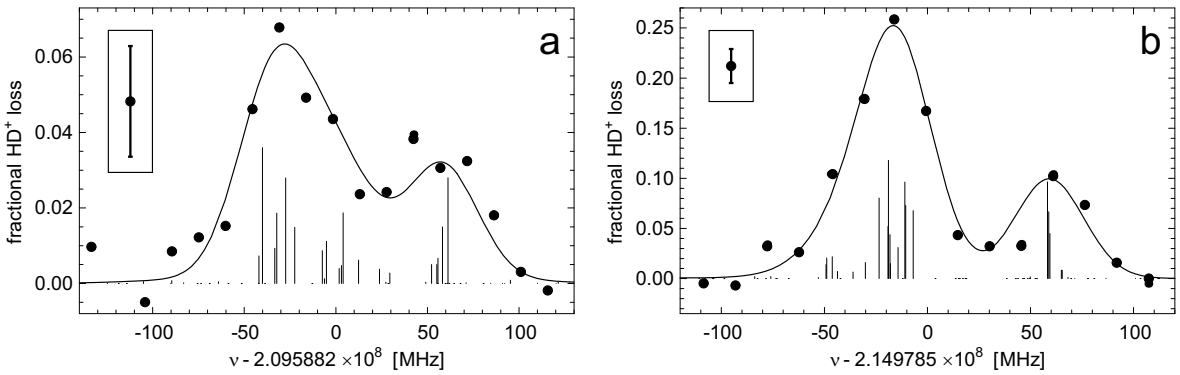


**Figure 5.8:**
Rovibrational transition spectra with partially resolved hyperfine splitting. (a) The (v'=4, N'=1) ← (v=0, N=2) transition at 1430 nm, (b) The (v'=4, N'=3) ← (v=0, N=2) transition at 1395 nm. The curves are fits to the data (•), where the theoretical "stick" spectra were broadened by ≈40 MHz. The ordinate values are the molecular ion dissociation probability for a 5 s irradiation of 0.65 W/cm$^2$ IR and 10 W/cm$^2$ UV light. The insets show typical error bars [123].

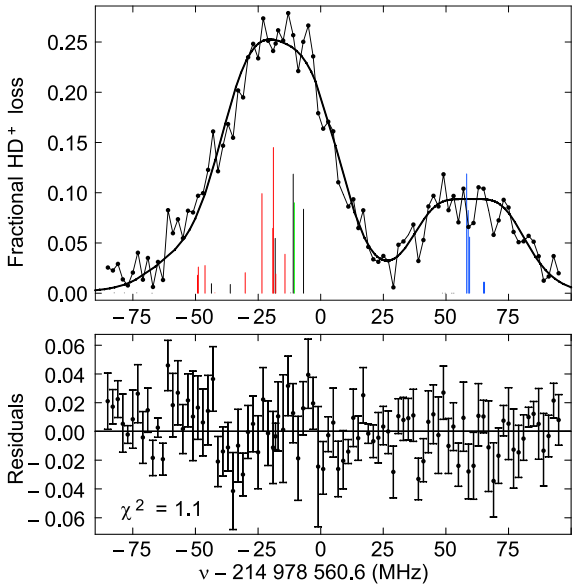


**Figure 5.9:**
Spectrum of the (v'=4, N'=3) ← (v=0, N=2) rovibrational transition in $HD^+$ (obtained as above). The offset frequency in the abscissa label is the measured result for the unperturbed transition frequency and is accurate to within 0.5 MHz. The smooth curve in the upper panel is a fit to the data. The strongest transitions in the theoretical hyperfine line spectrum (underneath the fit) can be grouped by their spin configurations, as indicated by the different colors used in the graph. For clarity, the data points are joined by line segments. The lower panel shows the differences between the individual data points (•) and the fitted curve. Frequency error bars (not shown) are smaller than the dots representing the data points, see [125] for details.

It thus appears that the experimental method demonstrated for $HD^+$ provides a new approach to determine the electron-to-proton mass ratio $m_e/m_p$ with improved accuracy in the near future, when combined with slightly improved theoretical calculations, see [125] for details. In particular, when the experimental accuracy improves by more than one order of magnitude and provided that the uncertainty in the theoretical rovibrational energies improves by a factor of two, a competitive value for $m_e/m_p$ could already be obtained. On the experimental side, this requires the development of a new ion trap (currently under construction in our institute) which enables Doppler-free infrared spectroscopy in the Lamb-Dicke regime. In addition, a significant increase in the spectroscopic accuracy (more than one order of magnitude) accuracy could be achieved by performing rf spin flip spectroscopy in combination with the REMPD method, in order to determine the hyperfine Hamiltonian and the Zeeman effect, or by THz rotational spectroscopy.

## 5.2 Molecular thermometry

An important question is to what extent the rotational motion of sympathetically cooled molecules couples to their translational motion, i.e., whether the internal state population can be manipulated by cooling the external degrees of freedom of molecules. For this purpose, methods for the precise measurement of the internal state population of SC molecular ions are required. Such methods are also interesting for further applications: (i) for the implementation of a molecular thermometer, in order to measure the temperature of the ambient blackbody radiation, and (ii) for the demonstration of schemes for internal state manipulation of molecules using suitable laser sources or by collisions with laser-cooled neutral atoms (from magneto-optical traps, for example).
So far, Drewsen an coworkers found that in sympathetically cooled $MgH^+$ ions the effective rotational temperature exceeds the translational temperature by more than two orders of magnitude [126]. This indicates a very weak coupling between external and internal degrees of freedom. In order to deduce a lower limit for the internal temperature of the molecular ions, data from rotational resonance-enhanced multiphoton photodissociation experiments were compared with results from theoretical simulations. From the measurements it was concluded that the rotational temperature of the $MgH^+$ ions is higher than 120 K. However, the technique was not suited for measuring the rotational temperature of the ions accurately, in order to actually determine the coupling between internal and external degrees of freedom.
In this work, (1+1') REMPD laser spectroscopy was used to measure the rotational level distribution of trapped molecular ions ($HD^+$) cooled into Coulomb crystals, leading to a much more accurate determination of their (internal) temperature compared to the previous technique. The translational temperature of the $HD^+$ ions was in the 10 millikelvin regime [111]. In the experiment, the $HD^+$ loss rate was measured for rovibrational transitions starting from lower rotational levels N=0 to N=6. For this

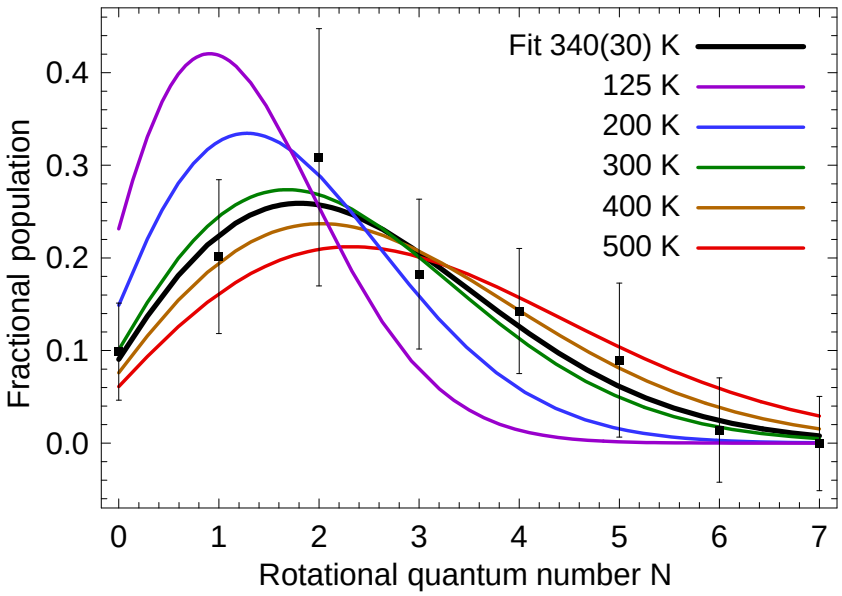


**Figure 5.10:**
Blackbody thermometry with cold trapped $HD^+$ molecular hydrogen ions. For the rotational temperature measurement (1+1') REMPD laser spectroscopy was used [111]. Colored curves represent the rotational state distribution given by Boltzmann statistics for different temperatures. The black curve is a fit to the measured data points (•).

purpose, the IR laser interrogating the ions was tuned to the maximum of individual rovibrational transitions and broadened to approximately 200 MHz, in order to cover their entire hyperfine spectrum.
The fractional state population was deduced by fitting the data taking into account population redistribution due to coupling to the blackbody radiation. Under the experimental conditions given, the internal (rotational) degrees of freedom turn out to be independent of the translational degrees of freedom. The effective rotational temperature found was close to room temperature (340 K), within the measurement accuracy ($\pm$30 K). The results obtained are shown in Fig.5.10.
The method implemented is useful, since it can be applied to other molecular species. Furthermore, in the near absence of background gas collisions it allows to directly relate the rotational temperature of the ions to the temperature of the ambient blackbody radiation (BBR). This feature (among others, see [124, 127]) suggests the use of molecular ions, such as $HD^+$ or $CO^+$, for BBR thermometry with possible applications in frequency metrology, i.e., it may help to improve the accuracy of frequency standards based on trapped atomic ions (see [111] for a detailed discussion).
One far-reaching perspective in the field cold trapped molecular ions is to perform experiments on translationally localized molecules prepared in specific internal (quantum) states. Several methods were proposed to cool the internal degrees of freedom of the molecules, using lasers or even lamps (see, e.g., [91] and references therein), or us-

ing cryogenic techniques, e.g. collisions with cold ($\mu$K-regime) neutral atomic gases. The method developed in this work for the internal temperature measurement can be a useful tool for future studies in this direction.

# Chapter 6

# Summary and Outlook

## 6.1 Summary

In summary, this work presents various novel results in the field of cold, trapped atomic and molecular ions:

- Methods for the production of cold (<100 mK), confined atomic and molecular ions spanning the mass range 1-470 amu (ranging from protons to polyatomic molecules containing 42 atoms) were developed. One of the trap apparatus developed combines an electrospray ion source with a laser cooling trap, a unique device worldwide.
- The properties of cold one-component and multi-component ion plasmas were studied in isotropic and anisotropic trap potentials.
- Various destructive and non-destructive techniques for characterization and analysis of the content of cold non-neutral plasmas were developed. Furthermore, techniques for the manipulation of cold ion plasmas were developed.
- Molecular dynamics simulations were used, in order to deduce ion numbers, translational temperatures, motional resonance spectra and cooling and heating rates, including rf micromotion. The simulations were also used to model the mass-specific trap modes of the particles, in order to obtain motional resonance spectra of multi-species ion crystals and to study their complicated coupling effects.
- Chemical ion-neutral reactions between cold trapped atomic and molecular ions and neutral gases were investigated, with a resolution down to the single-particle level. Reaction rates for several reactions were measured, for the first time.
- Methods for the controlled production of cold molecular ions of astrophysical and metrological relevance using (multi-step) chemical reactions were developed.

- The feasibility of high-resolution rovibrational spectroscopy on cold trapped molecular ions was demonstrated, for the first time.
- (1+1') REMPD laser spectroscopy was applied to measure the frequency of a rovibrational transition in cold, trapped $HD^+$ ions with a relative accuracy of 2.3 ppb (corresponding to 0.5 MHz absolute accuracy), which is 165 times more accurate than the best previous result. The value deduced for the electron-to-proton mass ratio $m_e/m_p$ (accuracy ≈5 ppb) agrees well with the 2002 CODATA recommended value.
- A relatively precise method for the measurement of the rotational temperature of translationally cold ions was implemented. The method was applied to cold $HD^+$ ions, but is generally applicable to a variety of other species. The experimental results obtained show that sympathetic cooling of translational degrees of freedom does not affect the internal degrees of freedom of the molecular ions.

## 6.2 Outlook

The results achieved so far offer the possibility for further developments in several new directions, such as:

- the sympathetic cooling to complex molecular ions with masses up to 25,000 amu,
- the characterization of the properties of large multi-species ion plasmas containing 5 or more species,
- the measurement of rovibrational or rotational transitions in $HD^+$ with increased accuracy at the level of the actual theoretical accuracy or better, using two-photon spectroscopy, rf spin flip in combination with the REMPD method, or THz rotational spectroscopy,
- the study of laser-induced fluorescence of complex molecules under UHV conditions,
- the measurement of photodissociation rates, transitions frequencies between triplet and singlet states, and triplet state life times, as well as the implementation of (1+1') REMPD spectroscopy on polyatomic molecules,
- the investigation of collisions between cold trapped atomic/molecular ions and cold laser-cooled neutral atoms from a magneto-optical trap.

The extension of sympathetic cooling to very heavy, complex molecular ions requires these ions to be highly charged, in order to ensure efficient sympathetic cooling. This

can be reached using the electrospray ionization source implemented. For the demonstration of (1+1') REMPD spectroscopy schemes, the main challenge arises from the fact that the internal level population of translationally cold polyatomic molecules will be distributed over many rovibrational levels. Therefore, the accuracy of secular excitation mass spectroscopy, used for detection, will have to be significantly increased, which can be achieved by reducing the noise induced on the trap electrodes by external fields. Alternatively, cryogenic techniques or cold neutral atomic gases can be used for cooling the inner degrees of freedom of molecular ions. This approach requires either the development of a cold shield around the trap region or of a dual ion-neutral trap for cold molecular ions and neutral atoms.

Other studies that appear quite realistic on the basis of the achieved progress are: (i) the extension of high-resolution REMPD spectroscopy to other simple molecular systems, such as the astrophysically relevant $H_3^+$ ion ([85]) or other molecular ions with a relatively simple hyperfine structure of the rovibrational transitions, such as diatomic molecular hydrides, e.g., $ArH^+$ and $ArD^+$ [59], (ii) the demonstration of high-sensitivity laser spectroscopy of complex molecules like biomolecules, in order to study slow internal processes and to measure laser-induced conformational changes, and (iii) the coherent state preparation of molecular systems, in order to conduct chemical reactions at the quantum level. The relevance of the molecular systems investigated here for fundamental physics studies, such as the measurement of fundamental constants, has already been pointed out.

On the side of high-resolution spectroscopy of cold trapped $HD^+$ molecular ions the main challenge will be to increase the spectroscopic accuracy by at least one order of magnitude, in order to test the theoretical calculations at their current level of accuracy or better and to obtain a competitive value for the electron-to-proton mass ratio $m_e/m_p$. With relatively straightforward modifications to the apparatus, the micromotion induced sidebands limiting the present spectroscopic resolution can be eliminated.

Furthermore, a significant increase in the spectroscopic accuracy (by more than one order of magnitude) could be achieved by performing rf spin flip spectroscopy in combination with the REMPD method or THz rotational spectroscopy. In particular, since the ions are localized in space to better than 10 $\mu$m, Doppler-free rotational infrared spectroscopy in the Lamb-Dicke regime will be possible. The spectral resolution is expected to be better than 1 ppb, limited only by weak relaxation processes, such as collisions with background gas, or fluctuating technical fields.

Most of the problems anticipated for ion crystals containing several ten or hundred of cold $HD^+$ ions will be virtually absent, or may be substantially alleviated otherwise, by turning to quantum-logic-enabled spectroscopy (QLES), as proposed and demonstrated by Wineland and coworkers for atomic ions [128, 129]. The method would involve using a single ultracold $HD^+$ molecular ion in the Lamb-Dicke regime, coupled to a single $Be^+$ atomic ion, which is used for both cooling the translational energy of the $HD^+$ and state-selective detection of the molecular state.

This may lead to accuracies far beyond those envisioned so far, and could be essential for performing tests of time-independence of $m_e/m_p$ with competitive accuracy, and for detecting the effects of parity violation on the vibrational energies of molecules.

# Bibliography

[1] K. Davis, M-O. Mewes, M. Andrews, M. van Druten, D. Durfee, D. Kurn, and W. Ketterle, "Bose-Einstein Condensation in a Gas of Sodium Atoms" Phys. Rev. Lett. **75**, 3969 (1995).

[2] J.R. Abo-Shaeer, C. Raman, and W. Ketterle, "Formation and Decay of Vortex Lattices in Bose-Einstein Condensates at Finite Temperatures", Phys. Rev. Lett. **88**, 070409 (2002).

[3] J.K. Chin, D.E. Miller, Y. Liu, C. Stan, W. Setiawan, C. Sanner, K. Xu and W. Ketterle, "Evidence for superfluidity of ultracold fermions in an optical lattice", Nature **443**, 961 (2006).

[4] M.R. Matthews, B.P. Anderson, P.C. Haljan, D.S. Hall, C.E. Wieman, and E.A. Cornell, "Vortices in a Bose-Einstein Condensate", Phys. Rev. Lett. **83**, 2498 (1999).

[5] H.S. Margolis, G.P. Barwood, G. Huang, H.A. Klein, S.N. Lea, K. Szymaniec, P. Gill "Hertz-Level Measurement of the Optical Clock Frequency in a Single $^{88}Sr^{+}$ Ion", Science **306**, 1355 (2004).

[6] W.H. Oskay, S.A. Diddams, E.A. Donley, T.M. Fortier, T.P. Heavner, L. Hollberg, W.M. Itano, S.R. Jefferts, M.J. Delaney, K. Kim, F. Levi, T.E. Parker, and J.C. Bergquist, "Single-Atom Optical Clock with High Accuracy", Phys. Rev. Lett. **97**, 020801 (2006).

[7] T.P. Heavner, S.R. Jefferts, E.A. Donley, J.H. Shirley, and T.E. Parker, "Recent Improvements in NIST-F1 and a Resulting Accuracy of $\delta f/f = 0.61 \times 10^{-15}$", IEEE Trans. Instr. Meas. **54**, 842 (2005).

[8] Special issue:"Quo vadis, cold molecules?", Eds. J. Doyle, B. Friedrich, R.V. Krems, and F. Masnou-Seeuws, Eur. Phys. J. D **31**(2), 149 (2004).

[9] Special issue on cold molecules, Eds. O. Dulieu, M. Raoult, E. Tiemann, J. Phys. B: At. Mol. Opt. Phys. **39**, S813 (2006).

[10] M.D. Di Rosa, "Laser-cooling molecules", Eur. Phys. J. D **31**, 395 (2004).

[11] D. Gerlich and S. Schlemmer, "Deuterium fractionation in gas phase reactions measured in the laboratory", Plan. and Space Science **50**, 1287 (2002).

[12] D. DeMille , "Quantum Computation with Trapped Polar Molecules", Phys. Rev. Lett. **88**, 067901 (2002).

[13] U. Fröhlich, B. Roth, P. Antonini, C. Lämmerzahl, A. Wicht, and S. Schiller, "Ultracold Trapped Molecules: Novel Systems for Tests of the Time-Independence of the Electron-to-Proton Mass Ratio", Lect. Notes Phys. **648**, 297 (2004), **attached to this work**.

[14] C. Schwob, L. Jozefowski, B. de Beauvoir, L. Hilico, F. Nez, L. Julien, and F. Biraben, "Optical Frequency Measurement of the 2S-12D Transitions in Hydrogen and Deuterium: Rydberg Constant and Lamb Shift Determinations", Phys. Rev. Lett. **82**, 4960 (1999).

[15] P. Gill, Ed., *Proceedings of the 6th Symposium on Frequency Standards and Metrology*, World Scientific, Singapore (2002).

[16] D. Gerlich, E. Herbst, and E. Roueff, "$H_3^+ + HD \leftrightarrow H_2D^+ + H_2$: low-temperature laboratory measurements and interstellar implications", Planetary and Space Science **50**, 1275 (2002); O. Asvany, I. Savic, S. Schlemmer, and D. Gerlich, "Variable temperature ion trap studies of $CH_4^+ + H_2$, HD and $D_2$: negative temperature dependence and significant isotope effects", Chem. Phys. **298**, 97 (2004).

[17] T. Glenewinkel-Meyer and D. Gerlich, "Single and Merged Beam Studies of the Reaction $H_2^+(v = 0, 1; j = 0, 4) + H_2 \rightarrow H_3^+ + H$", Israel J. Chem. **37**, 343 (1997).

[18] J.D. Weinstein, R. deCarvalho, T. Guillet, B. Friedrich, and J.M. Doyle, "Magnetic trapping of calcium monohydride molecules at millikelvin temperatures", Nature **395**, 148 (1998).

[19] F.M.H. Crompvoets, H.L. Bethlem, R.T. Jongma, and G. Meijer, "A prototype storage ring for neutral molecules", Nature **411**, 174 (2001).

[20] T. Rieger, T. Junglen, S.A. Rangwala, P.W.H. Pinkse, and G. Rempe, "Continuous Loading of an Electrostatic Trap for Polar Molecules", Phys. Rev. Lett. **95**, 173002 (2005).

[21] M. Wewer and F. Stienkemeier, "Molecular versus excitonic transitions in PTCDA dimers and oligomers studied by helium nanodroplet isolation spectroscopy", Phys. Rev. B **67**, 125201 (2003).

[22] M.S. Elioff, J.J. Balentini, and D.W. Chandler, "Subkelvin Cooling NO Molecules via "Billiard-like" Collisions with Argon", Science **302**, 1940 (2003).

[23] M. Gupta and D.R. Herschbach, "Slowing and Speeding Molecular Beams by Means of a Rapidly Rotating Source", J. Phys. Chem. A **105**, 1626 (2001).

[24] P.F. Barker and M.N. Shneider, "Slowing molecules by optical microlinear deceleration", Phys. Rev. A **66**, 065402 (2002).

[25] V. Vuletic, A.T. Black, and J.K. Thompson, "External-Feedback Laser Cooling of Gases", quant-ph/0410168 (2004).

[26] P. Bowe, L. Hornekaer, C. Brodersen, M. Drewsen, J. S. Hangst, and J. P. Schiffer, "Sympathetic crystallization of trapped ions", Phys. Rev. Lett. **82**, 2071 (1999).

[27] D.J. Larson, J.C. Bergquist, J.J. Bollinger, W.M. Itano, and D.J. Wineland, "Sympathetic Cooling of Trapped Ions: A Laser-Cooled Two-Species Nonneutral Ion Plasma", Phys. Rev. Lett. **57**, 70 (1986).

[28] R.E. Drullinger, D.J. Wineland, and J.C. Bergquist, "High-Resolution Optical Spectra of Laser Cooled Ions", Appl. Phys. **22**,365 (1980).

[29] M.G. Raizen, J.M. Gilligan, J.C. Bergquist, W.M. Itano, and D.J. Wineland, "Ionic crystals in a linear Paul trap", Phys. Rev. A **45**, 6493 (1992).

[30] I. Waki, S. Kassner, G. Birkl, and H. Walther, "Observation of ordered structures of laser-cooled ions in a quadrupole storage ring", Phys. Rev. Lett. **68**, 2007 (1992).

[31] P. Bowe, L. Hornekær, C. Brodersen, M. Drewsen, J.S. Hangst, and J.P. Schiffer, "Sympathetic Crystallization of Trapped Ions", Phys. Rev. Lett. **82**, 2071 (1999).

[32] G. Modugno, G. Ferrari, G. Roati, R.J. Brecha, A. Simoni, and M. Inguscio, "Bose-Einstein Condensation of Potassium Atoms by Sympathetic Cooling ", Science **294**, 1320 (2001).

[33] T.J. Harmon, N. Moazzan-Ahmadi, and R.I. Thompson, "Instability heating of sympathetically cooled ions in a linear Paul trap", Phys. Review A **67**, 013415(8) (2003).

[34] S. Schiller and C. Lämmerzahl, "Molecular dynamics simulation of sympathetic crystallization of molecular ions", Phys. Rev. A **68**, 053406 (2003).

[35] L. Gruber, J.P. Holder, D. Schneider, "Formation of Strongly Coupled Plasmas from MultiComponent Ions in a Penning", Physica Scripta **71**, 60 (2005).

[36] T. Hasegawa and T. Shimizu, "Resonant oscialltion modes of sympathetically cooled ions in a radio-frequency trap", Phys. Rev. A **66**, 063404 (2002).

[37] M.A. van Eijkelenborg, M.E.M. Storkey, D.M. Segal, and R.C. Thompson, Sympathetic cooling and detection of molecular ions in a Penning trap", Phys. Rev. A **60**, 3903 (1999).

[38] H. Imajo, K. Hayasaka, R. Ohmukai, U. Tanaka, M. Watanabe, and S. Urabe, "High-resolution ultraviolet spectra of sympathetically-laser-cooled $Cd^+$ ions", Phys. Rev. A **53**, 122-125 (1996).

[39] Y. Kai, K. Toyoda, M. Watanabe, and S. Urabe, "Motional Resonances of Sympathetically Cooled $^{44}Ca^+$, $Zn^+$, or $Ga^+$ Ions in a Linear Paul Trap", Jpn. J. Appl. Phys. **40**, 5136-5140 (2001).

[40] B.B. Blinov, L. Deslauriers, P. Lee, M.J. Madsen, R. Miller, and C. Monroe, "Sympathetic cooling of trapped $Cd^+$ isotopes", Phys. Rev. A **65**, 040304(R) (2002).

[41] T. Baba and I. Waki, "Laser-cooled fluorescence mass spectrometry using laser-cooled barium ions in a tandem linear ion trap", J. Appl. Phys. **89**, 4592 (2001).

[42] K. Molhave and M. Drewsen, "Formation of translationally cold $MgH^+$ and $MgD^+$ molecules in an ion trap", Phys. Rev. A **62**, 011401 (2000).

[43] M. Drewsen, A. Mortensen, R. Martinussen, P. Staanum, and J.L. Sorensen, "Nondestructive Identification of Cold and Extremely Localized Single Molecular Ions", Phys. Rev. Lett. **93**, 243201 (2004).

[44] T. Baba and I. Waki, "Chemical reaction of sympathetically laser-cooled molecular ions", J. Chem. Phys. **116**, 1858 (2002).

[45] W. Paul, O. Osberghaus, and E. Fischer, "Ion cage", *Forschungsberichte des Wirtschafts- und Verkehrsministeriums Nordrhein Westfalen* **415**, Westdeutscher Verlag, Köln (1958).

[46] E. Fischer, "Three-dimensional stabilization of charged particles in a quadrupole field", Z. Phys. **156**, 1 (1959).

[47] R.F. Wuerker, H. Shelton, and R.V. Langmuir, "Electrodynamic Containment of Charged Particles", J. Appl. Phys. **30**, 342 (1959).

[48] P.K. Gosh, *"Ion Traps"*, Oxford Univ. press, New York (1995).

[49] A. Ostendorf, *"Sympathetische Kühlung von Molekülionen durch lasergekühlte Bariumionen in einer linearen Paulfalle"*, Ph.D. thesis, Heinrich-Heine University Düsseldorf (2006).

[50] H. Schnitzler, *"Development of an Experiment for Trapping, Cooling and Spectroscopy of Molecular Hydrogen Ions"*, Ph.D. thesis, Konstanz University (2001).

[51] H. Schnitzler, U. Fröhlich, T.K.W. Boley, A.E.M. Clemen, J. Mlynek, A. Peters, and S. Schiller, "All-solid-state tunable continuous-wave ultraviolet source with high spectral purity and frequency stability", Appl. Optics **41**, 7000 (2002).

[52] B. Roth, A. Ostendorf, H. Wenz, and S. Schiller, "Production of large molecular ion crystals via sympathetic cooling by laser-cooled $Ba^+$", J. Phys. B: At. Mol. Opt. Phys. **38**, 3673 (2005), **attached to this work**.

[53] B. Roth, U. Fröhlich, and S. Schiller, "Sympathetic cooling of $^4He^+$ ions in a radiofrequency trap", Phys. Rev. Lett. **94**, 053001 (2005), **attached to this work**.

[54] P. Blythe, B. Roth, U. Fröhlich, H. Wenz, and S. Schiller, "Production of Ultracold Trapped Molecular Hydrogen Ions", Phys. Rev. Lett. **95**, 183002 (2005), **attached to this work**.

[55] D.H.E. Dubin and T.M. O'Neil, "Trapped nonneutral plasmas, liquids, and crystals (the thermal equilibrium states)", Rev. Mod. Phys. **71**, 87 (1999).

[56] W.L. Slattery, G.D. Doolen, and H.E. DeWitt, Phys. Rev. A **21**, 2087 (1980).

[57] A. Ostendorf, C.B. Zhang, M.A. Wilson, D. Offenberg, B. Roth, and S. Schiller, "Sympathetic Cooling of Complex Molecular Ions to Millikelvin Temperatures", Phys. Rev. Lett. **97**, 243005 (2006), **attached to this work**.

[58] B. Roth, P. Blythe, H. Wenz, H. Daerr, and S. Schiller, "Ion-neutral chemical reactions between ultracold localized ions and neutral molecules with single-particle resolution", Phys. Rev. A **73**, 042712 (2006), **attached to this work**.

[59] B. Roth, P. Blythe, H. Daerr, L. Patacchini, and S. Schiller, "Production of ultracold diatomic and triatomic molecular ions of spectroscopic and astrophysical interest", J. Phys. B: At. Mol. Opt. Phys. **39**, S1241 (2006), **attached to this work**.

[60] L. Hornekær, "Single and Multi-Species Coulomb Ion Crystals: Structures, Dynamics and Sympathetic Cooling", Ph.D. thesis, Aarhus Univ. (2000).

[61] T. Baba and I. Waki, "Cooling and Mass-Analysis of Molecules Using Laser-Cooled Atoms", Jpn. J. Appl. Phys. **35**, L1134 (1996).

[62] D.J. Wineland, C. Monroe, W.M. Itano, D. Leibfried, B.E. King, and D.M. Meekhof, "Experimental Issues in Coherent Quantum-State Manipulation of Trapped Atomic Ions", J. Res. Natl. Inst. Stand. Technol. **103**, 259 (1998).

[63] V.L. Ryjkov, X.Z. Zhao, and H.A. Schuessler, "Sympathetic cooling of fullerene ions by laser-cooled $Mg^+$ ions in a linear rf trap", Phys. Rev. A **74**, 023401 (2006).

[64] J. Eschner, B. Appasamy, and P.E. Toschek, "Stochastic Cooling of a Trapped Ion by Null Detection of Its Fluorescence", Phys. Rev. Lett. **74**, 2435 (1995).

[65] J. Eschner, G. Morigi, F. Schmidt-Kaler, and R. Blatt, "Laser cooling of trapped ions", J. Opt. Soc. Am. B **20**, 1003 (2003).

[66] R.C. Davidson, *Physics of Nonneutral Plasmas*, Imperial College Press (2001).

[67] N. Kjaergaard and M. Drewsen, "Observation of a Structural Tansition for Coulomb Crystals in a Linear Paul Trap" Phys. Rev. Lett. **91**, 095002 (2003).

[68] A. Mortensen, E. Nielsen, T. Matthey, and M. Drewsen, "Observation of Three-Dimensional Long-Range Order in Small Ion Coulomb Crystals in an rf Trap" Phys. Rev. Lett. **96**, 103001 (2006).

[69] L.R. Brewer, J.D. Prestage, J.J. Bollinger, W.M. Itano, D.J. Larson, and D.J. Wineland, "Static properties of a non-neutral $^9Be^+$-ion plasma", Phys. Rev. A **38**, 859 (1988).

[70] D.H.E. Dubin, "Equilibrium and dynamics of uniform density ellipsoidal non-neutral plasmas", Phys. Fluids B **5**, 295 (1992).

[71] X.-P. Huang, J.J. Bollinger, T.B. Mitchell, W.M. Itano, and D.H.E. Dubin, "Precise control of the global rotation of strongly coupled ion plasmas in a Penning trap", Phys. Plasmas **5**, 1656 (1998).

[72] U. Fröhlich, B. Roth, and S. Schiller, "Ellipsoidal Coulomb crystals in a linear radiofrequency trap" Phys. Plasmas **12**, 073506 (2005), **attached to this work**.

[73] D.J. Berkeland, J.D. Miller, J.C. Bergquist, W.M. Itano, and D.J. Wineland , "Minimization of ion micromotion in a Paul trap", J. Appl. Phys. **83**, 5025 (1998).

[74] In the group of Parks et al. (see [94]), laser-induced fluorescence detection of trapped molecular ions (singly charged Rhodamine 640 and AlexaFluor350 ions) in the presence of helium buffer was implemented. The ions were exposed to Nd:YAG laser pulses at 532 nm and 355 nm. The technique was used to measure the laser-induced fragmentation of AlexaFluor350 ions.

[75] M. Welling *et al.*, "Ion/molecule reactions, mass spectrometry and optical spectroscopy in a linear ion trap", Int. J. Mass. Spectr. and Ion Proc. **172**, 95-114 (1998).

[76] B. Roth, P. Blythe, and S. Schiller, "Motional Resonance Coupling in Cold Multi-Species Coulomb Crystals", Phys. Rev. A **75**, 023402 (2007), **attached to this work**.

[77] G. Morigi and Shmuel Fishman, "Eigenmodes and Thermodynamics of a Coulomb Chain in a Harmonic Potential", Phys. Rev. Lett. **93**, 170602 (2004).

[78] V.L. Ryjkov, X.Z. Zhao, and H.A. Schuessler, "Simulations of the rf heating rates in a linear quadrupole ion trap", Phys. Rev. A **71**, 033414 (2005).

[79] X.Z. Zhao, V.L. Ryjkov, and H.A. Schuessler, "Fluorescence profiles and cooling dynamics of laser-cooled $Mg^+$ ions in a linear rf trap", Phys. Rev. A **73**, 033412 (2006).

[80] M. Bussmann, U. Schramm, D. Habs, V.S. Kolhinen, and J. Szerpypo, "Stopping highly charged ions in a laser-cooled one component plasma of $^{24}Mg^+$ ions", Int. J. Mass. Spectrom. **251**, 179 (2006).

[81] C.B. Zhang, D. Offenberg, B. Roth, M.A. Wilson, and S. Schiller, "Molecular dynamics simulations of cold multi-species ion ensembles in a linear Paul trap", Phys. Rev. A **76**, 012719 (2007), **attached to this work**.

[82] D. Gerlich, "Inhomogeneous rf fields: a versatile tool for the study of processes with slow ions", *Advances in Chemical Physics: State-selected and state-to-state ion molecule reaction dynamics* Vol. LXXXII, John Wiley & Sons, New York (1992).

[83] E. Herbst, "The astrochemistry of $H_3^+$", Phil. Trans. R. Soc. Lond. A **358**, 2523 (2000).

[84] See, e.g., "Astronomy, Physics and Chemistry of $H_3^+$", *Phil. Trans. R. Soc. Lond. A* **358**, Nr. 1774, *The Royal Society* (2000), and J. Mikosch, H. Kreckel, R. Wester, R. Plail, J. Glosik, D. Gerlich, D. Schwalm and A. Wolf, "Action spectroscopy and temperature diagnostics of $H_3^+$ by chemical probing", J. Chem. Phys. **121**, 11030 (2004).

[85] T.R. Geballe and T. Oka, "A Key Molecular Ion in the Universe and in the Laboratory", Science **312**, 1610 (2006).

[86] J.B. Hasted, "Physics of Atomic Collisions", London: Butterworths (1964).

[87] D.A. Church, "Charge-changing collisions of stored, multiply-charged ions", J. Mod. Optics **39**(2), 423 (1992).

[88] J.K. Kim, L.P. Theard, and W.T. Huntress Jr., "Proton Transfer Reactions from $H_3^+$ Ions To $N_2$, $O_2$, and CO molecules", Chem. Phys. Lett. **32**, 610 (1975); A.E. Roche, M.M. Sutton, D.K. Rohme, and H.I. Schiff, "Determination of Proton Affinity from the Kinetics of Proton Transfer Reactions. I. Relative Proton Affinities", J. Chem. Phys. **55**, 5840 (1971).

[89] N.G. Adams and D. Smith, "A Further Study of the Near-Thermoneutral Reactions $O_2H^+ \leftrightarrow H_3^+ + O_2$", Chem. Phys. Lett. **105**, 604 (1984).

[90] I.S.Vogelius, L.B. Madsen, and M. Drewsen, "Rotational cooling of heteronuclear molecular ions $^{1,2,3}\Sigma$, and $^2\Pi$ electronic ground states", Phys. Rev. A **70**, 053412 (2004).

[91] I.S. Vogelius, L.B. Madsen, and M. Drewsen, "Blackbody-Radiation-Assisted Laser Cooling of Molecular Ions", Phys. Rev. Lett. **89**, 173003 (2002).

[92] N. Balakrishnan, A.B. Alekseyev, and R.J. Buenker, "Ab initio quantum mechanical investigation of the photodissociation of HI and DI", Chem. Phys. Lett. **341**, 594 (2001); D.B. Kokh, A.B. Alekseyev, and R.J. Buenker, "Theoretical study of the UV absorption in $Cl_2$: Potentials, transition moments, extinction coefficients, and Cl*/Cl branching ratio", J. Chem. Phys. **120**, 11549 (2004).

[93] A. Bertelsen, I.S. Vogelius, S. Jorgensen, R. Kosloff, and M. Drewsen, "Photodissociation of Cold $MgH^+$ ions", Eur. Phys. J. D **31**, 403 (2004).

[94] J.T. Khoury, S. Rodriguez-Cruz, J.H. Parks, "Pulsed fluorescence measurements of trapped molecular ions with zero background detection", J. Am. Soc. Mass Spectrom. **13**, 696 (2002).

[95] K.B. Jefferts, "Hyperfine Structure in the Molecular Ion $H_2^+$", Phys. Rev. Lett. **23**, 1476 (1969).

[96] W.H. Wing, G.A. Ruff, W.E. Lamb, J.J. Spezeski, "Observation of the Infrared Spectrum of the Hydrogen Molecular Ion $HD^+$", Phys. Rev. Lett. **36**, 1488 (1976).

[97] A. Carrington, "Microwave Spectroscopy at the Dissociation Limit", Science **274**, 1327 (1996).

[98] A.D.J. Critchley, A.N. Hughes, I.R. McNab, "Direct Measurement of a Pure Rotation Transition in $H_2^+$", Phys. Rev. Lett. **86**, 1725 (2001).

[99] J.J. Spezeski, Ph.D. thesis, Yale University (1977).

[100] Y.P. Zhang, C.H. Cheng, J.T. Kim, J. Stanojevic, and E.E. Eyler, "Dissociation Energies of Molecular Hydrogen and the Hydrogen Molecular Ion", Phys. Rev. Lett. **92**, 203003 (2004), and references therein.

[101] R.E. Moss, "Calculations for the vibration-rotation levels of $H_2^+$ in its ground and first excited electronic states", Molecular Physics **80**, 1541 (1993).

[102] R.E. Moss, "Calculations for vibration-rotation levels of $HD^+$, in particular for high $N$", Molecular Physics **78**, 371 (1993).

[103] M.M. Cassar and G.W.F. Drake, "High precision variational calculations for $H_2^+$", J. Phys. B **37**, 2485 (2004).

[104] H. Li, J. Wu, B.-L. Zhou, J.-M. Zhu, and Z.-C. Yan, "Calculations of energies of the hydrogen molecular ion", Phys. Rev. A **75**, 012504 (2007).

[105] V.I. Korobov, "Leading-order relativistic and radiative corrections to the rovibrational spectrum of $H_2^+$ and $HD^+$ molecular ions", Phys. Rev. A **74**, 052506 (2006).

[106] D. Bakalov, V.I. Korobov, and S. Schiller, "High-Precision Calculation of the Hyperfine Structure of the $HD^+$ Ion", Phys. Rev. Lett. **97**, 243001 (2006).

[107] R. Holzwarth, Th. Udem, T.W. Hänsch, C. Knight, W.J. Wadsworth, and P.St.J. Russell, "Optical Frequency Synthesizer for Precision Spectroscopy", Phys. Rev. Lett. **85**, 2264 (2000).

[108] J. F. Babb, in *Current Topics in Physics*, edited by Y.M. Cho, J.B. Hong, and C.N. Yang (World Scientific, Singapore, 1998), p. 531.

[109] S. Schiller and V. Korobov, "Tests of time independence of the electron and nuclear masses with ultracold molecules", Phys. Rev. A **71**, 032505 (2005).

[110] J.P. Uzan, "The fundamental constants and their variation: observational and theoretical status", Rev. Mod. Phys. **75**, 403 (2003).

[111] J.C.J. Koelemeij, B. Roth, and S. Schiller, "Cold molecular ions for blackbody thermometry and possible application to ion-based frequency standards", Phys. Rev. A **76**, 023413 (2007), **attached to this work**.

[112] B. Roth, J. Koelemeij, S. Schiller, L. Hilico, J.-P. Karr, V. Korobov, and D. Bakalov, "Precision Spectroscopy of Molecular Hydrogen Ions: Towards Frequency Metrology of Particle Masses", in *Precision Physics of Simple Atoms and Molecules*, Lect. Notes Phys. **745**, 205, Springer (2008), **attached to this work**.

[113] P.J. Mohr and B.N. Taylor, "CODATA recommended values of the fundamental physical constants: 2002", Rev. Mod. Phys. **77**, 1 (2005).

[114] J. Verdu, S. Djekic, S. Stahl, T. Valenzuela, M. Vogel, G. Werth, T. Beier, H.J. Kluge, W. Quint, "Electronic g Factor of Hydrogenlike Oxygen $^{16}O^{7+}$", Phys. Rev. Lett. **92**, 093002 (2004).

[115] X. Calmet and H. Fritsch, "The cosmological evolution of the nucleon mass and the electroweak coupling constants", Eur. Phys. J. C **24**, 639 (2002).

[116] P. Langacker, G. Segre, and M. Strassler, "Implications of gauge unification for time variation of the fine structure constant", Phys. Lett. B **528**, 121 (2002).

[117] V.V. Flambaum, D.B. Leinweber, A.W. Thomas, and R.D. Young, "Limits on variations of the quark masses, QCD scale, and fine structure constant", Phys. Rev. D **69**, 115006 (2004).

[118] J.K. Webb, M.T. Murphy, V.V. Flambaum, V.A. Dzuba, J.D. Barrow, C.W. Churchill, J.X. Prochaska, and A.M. Wolfe, "Further Evidence for Cosmological Evolution of the Fine Structure Constant", Phys. Rev. Lett. **87**, 091301 (2001).

[119] R. Srianand, H. Chand, P. Petitjean, and B. Aracil, "Limits on the Time Variation of the Electromagnetic Fine-Structure Constant in the Low Energy Limit from Absorption Lines in the Spectra of Distant Quasars", Phys. Rev. Lett. **92**, 121302 (2004).

[120] R. Quast, D. Reimers, and S. Levshakov, "Probing the variability of the fine-structure constant with the VLT/UVES", Astron. Astrophys. **415**, L7 (2004).

[121] E. Reinhold, R. Buning, U. Hollenstein, A. Ivanchik, P. Petitjean, and W. Ubachs, "Indication of a Cosmological Variation of the Proton-Electron Mass Ratio Based on Laboratory Measurement and Reanalysis of $H_2$ Spectra", Phys. Rev. Lett. **96**, 151101 (2006).

[122] M. Tadjeddine and G. Parlant, "Computed photodissociation cross sections of $HD^+$ and Franck-Condon factors for the ionization of HD", Molecular Physics **33**, 1797 (1977); A. Kondorskiy, priv. comm. (2006).

[123] B. Roth, J.C.J. Koelemeij, H. Daerr, and S. Schiller, "Rovibrational spectroscopy of trapped molecular hydrogen ions at millikelvin temperatures", Phys. Rev. A **74**, 040501(R) (2006), **attached to this work**.

[124] B. Roth, J. Koelemeij, H. Daerr, I. Ernsting, S. Jorgensen, M. Okhapkin, A. Wicht, A. Nevsky, and S. Schiller, "Trapped Ultracold Molecular Ions: Candidates for an Optical Molecular Clock for a Fundamental Physics Mission in Space", in *Proc. of the 6th Internat. Conf. on Space Optics*, ESTEC, Noordwijk, The Netherlands, ESA-SP 621 (2006), **attached to this work**.

[125] J. Koelemeij, B. Roth, I. Ernsting, A. Wicht, and S. Schiller, "Vibrational spectroscopy of cold $HD^+$ with 2 ppb accuracy", Phys. Rev. Lett. **98**, 173002 (2007), **attached to this work**.

[126] A. Bertelsen, S. Jorgensen, and M. Drewsen, "The rotational temperature of polar molecular ions in Coulomb crystals", J. Phys. B: At. Mol. Opt. Phys. **39**, L83 (2006).

[127] B. Roth, H. Daerr, J. Koelemeij, A. Nevsky, and S. Schiller, "Ultracold Molecular Hydrogen Ions in a Linear Radiofrequency Trap: Novel Systems for Molecular

Frequency Metrology", Proc. '20th European Frequency an Time Forum EFTF', Braunschweig, Germany (2006), **attached to this work**.

[128] D.J. Wineland, J.C. Bergquist, J.J. Bollinger, R.E. Drullinger, and W.M. Itano, "Quantum computers and atomic clocks", in *Proceedings of the 6th Symposium on Frequency Standards and Metrology*, edited by P. Gill, World Scientific, Singapore, p. 361 (2002).

[129] P.O. Schmidt, T. Rosenband, C. Langer, W.M. Itano, J.C. Bergquist, and D.J. Wineland, "Spectroscopy Using Quantum Logic", Science **309**, 749 (2005).

# Appendix A

# Zusammenfassung

Das Gebiet der kalten Moleküle ist ein neues Gebiet der Quantenoptik, welches in den letzten Jahren immer mehr in den Mittelpunkt eines breiten interdisziplinären Interesses gerückt ist. Nach den aufsehenerregenden Erfolgen, welche bei den ukltrakalten, neutralen und geladenen Atome erzielt werden konnten, sind in den letzten Jahren vielfältige Anstrengungen unternommen worden, Methoden und Techniken zu entwickeln, um auch Moleküle in der Gasphase auf Temperaturen im Millikelvin-Berreich und darunter abzukühlen. Insbesondere sind universell einsetzbare Methoden von Interesse, welche für eine breite Klasse von Molekülen geeignet sind.
Neben der Demonstration solcher Techniken sind neuerdings auch erste Anwendungen kalter Moleküle zum Gegenstand intensiver Forschungsaktivitäten geworden. Beispielsweise sind kalte Moleküle interessante Modellsysteme zur Untersuchung fundamentaler Fragestellungen der Grundlagenforschung. Sie sind insbesondere geeignet zur Spektroskopie an Rotations- und Vibrationsübergängen in Molekülen mit höchster Auflösung. Der Einsatz moderner Lasertechnologie bei solchen Messungen verspricht eine Steigerung der spektroskopischen Genauigkeit um mehrere Größenordnungen, ähnlich der Genauigkeit, wie sie in atomaren Systemen erzielt werden konnte, und eröffnet die Perspektive einer präzisen Messungen fundamentaler Konstanten in der Natur. Weitere potenzielle Anwendungen kalter molekularer Systeme sind die Untersuchung langsamer Prozesse in komplexen Molekülen und die Untersuchung von Ion-Neutral Kollisionen bei niedrigen Temperaturen. Die exakte Präparation von Quantenzuständen in kalten molekularen Systemen eröffnet auch die Möglichkeit der Untersuchung interner Kohärenzen, der Implementierung eines Quantencomputers mit Molekülen sowie der Entwicklung neuer Uhren in der Frequenzmetrologie.
In dieser Arbeit werden Beiträge zu den obigen Themengebieten beschrieben. Die Arbeiten sind am Institut für Experimentalphysik der Heinrich-Heine Universität Düsseldorf im Zeitaum von Januar 2002 bis Januar 2007 entstanden. Im Einzelnen wurden folgende Themengebiete bearbeitet:

- Methoden zur Erzeugung kalter ($<$100 mK), gespeicherter atomarer und molekularer Ionen in Massenbereich 1-470 amu wurden entwickelt. Dabei konnten,

unter anderem, leichte Ionen, wie etwa Protonen, Wasserstoffmoleküle und Heliumatome, welche von Bedeutung für die Fundamentalphysik sind, aber auch schwere polyatomare Moleküle bestehend aus bis zu 42 Atomen, wie etwa Alexa-Fluor und Glycerrhetinsäure, mit Massen im Bereich von 470 amu erzeugt werden.

- Die Eigenschaften der so erzeugten ein- und mehrkomponentigen Ionenplasmen konnten systematisch untersucht und charakterisiert werden, beispielsweise als Funktion der Symmetrie des Fallenpotentials (sphärisch symmetrisch oder ellipsoidal).

- Verschiedene neuartige destruktive und nichtdestruktive Techniken für den Nachweis gekühlter Teilchenspezies wurden entwickelt, welche essentiell für eine massenspektroskopische Analyse der Ionenkristalle sind. Methoden zur präzisen Manipulation der Ionenkristalle sind ebenfalls demonstriert worden.

- Die komplexe Dynamik der erzeugten Vielteilchensysteme wurde anhand von numerischen Simulationen untersucht. Dadurch konnten die in den kalten Plasmen enthaltenen Teilchenzahlen bestimmt sowie obere Grenzen für die erzielten translatorischen Temperaturen abgeschätzt werden. Die Simulationen wurden erstmals auf mehrkomponentige Plasmen unter Einbeziehung aller relevanter Heizeffekte ausgedehnt. Sie wurden ebenfalls zur Bestimmung von Kühl- und Heizraten sowie zur Simulation teilchenspezifischer Fallenmoden und ihrer Kopplung in der Falle eingesetzt und sind unverzichtbarer Bestandteil der Analyse der Ionenkristalle.

- Reaktionen zwischen sympathetisch gekühlten Atomen und Molekülen und neutralen Teilchen konnten untersucht werden. Mit der entwickelten Methode wurde eine Auflösung im Bereich einzelner Ionen erreicht. Die Methode eignet sich insbesondere zur Untersuchung einer Vielzahl chemischer Reaktionen mit kalten Reaktionspartnern, welche für die Chemie im interstellaren Medium von Bedeutung sind. Reaktionenraten für mehrere solcher Reaktionen konnten gemessen werden.

- Die Möglichkeit der Kontrolle chemischer Reaktionssequenzen wurde genutzt, um kalte, nahezu lokalisierte, astrophysikalisch und metrologisch relevante Molekülionen zu erzeugen.

- Hochauflösende Rotations-Vibrations-Spektroskopie an kalten Molekülionen wurde erstmals demonstriert.

- Mittels (1+1') REMPD Laserspektroskopie wurde die Frequenz rovibronischer Übergänge in $HD^+$-Ionen erstmals absolut vermessen. Dabei kam ein Femtosekunden-Frequenzkamm zum Einsatz. Die erzielte spektroskopische Genauigkeit liegt bei 2.3 ppb (absolute Genauigkeit 0.5 MHz) und stellt die bisher genaueste Messung an $HD^+$ dar. Verglichen mit früheren Ergebnissen and $HD^+$

konnte die spektroskopische Genauigkeit um einen Faktor 165 gesteigert werden. Aus der gemessenen Übergangsfrequenz konnte das Elektron-zu-Proton-Massenverhältnis $m_e/m_p$ mit einer Genauigkeit von etwa 5 ppb hergeleitet werden. Das erzielte Ergebnis ist in guter Übereinstimmung mit dem im Jahr 2002 von der CODATA-Komission empfohlenen Wert für $m_e/m_p$. Das enorme Potenzial dieser Spektroskopie-Methode, welches zur Steigerung der erzielten Genauigkeit um mehrere Größenordnungen führen kann, konnte somit demonstriert werden.

- Eine relativ genaue Methode zur Messung der Rotationstemperatur translatorisch kalter Moleküle wurde entwickelt. Die Methode wurde auf $HD^+$-Ionen angewandt. Auf diese Weise konnte gezeigt werden, dass die sympathetische Kühlung der translatorischen Freiheitsgrade gespeicherter Molekülionen nicht an deren interne Freiheitsgrade koppelt. Mittels der entwickelten Methode kann diese Tatsache dazu ausgenutzt werden, um die Temperatur der umgebenden Scharzkörperstrahlung zu bestimmen oder um die Manipulation interner Freiheisgrade kalter gespeicherter Molekülionen durch lasergekühlte, neutralen Atome (beispielsweise aus einer magnetooptischen Falle) zu untersuchen.

Insgesamt wurde in dieser Arbeit das breite Anwendungspotenzial der sympathetischen Kühlung demonstriert. Es konnte gezeigt werden, dass die einzigartigen Eigenschaften der erzeugten kalten Ionenplasmen sich für eine Vielzahl von neuartigen Untersuchungen eignen, welche zur Entdeckung neuer physikalischer Effekte in Vielteichensystemen und zur spektroskopischen Messungen mit allerhöchster Auflösung führen können. Weitere potenzielle Entwicklungen auf dem Gebiet der kalten Atom- und Molekülionen wurden aufgezeigt.

# Appendix B

# Publications in refereed journals

B. Roth, U. Fröhlich, and S. Schiller, "Sympathetic cooling of $^4He^+$ ions in a radiofrequency trap", Phys. Rev. Lett. **94**, 053001 (2005).

U. Fröhlich, B. Roth, and S. Schiller, "Ellipsoidal Coulomb crystals in a linear radiofrequency trap" Phys. Plasmas **12**, 073506 (2005).

P. Blythe, B. Roth, U. Fröhlich, H. Wenz, and S. Schiller, "Production of Ultracold Trapped Molecular Hydrogen Ions", Phys. Rev. Lett. **95**, 183002 (2005).

B. Roth, A. Ostendorf, H. Wenz, and S. Schiller, "Production of large molecular ion crystals via sympathetic cooling by laser-cooled $Ba^+$", J. Phys. B: At. Mol. Opt. Phys. **38**, 3673 (2005).

B. Roth, P. Blythe, H. Wenz, H. Daerr, and S. Schiller, "Ion-neutral chemical reactions between ultracold localized ions and neutral molecules with single-particle resolution", Phys. Rev. A **73**, 042712 (2006).

A. Ostendorf, C.B. Zhang, M.A. Wilson, D. Offenberg, B. Roth, and S. Schiller, "Sympathetic Cooling of Complex Molecular Ions to Millikelvin Temperatures", Phys. Rev. Lett. **97**, 243005 (2006).

B. Roth, P. Blythe, H. Daerr, L. Patacchini, and S. Schiller, "Production of ultracold diatomic and triatomic molecular ions of spectroscopic and astrophysical interest", J. Phys. B: At. Mol. Opt. Phys. **39**, S1241 (2006).

B. Roth, J.C.J. Koelemeij, H. Daerr, and S. Schiller, "Rovibrational spectroscopy of trapped molecular hydrogen ions at millikelvin temperatures", Phys. Rev. A **74**, 040501(R) (2006).

B. Roth, P. Blythe, and S. Schiller, "Motional Resonance Coupling in Cold Multi-Species Coulomb Crystals", Phys. Rev. A **75**, 023402 (2007).

J. Koelemeij, B. Roth, I. Ernsting, A. Wicht, and S. Schiller, "Vibrational spectroscopy of cold $HD^+$ with 2 ppb accuracy", Phys. Rev. Lett. **98**, 173002 (2007).

C.B. Zhang, D. Offenberg, B. Roth, M.A. Wilson, and S. Schiller, "Molecular dynamics simulations of cold multi-species ion ensembles in a linear Paul trap", Phys. Rev. A **76**, 012719 (2007).

J.C.J. Koelemeij, B. Roth, and S. Schiller, "Cold molecular ions for blackbody thermometry and possible application to ion-based frequency standards", Phys. Rev. A **76**, 023413 (2007).

# Sympathetic Cooling of $^4He^+$ Ions in a Radio-Frequency Trap

B. Roth, U. Fröhlich, and S. Schiller

*Institut für Experimentalphysik, Heinrich–Heine–Universität Düsseldorf, 40225 Düsseldorf, Germany*

(Received 23 July 2004; published 7 February 2005)

We have generated Coulomb crystals of ultracold $^4He^+$ ions in a linear radio-frequency trap, by sympathetic cooling via laser-cooled $^9Be^+$. Stable crystals containing up to 150 localized $He^+$ ions at $\sim$20 mK were obtained. Ensembles or single ultracold $He^+$ ions open up interesting perspectives for performing precision tests of QED and measurements of nuclear radii. This Letter also indicates the feasibility of cooling and crystallizing highly charged atomic ions using $^9Be^+$ as coolant.

DOI: 10.1103/PhysRevLett.94.053001 PACS numbers: 32.80.Pj, 42.50.−p

The two-body Coulomb system is one of the most fundamental in physics, and has been central in the development of quantum mechanics, relativistic quantum mechanics, and QED. In nuclear physics, the study of these systems can provide an alternative method for precise determination of nuclear sizes [1]. Hydrogenlike systems studied include the hydrogen atom and its isotopes, muonic hydrogen, the helium ions, muonium, and positronium. More recently, heavy (high-$Z$) hydrogenlike ions have become available [2] and are being used, e.g., for exploring strong-field QED [3] and for measuring the electron mass [4]. Among the low-$Z$ atomic systems, hydrogen has been the most extensively studied, in particular, by laser spectroscopy. This has resulted, among others, in the most precise measurement of a fundamental constant, the Rydberg constant [5]. While the helium ions $^3He^+$ and $^4He^+$ are important systems because they are complementary to the hydrogen atom, they have been much less studied. Precision measurements of transition frequencies in $He^+$ ions could provide (i) an independent (metrologically significant) determination of the Rydberg constant, (ii) an independent determination of the nuclear charge radii and the isotope shift, assuming QED (Lamb shift) calculations are correct, or (iii) a test of QED, using independent radius data (from scattering measurements) as input.

Precise values of the He nuclear radii can test theoretical nuclear methods and force models, which accurately describe these special nuclei ($^3He$ is the only stable three-particle nucleus, $^4He$ is the lightest closed-shell nucleus). The possibility of QED tests with He ions is attractive because the QED corrections scale with high powers of $Z$ (some of the theoretically unknown contributions scale as $Z^6$), and thus their relative contribution to transition frequencies is larger than in hydrogen. Also, the available independent $^4He^+$ nuclear radius measurements agree, in contrast to the situation in hydrogen.

On the experimental side, the hyperfine structure of $^3He^+$ has been measured in both the electronic $1S$ ground state and the $2S$ excited state [6]. The Lamb shift of the $2S$ state in $^4He^+$ has been determined from the spontaneous emission anisotropy with 170 kHz uncertainty and compared to theoretical calculations [7,8]. The $^3He/^4He$ squared nuclear radius difference has been determined at the 0.4% level from the isotope shift in neutral helium using laser spectroscopy [9].

A significant extension of these studies would be accessible via high-resolution laser spectroscopy of helium ions, which has not been performed so far. Measurements of the $1S$-$2S$ and $2S$-$3S$ two-photon transition frequencies (at 61 and 328 nm, with linewidths 167 Hz and 16 MHz, respectively) have been proposed [10,11]. For example, a $1S$-$2S$ measurement with reasonable experimental uncertainty $<$30 kHz would test the nuclear and the recently improved theoretical QED contributions at their current accuracy level [12]. A measurement of the isotope shift with a similar accuracy would improve the value of the squared nuclear charge radius difference by an order of magnitude.

One important aspect in these future precision experiments will be the availability of trapped ultracold helium ions, in order to minimize the influence of Doppler broadening or shifts and to allow a precise study of systematic effects. The experience with trapped ions for atomic clocks has shown the success of this approach [13].

In this Letter we report on the first production of an ultracold sample of $^4He^+$. While trapping of these ions is straightforward using a Paul-type trap [14], cooling is more difficult. Direct laser cooling appears impractical at present, since the generation of the required continuous-wave deep-UV 30 nm radiation is a challenging problem in itself. An alternative and flexible method is sympathetic (interaction) cooling, where ''sample'' particles of one species are cooled by an ensemble of directly cooled (often by laser cooling) particles of another species via their mutual interaction. This method was first demonstrated for ions in Penning traps [15,16], and later in Paul traps [17–19]. Under strong cooling, the mixed-species ensemble forms a Coulomb crystal. In sympathetic crystallization of large ensembles a minimum mass ratio range $m_{sc}/m_{lc}$ of 0.6 between sympathetically cooled and laser-cooled ions has so far been achieved [20]. Recent molecular dynamics simulations showed that sympathetic cooling

 

in an ion trap down to a mass ratio of 0.3 should be possible [21,22]. A two-ion sympathetically cooled crystal exhibited a mass ratio of 0.38 [23]. In the present work we have used the lightest atomic ion suitable for practical laser cooling, $^9Be^+$, for which the mass ratio to $^4He^+$ is 0.44.

We use a linear quadrupole trap to simultaneously store $Be^+$ and $He^+$ ions. It consists of four cylindrical electrodes, each sectioned longitudinally into three parts. A necessary condition for stable trapping is a stability parameter, $q = 2QV_{\rm rf}/m\Omega^2 r_0^2 < 0.9$. Here, $Q$ and $m$ are the charge and the mass of the trapped ions, $V_{\rm rf}$ and $\Omega$ are the amplitude and the frequency of the rf driving field and $r_0 = 4.3$ mm is the distance from the trap centerline to the electrodes. Trap operation at small $q$ parameters is favorable since rf-heating effects are less pronounced. We operate our trap at $\Omega = 2\pi \times 14.2$ MHz and $V_{\rm rf} = 380$ V where $q \simeq 0.04$ (0.1) for $Be^+$ ($He^+$). For such small $q$ one can approximate the motion of ions (in the absence of interactions) by that in an effective time-independent harmonic potential $U_{\rm trap}(x, y, z) = \frac{m}{2}[\omega_r^2(x^2 + y^2) + \omega_z^2 z^2]$. The $z$ axis is along the trap centerline. Oscillations transverse to the $z$ axis occur with frequency $\omega_r = (\omega_0^2 - \omega_z^2/2)^{1/2}$, with $\omega_0 = QV_{\rm rf}/\sqrt{2}m\Omega r_0^2$ being the limiting value for a very prolate trap. The longitudinal frequency $\omega_z = (2\kappa QV_{\rm EC}/m)^{1/2}$ is obtained from a dc potential $V_{\rm EC}$ applied to the eight end sections (end caps) of the electrodes, where $\kappa \approx 3 \times 10^{-3}$ mm$^{-2}$ is a constant determined by the trap geometry.

For laser cooling of $Be^+$ ions we produce light resonant with the $^2S_{1/2}(F = 2) \rightarrow {}^2P_{3/2}$ transition at 313 nm by doubly resonant sum frequency generation, frequency stabilized to a hyperfine transition of molecular iodine [24]. The $Be^+$ fluorescence is simultaneously recorded with a photomultiplier and a CCD camera.

First, we load the trap with $He^+$ ions by leaking He gas into the vacuum chamber at a pressure of $10^{-8}$ mbar and ionizing it *in situ* by a 750 eV electron beam. The loading rate is controlled by the partial pressure of neutral He gas and the electron beam intensity. Subsequently, $Be^+$ ions are produced by ionizing neutral atoms evaporated from a Be oven with the same electron beam. During $Be^+$ loading the cooling and repumper lasers are continuously scanned over a 5 GHz interval below resonance.

One of the well-known signs for a phase transition from the fluid ion plasma to an ordered crystal state is the appearance of a sudden drop in the detected fluorescence attributed to the reduction in the particle velocities and thus Doppler broadening. Once this occurs, the cooling laser frequency is held constant at a red detuning of approximately half the natural linewidth (60 MHz) from the $Be^+$ resonance. Under this condition the crystals are stable, with a particle loss half time of $\sim$3 h.

Figure 1 shows three prolate two-component ion crystals containing $Be^+$ and $He^+$. The crystals display the well-known shell structure and enclose an inner dark region originating from the incorporated sympathetically cooled particles having a lower mass-to-charge ratio than that of the atomic coolants. Their location on axis is due to the stronger effective potential ($\sim Q^2/m$ for a strongly prolate trap, $\omega_r \gg \omega_z$) experienced by them as compared to the $Be^+$ ions. While Fig. 1(a) was taken with an axially symmetric potential, in Fig. 1(b) and 1(c) a static quadrupole potential $V_{\rm DC}$ was added The added potential turns the spheroidal crystal into an ellipsoid, squeezing the crystal in a direction at 45° to the observation direction [25]. This results in a redistribution of the ions such that fewer or no $Be^+$ ions remain in front and behind the $He^+$ ions. The shapes of large Coulomb crystals containing a small relative amount of $He^+$ ions agree well with the cold fluid plasma model [25,26].

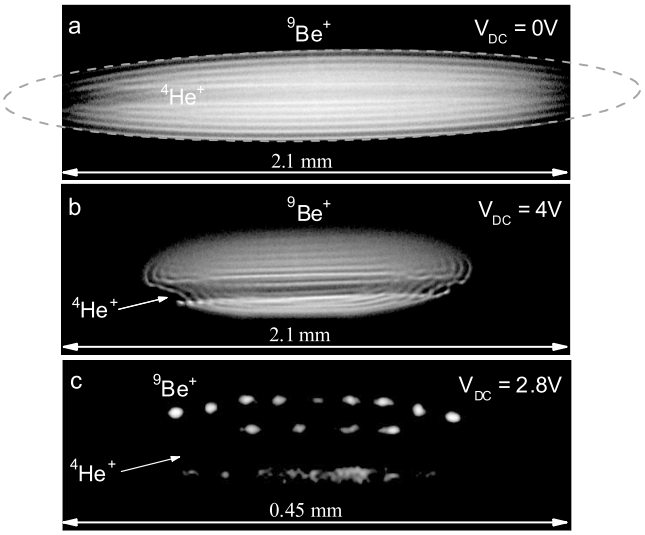


FIG. 1. CCD images of two-component Coulomb crystals (integration time: 2 s). (a) Spheroidal crystal. The ellipse is a fit to the crystal boundary with a semiaxes ratio $R/L = 0.16$. (b),(c) Ellipsoidal crystal. The inner dark cores contain $\approx$ 150, 30, and 5 sympathetically crystallized $He^+$ ions, respectively. The trap axis $z$ is horizontal. For (a),(c) the cooling laser beam direction is to the right, for (b) two counterpropagating beams were used. The asymmetric ion distribution for (b),(c) is attributed to static stray potentials.

The number of crystallized particles is estimated by performing molecular dynamics (MD) simulations and varying the number of particles until the observed CCD image is reproduced. While for single-species structures one may obtain the particle number from the cold fluid model, which yields a particle density $n_0 = \epsilon_0 V_{\rm rf}^2/m\Omega^2 r_0^4$ ($\approx 3.1 \times 10^4$ mm$^{-3}$ for $Be^+$), together with measured dimensions, here the MD approach is better suited. It is applicable to multispecies structures, in addition produces detailed structural information, and reduces uncertainties related to the calibration of the imaging system magnification. For example, MD simulations of the crystal in Fig. 1(a) show that it contains approximately $6.2 \times 10^3$ $Be^+$ ions and 150 $He^+$ ions. The radial intershell distance is obtained as 29 $\mu$m. This value agrees well with the

result calculated for infinite planar plasma crystals, $1.48(3/4\pi n_0)^{1/3} = 29.2\ \mu$m. According to the simulations, the $He^+$ ions are arranged in a zigzag configuration along the trap axis for two-thirds of the crystal, with a pitch spacing of $\approx 40\ \mu$m. In the remaining third (left end) the $He^+$ ions form a linear string, as evidenced by the smaller radial extension of the inner dark core. The asymmetric distribution is caused by light pressure forces on the $Be^+$ ions. Embedded strings were also observed in a mixed crystal of $Ca^+$ and $Mg^+$ ions where both ions were laser cooled [27].

An alternative way to roughly estimate the number of sympathetically cooled $He^+$ ions is as follows. Crystallized ions of any species are in force equilibrium at their locations $\mathbf{r}_i$. Thus, in a region occupied by a particular species, the space charge electric field takes on the values $Q\mathbf{E}(\mathbf{r}_i) = \nabla U_{\text{trap}}(\mathbf{r}_i)$. Consider now a closed smooth surface that is chosen such that it closely approaches many ion loci $\mathbf{r}_i$. We assume this relation approximately holds on the entire surface. Applying Gauss's law, the total charge $Q_e$ enclosed by the surface is given by $Q_e = \epsilon_0 V_e \Delta U_{\text{trap}}/Q$, where $V_e$ is the volume enclosed by the surface and a harmonic trap has been assumed, $\Delta U_{\text{trap}}(\mathbf{r}) = \text{const}$. The Laplacian also determines the constant charge density $\rho = \epsilon_0 \Delta U_{\text{trap}}/Q = n_0 Q$ of an ion species within the liquid charge model. Thus, the enclosed charge is simply the "displaced charge," $Q_e = \rho V_e$. We now apply this to the heavier particle species surrounding a cylindrical core containing lighter ions. Taking as the surface the cylinder bounded by the innermost $Be^+$ shell in Fig. 1(a) (radius $r_{\text{shell}} \simeq 35\ \mu$m) and extending to the ends of the dark core (length $\approx 2.2$ mm), the estimate for the light species number is $N_{\text{He}} = Q_e/Q_{\text{He}} = Q_{\text{Be}} n_{0,\text{Be}} V_e/Q_{\text{He}} \simeq 260$. This is in reasonable agreement with the MD simulations, considering that the $r_{\text{shell}}$ varies over the crystal length and the approximations made.

In order to identify the sympathetically cooled and crystallized ions we have performed mass spectroscopy by mass-selective excitation of transverse (secular) motion in the trap. A plate electrode was placed between two trap rods and an ac voltage applied. A secular scan is taken by varying the excitation frequency $\omega_{\text{ext}}/2\pi$ and recording the $Be^+$ fluorescence with the photomultiplier. The secular excitation pumps energy into the crystal; the resulting higher $Be^+$ ion velocities imply a line broadening. This leads to less fluorescence if the laser frequency lies near resonance, as is the case when the detuning is optimized for maximum cooling. Since the species are strongly coupled by Coulomb interaction, heating of one species will lead to energy transfer to the others.

Figure 2 shows images for a large two-component ion crystal before [2(a)] and after [2(c)] secular scans. Initially, the secular scan shows the presence of both $Be^+$ (283 kHz) and $He^+$ (685 kHz). The former value is close to the calculated value of 271 kHz. Regarding the $He^+$ resonance, we notice both an increase in fluorescence before resonance, and a substantial shift of the resonance peak from the theoretical value (613 kHz). We attribute this spread and shift to a modification of the secular frequency $\omega_r$, which is a single-particle property, by the $z$ dependence of the $Be^+$ ion distribution. The permanent increase of the fluorescence intensity before reaching the sharp $He^+$ secular excitation peak is due to partial removal of $He^+$ ions from the crystal by the high excitation amplitude.

After a few secular excitation cycles the $He^+$ ions were nearly completely removed from the trap, Fig. 2(c), leaving behind a nearly pure $Be^+$ ion crystal, as evidenced by the absence of secular resonance in Fig. 2(d). The small number of impurities remaining in the left end of the crystal did not lead to a fluorescence signal. Note that the visible crystal size has decreased substantially because of $Be^+$ ion loss. Nevertheless, the absolute fluorescence intensity of the final $Be^+$ crystal is essentially equal to the level at the end of the first secular scan. This may be explained by a lower ion temperature or reduced micromotion. Moreover,

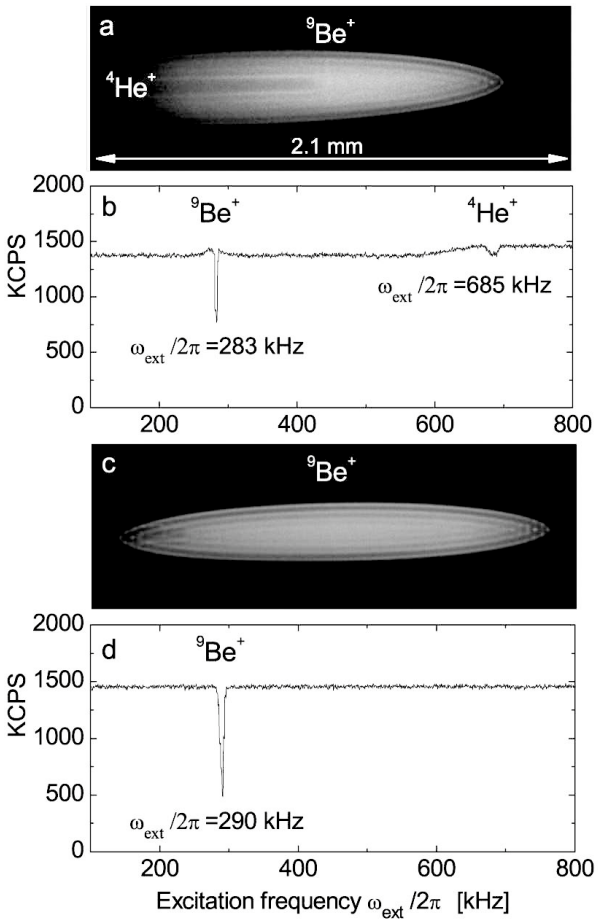


FIG. 2. (a) Prolate two-component Coulomb crystal (cooling laser beam direction to the right). (b) Corresponding $Be^+$ fluorescence signal vs secular excitation frequency $\omega_{\text{ext}}/2\pi$. (c) Ion crystal after removal of $He^+$ through repeated secular excitation. (d) Corresponding secular excitation spectrum. Time between (a),(b) and (c),(d): 5 min. Frequency scans are toward increasing frequency.

a shift of the crystal with respect to the trap occurred in the direction of the propagation of the laser beam. We attribute this to stronger light pressure forces experienced by the $Be^+$ ions, which is consistent with the increased fluorescence level per ion.

A central question concerning sympathetically cooled ions is their translational temperature; several observations can shed light on the answer. A direct measurement on $^{24}Mg^+$ embedded in a laser-cooled $^{40}Ca^+$ crystal yielded an upper limit of 45 mK, deduced from the $^{24}Mg^+$ laser excitation linewidth [20]. In a two-ion crystal sympathetic cooling to the Doppler limit ($<1$ mK) has been shown [23]. MD simulations for small particle numbers have shown that sympathetic ions caged by laser-cooled ions are essentially in thermal equilibrium with the latter at the Doppler temperature [22]. Thus, an estimate of the sympathetic temperature may be obtained from the temperature of the laser-cooled ions. We deduce a direct upper limit for the translational temperature of the $Be^+$ from the spectral line shape of their fluorescence as the cooling laser is tuned towards resonance and the ion ensemble crystallizes. We fit an appropriate Voigt profile to each point of the recorded fluorescence curve to determine the $Be^+$ temperature. For small crystals ($<1000$ particles), we find an upper limit at the end of the scan of 42 mK. An indirect upper limit is obtained by comparing the size of the ion spots with MD simulations; here we find a tighter limit of $<20$ mK for the $Be^+$ temperature. We therefore deduce, assuming thermal equilibrium, that the $He^+$ temperature is $<20$ mK.

In summary, we have sympathetically cooled and crystallized $He^+$ ions using laser-cooled $Be^+$ ions in a linear Paul trap. Large Coulomb crystals of $\sim 6.2 \times 10^3$ $Be^+$ ions contained about 150 $He^+$ ions, arranged in a zigzag structure centered on the trap axis. The mass ratio of 0.44 between sympathetically cooled and laser-cooled ions is the lowest achieved so far for large ion ensembles in a Paul trap. We estimate the temperature of the crystallized $He^+$ ions at below 20 mK.

Translationally cold and immobilized $He^+$ ions are a promising system for high precision spectroscopy and might lead to more precise atomic and nuclear constants. The weak $1S$-$2S$ transition in $He^+$ could be detected with a high signal to noise ratio using a single adjacent $Be^+$ ion as a ''quantum sensor,'' rather than by direct detection of its fluorescence [28]. Significant progress in this direction has been achieved [23,29]. Moreover, sympathetically cooled $He^+$ opens up perspectives for studies of cold collisions and cold chemistry, e.g., generation of $^3HeH^+$ molecules, whose hyperfine structure is of interest in fundamental physics [30].

The $^4He^+/^9Be^+$ cooling and crystallization results also have implications for the possibility of achieving this with highly charged atomic ions (HCAI). Favorably, the $q$ parameters are similar and the effective potential is steeper for the HCAIs than for the $^9Be^+$. Under appropriate conditions, the laser-cooled $^9Be^+$ ions are expected to cage the HCAIs, leading to efficient cooling.

We thank the Deutsche Forschungsgemeinschaft (DFG) and the EU network HPRN-CT-2002-00290 for support. We are grateful to D. Leibfried for helpful suggestions, H. Wenz for the MD simulations, and S. Karshenboim for discussions.

*Note added.*—We have also produced two-species Coulomb crystals containing $^3He^+$ reliably.

[1] See, e.g., *Precision Physics of Simple Atomic Systems*, edited by S. G. Karshenboim *et al.* (Springer, New York, 2001); M. I. Eides *et al.*, Phys. Rep. **342**, 63 (2001).
[2] J. D. Gillaspy, J. Phys. B **34**, R93 (2001).
[3] See, e.g., V. M. Shabaev *et al.*, Phys. Rev. Lett. **86**, 3959 (2001), and references therein.
[4] J. Verdu *et al.*, Phys. Rev. Lett. **92**, 093002 (2004).
[5] B. de Beauvoir *et al.*, Eur. Phys. J. D **12**, 61 (2000).
[6] H. A. Schuessler *et al.*, Phys. Rev. **187**, 5 (1969); M. H. Prior and E. C. Wang, Phys. Rev. A **16**, 6 (1977); for the theory, see S. G. Karshenboim and V. G. Ivanov, Eur. Phys. J. D **19**, 13 (2002).
[7] A. van Wijngaarden *et al.*, Phys. Rev. A **63**, 012505 (2000).
[8] U. D. Jentschura and G. W. F. Drake, Can. J. Phys. **82**, 103 (2004).
[9] D. Shiner *et al.*, Phys. Rev. Lett. **74**, 3553 (1995).
[10] J. L. Flowers *et al.*, NPL Report No. CBTLM 11 (2001); T. W. Hänsch (private communication).
[11] S. A. Burrows *et al.*, in *Laser Spectroscopy*, edited by R. Blatt *et al.* (World Scientific, River Edge, NJ, 1999), Vol. 14.
[12] QED uncertainty without nuclear radius effect $\sim 6 \times 10^4$ Hz, nuclear radius effect uncertainty $\sim 7 \times 10^4$ Hz [1,8], uncertainty due to Rydberg constant $\sim 8 \times 10^4$ Hz. For the $2S$-$3S$ transition, the situation is somewhat less favorable due to a larger relative contribution of the $R_\infty$ uncertainty and the larger transition linewidth.
[13] See, e.g., *Proceedings of the 6th Symposium on Frequency Standards and Metrology*, edited by P. Gill (World Scientific, River Edge, NJ, 2002).
[14] F. G. Major and H. G. Dehmelt, Phys. Rev. **170**, 91 (1968).
[15] R. Drullinger *et al.*, Appl. Phys. **22**, 365 (1980).
[16] D. Larson *et al.*, Phys. Rev. Lett. **57**, 70 (1986).
[17] M. Raizen *et al.*, Phys. Rev. A **45**, 6493 (1992).
[18] I. Waki *et al.*, Phys. Rev. Lett. **68**, 2007 (1992).
[19] P. Bowe *et al.*, Phys. Rev. Lett. **82**, 2071 (1999).
[20] L. Hornekær, Ph.D. thesis, Aarhus University, 2000.
[21] T. Harmon *et al.*, Phys. Rev. A **67**, 013415 (2003).
[22] S. Schiller and C. Lämmerzahl, Phys. Rev. A **68**, 053406 (2003).
[23] M. D. Barrett *et al.*, Phys. Rev. A **68**, 042302 (2003).
[24] H. Schnitzler *et al.*, Appl. Opt. **41**, 7000 (2002).
[25] U. Fröhlich *et al.* (to be published).
[26] L. Turner, Phys. Fluids **30**, 3196 (1987).
[27] L. Hornekær *et al.*, Phys. Rev. Lett. **86**, 1994 (2001).
[28] D. J. Wineland *et al.*, in Ref. [13], pp. 361–368.
[29] B. B. Blinov *et al.*, Phys. Rev. A **65**, 040304(R) (2002).
[30] S. G. Karshenboim (private communication).

# Ellipsoidal Coulomb crystals in a linear radio-frequency trap

U. Fröhlich, B. Roth, and S. Schiller
*Institut für Experimentalphysik, Heinrich-Heine-Universität Düsseldorf, 40225 Düsseldorf, Germany*

(Received 17 March 2005; accepted 1 June 2005; published online 1 July 2005)

A static quadrupole potential breaks the cylindrical symmetry of the effective potential of a linear rf trap. For a one-component liquid plasma at low temperature, the resulting equilibrium charge distribution is predicted to be an ellipsoid. Laser-cooled $^9Be^+$ ellipsoidal ion crystals were produced and good agreement was found between their shapes and the cold fluid prediction. In two-species mixtures, containing $^9Be^+$ and sympathetically cooled ions of lower mass, a sufficiently strong static quadrupole potential produces a complete spatial separation of the species. © *2005 American Institute of Physics*. [DOI: 10.1063/1.1976605]

## I. INTRODUCTION

One-component plasmas have attracted significant attention in the past since they represent simple multiparticle systems that can be studied under a variety of conditions with a high degree of experimental control. Detailed theoretical analysis, both by analytical and by molecular dynamics (MD) simulations, is possible.[1,2]

To overcome the Coulomb repulsion, the plasmas are confined in Penning- or Paul-type traps. Their temperature can be varied over many orders of magnitude. In particular, they can be efficiently cooled to the millikelvin range by laser cooling. Strong cooling results in phase transitions to a crystalline state, whose occurrence is described by the interaction parameter $\Gamma = Q^2/4\pi\epsilon_0 a k_B T$, the ratio between average nearest-neighbor Coulomb energy and thermal energy ($a$, average particle spacing; $Q$, particle charge). The MD simulations on infinite systems have shown that the plasma becomes liquidlike, i.e., exhibits spatial correlations for $\Gamma \geqslant 2$, without going through a discontinuous gas-liquid phase transition.[2] For $\Gamma > 170$ (Ref. 3) a phase transition to a crystal occurs. Coulomb crystals in hyperbolic[4] and linear Paul (rf) traps[5,6] have become of great importance in quantum optics, where they can be used to implement quantum gates or quantum memories[7] and can serve as systems for precision measurements on atomic or molecular ions.[8,9]

The spatial distribution of a trapped one-component gaseous plasma differs significantly from the liquid and crystalline state. This is described by Debye length $\lambda_D = (k_B T \epsilon_0 / n Q^2)^{1/2}$, which is the distance below which interactions between individual particles overcome collective effects.[2] Here, $n$ is the particle density of the plasma. When $\lambda_D$ is much larger than the spatial extent of the plasma, the Coulomb interaction is negligible, and the density is a local function of the trap potential only. For a harmonic potential, the density then has a Gaussian dependence on the coordinates, with plasma dimensions inversely proportional to the respective trap potential curvatures. When $\lambda_D$ is comparable to or smaller than the spatial extent of the plasma (as is the case for the plasmas presented in this paper), space charge becomes important.[10] The density is then a local function of both trap potential and space charge potential. Since the latter depends on the density distribution over the whole space, a self-consistent density distribution arises, whose shape exhibits a nontrivial dependence on the trap potential curvatures. For cylindrical trap potential symmetry, such plasmas are spheroids (ellipses of revolution) and have been studied both in linear rf and Penning traps.[11,12] In the absence of cylindrical symmetry the shape has been predicted to be that of an ellipsoid.[13] Ellipsoidal plasmas have already been observed and studied in Penning traps (see Ref. 14, and references therein). In this study we describe the observation and characterization of cold ellipsoidal plasmas in a linear rf trap. In particular, we have obtained ellipsoidal crystals containing two different ion species.

## II. LINEAR PAUL TRAP

The linear rf trap used in this experiment consists of four rods of radius $r'$ (inset in Fig. 2), each divided into three electrically isolated segments. A radio-frequency voltage $V_{rf}\sin \Omega t$ and a static voltage $V_{DC}$ are applied to the rods in a quadrupolar configuration. Confinement along the trap axis ($z$ axis) is achieved by raising the two end segments of each rod by a static voltage $V_{EC}$. When the Mathieu stability parameter $q = 2QV_{rf}/mr_0^2\Omega^2 \ll 1$, the independent motion of the trapped ions (mass $m$) can be adequately described by the motion in a harmonic effective potential (pseudopotential) $U_{\text{trap}}(\mathbf{r}) = m\Sigma\omega_i^2 x_i^2/2$,[15] and an additional jitter motion at the radio frequency $\Omega$, the so-called micromotion. $r_0$ is the minimum distance from the electrode surfaces to the trap axis. The axial ($\omega_z$) and transverse ($\omega_x$ and $\omega_y$) frequencies of the effective trap potential are given by $\omega_z^2 = 2\kappa Q V_{EC}/m$ and $\omega_{x,y}^2 = Q^2 V_{rf}^2/(2m^2\Omega^2 r_0^4) - \omega_z^2/2 \pm QV_{DC}/mr_0^2$, where $\kappa$ is a constant determined by the trap geometry. For vanishing static voltage $V_{DC}$, $\omega_x$ and $\omega_y$ are degenerate. With the application of a static voltage $V_{DC} \neq 0$, a static quadrupole potential is added to the effective trap potential, and the cylindrical symmetry is broken. The transverse trap frequencies $\omega_x$ and $\omega_y$ increase and decrease, respectively, until $\omega_y$ vanishes for a sufficiently large applied voltage $V_{DC}$, which implies that the ion motion along the $y$ direction becomes unstable.

 

## III. THEORETICAL DESCRIPTION

In the liquid phase, a trapped plasma in thermal equilibrium at a given temperature $T$ may be regarded as a macroscopic charged fluid with number density $n_f(\mathbf{r})$.[2,16] For example, this description leads to an expression for the equilibrium shape of the trapped plasma. A particularly simple analytical treatment is possible in the limit of an ultracold plasma when $T \to 0$. In this case, the equilibrium number density $n_f(\mathbf{r})$ is determined by the condition of no net force on any plasma region. However, at very low temperatures, the plasma does not remain liquid but crystallizes with the appearance of shells and a fairly complicated structure. While the fluid description may be expected to become inaccurate in this case, it has been shown to remain applicable as far as the shape of the outer boundary is concerned and as long as the crystals are sufficiently large. For linear rf traps, this comparison has so far only been performed for the case of cylindrical symmetry ($V_{DC}=0$).[11]

In the effective potential approximation, the absence of net force implies a balance between the electric field due to the space charge potential $\phi_f(\mathbf{r})$ and the trap force due to the effective potential: $Q\phi_f(\mathbf{r})+U_{\text{trap}}(\mathbf{r})=\text{const}$. The number density follows directly from Poisson's equation, $n_f(\mathbf{r}) = (\epsilon_0/Q^2)\Delta U_{\text{trap}}(\mathbf{r})$. For the harmonic effective potential of the linear rf trap with the above trap frequencies the number density is explicitly given by $n_0=\epsilon_0 V_{rf}^2/m\Omega^2 r_0^4$, which is constant within the fluid and independent of the static voltages $V_{DC}$ and $V_{EC}$.

The outer shape of the zero-temperature charged fluid with constant number density is an ellipsoid with principal axes $R_x$, $R_y$, and $L$ in the $x$, $y$, and $z$ directions, respectively.[13] With the additional boundary condition that the electric space charge potential $\phi_f(\mathbf{r})$ vanishes at infinity, the potential inside the fluid is given by

$$\phi_f(\mathbf{r}) = \frac{Qn_0}{4\epsilon_0}[A_x(R_x^2 - x^2) + A_y(R_y^2 - y^2) + A_z(L^2 - z^2)], \tag{1}$$

where the dimensionless functions $A_x$, $A_y$, and $A_z$ depend on the principal axes $R_x$, $R_y$, and $L$, respectively.[13] Force balance implies that $A_i$ satisfies $\omega_i^2 = Q^2 n_0 A_i/2m\epsilon_0$. The ratios of the principal axes $R_x/L$ and $R_y/L$ can thus be calculated by solving the set of equations

$$\left(\frac{\omega_x}{\omega_z}\right)^2 = \frac{A_x(R_x/L, R_y/L)}{A_z(R_x/L, R_y/L)},$$

$$\left(\frac{\omega_y}{\omega_z}\right)^2 = \frac{A_y(R_x/L, R_y/L)}{A_z(R_x/L, R_y/L)}. \tag{2}$$

For $V_{DC}=0$, $\omega_x$ and $\omega_y$ are equal, and the equilibrium shape of the zero-temperature charged fluid is a spheroid with radius $R=R_x=R_y$ and half length $L$. The two equations (2) then reduce to a single equation for the aspect ratio $R/L$. Hornekær *et al.*[11,17] have found good agreement between this theory and experimental aspect ratios of a large variety of spheroidal $^{40}Ca^+$ ion crystals, obtained by varying the endcap voltage $V_{EC}$ and the radio-frequency amplitude $V_{rf}$.

## IV. EXPERIMENT

We have tested the predictions of the charged fluid model in a fully anisotropic effective trap potential using a laser-cooled $^9Be^+$ ensemble. The linear trap properties were $r_0=4.32$ mm and a radio frequency $\Omega/2\pi=14.2$ MHz with an amplitude $V_{rf}=380$ V. This resulted in a small Mathieu stability parameter of $q=0.055$, implying that the micromotion was relatively small and that the effective potential description is appropriate. For axial confinement, $V_{EC}=4.5$ V was applied to the trap end segments, giving rise to $\kappa=3.0\times10^{-3}/\text{mm}^2$, an axial frequency of $\omega_z=2\pi\times85$ kHz, and a transverse frequency of $\omega_r=2\pi\times268$ kHz. Experimentally, both values were obtained from a measurement of the transverse frequency as a function of $V_{EC}$, in the absence of $V_{DC}$. This was done by external excitation of the radial motion of gas phase $^9Be^+$ ions in the harmonic trap potential, which was detected by a drop of the fluorescence signal from the laser cooled $^9Be^+$ ions.[18]

When the effective trap potential is made anisotropic by the application of $V_{DC}$, the predicted instability limit is 4.96 V. We observe partial particle loss when $V_{DC}$ exceeds 4.2 V and total loss at $V_{DC}=4.9$ V. To prevent particle loss, we limited $V_{DC}$ to a maximum of 4.2 V, corresponding to an increase of the transverse trap frequency $\omega_x/2\pi$ from 268 kHz to 365 kHz and a decrease of $\omega_y/2\pi$ from 268 kHz to 104 kHz. Experimentally, the two transverse frequencies $\omega_x$ and $\omega_y$ can be measured by secular excitation.

The trap was loaded with $^9Be^+$ ions by evaporating beryllium atoms from an oven and ionizing them in the trap center by electron impact. The trapped $^9Be^+$ ions, initially forming a hot plasma cloud of $\approx1000$ K, were laser cooled by laser radiation at 313 nm until they finally underwent a phase transition to a crystalline state with a temperature of a few millikelvin. A description of the all-solid-state laser system is given in Ref. 19. To image the $^9Be^+$ ion crystals, a charge-coupled device (CCD) camera was placed transverse to the trap axis.

## V. RESULTS

Figure 1 shows an ion crystal containing $\simeq2\times10^3$ $^9Be^+$, at different values of $V_{DC}$. The estimate of the ion number in Fig. 1(a) is obtained from MD simulations in which the observed structure (especially the number of shells) is reproduced.[20] For the test of the calibration of the CCD optics magnification as well as the determination of absolute dimensions of the ion plasmas, we also use the MD simulations. As a check, multiplying the volume $4\pi R_{45}^2 L/3$ of the crystal shown in Fig. 1(a) and the cold fluid model density $n_0$, we obtain the value $\simeq2\times10^3$. This agrees well with the MD results and implies that the model is applicable for large crystals. The left central part of the ion crystal shown in Fig. 1(a) contains a dark region, which consists of sympathetically cooled ions originating from the residual gas and having a mass smaller than that of $^9Be^+$, pushed to one side by radiation pressure.[21]

In the outer region of the crystal shown in Fig. 1, the ions are arranged in concentric shells while the inner region is smeared out. The size of the smeared out region appears to

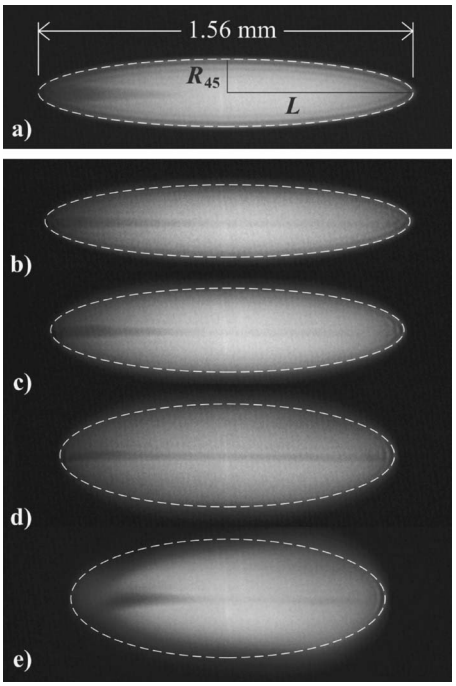


FIG. 1. CCD images of a large ion crystal containing $\simeq 2\times 10^3$ $^9Be^+$, taken perpendicular to the $z$ axis and at 45 ° to the $x$ and $y$ axes, for different values of $V_{DC}$. Dashed lines, fits of ellipses with principal axes $R_{45}$ and $L$ to the outermost shells. (a) $V_{DC}=0$, the effective trap potential has cylindrical symmetry. The ion crystal is a prolate spheroid with radius $R_x=R_y=R_{45}$ and half length $L$. The aspect ratio $R_{45}/L=0.178$. (b)–(e) $V_{DC}\neq 0$, the cylindrical symmetry is broken and the crystal is an ellipsoid with principal axes $R_x<R_{45}$, $R_y>R_{45}$ and $L$. With increasing $V_{DC}$ the crystal expands in the $y$ direction and compresses in the $x$ and $z$ directions, while maintaining the constant volume. $V_{DC}$ is set to 1.8 (b), 2.8 (c), 3.6 (d), and 4.2 V (e), leading to an aspect ratio of $R_{45}/L=0.193$ (b), 0.235 (c), 0.309 (d), and 0.413 (e). For a definition of $R_x$, $R_y$, and $R_{45}$ see inset of Fig. 2.

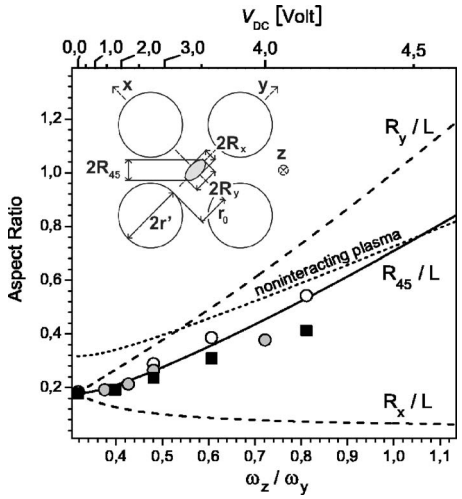


FIG. 2. Comparison of the aspect ratio $R_{45}/L$ of a partially crystallized $^9Be^+$ plasma and the cold fluid prediction (solid and dashed lines) for zero-temperature ellipsoidal plasmas, as a function of the ratio $\omega_z/\omega_y$ between the axial and the smallest transverse trap frequency. Full squares, large crystals from Fig. 1. Open (gray) circles, small (medium-size) crystals from Fig. 3. Dotted line, $R_{45}/L$ for a low-density plasma in the gas phase with negligible particle interactions, where $R_x/L=\omega_z/\omega_x$, $R_y/L=\omega_z/\omega_y$. Inset, cross section of linear trap and of ellipsoidal plasma. Observation direction as in Fig. 1.

increase with the applied static quadrupole potential $V_{DC}$. There are several possible explanations for the observed structures. For nonzero $V_{DC}$, the cylindrical trap potential symmetry is broken. This induces changes in the shape and local order of the crystal, reducing the number of ion shells, as confirmed by the MD simulations. This effect is not directly related to temperature and increases with $V_{DC}$. Therefore, the CCD camera pictures which display the line-of-sight-integrated fluorescence of the ion crystal cannot resolve individual shells or ions in the inner region any more. Another contribution to the observed smearing of the crystal structure could originate from a larger average micromotion energy of the ions due to the crystal shape change which could lead to heating.

In contrast to the observation of large plasmas, we found that under similar laser-cooling parameters small plasmas containing only a few hundred $^9Be^+$ ions do not show a smeared-out core and could always be resolved by the CCD camera. However, these plasmas, see Fig. 3 and discussion below, are also consistent with the assumption of a larger average micromotion energy of particles in the outer shells of the crystal.

For all plasmas produced so far the ellipsoidal deformation is a reversible process if the maximum value of $V_{DC}$ is kept within the range stated above: after turning $V_{DC}$ off, the principal axes $R_{45}$ and $L$ of the crystal returned to the initial values, indicating that no ions were lost during deformation. The outer boundaries of the crystals in Fig. 1 can be well described by ellipses with the principal axes $R_{45}$ and $L$. Since the CCD camera takes a projection along an axis at 45° with respect to the $x$ and $y$ axes, the principal axis $R_{45}$ of each ellipse is related to the principal axes $R_x$ and $R_y$ of the corresponding ellipsoid by $R_{45}=[(R_x^2+R_y^2)/2]^{1/2}$. For the last crystal in the sequence, the boundary shows clear deviations from an ellipse; we attribute this to the presence of sympathetically cooled impurities of higher mass than $^9Be^+$, located at larger radii as compared to $^9Be^+$. The asymmetry along the trap axis is caused by cooling light pressure, which is not felt by the sympathetically cooled ions. In this case, the elliptical fit has been chosen to match the fragments of the outermost shell, which still exist at the left and right ends of the crystal.

Figure 2 shows a comparison between the measured aspect ratio $R_{45}/L$ and the theoretical result from Eq. (2). The agreement between the experiment and the theory is good, considering that the $^9Be^+$ ion crystals did exhibit two phases and were not pure. In addition, a systematic deviation between the theory and the experiment is expected at the largest applied voltages $V_{DC}$ because then the smallest ellipsoid dimension $R_x$ becomes comparable to the shell spacing. In this limit, the cold fluid model continuum description is inaccurate.

The cold fluid model also determines the relative change of the crystal length $2L$ when $V_{DC}$ is changed. For the actual trap settings $2L$ is expected to decrease to 83% from its initial value, when changing $V_{DC}$ from 0 to 4.2 V. The length of the crystal in the last image in Fig. 1(e) is 84% of the initial one (a), which is in good agreement with the expected compression. Therefore, while at large $V_{DC}$ the observed transverse crystal shape starts to deviate from the predictions

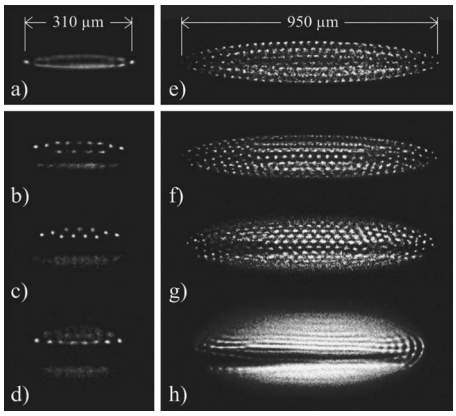


FIG. 3. Left, small crystal containing $\simeq 20\ ^9Be^+$ ions and a smaller number of sympathetically cooled impurity ions at different values of the static voltage $V_{DC}$: 0 V (a), 2.8 V (b), 3.6 V (c), and 4.2 V (d). Right, medium-size crystal containing $\simeq 500\ ^9Be^+$ ions. $V_{DC}$ is set to 0 V (a), 1.4 V (b), 2.8 V (c), and 4.0 V (d). The asymmetric ion distribution in (b)–(d) and (f)–(h) is due to stray electric fields.

of the cold fluid model, the axial shape is still in good agreement since the axial dimension of the crystal remains large compared to the shell spacing.

While for the large Coulomb crystals a spatially averaged description is a good first approximation, in small crystals one may expect effects related to the particle structure to show up clearly. As an example, Figs. 3(a)–3(d) show a crystal containing about 20 $^9Be^+$ ions and several sympathetically cooled low-mass impurities. In an effective trap potential with cylindrical symmetry, the crystal exhibits a single $^9Be^+$ shell [Fig. 3(a)]. This shell appears smeared out in the CCD image (exposure time, 2 s), possibly because of a rotationlike diffusion of the ions around the trap axis. In the ellipsoidal crystals, Figs. 3(b)–3(d), this diffusion is suppressed because it would require overcoming an energy barrier, and therefore the image shows individual ions. The most apparent property arising when the static quadrupole voltage $V_{DC}$ is increased is the completely dark region containing the sympathetically cooled particles. Furthermore, some of the fluorescence spots representing $^9Be^+$ ions, mainly those at larger distances from the trap center, appear smeared out and show a reduced intensity. We attribute this to heating induced by the micromotion occurring at the locations of these ions. As a test, we shifted the crystal by means of an additional static voltage applied to one trap electrode. This caused a rearrangement of the $^9Be^+$ relative to the dark core, but those ions that appeared well defined were always in the same region. However, for the static quadrupole voltages applied no ions are located in the front or the back of the dark region. Therefore, unlike for large ion crystals, we do not observe a smearing out of the crystal core as $V_{DC}$ is increased.

Although the small crystals in Figs. 3(a)–3(d) do not exhibit closed boundaries, we could still fit ellipses to them. In order to compare such small crystals with the cold fluid model, half of the typical shell spacing of 29 $\mu$m was added to $R_{45}$ and $L$ before calculating the ratio $R_{45}/L$. The results are indicated by open circles in Fig. 2. Even for this case there is a good agreement with the cold fluid model. Finally, in Figs. 3(e)–3(h) we also present a medium-sized crystal containing $\simeq 500\ ^9Be^+$ ions and, again, additional low-mass impurities. The corresponding aspect ratio data as well as an additional data point for $V_{DC}=2.2$ V, reported in Fig. 2, also show good agreement with the theory. However, for large and medium-sized crystals a deviation between the theory and the experiment becomes obvious as the values for the static voltage $V_{DC}$ increase. Our MD simulations show that the observed deviations can be explained by small ($<15\%$) admixtures of sympathetically cooled molecular impurities, in particular, $H_2^+/H_3^+$ ions close to the trap axis originating from residual gas contaminants and $BeH^+$ ions located in the outer regions of the crystals formed by chemical reactions.

The pronounced asymmetric ion distribution in the small, Figs. 3(a)–3(d), as well as in the medium-sized crystals, Figs. 3(e)–3(h), is not due to the broken cylindrical symmetry of the trap potential, as this does not produce any visible asymmetry in the CCD images. Instead, we attribute the asymmetric ion distribution to stray potentials. While it was not possible to compensate for these imperfections by additional static voltages, it was always possible to reverse the asymmetry by means of these voltages. Our MD simulations confirm this interpretation.

A direct estimate for the translational temperature of the $Be^+$ is obtained from the spectral line shape of its fluorescence as the cooling laser is tuned toward resonance and the ion ensemble crystallizes. Since the temperature of the particles changes during the frequency scan, we fit a Voigt profile to each point of the recorded fluorescence curve to determine an upper limit for the $Be^+$ temperature. For small crystals ($<1000$ particles), we find an upper limit for the temperature at the end of the scan of 42 mK. However, the accuracy of this method is limited due to the experimental resolution. An indirect upper limit is obtained by comparing the size of the ion spots with MD simulations, where we find a tighter limit of $<10$ mK for the $Be^+$ temperature. We deduce, assuming thermal equilibrium, that the temperature of the sympathetically cooled impurity ions in Fig. 3 is $<10$ mK.

## VI. CONCLUSIONS AND OUTLOOK

In summary, we have studied the static behavior of Coulomb crystals in a fully anisotropic effective trap potential and found a good agreement with the simple cold fluid plasma model for small anisotropy. For larger anisotropy, deviations could be explained by the presence of additional, sympathetically cooled, ion species. From an experimental point of view, the ability to reversibly deform a crystal allows us to separate lower-mass sympathetically cooled ions from the laser-cooled ions. This allows us to obtain a clearer picture of the impurity ion ensemble, without any background or foreground fluorescence from the laser-cooled ions. It will also permit us to manipulate the sympathetically cooled ions in a more direct way. The ability to generate a variety of ellipsoidal crystals opens up several directions for further study, e.g., oscillation modes of such crystals and, in particular, the modes of two-species crystals. These modes could be of importance for identification of the nonfluorescent species. On the theoretical side, it is of interest to per-

form detailed studies of structures using the MD simulations, which are able to fully take into account the particle nature of the cold plasmas. As an example, our MD simulations have shown that in strongly squeezed ellipsoids ion rings can occur. These represent a novel low-dimensional structure whose detailed investigation should be of significant interest.

## ACKNOWLEDGMENTS

The authors thank H. Wenz for the MD simulations. This work was supported by the Deutsche Forschungsgemeinschaft and the EU Network HPRN-CT-2002-00290 "Ultracold Molecules."

[1] R. C. Davidson, *Physics of Nonneutral Plasmas* (Imperial College Press, London, 2001).
[2] D. H. E. Dubin and T. M. O'Neil, Rev. Mod. Phys. **71**, 87 (1999).
[3] W. L. Slattery, G. D. Doolen, and H. E. DeWitt, Phys. Rev. A **21**, 2087 (1980).
[4] F. Diedrich, E. Peik, J. M. Chen, W. Quint, and H. Walther, Phys. Rev. Lett. **59**, 2931 (1987).
[5] M. G. Raizen, J. M. Gilligan, J. C. Bergquist, W. M. Itano, and D. J. Wineland, J. Mod. Opt. **39**, 233 (1992).
[6] M. Drewsen, C. Brodersen, L. Hornekær, and J. S. Hangst, Phys. Rev. Lett. **81**, 2878 (1998).
[7] M. D. Lukin, S. F. Yelin, and M. Fleischhauer, Phys. Rev. Lett. **84**, 4232 (2000).
[8] D. J. Berkeland, J. D. Miller, J. C. Bergquist, W. M. Itano, and D. J. Wineland, Phys. Rev. Lett. **80**, 2089 (1998).
[9] S. Schiller and C. Lämmerzahl, Phys. Rev. A **68**, 053406 (2003); S. Schiller and V. I. Korobov, *ibid.* **71**, 032505 (2005).
[10] Note, however, that $\lambda_D$ can be comparable to or smaller than the plasma extension and the plasma can still be gaseous, i.e., $\Gamma < 2$. Such a plasma can still be described within the charged fluid model, as is the case for liquidlike plasmas, i.e., $\Gamma \geqslant 2$.
[11] L. Hornekær, N. Kjærgaard, A. M. Thommesen, and M. Drewsen, Phys. Rev. Lett. **86**, 1994 (2001).
[12] L. R. Brewer, J. D. Prestage, J. J. Bollinger, W. M. Itano, D. J. Larson, and D. J. Wineland, Phys. Rev. A **38**, 859 (1988).
[13] D. H. E. Dubin, Phys. Fluids B **5**, 295 (1992).
[14] X.-P. Huang, J. J. Bollinger, T. B. Mitchell, and W. M. Itano, Phys. Plasmas **5**, 1656 (1998).
[15] H. G. Dehmelt, Adv. At. Mol. Phys. **3**, 53 (1967).
[16] L. Turner, Phys. Fluids **30**, 3196 (1987).
[17] L. Hornekær, Ph.D. thesis, Aarhus University, 2000.
[18] T. Baba and I. Waki, Jpn. J. Appl. Phys., Part 1 **35**, L1134 (1996).
[19] H. Schnitzler, U. Fröhlich, T. K. W. Boley, A. E. M. Clemen, J. Mlynek, A. Peters, and S. Schiller, Appl. Opt. **41**, 7000 (2002).
[20] H. Wenz (private communication).
[21] B. Roth, U. Fröhlich, and S. Schiller, Phys. Rev. Lett. **94**, 053001 (2005).

# Production of Ultracold Trapped Molecular Hydrogen Ions

P. Blythe, B. Roth, U. Fröhlich, H. Wenz, and S. Schiller

*Institut für Experimentalphysik, Heinrich-Heine-Universität Düsseldorf, 40225 Düsseldorf, Germany*

(Received 20 May 2005; published 26 October 2005)

We have cooled ensembles of the molecular hydrogen ions $H_2^+$, $H_3^+$, and all their deuterated variants to temperatures of a few mK in a radio frequency trap, by sympathetic cooling with laser-cooled beryllium ions. The molecular ions are embedded in the central regions of Coulomb crystals. Mass spectroscopy and molecular dynamics simulations were used to accurately characterize the properties of the ultracold multispecies crystals. We demonstrate species-selective purification of multispecies ensembles. These molecules are of fundamental importance as the simplest of all molecules, and have the potential to be used for precision tests of molecular structure theory, tests of Lorentz invariance, and measurements of electron to nuclear mass ratios and their time variation.

DOI: 10.1103/PhysRevLett.95.183002 PACS numbers: 32.80.Pj, 33.20.−t, 42.50.−p

Ultracold molecules represent a new frontier in the field of quantum optics and are excellent systems for high-precision measurements. One of the most promising applications for trapped ultracold molecules (ions or neutrals) is high-precision spectroscopic measurements, for example, of fundamental constants such as particle mass ratios [1], nuclear properties [2], QED effects [3], parity violation in enantiomers [4], searches for a permanent electric dipole moment of the electron [5], and Lorentz invariance [6].

Among molecules, $H_2^+$ and its isotopomers $HD^+$, $D_2^+$, etc., are of fundamental importance since they are the simplest molecules, containing only one electron and two simple nuclei. Their energy levels and transition rates can be calculated with a high degree of accuracy [1,3,7–9], providing reliable theoretical results for comparison with experiment. A number of such measurements have been performed to date [10–16]. These measurements have been limited by systematic shifts and broadening effects to spectroscopic accuracies around 1 part in $10^6$. New high-precision spectroscopic measurements on molecular hydrogen ions could yield much more precise energy values, improving on these measurements by 4 orders of magnitude or more. They could then yield an improved determination of the deuteron quadrupole moment, and also open an independent route toward determination of the electron-proton mass ratio $m_e/m_p$ [17]. This involves measurements of one or more rovibrational transition frequencies in $HD^+$ and $H_2^+$ and comparison with precise first-principles calculations of the energies of these states as a function of $m_e/m_p$. Furthermore, measurements of ratios of the transition frequencies as a function of time allow a direct test of the time independence of nuclear-to-electron mass ratios ($m_p/m_d$ and $m_e/m_p$) [1].

For high measurement accuracy, cold, well-localized samples of these molecular ions are required in order to eliminate first-order Doppler shifts (in the Lamb-Dicke regime), to minimize second-order Doppler shifts, and to reduce other systematic effects.

$H_2^+$, $H_3^+$, and their deuterated isotopomers are also among the most abundant molecules in interstellar clouds, and precision studies of their chemistry and dissociative recombination are of importance in understanding the properties and evolution of such clouds [15,18]. The degree of control enabled by the ability to trap well-localized, cold molecules for long periods of time (up to several hours), in a tightly controlled chemical environment, combined with molecular quantum state preparation techniques, could open new approaches to these studies.

Several alternative methods to produce cold and ultracold molecules have emerged recently, such as deceleration of supersonic beams [5], selection of translationally cold molecules from a gaseous ensemble [19], buffer gas cooling with cold helium gas [20], implantation of molecules into cryogenic droplets of He [21], photoassociation of laser-cooled neutral atoms [22], and production of ultracold molecules via Feshbach resonances [23]. Neutral molecular Bose-Einstein condensation has also been achieved [24,25].

Another powerful method which can be applied to a wide variety of both charged and neutral species is sympathetic cooling [26–30]. For ions, the cooling of particles of one species by an ensemble of directly (laser) cooled particles of another species is very efficient due to their long-range electrostatic interaction. For sufficiently strong cooling, an ordered structure (Coulomb crystal) is produced [31]. In this work we report sympathetic cooling of molecular hydrogen ions, and their embedding and localization in Coulomb crystals of singly ionized beryllium.

We use a linear quadrupole trap to simultaneously store both $Be^+$ and molecular ions. The radio frequency trap is driven at 14 MHz, with a peak-to-peak amplitude of 380 V. This results in a radial Mathieu stability parameter $q_r \simeq 0.04$ for the $Be^+$ [32], giving a radial secular oscillation frequency of 280 kHz. For the molecular hydrogen isotopomers $q_r$ lies between $\sim 0.05$ ($D_3^+$) and $\sim 0.2$ ($H_2^+$).

 

The trap is enclosed in a UHV chamber kept below $10^{-10}$ mbar. The chamber is equipped with a leak valve for the controlled introduction of gases, whose pressure may be measured by an ion gauge. The all-solid-state 313 nm laser system for cooling of $Be^+$ has been described elsewhere [33].

To load $Be^+$ ions into the trap, atoms are thermally evaporated from a beryllium wire, and ionized an electron beam. The molecular loading is achieved by leaking in neutral gas at a pressure of $\sim 3 \times 10^{-10}$ mbar, ionized by an electron beam with an energy of 200 eV, and a current of $\sim 30$ $\mu$A, for a loading time of 5 s. This produces mixed-species crystals like those shown in Figs. 1(a) and 1(b). The ions with a higher charge-to-mass ratio (in this case the molecular ions) experience a stronger trap pseudopotential, and thus form a dark (nonfluorescing) core to the crystal. The asymmetric distribution of species along the $z$ axis observed in Fig. 1(b) is caused by the light pressure of the cooling laser on the beryllium ions.

The observed crystals are faithfully reproduced by our molecular dynamics (MD) simulations, which include the full Coulomb interaction between all the ions, the effects of radiation pressure, and finite ion temperatures. Because of the close agreement between simulation and experiment, we can use the modeling to extract information such as the number, three-dimensional spatial distribution, and temperature of the different ion species from our CCD images.

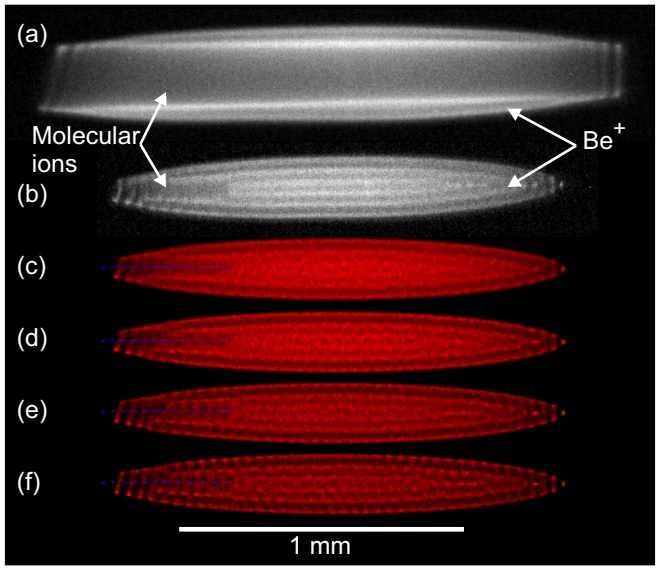


FIG. 1 (color online). Fluorescence images of (a) a large ion crystal with a high fraction of sympathetically cooled ions (approximately 1200 light ions and 800 $Be^+$ ions), (b) a smaller crystal containing around 690 $Be^+$ ions, and 12 $HD^+$ ions, and simulated images of this crystal at (c) 20, (d) 12, (e) 8, and (f) 6 mK. In the simulations, the beryllium ions are shown in red (gray) and the $HD^+$ ions in blue (not shown in print). The simulations show this crystal to be around 10 mK in temperature. Laser cooling beam propagation is to the right, along the $z$ axis.

The number of ions of different species given in Fig. 1(b) was found in this way.

We identify the trapped species by their mass-dependent motional frequencies. For individual ions in a radio frequency trap, the oscillation frequency is inversely proportional to their mass. In mixed-species crystals, the frequencies can be shifted by mutual Coulomb interactions of the species. In these experiments, this effect is not large enough to affect our use of the motional spectra for species identification. We excite the ions motion in the $x$-$y$ plane using an external electrode parallel with the $z$ axis of the trap. An oscillating potential is applied and the $Be^+$ fluorescence recorded as a function of excitation frequency. When the applied potential is resonant with a motional frequency of a crystal component, the ions are heated and the fluorescence of the beryllium ions in the crystal is affected. This heating causes an increase in fluorescence when the cooling laser is detuned far to the red of the cooling transition, as is the case here.

Figure 2 shows the motional excitation spectrum of a cold crystal with a small, stringlike molecular core following the loading of neutral HD gas. The spectrum shows three motional resonances. These are the signatures of individual sympathetically cooled species. The species other than $HD^+$ are generated by chemical reactions during the loading process, whereby the directly ionized $HD^+$ gas reacts with neutral HD background gas, forming various di- and triatomic molecular ions, including $H_2D^+$ and $HD_2{}^+$, and (undetected) neutral atoms. The reactions of the diatomic hydrogen molecules with their positively charged ions to form triatomic molecular ions (e.g., $H_2{}^+ + H_2 \rightarrow H_3{}^+ + H$) are exothermic by around 1.7 eV. The signature of the $D^+$ ions is also present, and this may be produced by direct electron-impact dissociation of neutral $D_2$ molecules. Similarly, during loading of neutral $H_2$ gas, significant amounts of $H_3{}^+$ can be generated, as seen in Fig. 3. Excitation of ion clouds after the loading of $H_2$ gas shows a strong response at a mass of 3 atomic mass units, and a weaker response at mass 2, indicating that the majority component in the trap is $H_3{}^+$. Finally, after $D_2$

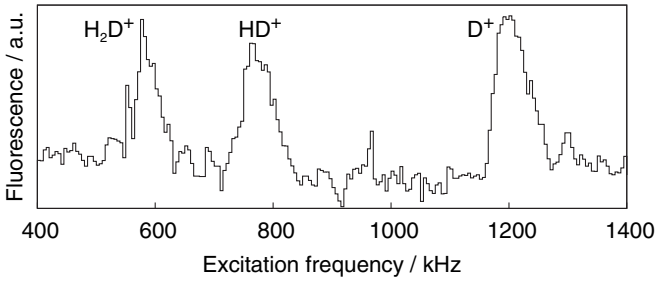


FIG. 2. Typical motional excitation spectrum of a crystal following the loading of HD gas. The resonance frequencies are perturbed from their single-ion values due to the Coulomb interactions between the different trapped species [39].

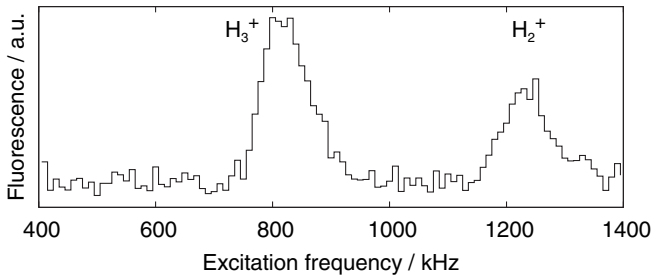


FIG. 3. Motional excitation spectrum of a crystal following the inlet and ionization of $H_2$ gas, showing the presence of both $H_3^+$ and $H_2^+$ ions.

loading, measurements show the presence of ions with masses 2 ($D^+$), 4 ($D_2^+$), and 6 ($D_3^+$).

It is possible to gain information about the core temperature from the observed crystal structures. The thermal motion of the fluorescing ions leads to blurring of our CCD images, and these can be compared with simulated images (Fig. 1). For the experimental crystal of Fig. 1, agreement is found for a $Be^+$ temperature of 8 mK. This sets an upper limit, as our experimental images are also limited in sharpness by our detection optics, CCD resolution, and sensor noise. The upper limit varies depending on crystal size and cooling parameters, and is typically in the range 5–15 mK. These temperatures are consistent with measurements of the fluorescence line shape of the beryllium ions.

For all species of molecular ions studied here, our MD simulations show that the core of the crystal, sympathetically cooled by the laser-cooled beryllium ions, is also crystalline and is strongly thermally coupled to the beryllium ions. The strength of this coupling allows us to estimate an upper temperature limit for the core ions, which is typically within a factor of 2 of the beryllium temperature. We may therefore conclude that the sympathetically cooled molecular ions have temperatures in the region of 10–30 mK. We have found that smaller crystals are generally colder. This may be compared with a demonstration of sympathetic cooling to the Doppler-limit for laser cooling ( $\sim 1$ mK) in a two-ion crystal [34].

Crystals with a single species of sympathetically cooled particles may be required for future experiments. By detuning the cooling laser far from resonance, an ion crystal can undergo a phase transition to a disordered fluid state. In this situation, the coupling between different ion species is much weaker than in the crystalline state, and the secular motion of the unwanted species can be strongly excited, ejecting the ions from the trap, with minimal effect on other species. The ions can then be recrystallized by retuning the cooling laser close to resonance (Fig. 4). This procedure can be used to remove as many different species as required, producing highly pure two-component crystals.

In summary, we have produced ultracold multicomponent ion crystals containing one or more species of molecular hydrogen ion isotopomer, embedded in a $Be^+$ ion ensemble. Species cooled were $H_2^+$, $H_3^+$, $HD^+$, $H_2D^+$, $HD_2^+$, $D^+$, $D_2^+$, and $D_3^+$ ions. The number of molecules can be varied between a few and several thousand. The mass ratio of 0.22 between sympathetically cooled and laser-cooled ions is the lowest achieved so far for large ion crystals in a Paul trap.

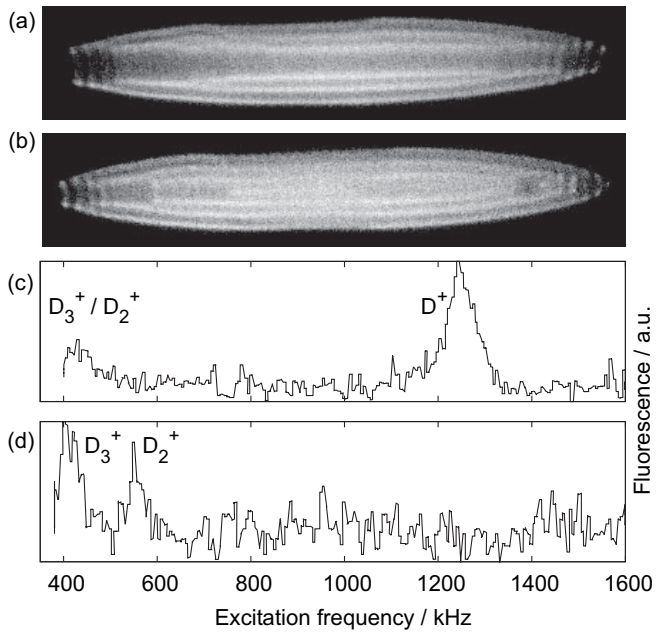


FIG. 4. Partial purification of a mixed-species crystal, following loading of $D_2$ gas. CCD images (a) before and (b) after the ejection of mass 2 ions (deuterons), with corresponding motional spectra (c) and (d), respectively.

The crystals are suitable for further experiments, such as the study of mixed-species collective plasma phenomena, cold chemistry, and collisions. The cold molecular ions could be combined with a source of cold neutral species (such as a magneto-optical trap or a cold molecular beam) for ultracold ion-neutral reaction studies. The purified single molecular species crystals obtained are the basis for first laser spectroscopy studies of cold molecular ions. Rovibrational transitions can be detected by selective photodissociation from the excited vibrational level and detection of the product ions or of changes in the crystal structure.

The molecular ions produced in this work are translationally cold, and, due to the energies and decay times of higher vibrational states, we expect them to be vibrationally cold. They are, however, expected to be rotationally warm (around 300 K) due to the blackbody radiation environment of the ion trap and the lack of strong coupling between the internal and external degrees of freedom [35]. For maximizing signal strength, and enabling precise control of molecular states for future precision tests of fundamental physics, cooling of the molecules' rotational energy will be required. Several schemes suitable for application

to hydrogen molecular ions have been proposed [36,37]. For achieving ultimate precision, it appears possible to use a single molecular ion coupled to a single atomic ion, which acts as both coolant and indicator of the molecular state [38]. In order to exploit this technique, it will be necessary to implement the above, or a similar, rotational cooling scheme.

We thank the Deutsche Forschungsgemeinschaft (DFG) and the EU network HPRN-CT-2002-00290 for support. P. B. was also supported by the Alexander-von-Humboldt Stiftung, U. F. by the Düsseldorf Entrepreneurs Foundation.

[1] S. Schiller and V. Korobov, Phys. Rev. A **71**, 032505 (2005); L. Hilico *et al.*, Eur. Phys. J. D **12**, 449 (2000).
[2] J. F. Babb, in *Current Topics in Physics*, edited by Y. M. Cho, J. B. Hong, and C. N. Yang (World Scientific, Singapore, 1998), Vol. 2, p. 531.
[3] V. I. Korobov, Phys. Rev. A **70**, 012505 (2004).
[4] J. Crassous *et al.*, Chem. Phys. Chem. **4**, 541 (2003).
[5] M. R. Tarbutt *et al.*, Phys. Rev. Lett. **92**, 173002 (2004).
[6] H. Müller *et al.*, Phys. Rev. D **70**, 076004 (2004).
[7] R. D. Ray and P. R. Certain, Phys. Rev. Lett. **38**, 824 (1977).
[8] C. A. Leach and R. E. Moss, Annu. Rev. Phys. Chem. **46**, 55 (1995).
[9] Z.-C. Yan, J.-Y. Zhang, and Y. Li, Phys. Rev. A **67**, 062504 (2003).
[10] C. B. Richardson, K. B. Jefferts, and H. G. Dehmelt, Phys. Rev. **165**, 80 (1968).
[11] K. B. Jefferts, Phys. Rev. Lett. **23**, 1476 (1969).
[12] W. H. Wing *et al.*, Phys. Rev. Lett. **36**, 1488 (1976).
[13] A. Carrington, I. McNab, and C. Montgomerie, J. Phys. B **22**, 3551 (1989).
[14] Z. W. Fu, E. A. Hessels, and S. R. Lundeen, Phys. Rev. A **46**, R5313 (1992).
[15] Z. Amitay *et al.*, Science **281**, 75 (1998).
[16] A. D. J. Critchley, A. N. Hughes, and I. R. McNab, Phys. Rev. Lett. **86**, 1725 (2001).
[17] U. Fröhlich *et al.*, Lect. Notes Phys. **648**, 297 (2004).
[18] Special issue on the Physics, Chemistry and Astronomy of $H_3^+$, edited by Takeshi Oka [Phil. Trans. R. Soc. A **358**, 2363 (2000)].
[19] S. A. Rangwala *et al.*, Phys. Rev. A **67**, 043406 (2003).
[20] J. D. Weinstein *et al.*, Nature (London) **395**, 148 (1998).
[21] M. Wewer and F. Stienkemeier, Phys. Rev. B **67**, 125201 (2003).
[22] A. Fioretti *et al.*, Phys. Rev. Lett. **80**, 4402 (1998).
[23] S. Dürr *et al.*, Phys. Rev. Lett. **92**, 020406 (2004).
[24] M. Greiner, C. A. Regal, and D. S. Jin, Nature (London) **426**, 537 (2003).
[25] S. Jochim *et al.*, Science **302**, 2101 (2003).
[26] P. Bowe *et al.*, Phys. Rev. Lett. **82**, 2071 (1999).
[27] D. J. Larson *et al.*, Phys. Rev. Lett. **57**, 70 (1986).
[28] M. A. van Eijkelenborg *et al.*, Phys. Rev. A **60**, 3903 (1999).
[29] S. Schiller and C. Lämmerzahl, Phys. Rev. A **68**, 053406 (2003).
[30] B. Roth, U. Fröhlich, and S. Schiller, Phys. Rev. Lett. **94**, 053001 (2005).
[31] R. Blümel *et al.*, Nature (London) **334**, 309 (1988).
[32] D. J. Berkeland *et al.*, J. Appl. Phys. **83**, 5025 (1998).
[33] H. Schnitzler *et al.*, Appl. Opt. **41**, 7000 (2002).
[34] M. D. Barrett *et al.*, Phys. Rev. A **68**, 042302 (2003).
[35] A. Bertelsen, S. Jørgensen, and M. Drewsen, physics/0504128.
[36] I. S. Vogelius, L. B. Madsen, and M. Drewsen, Phys. Rev. A **70**, 053412 (2004).
[37] I. S. Vogelius, L. B. Madsen, and M. Drewsen, Phys. Rev. Lett. **89**, 173003 (2002).
[38] D. J. Wineland *et al.*, in *Proceedings of the Sixth Symposium on Frequency Standards and Metrology*, edited by P. Gill (World Scientific, Singapore, 2002), p. 361.
[39] T. Hasegawa and T. Shimizu, Phys. Rev. A **66**, 063404 (2002).

INSTITUTE OF PHYSICS PUBLISHING JOURNAL OF PHYSICS B: ATOMIC, MOLECULAR AND OPTICAL PHYSICS

J. Phys. B: At. Mol. Opt. Phys. **38** (2005) 3673–3685 doi:10.1088/0953-4075/38/20/004

# Production of large molecular ion crystals via sympathetic cooling by laser-cooled $Ba^+$

**B Roth, A Ostendorf, H Wenz and S Schiller**

Institut für Experimentalphysik, Heinrich-Heine-Universität Düsseldorf, 40225 Düsseldorf, Germany

Received 17 March 2005, in final form 2 August 2005
Published 26 September 2005
Online at stacks.iop.org/JPhysB/38/3673

**Abstract**

We have produced ensembles of cold $^{16}O_2^+$, $^{40}Ar^+$, $^{12}C^{16}O_2^+$, and various isotopes of barium ions ($^{135}Ba^+$, $^{136}Ba^+$ and $^{137}Ba^+$) via sympathetic cooling with laser-cooled $^{138}Ba^+$ in a linear radiofrequency trap. The sympathetically cooled species were embedded in the centre of large $^{138}Ba^+$ Coulomb crystals containing up to 2000 ions and were identified by motional resonance excitation. Crystals with molecular fractions exceeding 70% were obtained. The observed multi-species crystal structures agree well with results from molecular dynamics simulations. The simulations were also used to deduce an upper limit for the translational temperature of the molecular ions, as low as 20 mK.

(Some figures in this article are in colour only in the electronic version)

## 1. Introduction

Cold pure and mixed-species ion plasmas with translational temperatures in the millikelvin range are attractive systems for quantum optics, molecular physics, fundamental physics, precision metrology and chemical physics [1–14]. The wide range of possible applications calls for the development of methods for reliable and reproducible samples of cold atomic and molecular ion species with well-characterized composition. Direct cooling methods, such as laser cooling, successfully used for numerous neutral atoms and atomic ions, cannot be easily applied to many atomic species due to the limited range of laser sources available. Laser cooling of molecules is not feasible due to the lack of closed optical transitions. A powerful method for the (indirect) cooling of a wide variety of atomic and molecular ions, independent of their internal level structure, is sympathetic cooling [8, 9, 11]. Here, particles of one species are cooled by an ensemble of directly cooled, usually laser-cooled, atoms via their mutual interaction. The absence of closed transitions in molecules also implies that fluorescence detection will typically not be applicable, so that alternative techniques are required for the identification of sympathetically cooled species [14–16].

  

Sympathetic cooling of several species of atomic ions was achieved by using laser-cooled $^{9}Be^{+}$ [5], $^{24}Mg^{+}$ [17–19], $^{40}Ca^{+}$ [20] and $^{114}Cd^{+}$ [21] as coolants, in both Penning and radiofrequency traps. Cold molecular ions ($MgH^{+}$) have been formed by reactions of $H_2$ with optically excited $Mg^{+}$, sympathetically cooled, and their photo-dissociation studied [8, 10, 22]. Cold $BeH^{+}$ and $BeD^{+}$ ions have been produced in a similar way [7]. Recently, we have demonstrated reliable production of cold molecular hydrogen isotopomers and helium isotopes, via sympathetic cooling with laser-cooled $Be^{+}$ in a linear Paul trap [5, 23]. Chemical reactions between sympathetically cooled particles and neutral reactants were studied, using $^{138}Ba^{+}$ as a coolant [15]. Extraction of the product ions from the trap and detection was demonstrated for small $^{138}Ba^{+}$ ion crystals containing sympathetically cooled species. However, sympathetic cooling of ions in large $^{138}Ba^{+}$ crystals has not been reported so far.

In this work, we report the production of large $^{138}Ba^{+}$ ion crystals in a linear Paul trap containing up to 2000 particles. Up to 250 $^{16}O_2^{+}$, $^{40}Ar^{+}$ and $^{12}C^{16}O_2^{+}$ ions were sympathetically cooled and embedded inside the cold crystallized structures. In addition, other barium isotopes, $^{135}Ba^{+}$, $^{136}Ba^{+}$ and $^{137}Ba^{+}$, and molecular ions, such as $^{138}Ba^{16}O^{+}$, produced by chemical reactions with residual gas molecules, were sympathetically cooled and crystallized. We identified trapped ion species by excitation of their oscillation modes and determined their temperature.

## 2. Experiment

A linear radio frequency ion trap (Paul trap) is used to simultaneously store the atomic coolant ($^{138}Ba^{+}$) and the sympathetically cooled particles. The trap is enclosed in an ultra-high vacuum chamber at below $1 \times 10^{-10}$ mbar. Neutral gases can be introduced into the chamber via a leak valve. The linear Paul trap consists of four cylindrical electrodes, each sectioned longitudinally into three parts. The overall length of the electrodes is 10 cm, the central trapping region being 2 cm long. Stable trapping of $^{138}Ba^{+}$ is achieved with a Mathieu stability parameter, $q\left(=2QV_{\mathrm{RF}}/m\Omega^2 r_0^2\right) \approx 0.05$, with $Q$ and $m$ being the atomic charge and mass, respectively. $V_{\mathrm{RF}}$ and $\Omega$ are the amplitude and frequency of the rf driving field and $r_0 = 4.3$ mm is the distance from the trap centre to the electrodes. The radial (transverse) confinement of the ions is achieved by applying an rf drive at a frequency $\Omega$ of $2\pi \times 2.9$ MHz and an amplitude of up to 800 V to the trap electrodes. For the sympathetically cooled particles studied here this gives a stability parameter $q$ in the range 0.05–0.15. The effective trap potential is given by

$$U_{\mathrm{trap}}(x, y, z) = \frac{m}{2}\left(\omega_r^2(x^2 + y^2) + \omega_z^2 z^2\right), \tag{1}$$

with the $z$-axis along the trap centreline. The transverse oscillation frequency is

$$\omega_r = \left(\omega_0^2 - \omega_z^2/2\right)^{1/2}, \tag{2}$$

with $\omega_0 = QV_{\mathrm{RF}}/\sqrt{2}m\Omega r_0^2$. In the longitudinal direction, the oscillation frequency is given by $\omega_z = (2\kappa QV_{\mathrm{EC}}/m)^{1/2}$, where $V_{\mathrm{EC}}$ is a static potential added to the eight end sections (endcaps) of the electrodes to ensure confinement along the $z$-axis. The factor $\kappa \approx 3 \times 10^{-3}$ mm$^{-2}$ is a constant determined by the trap geometry.

$^{138}Ba^{+}$ ions are laser cooled on the $6^2S_{1/2} \rightarrow 6^2P_{1/2}$ transition at 493.4 nm. In addition, a repumper laser at 649.8 nm is necessary to prevent optical pumping to the metastable $5^2D_{3/2}$ state. In our set-up, the cooling laser radiation is generated by non-resonant sum frequency generation (SFG) of two solid-state lasers, a single frequency Nd:YAG laser at 1064 nm with an output power of 6 W and a Ti:Sapphire laser with 700 mW at 920 nm, in a periodically poled KTP crystal. Absolute frequency stability of the Nd:YAG laser is provided by frequency

doubling a small part of the laser radiation and locking to a line of the sub-Doppler hyperfine spectrum in iodine via modulation transfer spectroscopy. The Ti:Sapphire laser has a built-in reference cavity for stabilization. Output powers of 40 mW were achieved with this set-up. As a repumper, an external cavity laser diode at 649.8 nm was used with an output power of ∼10 mW. The linewidth of the repumper laser was measured to be 300 kHz, via cavity ring-down spectroscopy in a monolithic bow-tie cavity. For laser cooling of the barium ions, the two laser beams are linearly polarized in the vertical direction (transverse to the $z$-axis) and propagate along $z$. The effect of radiation pressure force on the produced cold ion plasmas is reduced, if required, by using two counterpropagating cooling laser beams. To maintain fluorescence, magnetic fields in the few gauss range are applied to the trap. The direction of the magnetic field is parallel to $z$.

For loading the trap, neutral atoms are evaporated from a barium oven and ionized *in situ* by a 500 eV electron beam crossing the trap centre. During $Ba^+$ loading, the cooling and repumper lasers are manually set to a frequency red detuned from the atomic resonance by several natural linewidths. The $^{138}Ba^+$ fluorescence is simultaneously recorded with a photomultiplier and an intensified CCD (ICCD) camera. A magnification of 10 was chosen for the imaging system of the ICCD camera.

For strong cooling, the $Ba^+$ ion cloud undergoes a phase transition from the fluid ion plasma to an ordered state, a Coulomb crystal. This phase transition reveals itself by a sudden increase in the detected fluorescence level, caused by the reduction in the particle velocities, and the consequently smaller Doppler broadening. Once the phase transition occurs, the frequencies of the lasers are adjusted for maximum cooling rate, controlled via continuous imaging of the cold ion plasma using the ICCD. The generated ion crystals are stable under these conditions, provided that the temperature stability of the laser environment is sufficiently stable. Typical storage times are in the range of a few hours. No significant particle losses were observed even when the laser radiation was blocked or strongly detuned for several minutes, see also [24].

If necessary, mass-selective cleaning of the trap is applied to eject heavy impurity particles, e.g. $BaO^+$, formed by chemical reactions during loading. To this end, we add a static quadrupole potential $V_{DC}$ to the trap until the $a$-parameter $\left(a = 4QV_{DC}/m\Omega^2 r_0^2\right)$ of the unwanted species lies outside the Mathieu stability range [25]. Thus, stable trapping of particles exceeding the mass of the atomic coolants is prevented.

## 3. Molecular dynamics simulations

In the simulations we solve Newton's equations of motion for laser-cooled and sympathetically cooled ions in the quasi-potential approximation

$$m_i \ddot{\mathbf{x}}_i = Q_i \nabla (U_{\text{trap}}(\mathbf{x}_i)) + \mathbf{F}_{C,i}(\{\mathbf{x}_j\}) + \mathbf{F}_{\mathbf{L}}(\dot{\mathbf{x}}_i), \tag{3}$$

where $i = 1, \ldots, N_{LC} + N_{SC}$. $N_{LC}$ and $N_{SC}$ are the number of laser-cooled (LC) and sympathetically cooled (SC) ions, respectively. $m_i$, $Q_i$ and $\mathbf{x}_i = (x_i, y_i, z_i)$ are the masses, charges and positions of the particles. $\mathbf{F}_{C,i}(\{\mathbf{x}_j\}) = (Q_i/4\pi\epsilon_0)\nabla_i \Sigma_j Q_j/r_{ij}$ is the Coulomb force and $r_{ij}$ is the distance between two ions. Trap asymmetries due to electric offset potentials are added to the quasi-potential $U_{\text{trap}}$. For simplicity, simulations are performed using a continuous linear viscous damping force $\mathbf{F}_{\mathbf{L}} = -\beta\dot{\mathbf{x}}_i$ in the horizontal direction. The friction coefficient $\beta$ is chosen well below the maximum value for transitions at optical wavelengths [26]. We have used stronger cooling forces $\mathbf{F}_{\mathbf{L}}$ to speed up cooling. Micromotion is not included because it is not expected to be important for the crystals presented here (see also section 4.4).

The equations of motion are numerically solved using the Leapfrog algorithm which is computationally less expensive than other methods, e.g. the higher-order Runge–Kutta algorithm. Moreover, the conservation of energy is respected, even at large time steps. Sympathetic cooling by laser-cooled $^{138}Ba^{+}$ can be simulated for up to four ion species. Heating processes for particular species can be added. In order to produce simulated images for a comparison with CCD images, projections of the particle positions on the observation plane are generated for a time series and superimposed.

## 4. Results

### *4.1. Barium ion crystals*

Figure 1 shows several $Ba^{+}$ ion crystals, (a), (b), (d) and (f), together with results from molecular dynamics (MD) simulations, (c) and (e). The prolate crystal in figure 1(a) is a typical example of a large barium ion crystal obtained with our apparatus. The cooling laser frequency was adjusted for maximum cooling power. The crystal contains ≈2000 laser-cooled (LC) $^{138}Ba^{+}$ and ≈1000 sympathetically cooled (SC) barium isotopes. It has an overall length of ≈2 mm along the $z$-axis and an extension of ≈0.1 mm in the vertical direction.

Figure 1(b) shows a medium-sized mixed-species barium crystal containing ≈200 $^{138}Ba^{+}$ and ≈100 other barium isotopes ($^{135}Ba^{+}$, $^{136}Ba^{+}$ and $^{137}Ba^{+}$). Due to light pressure forces on the LC particles the SC ions are located on the left end of the crystal, see also [9].

In figure 1(c) the result of MD simulations for the ion crystal shown in (b) is presented. In the simulations, the number of ions is varied until the observed crystal structure is reproduced. Typical observed radial intershell spacings for the LC ions are ≈19 $\mu$m, in good agreement with the value obtained from the MD simulations.

The influence of SC-cooled particles and light pressure forces on the formed crystal structures is illustrated in figures 1(d)–(f). Figures 1(d), (e) show an ion string. As is well known, the ion distances increase away from the string centre. For this string, the spacing between adjacent $^{138}Ba^{+}$ ions varies between 31 $\mu$m and 55 $\mu$m. The string contains 20 $^{138}Ba^{+}$ and approximately ten other barium isotopes, located at the left end of the crystal, as obtained from the simulations, figure 1(e). Occasionally, the ions collide with neutral background gas or hot ions present in the trap. Thus, individual ions may be kicked out of their position in the string, then re-cooled and again embedded in the crystal, but at a different position [9]. This is the case for the single $^{138}Ba^{+}$ ion on the left end of the crystal in figure 1(d) where random jumps were observed. For a different crystal structure, figure 1(f), where the LC (and SC) ions are arranged in a zig-zag configuration, the observed pitch varies between ≈27 $\mu$m and ≈34 $\mu$m.

### *4.2. Micromotion reduction*

The images of the Coulomb crystals in figure 1, in particular the outermost regions (in the radial direction) of the large structures, are blurred. This is attributed to residual micromotion, depending on the distance of the particles from trap centre and the symmetry of the effective trap potential. The distortion of the effective potential is mainly due to stray fields and the partial coating of the trap electrodes during evaporation of neutral barium from the oven. By adding additional static offset potentials to the central trap segments, the distortion can be compensated. A direct measurement of the micromotion can be obtained by correlating the fluorescence rate of the atomic coolants to the rf amplitude of the trap [27]. For our set-up, the photomultiplier (PMT) count rate is typically smaller than the rf field frequency (≈1 MHz

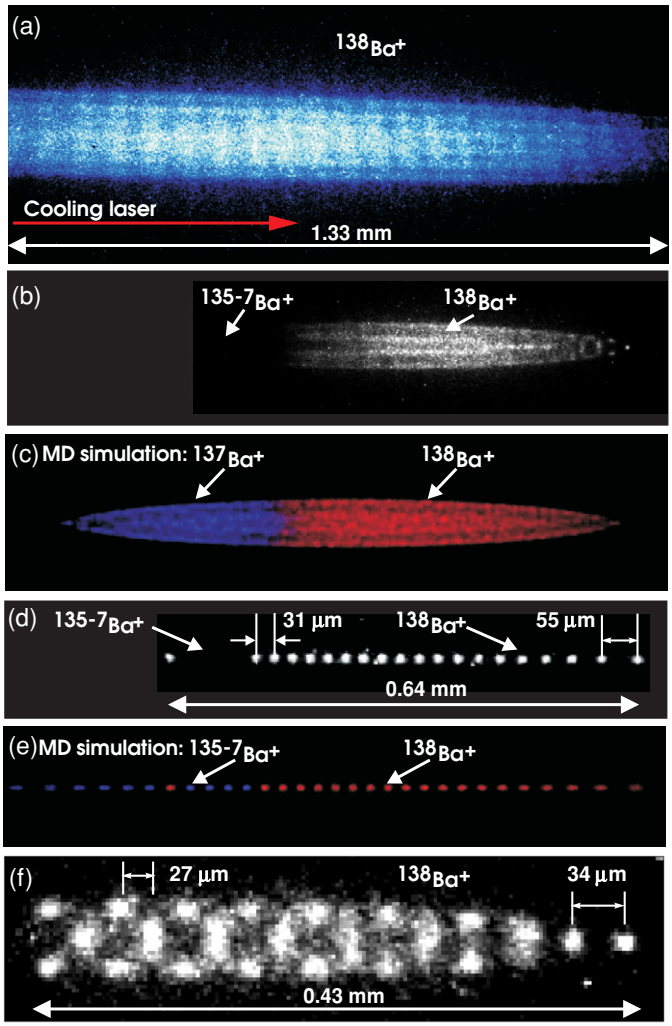


**Figure 1.** ICCD camera images of different $^{138}Ba^+$ crystals. The cooling and repumper laser beam directions are to the right. Camera integration time was 1 s. (a) Large Coulomb crystal containing ≈2000 $^{138}Ba^+$ ions and ≈1000 sympathetically cooled (SC) barium isotopes, located on the left side of the crystal. (b) ion crystal containing ≈200 $^{138}Ba^+$ and ≈100 other barium isotopes, predominantly $^{137}Ba^+$ and smaller admixtures of $^{135}Ba^+$ and $^{136}Ba^+$. (c) MD simulation of the crystal shown in figure 1 (b). LC ions, $^{138}Ba^+$: red, SC ions, $^{137}Ba^+$: blue. The translational temperature for LC and SC ions is approximately 20 mK, according to the simulations. (d) ion string consisting of 20 $^{138}Ba^+$ ions and eight other barium isotopes. The location of the SC ions is marked by arrows. (e) MD simulation of the ion string in (d). (f) Zig-zag structure of a $Ba^+$ ion crystal. The indicated dimensions are measured after calibration of the optical system.

versus $\Omega/2\pi = 2.75$ MHz, for this measurement). The PMT provides the start trigger pulse for a time-to-amplitude converter (TAC 567, EG&G Ortec). The stop pulse is provided by the zero crossing (or a slope) of the rf field. A multi-channel-analyser (MCA 917, EG&G Ortec) bins the counts according to the time delay between the start and the stop pulse.

The result of such a correlation measurement is shown in figure 2. Typically, for the recorded count rate, one obtains a single oscillation with a period $\sim 2\pi/\Omega$ and an amplitude proportional to the micromotion amplitude. The modulation amplitude was reduced by a

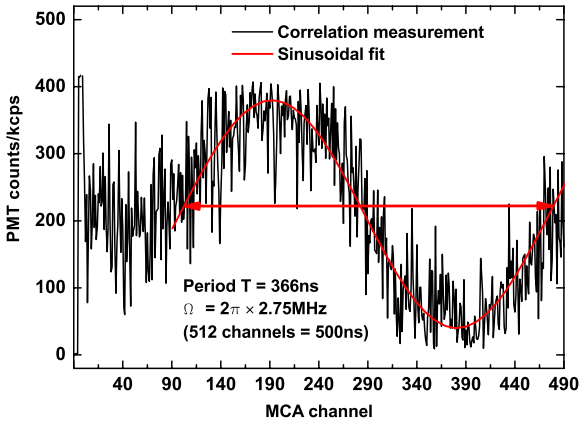


**Figure 2.** Correlation of the fluorescence emission rate with trap modulation, detected with a PMT in photon count mode. The initial part of the fluorescence curve (MCA channels 0–90) is flattened due to electronic noise.

factor of ≈2 by adding static offset potentials of up to 0.2 V to the central electrodes. This led to sharper ICCD images. In order to minimize or eliminate the micromotion excitation in all dimensions, a more complicated set-up involving three laser beams is required [27].

### *4.3. Sympathetic cooling and crystallization*

*4.3.1. $BaO^+$.* Cold $^{138}BaO^+$ molecular ions were produced by chemical reactions with background $CO_2$ molecules evaporated from the filaments of the electron gun and the barium oven:

$$Ba^+ + CO_2 \longrightarrow BaO^+ + CO. \tag{4}$$

This reaction is exothermic by several eV [28–30]. Direct formation of $BaO^+$ via the reaction $Ba^+ + O_2 \longrightarrow BaO^+ + O$ is precluded by its (measured) endothermicity even with optically excited $Ba^+$, see [31], apart from the negligible partial pressure of oxygen in our chamber. Similarly, chemical reactions between ground state and excited state $Ba^+$ and neutral $H_2$ gas, also present in the ultra-high vacuum system, are also endothermic by several eV, see [29], and therefore do not occur under our experimental conditions. These facts were verified by exposing large barium ion crystals to neutral hydrogen or oxygen gas, where no chemical reactions could be observed for typical exposure times of several minutes.

As shown in figure 3(a), the $BaO^+$ ions are located in the outer shell of the crystal. According to our simulations, (figure 3(b)), the crystal contains ≈250 $^{138}Ba^+$, 125 $^{135-7}Ba^+$ and 100 $^{138}BaO^+$ ions. The substantial formation of $BaH^+$ ions can be excluded, since the simulated structures, (figure 3(c)), are in clear disagreement with the observed ones. In particular, the simulations show how the light force causes the $BaH^+$ ions being located more on the left part of the crystal, together with the other barium isotopes, due to the similarity of mass. Furthermore, the shape of the crystal structure has changed. Whereas in the presence of SC $BaO^+$, the outermost $^{138}Ba^+$ ion shell has a flat shape over the whole length of the crystal, the longitudinal separation between $^{138}Ba^+$ and $^{138}BaH^+$ ions in figure 3(c) is more pronounced and abrupt, not observed in experiment (figure 3(a)). The location of the molecular ions on the lower side of the crystal is caused by small asymmetries of the effective trap potential, taken into account in the simulations. The laser-cooled and sympathetically cooled particles have a translational temperature of ≈20 mK, see below. The right end of the experimental structure

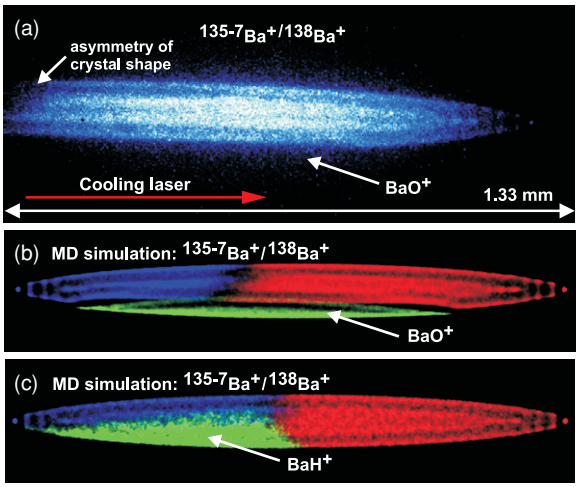


**Figure 3.** (a) Multi-species crystal of approximately 250 $^{138}Ba^+$, 125 $^{135-7}Ba^+$ and 100 $^{138}Ba^{16}O^+$ ions. The particle numbers were obtained from a MD simulation (b) that reproduced the observed crystal. (c) MD simulation of the multi-species ion crystal from (b) where $^{138}Ba^1\,H^+$ ions instead of $^{138}Ba^{16}O^+$ ions were used.

in figure 3(a) appears tilted. This is caused by sympathetically cooled barium isotopes and, again, by small asymmetries of the effective trap potential, leading to a displacement of the ions from the centre of the trap, as confirmed by the simulations (figure 3(b)).

*4.3.2. Light molecular ions.* After large barium ion crystals were formed and purified as described above, $^{16}O_2^+$, $^{40}Ar^+$ and $^{12}CO_2^+$ ions were produced by leaking $O_2$, Ar or $CO_2$ gas into the vacuum chamber at a partial pressure of $10^{-8}$ mbar and ionizing it *in situ* in the trap by a 200 eV electron beam. The loading rate was controlled by the partial pressure of the neutral gas and the electron beam intensity. As a consequence of sympathetic cooling and crystallization of the molecular ions, a dark inner region evolves in the initially pure crystals. According to equation (1), the lighter molecular species experience a stronger effective potential and are therefore embedded closer to the $z$-axis of the trap. As an example, a cold multi-species ion crystal containing $^{138}Ba^+$, $^{135-7}Ba^+$, $Ba^{16}O^+$, $^{40}Ar^+$ and $^{12}C^{16}O_2^+$ is shown in figure 4(a). Using the simulations the number of LC (≈300) and SC-cooled particles (≈590) were deduced. For simplicity, the simulations were run with a single lighter SC ion species of mass = 42. With these numbers the resulting crystal structures were modelled for different translational temperatures of the $^{138}Ba^+$ (see below). Agreement between the predicted and the observed crystal structure is achieved for a translational temperature of ≈20 mK for $^{138}Ba^+$, the temperature of the SC ions being very similar, figure 4(b).

### *4.4. Crystal temperature*

Upper limits for the translational temperatures of the LC and SC ions in crystals of arbitrary shape and composition can be deduced from MD simulations. The size of the ion fluorescence spots in the ICCD images is compared to the simulation results performed for a range of temperatures. Figures 5(a)–(d) show the computed spatial distribution as a function of temperature for an ion crystal containing 360 $^{138}Ba^+$ and 180 atoms of the barium isotopes $^{135}Ba^+$, $^{136}Ba^+$ and $^{137}Ba^+$. The corresponding experimental ion crystal, figure 5(e), is consistent with a temperature between 4 and 10 mK (the $^{138}Ba^+$ Doppler temperature is

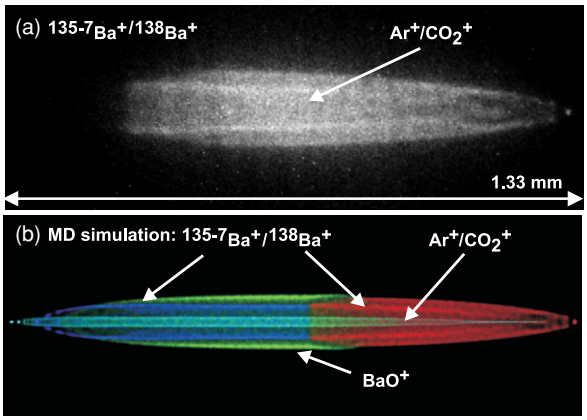


**Figure 4.** (a) Multi-species ion crystal following loading with a mixture of Ar and $CO_2$ gas, containing ≈300 $^{138}Ba^+$ (red), ≈150 barium isotopes (blue, embedded on the left end of the crystal), ≈240 $^{138}Ba^{16}O^+$ ions (green, located in the outermost shells) and ≈200 $^{40}Ar^+$ plus $^{12}C^{16}O_2^+$ ions in approximately equal proportions (light blue, embedded around the $z$-axis). The lighter SC particles were identified via motional resonance excitation, see below. The asymmetry of the ion crystal in the horizontal direction (along the $z$-axis) is due to light pressure forces. (b) MD simulation of the crystal shown in figure 4(a). The simulations show the whole crystal and are thus not to scale with the experimental images.

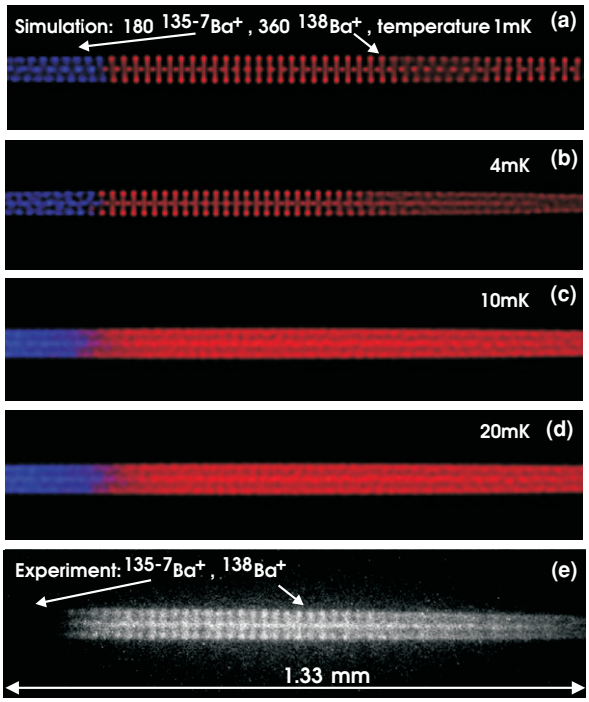


**Figure 5.** Comparison between simulated (a)–(d) and measured (e) $Ba^+$ ion crystal structures. In the simulations, the translational temperature of the $Ba^+$ crystal was varied. Note that (e) is magnified compared to (a)–(d).

0.15 mK). The obtained estimate for the LC particles is consistent with direct temperature measurements we performed, see also [32, 33, 5, 18]. Because of the Coulomb coupling between LC and SC ions, the temperature of the latter influences the former. Because of this we can infer information about the SC ion temperature from the LC ion temperature, which is manifested through the CCD images. For example, if in the simulations of light ions (e.g. $O_2^+$, $Ar^+$, $CO_2^+$) embedded in the centre of the ion crystal they are kept at a temperature $>50$ mK (by adding a heating source), the $Ba^+$ ion spots surrounding the molecular ions are much more blurred than observed experimentally. Similarly, for the case of $BaO^+$ ions located at the edge of a $Ba^+$ crystal, the observed $Ba^+$ ion spot size in the outermost shell is inconsistent with a $BaO^+$ temperature $>50$ mK. Tighter upper limits can be set by stimulating the balance between heating and cooling rates for the SC particles. The cooling is provided by the LC particles kept at a constant temperature chosen so that simulated and measured images agree. Heating occurs due to collisions with background particles and due to rf heating. Rf heating is negligible for crystals at $\ll 1$ K and small $q$. This has been shown both experimentally [24] and by MD simulations [34, 35]. The background collision heating rate was estimated at $\approx 1$ K/particles from experimental observations of random jumps of individual $Ba^+$ ions, induced by collisions, in small mixed-species crystals. The relevant cooling rates were extracted from the simulations (see also [36]). We find, both for SC particles in the centre and for heavy SC particles at the $Ba^+$ crystal boundary that the SC ion temperature is at most not larger than a factor of 2 of the $Ba^+$ temperature. Our results do not indicate a major effect on the SC temperature due to the significantly different mass ratio $m_{SC}/m_{LC}$ for the two cases [37].

Furthermore, for the crystals shown, small asymmetries of the trap potential lead to a good coupling between longitudinal and radial degrees of freedom of the $Ba^+$ ions, and thus, also to more efficient sympathetic cooling rates. This was checked by carefully aligning the laser beams along the trap symmetry axis which leads to a reduced coupling between, and therefore, to a reduced cooling rate for the radial degrees of freedom of LC (and SC) ions. Experimentally, this becomes obvious from a more blurred shell structure of the ion crystal, induced by an uncorrelated rotation-like diffusion of the ions around the trap symmetry axis, also seen in the simulations.

### *4.5. Mass spectroscopy*

The trapped ion species are identified by excitation of their motion in the radial direction. For this purpose, a low-frequency rf field is added with opposite phase to the two orthogonal pairs of the central electrodes. When the frequency of the excitation field is resonant with a mode frequency of a trapped ion species the $^{138}Ba^+$ fluorescence level changes. This is due to heating of the excited ion species, which in turn leads to heating of the LC ions via Coulomb interaction, and thus to a change of the observed fluorescence. For the large crystals studied here, this method allows for the identification of trapped ion species when the relative difference between their mass-to-charge ratios $m/q$ is larger than $\approx 10\%$. For a single molecular ion trapped and sympathetically cooled by a single atomic ion, very high $q/m$ resolution in the $10^{-4}$ range can be achieved, see [16].

For $\omega_0 \gg \omega_z$, the radial oscillation frequency for a single trapped SC ion with mass $m_{SC}$ is approximately given by

$$\omega_{r,SC} = \frac{m_{Ba}}{m_{Sc}} \omega_{r,Ba}, \tag{5}$$

with $\omega_{r,Ba}$ ($m_{Ba}$) being the corresponding radial oscillation frequency (mass) of $^{138}Ba^+$. The shape of the observed secular spectra depends strongly on the applied excitation amplitude and the laser cooling rates, see e.g. [15, 38, 39].

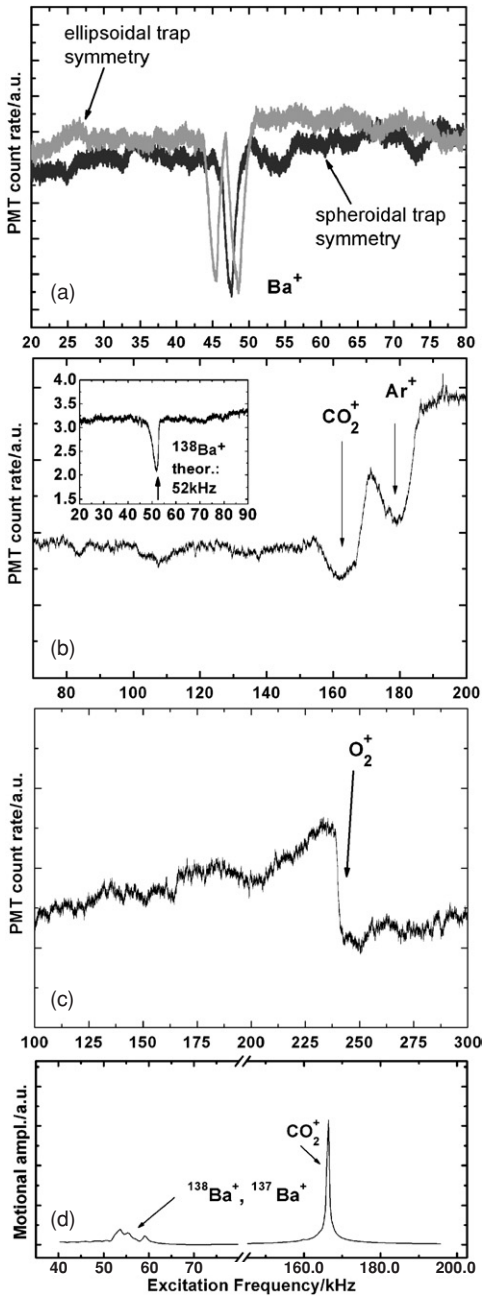


**Figure 6.** (a) Motional resonance spectrum for a barium ion crystal. Individual resonances for the different barium isotopes were not resolved. Secular excitation amplitude: 0.1 V. Sweep directions: towards higher frequency. Black (grey) line: for spheroidal (ellipsoidal) symmetry of the trap potential. (b) Motional spectrum for the crystal displayed in figure 4(a). Secular excitation amplitude: 0.2 V. The inset shows the measured barium resonance frequency for that crystal. (c) Motional spectrum following loading of $O_2$. Modulation amplitude: 0.2 V. (d) Motional resonance spectrum for a three-component ion crystal containing $^{138}Ba^+$, $^{137}Ba^+$ and $^{12}C^{16}O_2^+$, as obtained from MD simulations. The simulated crystal is comparable in size, shape and contained ion number to the crystal in figure 4(a).

Figure 6 displays four motional resonance spectra obtained for different ion crystals. The different barium isotopes were not resolved. Figure 6(a) shows the result obtained for an ion crystal containing only barium, and figures 6(b), (c) show spectra for cold multi-component ion crystals. In the latter, relatively large excitation amplitudes were applied, thereby ejecting a certain fraction of ions with each sweep, and the size of the dark crystal core was reduced with repeated excitation sweeps. For a symmetric trap potential, the expected single-particle motional frequency of the $^{138}Ba^+$ is 46 kHz, in good agreement with the experimental result. Figure 6(a) also shows a measurement of the motional spectrum for a non-radially symmetric trap potential (grey line), obtained by applying static quadrupole voltages $V_{DC}$ of $\approx$10 mV to the central electrodes. In this case, the degeneracy between the transverse oscillation modes (with respect to the $x$ and $y$ axes) is removed. The transverse frequencies are then given by $\omega_{x,y}^2 = Q^2 V_{RF}^2 / (2m^2\Omega^2 r_0^4) - \omega_z^2/2 \pm Q V_{DC}/m r_0^2$. Since for $V_{DC} = 0$, $\omega_x$ and $\omega_y$ are degenerate, motional resonance excitation can be used as an indicator for compensation of stray fields.

The observed motional frequencies depend on various parameters. For example, the frequency sweep direction during excitation (from low-to-high or opposite) and the excitation amplitude induce a systematic shift of the motional frequencies. A detailed discussion of these line shifting effects can be found in e.g. [38, 39]. Furthermore, line shifts in the motional spectra are induced by coupling between different ion species in the trap, via their Coulomb interaction, which can lead to significant deviations between the measurement and the value of equation (5), which is a single-particle property [39]. In particular, the coupling between $^{138}Ba^+$ and sympathetic particles leads to a shift of all measured frequencies to higher values. However, for the spectra shown in figures 6(b), (c) the upward shift of the frequencies was compensated by a large excitation amplitude, the latter leading to an opposite shift of the resonance frequency (for a sweep direction towards higher frequencies). In the spectra in figures 6(b), (c) significant changes in the barium fluorescence were found for $\approx$160 kHz, $\approx$180 kHz (b) and $\approx$230 kHz (c), which can be attributed to the excitation of cold and crystallized $^{12}C^{16}O_2^+$, $^{40}Ar^+$ and $^{16}O_2^+$, respectively. The net result of the two compensating effects are frequency values close to the single-particle values of 163 kHz for $^{12}C^{16}O_2^+$, 179 kHz for $^{40}Ar^+$ and 224 kHz for $^{16}O_2^+$.

Using the MD simulations, the motional frequency spectrum for pure and mixed-species ion crystals can be computed. As an initial condition, the positions of all particles of a simulated crystal are shifted in the $x$-direction. Subsequently, the particles perform damped oscillations around their equilibrium positions. The Fourier transform of the sum of the $x$-coordinates of each species is computed. It can be regarded as an indicator of the resonance spectrum for periodic excitations, as performed experimentally. The computed motional frequency spectrum for a three-component ion crystal containing $^{138}Ba^+$, $^{137}Ba^+$ and $^{12}C^{16}O_2^+$ ions is shown in figure 6(d). The obtained frequency for the $^{12}C^{16}O_2^+$ (166 kHz) is in good agreement with the measured value at 160 kHz (figure 6(b)). Furthermore, in the simulations different barium isotopes, such as $^{138}Ba^+$ and $^{137}Ba^+$, can be resolved. The motional frequencies of the three ion species are in good agreement with the values of equation (5). Note that for the simulation of the $^{12}C^{16}O_2^+$ motional spectrum, a larger excitation amplitude compared to that used for simulating the motional spectrum of the barium isotopes was applied.

## 5. Summary

In summary, we have employed sympathetic cooling by laser-cooled $^{138}Ba^+$ to produce cold, mixed-species ion crystals containing large fractions of $^{16}O_2^+$, $^{40}Ar^+$, $^{12}C^{16}O_2^+$, and various barium isotopes ($^{135}Ba^+$, $^{136}Ba^+$ and $^{137}Ba^+$). Large Coulomb crystals of up to 2000

particles were formed with translational temperatures as low as approximately 20 millikelvin. The ion species were identified by motional resonance excitation. Molecular dynamics simulations were performed for reproducing the observed mixed-species crystal structures and for modelling the motional resonance spectra. Good agreement was found between experimental and theoretical results for the shape of the ion crystals produced. The positions of the measured and simulated motional resonance frequencies agree with an accuracy of a few per cent. Moreover, the MD simulations allowed the estimation of the translational temperature of the ion species.

Cold multi-species ion plasmas are interesting systems for a broad field of research ranging from cold chemistry to precision measurements in fundamental physics. The obtained results represent a starting point for the sympathetic cooling of highly charged atomic ions [36], using a rf trap, and the extension of sympathetic cooling to complex molecules, e.g. proteins or polymers, with masses of many thousand amu [26].

## Acknowledgments

We acknowledge support from the Deutsche Forschungsgemeinschaft (DFG) in the framework of SPP1116 and the EU network 'Cold Molecules' HPRN-CT-2002-00290.

## References

[1] Schmidt-Kaler F *et al* 2003 Realization of the Cirac–Zoller controlled-NOT quantum gate *Nature* **422** 408–11
[2] Chiaverini J *et al* 2004 Realization of quantum error correction *Nature* **432** 602–5
[3] Karshenboim S G and Ivanov V G 2002 Hyperfine structure of the ground and first excited states in light hydrogen-like atoms and high-precision tests of QED *Eur. Phys. J.* D **19** 13–23
[4] See, e.g., Wineland D J *et al* 2002 *Proc. 6th Symp. on Freq. Standards and Metrology* ed P Gill (Singapore: World Scientific) pp 361–8
[5] Roth B *et al* 2005 Sympathetic cooling of $^4He^+$-ions in a radiofrequency trap *Phys. Rev. Lett.* **94** 053001
[6] Schiller S and Korobov V I 2005 Test of time-independence of the electron and nuclear masses with ultracold molecules *Phys. Rev.* A **71** 032505
[7] Fröhlich U, Roth B, Antonini P, Lämmerzahl C, Wicht A and Schiller S 2004 Ultracold trapped molecules: novel systems for test of the time-independence of the electron-to-proton mass ratio *Springer Lect. Notes Phys.* **648** 297–307
[8] Molhave K and Drewsen M 2000 Formation of translationally cold $MgH^+$ and $MgD^+$ molecules in an ion trap *Phys. Rev.* A **62** 011401(R)
[9] Bowe P, Hornekaer L, Brodersen C, Drewsen M, Hangst J S and Schiffer J P 1999 Sympathetic crystallization of trapped ions *Phys. Rev. Lett.* **82** 2071
[10] Bertelsen A *et al* 2004 Photo-dissociation of cold $MgH^+$ ions *Eur. Phys. J.* D **31** 403–8
[11] Larson D J, Bergquist J C, Bollinger J J, Itano Wayne M and Wineland D J 1986 Sympathetic cooling of trapped ions: a laser-cooled two-species nonneutral ion plasma *Phys. Rev. Lett.* **57** 70
[12] Drullinger R E, Wineland D J and Bergquist J C 1980 High-Resolution optical spectra of laser cooled ions *Appl. Phys.* **22** 365
[13] Glenewinkel-Meyer T and Gerlich D 1997 Single and merged beam studies of the reaction $H_2^+$ ($v = 0, 1$; $j = 0, 4$) + $H_2^+ \rightarrow H_3^+ + H$ *Isr. J. Chem.* **37** 343–52
[14] Welling M *et al* 1998 Ion/molecule reactions, mass spectrometry and optical spectroscopy in a linear ion trap *Int. J. Mass. Spectrom. Ion Process.* **172** 95–114
[15] Baba T and Waki I 2001 Laser-cooled fluorescence mass spectrometry using laser-cooled barium ions in a tandem linear trap *J. Appl. Phys.* **89** 4592
[16] Drewsen M *et al* 2004 Nondestructive identification of cold and extremely localized single molecular ions *Phys. Rev. Lett.* **93** 243201
[17] Hasegawa T and Shimizu T 2002 Resonant oscillation modes of sympathetically cooled ions in a radio-frequency trap *Phys. Rev.* A **66** 063404
[18] van Eijkelenborg M A, Storkey M E M, Segal D M and Thompson R C 1999 Sympathetic cooling and detection of molecular ions in a penning trap *Phys. Rev.* A **60** 3903

[19] Imajo H *et al* 1996 High-resolution ultraviolet spectra of sympathetically-laser-cooled $Cd^+$ ions *Phys. Rev.* A **53** 122–5
[20] Kai Y *et al* 2001 Motional resonances of sympathetically cooled $^{44}Ca^+$, $Zn^+$, or $Ga^+$ ions in a linear Paul trap *Japan. J. Appl. Phys.* **40** 5136–40
[21] Blinov B B *et al* 2002 Sympathetic cooling of trapped $Cd^+$ isotopes *Phys. Rev.* A **65** 040304(R)
[22] Bertelsen A, Jorgensen S and Drewsen M 2005 The rotational temperature of polar molecular ions in Coulomb crystals Preprint physics/0504128
[23] Blythe P, Roth B, Fröhlich U, Wenz H and Schiller S 2005 Production of cold trapped molecular hydrogen ions *Phys. Rev. Lett.* at press
[24] Schätz T *et al* 2001 Crystalline ion beams *Nature* **412** 717–20
[25] Fröhlich U, Roth B and Schiller S 2005 Ellipsoidal coulomb crystals in a linear radio-frequency trap *Phys. Plasmas* **12** 073506
[26] Schiller S and Lämmerzahl C 2003 Molecular dynamics simulation of sympathetic crystallization of molecular ions *Phys. Rev.* A **68** 053406(5)
[27] Berkeland D J *et al* 1998 Minimization of ion micromotion in a Paul trap *J. Appl. Phys.* **83** 5025–33
[28] Spears K G and Fehsenfeld F C 1972 Termolecular association reactions of Mg, Ca, and Ba ions *J. Chem. Phys.* **56** 5698
[29] Armentrout P B and Beauchamp J L 1980 Experimental and theoretical studies of the reaction $Ba^+(D_2,D)BaD^+$: sequential impulse model for endothermic reactions *Chem. Phys.* **48** 315
[30] Huber K P and Herzberg G 1979 *Molecular Spectra and Molecular Structure* (New York: Van Nostrand Reinhold)
[31] Johnsen R, Brown H L and Biondi M A 1970 Reactions of $Na^+$, $K^+$, and $Ba^+$ ions with $O_2$, NO, and $H_2O$ molecules *J. Chem. Phys.* **52** 5080
[32] Hornekær L 2000 Single and multi-species Coulomb ion crystals: structures, dynamics and sympathetic cooling *PhD Thesis* Aarhus University
[33] Barrett M D *et al* 2003 Sympathetic cooling of $^9Be^+$ and $^{24}Mg^+$ for quantum logic *Phys. Rev.* A **68** 042302
[34] Prestage J D *et al* 1991 Dynamics of charged particles in a Paul radio-frequency trap *Phys. Rev. Lett.* **66** 2964–7
[35] Ryjkov V L, Zhao X and Schuessler H 2005 Simulations of the rf heating rates in a linear quadrupole ion trap *Phys. Rev.* A **71** 033414
[36] Gruber L *et al* 2001 Evidence for highly charged ion Coulomb crystallization in multicomponent strongly coupled plasmas *Phys. Rev. Lett.* **86** 636–9
[37] Jensen M J *et al* 2005 Rapid heating of a strongly coupled plasma near the solid–liquid phase transition *Phys. Rev. Lett.* **94** 025001
[38] Baba T and Waki I 2002 Spectral shape of *in situ* mass spectra of sympathetically cooled molecular ions *Japan. J. Appl. Phys.* **92** 4109–16
[39] Roth B, Blythe P, Wenz H and Schiller S 2005 Motional resonance coupling in cold multi-species Coulomb crystals, in preparation

# Ion-neutral chemical reactions between ultracold localized ions and neutral molecules with single-particle resolution

B. Roth, P. Blythe, H. Wenz, H. Daerr, and S. Schiller
*Institut für Experimentalphysik, Heinrich-Heine-Universität Düsseldorf, 40225 Düsseldorf, Germany*
(Received 23 January 2006; published 19 April 2006)

Chemical reactions between ultracold $^9Be^+$ ions and room-temperature molecular hydrogen isotopomers and between ultracold $H_3^+$ ions and room-temperature $O_2$ have been studied in a laser-cooling ion trap apparatus. For small Coulomb crystals of beryllium ions, reactions can be followed at the single-ion level. We demonstrate characterization of a chemical reaction in which neither one of the reactants nor the product is directly detectable. In this case molecular dynamics simulations were used for the determination of ion numbers from images of the $^9Be^+$ ion ensemble. The observed reaction rates are in agreement with the Langevin ion-neutral reaction theory.

DOI: 10.1103/PhysRevA.73.042712 PACS number(s): 34.50.−s, 32.80.Pj, 42.50.−p

## I. INTRODUCTION

Chemical reactions between trapped molecular ions and neutral reactants are of significant interest to chemistry and astrophysics, and have been studied for many years at low temperatures. Multipole ion traps using neutral buffer gas as coolant have been used to reach temperatures down to 10 K, see, e.g., [1]. Reaction rates and branching ratios were deduced by extraction of the reaction products from the trap and counting, see [2] for examples.

It is desirable to extend such studies to state-specific reactions, which implies the necessity to prepare the reactants in particular quantum states and with well-defined collision energy. This requires a well-controlled environment in which undesired interactions and transitions between states are minimized. The ability to conduct and observe chemical reactions at the level of individual molecules in a cold, UHV environment has the potential to improve our understanding of important astrochemical reactions [3–5], through improvements in the accuracy of measurements of reaction rates and branching ratios [6], and by using narrow-bandwidth lasers to study chemical reactions state-selectively.

Regarding the ion side of this challenging program, significant progress was made in recent years in the generation of ensembles of ultracold ($<1$ K) pure and mixed-species ion plasmas in traps using laser cooling techniques. In particular, sympathetic cooling by laser-cooled atomic ions was used to cool ion species which cannot be directly laser cooled due to the lack of closed optical transitions. Various atomic and molecular ion species covering a broad mass range have been cooled to milliKelvin temperatures and brought to rest inside ordered structures, denoted by Coulomb crystals [7–10]. In these crystals the ions are located in well-defined shell structures. At the lowest temperatures reached ($<10$ mK) the ions remain mostly confined in the immediate vicinity of their equilibrium positions.

The next important development required in order to reach complete state preparation is internal cooling, i.e., population of a particular rovibrational level. This goal can be reached by collisions with cold neutral buffer gas and, possibly, laser cooling techniques. Such translationally and internally ultracold ensembles will be an important ingredient in the study of gas phase ion-neutral reactions and collision processes at the quantum level.

Thus far, a first study of chemical reactions with one ultracold partner has been demonstrated: chemical reactions between large ensembles of laser-cooled and crystallized $Ca^+$ ions, excited to the $^2P_{1/2}$ state, and neutral molecular oxygen gas at 300 K were investigated and reaction rates extracted [11]. Subsequently, the reaction products formed, $CaO^+$ ions, were exposed to 300 K neutral CO and reacted back to $Ca^+$ and $CO_2$. This reaction has been observed with sensitivities down to the single particle level [12]. Furthermore, ion-neutral reactions in which the molecular ions were sympathetically cooled to 10 K by laser-cooled $Mg^+$ ions were studied [13]. The reaction was detected by using the laser-cooled ions for monitoring the decrease of the reactant molecular ions, via mass spectroscopy.

In the present work we extend the works of Refs. [11,13] in several directions: (i) small ensembles, which could be interesting systems for quantum state preparation, (ii) reactions with the simplest molecules which are most easily amenable to *ab initio* calculation and which are of astrophysical importance, (iii) reactions in which the laser-cooled atomic ions in crystals are "spectators" only—thereby demonstrating that it is possible to detect and measure reactions in which neither one of the reactants nor the product is directly detectable, and (iv) employing MD simulations rather than mass spectroscopy for interpreting the observations and determining the reactant number decrease.

A first set of studied chemical reactions is between laser-cooled $^9Be^+$ ions and neutral molecular hydrogen isotopomers. Secular excitation mass spectroscopy was used to identify the reaction products. The reaction rates were deduced from the time evolution of the $Be^+$ ion number and/or of the spontaneous emission fluorescence rate, recorded by a CCD camera. The available reaction channels for this system are [14]

$$Be^+ + XY \rightarrow BeX^+ + Y \quad (1)$$

$$\rightarrow BeY^+ + X \quad (2)$$

 

$$\rightarrow \mathrm{Be}X + Y^+ \tag{3}$$

$$\rightarrow \mathrm{Be}Y + X^+ \tag{4}$$

$$\rightarrow \mathrm{Be} + XY^+, \tag{5}$$

where $\{X,Y\} \in \{\mathrm{H},\mathrm{D}\}$. These reactions do not proceed with the beryllium ion in its ground electronic state. For example, the reaction

$$\mathrm{Be}^+(^2S_{1/2}) + \mathrm{H}_2(X^1\Sigma_g^+) \rightarrow \mathrm{BeH}^+(X^1\Sigma^+) + \mathrm{H}(^2S_{1/2}) \tag{6}$$

is endothermic by 1.57 eV [14]. Similar values hold when replacing $H_2$ by HD or $D_2$. The endothermicities of the other possible reaction channels are: 2.45 eV for reactions 3 and 4, and 1.9 eV for reaction (5). Therefore, the $Be^+$ ion must be excited, e.g., to the $^2P_{3/2}$ state (by 3.9 eV photons) in order to react. However, we do not observe reactions (3), (4), and (5) even when $Be^+$ is electronically excited in our trap, probably due to the large kinetic energy transferred to the reaction products, $H^+$, $D^+$, or $HD^+$, leading to their loss from the trap.

The $Be^+$ ions in these experiments are continuously laser-cooled by a 313 nm all-solid-state laser system [15], and this simultaneously provides the (partial) excitation necessary for the reactions to proceed. By altering the intensity or detuning of the cooling laser, we can modify the excitation rate and hence the reaction rate, allowing for control of the process.

In mixed-species ion crystals containing laser-cooled (LC) $Be^+$ ions and sympathetically cooled (SC) triatomic hydrogen molecular ions, $H_3^+$, we have studied the reaction

$$\mathrm{H}_3^+ + \mathrm{O}_2 \rightarrow \mathrm{HO}_2^+ + \mathrm{H}_2 \tag{7}$$

and deduced the corresponding reaction rate. This reaction is nearly thermoneutral, see [18], and references therein. However, the reaction rates for the back reaction $HO_2^+ + H_2 \rightarrow H_3^+ + O_2$ were found to be smaller than for the forward direction [19].

The Langevin theory of ion-neutral reactions predicts, for suitably low temperatures, a reaction rate which is independent of temperature [16,17]. The reaction rate for beryllium ions in reactions (1)–(5) or $H_3^+$ ions in reaction (7) is given by

$$R_L = -dN_i(t)/dt = -k_L N_n N_i(t), \tag{8}$$

where $N_i$ denotes the ion number, $N_n$ is the (constant) number density of neutral reactants, and $k_L = -23.42\sqrt{\alpha/\mu} \times 10^{-10}$ cm$^3$/s is the Langevin coefficient. $\alpha$ is the polarizability of the neutral reactant and $\mu$ is the reduced mass of the reacting particles. For an initial ion number $N_{i,0}$ at time $t=0$ the number of remaining ions $N_i(t)$ is

$$N_i(t) = N_{i,0} e^{-k_L N_n t}. \tag{9}$$

## II. EXPERIMENTAL SETUP

We use a linear radio-frequency trap to simultaneously store both $Be^+$ and sympathetically cooled ions, e.g., $H_3^+$ ions. The trap is driven at $\Omega/2\pi = 14$ MHz, with a peak-to-peak amplitude $2V_{\mathrm{RF}} = 380$ V and is enclosed in an UHV chamber kept below $10^{-10}$ mbar. The chamber is equipped with a leak valve for the controlled introduction of gases, whose partial pressure is controlled by a quadrupole mass analyzer and an ion gauge.

Typically, we set the radial Mathieu stability parameter, $q = 2QV_{\mathrm{RF}}/m\Omega^2 r_0^2 \simeq 0.054$ for the $Be^+$, giving a radial secular oscillation frequency ("single particle frequency"), $\omega_r = (\omega_0^2 - \omega_z^2/2)^{1/2} \simeq 280$ kHz [9]. $Q$ and $m$ are the charge and the mass of the ions, $r_0 = 4.3$ mm is the distance from the trap center to the electrodes, and $\omega_0 = QV_{\mathrm{RF}}/\sqrt{2}m\Omega r_0^2$. The longitudinal frequency $\omega_z = (2\kappa QV_{EC}/m)^{1/2}$ is determined by the static potential $V_{EC}$ applied to the end sections of the trap to achieve confinement of the ions in the $z$ direction. $\kappa$ is a constant determined by the trap geometry. For the molecular hydrogen ions $q$ lies between 0.162 ($H_3^+$) and 0.240 ($H_2^+$).

The trapped ion species are identified by the spectroscopy of their motional frequencies. For this purpose, we excite the ions' motion in the time-averaged effective potential using an additional plate electrode between the two uppermost trap electrodes (at 45° to the $x$ and $y$ axes of the trap, parallel to the $z$ axis). An oscillating potential is applied to the electrode, at frequencies between 2 kHz and 3 MHz, and with an amplitude up to 10 V. The frequency of the excitation is scanned, while the $Be^+$ fluorescence is recorded. When the applied frequency is resonant with a motional frequency of a species in the crystal, that motion is excited, the ions are heated, and the fluorescence of the beryllium ions in the crystal is affected. The heating of the crystal causes an increase in fluorescence when the cooling laser is detuned sufficiently to the red of the cooling transition.

To load $Be^+$ ions into the trap, atoms are thermally evaporated from a beryllium wire, and ionized in the trap center by a 750 eV electron beam. This produces a large cloud of beryllium ions, along with impurities from ionization of background gas present in the vacuum chamber. The heavier impurities can be removed by temporarily applying a static quadrupole potential to the trap such that it becomes unstable for elements with a higher mass-to-charge ratio than that of $Be^+$.

For laser cooling of $Be^+$ ions we produce circularly polarized light resonant with the $^2S_{1/2}(F=2) \rightarrow {}^2P_{3/2}$ transition at 313 nm. The UV laser light is frequency stabilized to a hyperfine transition of molecular iodine. An acousto-optic modulator (AOM) allows us to shift the UV frequency within a range of 370 MHz while maintaining absolute frequency stability. Spontaneous emission to the metastable ground state $^2S_{1/2}(F=1)$ is prevented using a repumper red detuned by 1.250 GHz. The laser cooling beam is parallel to the symmetry axis ($z$ axis) of the trap. For definition of a quantization axis, magnetic fields in the few Gauss range are applied to the trap parallel to $z$.

## III. METHOD

### A. Preparation of ultracold pure and mixed-species ion crystals

Ensembles of $Be^+$ ions are produced, trapped, and subsequently laser-cooled so that they undergo a phase transition

to an ordered state, a Coulomb crystal [20]. Typically, the crystals studied here have translational temperatures of $\approx 10$ mK, as found by measurement of the spontaneous emission fluorescence line shape and confirmed by molecular dynamics (MD) simulations [10,21]. When required, light molecular ions, e.g., molecular hydrogen isotopomers, are produced via electron impact ionization of neutral gas introduced to the vacuum chamber at pressures of approximately. $4 \times 10^{-10}$ mbar. The loading rate is controlled by the partial pressure of the gas and the electron beam intensity. As a consequence of trapping and sympathetic crystallization of the molecular ions a dark inner region evolves in the initially pure $Be^+$ crystals. The lighter molecular species experience a stronger effective potential inside the trap and are therefore embedded closer to the symmetry axis of the trap. Usually, during the loading of molecular hydrogen ions into the trap, various lighter impurities (molecular hydrogen isotopomers) are produced by chemical reactions together with the species under study. Such impurities are removed by melting the crystal and subsequently exciting the resonant motion of a particular ion species at sufficiently large excitation amplitudes. This leads to the ejection of that particular species while leaving nearly undisturbed the species under study. The ion cloud is then recrystallized and a two-species ion crystal is obtained [9].

### B. Measurements

The above pure or mixed-species $Be^+$ ion crystals are the starting point for our studies. Since the reaction rate between LC $Be^+$ ions and hydrogen isotopomers depends on the relative population of the $^2P_{3/2}$ state in $Be^+$, prior to each measurement the fraction of excited $Be^+$ ions is determined. For this purpose, the cooling laser is tuned to maximum fluorescence, which corresponds to a relative population of the upper level of 50% (the laser intensity $I \approx 10$ mW/mm$^2$ is much larger than the saturation intensity $I_{sat}=0.8$ mW/cm$^2$), and the corresponding photon count rate recorded by a photomultiplier tube (PMT) is used for calibration. A particular level of excitation can be set by frequency-detuning the cooling laser to the red side of the atomic resonance using an AOM.

Subsequently, neutral reactants are leaked into the vacuum chamber at typical pressures between $2 \times 10^{-10}$–$2 \times 10^{-9}$ mbar. At these pressures the Langevin theory should still apply [17]. After the partial pressure of the introduced neutral reactant has reached a constant value the $Be^+$ fluorescence is recorded both with a PMT and with a charge-coupled device (CCD) camera as a function of time. In these measurements the PMT has a time resolution of 0.1 s, whereas the camera exposure time typically is in the range of 0.5–2 s.

The ion species involved were identified by secular excitation mass spectrometry, as described above. The chemical reaction process can be stopped at any time by closing the leak valve, and secular scans can be made to determine the presence of reaction products, e.g., $BeH^+$ and $BeD^+$. Individual features in the measured mass spectra were assigned to the different ion species contained in the crystal by comparison with spectra obtained from MD simulations, see also [21,22].

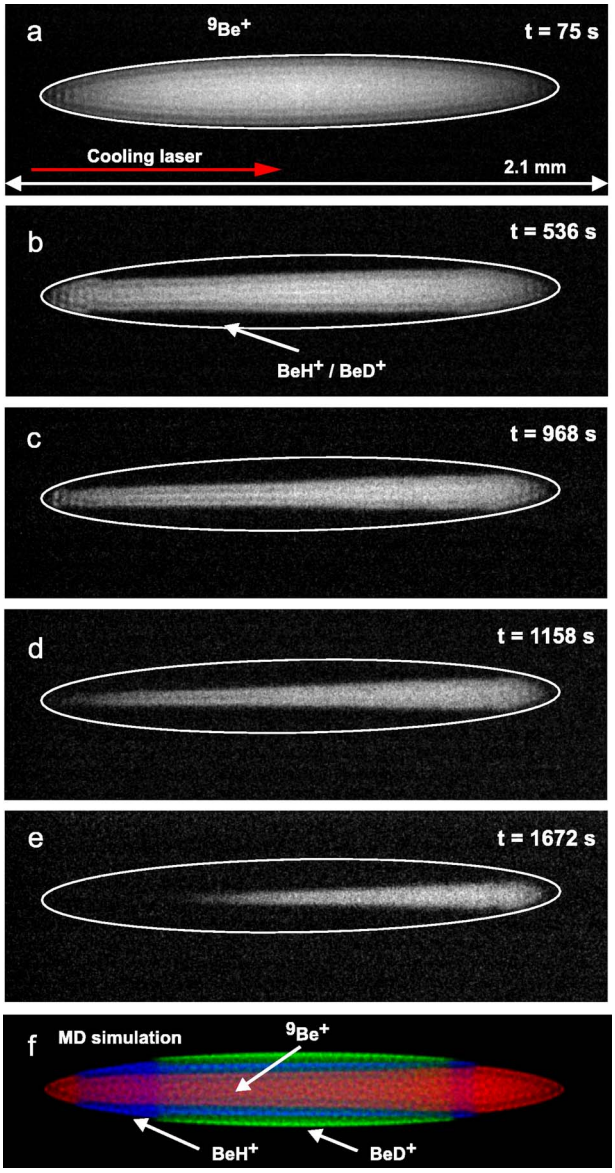


FIG. 1. (Color online) CCD camera image of an initially pure large $Be^+$ ion crystal following exposure to HD gas, leading to the formation of ultracold $BeH^+$ and $BeD^+$ molecular ions via chemical reactions. The ellipse is a fit to the initial $Be^+$ crystal boundary. The molecular ions formed are located in the dark area enclosed. The ion numbers determined using MD simulations are: (a) 2100 $Be^+$, (b) 900 $Be^+$, 1200 $BeH^+$ and $BeD^+$ (in approx. equal amounts), (c) 500 $Be^+$, 1600 $BeH^+$ and $BeD^+$, (d) 310 $Be^+$, 1700 $BeH^+$ and $BeD^+$, (e) 150 $Be^+$, 1700 $BeH^+$ and $BeD^+$. (f) MD simulation of the crystal in (b), with 900 $Be^+$ and 600 $BeH^+$ and $BeD^+$ ions, respectively, at approximately 15 mK.

During exposure to neutral hydrogen gases the observed $Be^+$ ion crystal changes its shape, as a consequence of the formation and sympathetic crystallization of $BeH^+$ and $BeD^+$, embedded in the outer regions of the crystal. For the example shown in Fig. 1, an initially pure $Be^+$ crystal (a) was exposed to neutral HD gas and its structural changes were observed as function of time, (b)–(e). A marked increase in

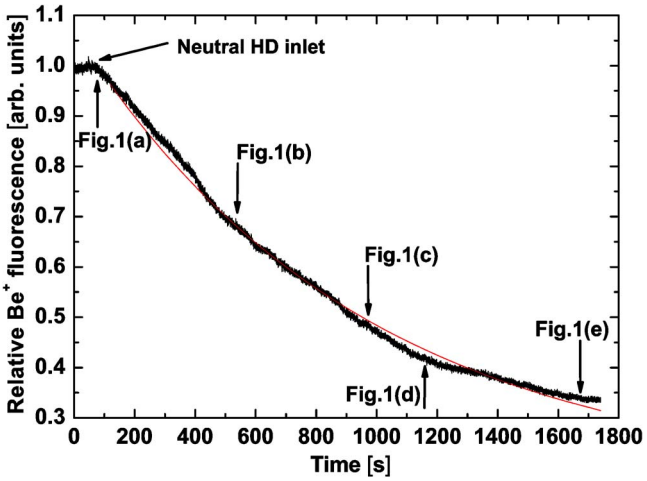


FIG. 2. (Color online) Decay of a $Be^+$ ion crystal containing initially ≈2100 $Be^+$ ions after exposure to HD gas. Relative population of the $^2P_{3/2}$ level of $Be^+$: 0.14. The line is an exponential fit to the data. CCD camera images in Fig. 1 were taken at the indicated times.

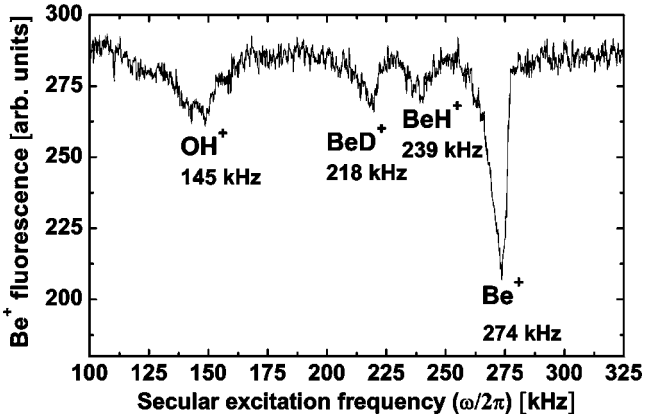


FIG. 3. Motional frequency spectrum for a laser-cooled $Be^+$ plasma after exposure to neutral HD gas. The spectrum was taken with the mixed-species plasma in the cloud state. The measured secular frequencies agree well with the calculated single-particle secular frequencies.

the temperature of the $Be^+$ ensemble is observed. The $Be^+$ ion temperature is determined by a balance between the (laser) cooling rate and the heating rate. The heating rate has a contribution arising from the SC particles, which are heated by collisions with background gas and by rf heating in the trap due to ion-ion interactions. This contribution becomes more important as the number of SC ions increases and the number of LC ions decreases. The translational temperature of the initially pure $Be^+$ crystal of ≈10 mK (a) increased to ≈40 mK (e) during the reaction. Thus, the increased $Be^+$ ion temperature directly reflects the formation of ultracold molecular ions. Also, due to the reduction of sympathetic cooling power a part of the molecular ions produced is lost from the trap. The observed lack of symmetry of the mixed-species crystal shape with respect to the *x*-*y* plane is due to the presence of the SC particles combined with the laser light pressure force that is exerted only on the LC particles. As the chemical reactions proceed in time, the total fluorescence rate of the $Be^+$ ions decreases, see Fig. 2.

A typical secular frequency spectrum obtained for the reaction is shown in Fig. 3. The spectrum was taken several minutes after exposing a $Be^+$ ion crystal to neutral HD with the ion ensemble in the cloud state. In this state the interpretation of the mass spectrum is much simpler than in the crystal state due to the reduction of interspecies coupling effects [22]. Ionic species with small differences of their mass-to-charge ratio can then be resolved more easily, e.g., $Be^+$, $BeH^+$, and $BeD^+$.

The spectrum shows three pronounced features stemming from LC ($Be^+$, 275 kHz) and SC particles ($BeH^+$, 248 kHz; $BeD^+$, 225 kHz). The calculated single-particle secular frequencies for the above species are 275 kHz ($Be^+$), 248 kHz ($BeH^+$), and 225 kHz ($BeD^+$), in good agreement with the experimental observation. An additional feature is obtained at 145 kHz, stemming from sympathetically cooled $OH^+$ ions. $OH^+$ impurity ions are formed during $Be^+$ loading by electron-impact ionization of residual background $H_2O$ molecules present in the vacuum chamber. Usually, prior to each measurement, such impurity ions are removed from the crystal, as described above.

The reaction of individual LC $Be^+$ ions with neutral molecular hydrogen gases can be observed as a function of time by either sudden jumps in the detected spontaneous emission fluorescence signal or by the disappearance of individual ions. This requires small ion ensembles. In Fig. 4(a) the fluorescence decay curve of a small $Be^+$ ion crystal (160 $Be^+$ ions) exposed to neutral HD gas is shown together with corresponding CCD images. The chemical reactions can indeed be followed with single particle resolution. Once the ion number has decreased so far that the $Be^+$ ions are arranged in a string discrete jumps in the fluorescence decay curve can be identified, which are correlated with the production of single molecular ions, see Fig. 4(b).

The reaction $H_3^+ + O_2 \rightarrow HO_2^+ + H_2$ was studied in a similar way. $H_3^+$ molecular ions are produced in a two-step process. First, $H_2^+$ ions are formed via electron impact ionization of neutral $H_2$ gas and embedded in the $Be^+$ ion crystal. Subsequently, the ions produced react with neutral $H_2$ via $H_2^+ + H_2 \rightarrow H_3^+ + H$ [10]. Figures 5(a)–5(c) show an initial two species ion crystal containing $Be^+$ and $H_3^+$ (a), which is exposed to neutral $O_2$ gas. As a consequence of the chemical reactions ultracold $HO_2^+$ ions are formed and the $H_3^+$ dark core disappears, Figs. 5(b) and 5(c). MD simulations of the mixed-species ion crystals in Figs. 5(a) and 5(c) are presented in Figs. 5(d) and 5(e), respectively. Since the structure of the simulated crystal is quite sensitive to the mass-to-charge ratio and the number of ions of each species, see also [21], the reproduction of the observed crystal shape by the simulations represents a first (indirect) identification of the produced species. The comparison between experimental images and simulated crystal structures allows for an estimate of the conversion efficiency of initial $H_3^+$ ions into $HO_2^+$ during exposure to molecular oxygen. We find that essentially all $H_3^+$ ions react with neutral $O_2$ and that the reaction products formed, $HO_2^+$, remain trapped and embedded in an outer "belt."

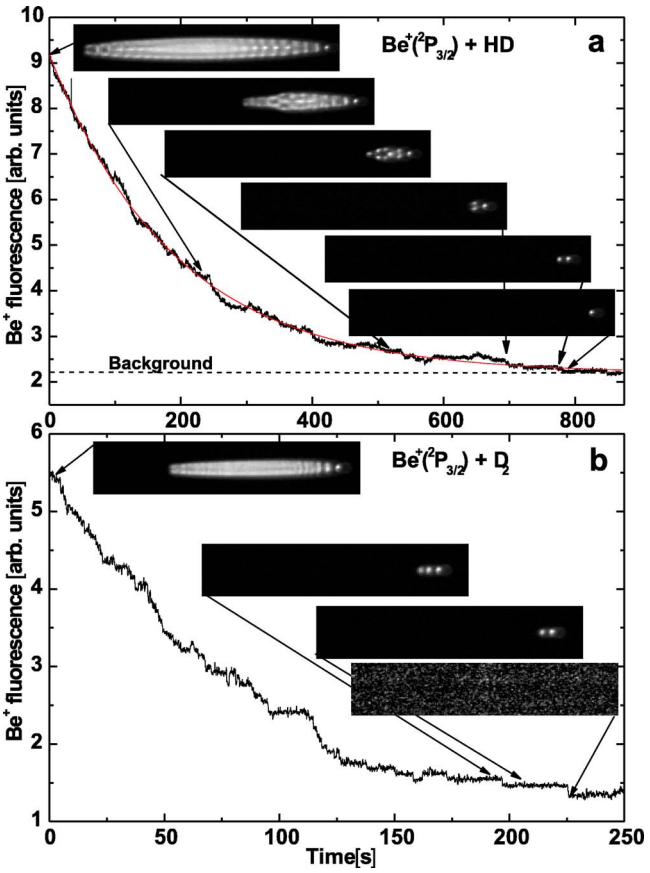


FIG. 4. (Color online) Decay of a small $Be^+$ ion crystal initially containing ≈160 $Be^+$ at ≈5 mK after exposure to neutral HD gas. Relative population of the $^2P_{3/2}$ level of $Be^+$: 0.42. The line is an exponential fit to the data. (b) Decay of a crystal containing initially ≈45 $Be^+$ ions after exposure to $D_2$ gas. Towards the end of the record two discrete steps in the fluorescence due to the formation of a single $BeD^+$ ion, and of two $BeD^+$ ions, respectively, are observed. Relative population of the $^2P_{3/2}$ level of $Be^+$: 0.23.

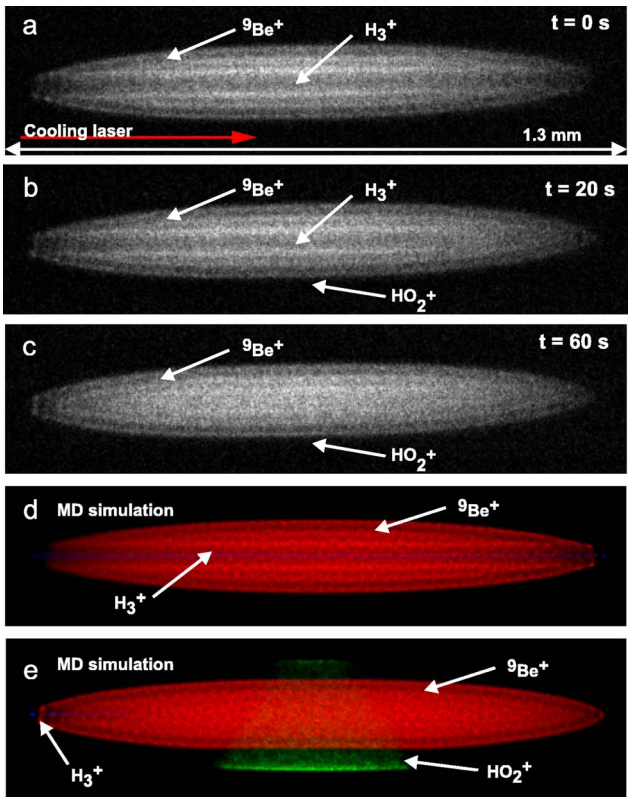


FIG. 5. (Color online) (a)–(c) Images of an initially pure $Be^+$-$H_3^+$ ion crystal exposed to neutral $O_2$ at $3\times10^{-10}$ mbar. $H_3^+$ disappears from the crystal core as $HO_2^+$ molecules are formed and embedded in the outer region of the crystal. Their presence leads to a slight flattening of the upper and lower edge of the crystal in image (c). (d) MD simulation of the crystal in (a) containing 1275 $Be^+$ and 80 $H_3^+$ ions at ≈30 mK. (e) MD simulation of the crystal in (c) containing 1275 $Be^+$, 3 $H_3^+$, and 75 $HO_2^+$ ions at ≈30 mK.

Direct identification is illustrated in Figs. 6(a)–6(c) where the secular excitation spectra for the mixed species ion crystal in Figs. 5(a) and 5(c) are shown. The secular excitation spectra in Figs. 6(a) and 6(b) were taken after loading of the $H_3^+$ into the crystal. Whereas the low mass secular scan (a) evidences the presence of $H_3^+$ ions, particles with mass-to-charge ratio larger than $Be^+$ are absent (b). The rise of the $Be^+$ fluorescence in Fig. 6(b) towards the end of the scan is due to excitation of the nearby (at 280 kHz) radial $Be^+$ trap mode by the large excitation amplitude used. The appearance of $HO_2^+$ ions is observed after the exposure of the $Be^+$-$H_3^+$ ion crystal to neutral molecular oxygen, Fig. 6(b). According to the simulations the translational temperature of LC and SC particles is at ≈30 mK.

### C. Analysis

The number of particles as a function of reaction time was determined by performing MD simulations corresponding to various time instants. The temperature of the SC particles was also determined by the simulations, see [9,21]. The size of the imaged ion fluorescence spots is compared to the simulation results leading to an estimate for the temperature of the LC particles. Due to the Coulomb interaction between LC and SC ions the temperature of the SC ions also influences the temperature of the LC ions, and thus, the ion structures observed. Therefore, from the temperature of the LC particles we can set upper limits for the SC temperature. The observed ion shell structures are consistent with a SC temperature well below 15 mK. The simulations show that, if the temperature of the SC particles embedded in the outer region of the crystal is kept at ⩾50 mK, the $Be^+$ ion shells close to the molecular ions would appear much more blurred, in contrast to observation. Tighter upper limits can be set by considering the balance between heating and cooling rates relevant for the SC particles. Typically, for the crystals studied here, the temperature of the SC ions is within a factor of 2 of the LC temperature.

While secular excitation mass spectroscopy is suitable to reliably detect LC and SC ion species in the produced crystals, it is not easily made quantitative, and thus, reaction rates cannot be determined by the size of the spectral features. In general, mass spectroscopy in large and mixed-species ion crystals is complicated by coupling between the trap oscillation modes of different species, induced by Coulomb inter-

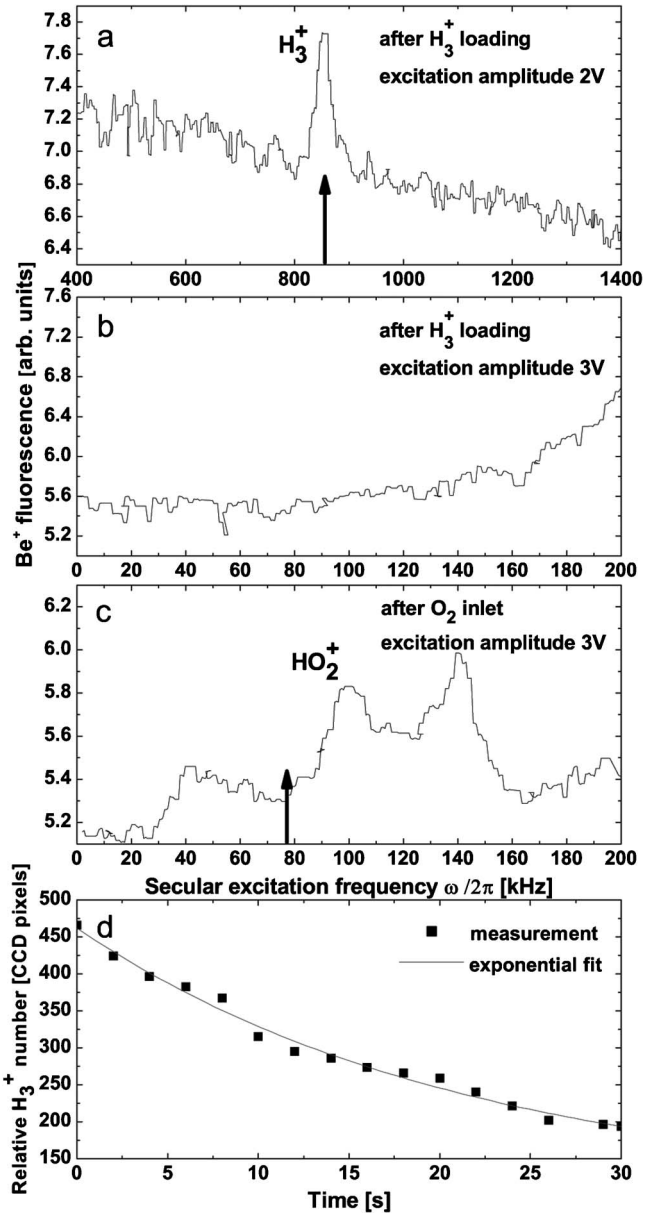


FIG. 6. Secular frequency spectrum of the crystal shown in Fig. 5 after loading of $H_3^+$ ions. (a) Low-mass range and (b) high-mass range. (c) shows the spectrum of the crystal after exposure to $O_2$ molecules, Fig. 5(c). The feature at around 100 kHz originates from the $HO_2^+$ ions formed. The calculated single-particle secular frequencies for $H_3^+$ and $HO_2^+$ are indicated by arrows. Due to the Coulomb coupling between the particles the measured frequency is shifted toward larger values [21,22], as confirmed by the simulations. The feature at around 50 kHz is due to the excitation of the axial $Be^+$ oscillation mode, see [26]. The feature at 140 kHz originates from a composite $HO_2^+$-$Be^+$ mode. (d) Relative $H_3^+$ number for the reaction $H_3^+ + O_2 \rightarrow HO_2^+ + H_2$ for the crystal shown in Figs. 5(a)–5(c). The $H_3^+$ number was derived by analyzing the decrease of the dark crystal core containing $H_3^+$ ions after exposure to neutral $O_2$.

action [22–25]. Instead, fluorescence detection or direct "ion counting" using CCD images allows for precise measurements of reaction rates with single particle sensitivity. In this

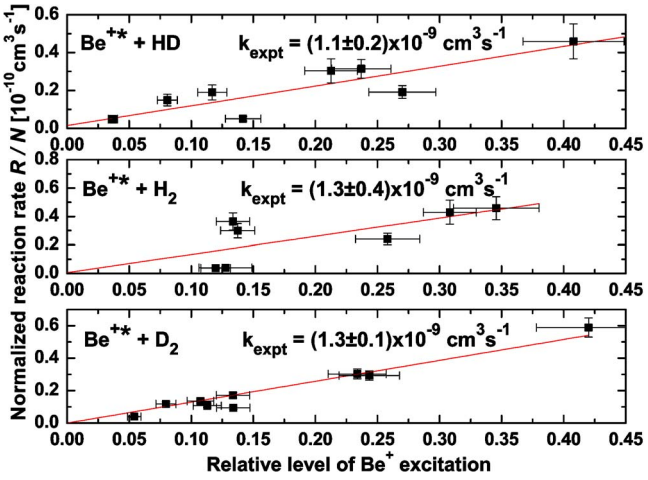


FIG. 7. (Color online) Normalized reaction rates per particle for the chemical reactions of excited $Be^+$ with $H_2$ (a), HD (b), and $D_2$ (c) as a function of the level of excitation. The reaction rates $R$ were obtained from least-squares exponential fits of the $Be^+$ fluorescence rate versus time. The lines are linear fits to the data. The reaction coefficient $k_{expt}$ is obtained from the slope of the fits.

work, fluorescence detection is used for crystals with large numbers of $Be^+$ ions, enabling a good signal to noise ratio, whereas for small and medium sized crystals (with ion numbers from a few ions up to several hundred) ion counting is more suitable. The latter has the potential for precise reaction rate measurements with good signal to noise ratio and almost no background events.

Reaction rates for the chemical reactions observed are obtained by least-squares fitting the fluorescence decay or particle loss curves versus time. Reactions were measured as a function of the excitation level and the partial pressure of the neutral gases. The corresponding Langevin coefficients are deduced by normalizing the reaction coefficients to the neutral reactant particle number density and the excitation level.

For the reactions between ultracold $H_3^+$ ions and neutral $O_2$ gas the reaction coefficient is deduced from least-squares fitting to the hydrogen ion loss rate. The latter is obtained from the CCD images by analyzing the decrease of the dark core as a function of time, see Fig. 6(d). The reaction coefficient is then determined in the same way as above, except that the excitation level of the $Be^+$ ions is irrelevant here.

## IV. RESULTS AND DISCUSSION

Figure 7 shows the reaction rates $R$ for the chemical reactions described in Eq. (1), normalized by the particle number density $N_n$ for $H_2$ (a), HD (b), and $D_2$ (c) as a function of the level of excitation. These reaction rates were obtained from least-squares fitting of the logarithm of the $Be^+$ fluorescence curve versus time. The main uncertainties for the measurements presented are the uncertainty of neutral reactant number density $N_n$ and the uncertainty associated with the determination of the level of $Be^+$ excitation, both included in Fig. 7 for each data point. For the measurements shown, the errors of $N_n$ are below 10%. Systematic errors stemming from $Be^+$ losses upon reaction with residual hydrogen gas are

TABLE I. Experimental and Langevin reaction coefficients and experimental uncertainties $\Delta k_{\text{expt}}$. The values for the electric dipole polarizabilities used in Eq. (8) to obtain $k_L$ are (in units of $10^{-24}$ cm$^3$): 0.8042 ($H_2$), 0.7976 (HD), 0.7921 ($D_2$), and 1.5812 ($O_2$) [27].

| Reaction | $k_{\text{expt}}$ (cm$^3$/s) | $\Delta k_{\text{expt}}$ (cm$^3$/s) | $k_L$ (cm$^3$/s) |
|---|---|---|---|
| $Be^+ + H_2$ | $1.3\times10^{-9}$ | $0.4\times10^{-9}$ | $1.6\times10^{-9}$ |
| $Be^+ + HD$ | $1.1\times10^{-9}$ | $0.2\times10^{-9}$ | $1.4\times10^{-9}$ |
| $Be^+ + D_2$ | $1.3\times10^{-9}$ | $0.1\times10^{-9}$ | $1.3\times10^{-9}$ |
| $H_3^+ + O_2$ | $1.1\times10^{-9}$ | $0.4\times10^{-9}$ | $1.7\times10^{-9}$ |

negligible for our experimental conditions. The slopes of the fitted lines in Fig. 7 give the reaction coefficients, and are summarized in Table I. The relative reaction rates have somewhat smaller uncertainties than the absolute reaction rates due to uncertainty in the absolute calibration of the ion gauge used. The reaction coefficients for the reactions studied are comparable to the Langevin values [Eq. (8)], which are all in the same range.

In Fig. 8 the measured reaction rates for the chemical reaction $H_3^+ + O_2 \rightarrow HO_2^+ + H_2$ are shown. The reaction rates were deduced from the CCD camera pictures by analyzing the $H_3^+$ loss rate as the rate of dark crystal core size reduction. From the analysis of the CCD camera images we obtain the particle loss rate in pixels/s which is translated into particles/s via the MD simulations. This can be done with an accuracy at the single ion level. The main uncertainties in this measurement come from estimating the particle number density $N_n$ ($<10\%$). Systematic errors due to reactions between $H_3^+$ and background hydrogen gas are below $(7.5\pm)\times10^{-3}$/s. The rate coefficient is obtained from the linear fit to the experimental data, and is listed in Table I.

The measured rate coefficients for all reactions studied are in reasonable agreement with the values calculated from Langevin theory. The uncertainties shown in Table I can be attributed to calibration errors of the ion gauge used, which is relevant here because of the low reactant pressures used, and the uncertainty in the laser excitation rate.

A reliable estimate of the number of SC ions of various species within a Coulomb crystal from the secular excitation spectrum is not (yet) available. Possibly, structural details might be used to determine ion numbers of SC species

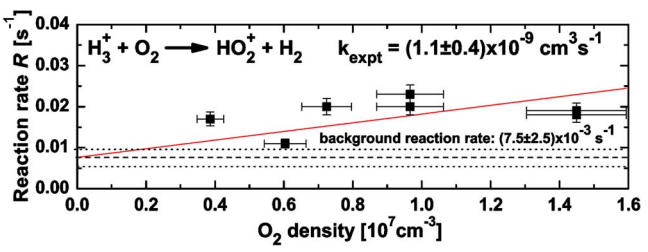


FIG. 8. (Color online) Reaction rates for the reaction $H_3^+ + O_2 \rightarrow HO_2^+ + H_2$ versus $O_2$ particle number density $N_n$. The line is a linear fit to the experimental data. The reaction coefficient $k_{\text{expt}}$ is obtained from the slope of the fit. The main uncertainties come from the measured particle number densities $N_n$.

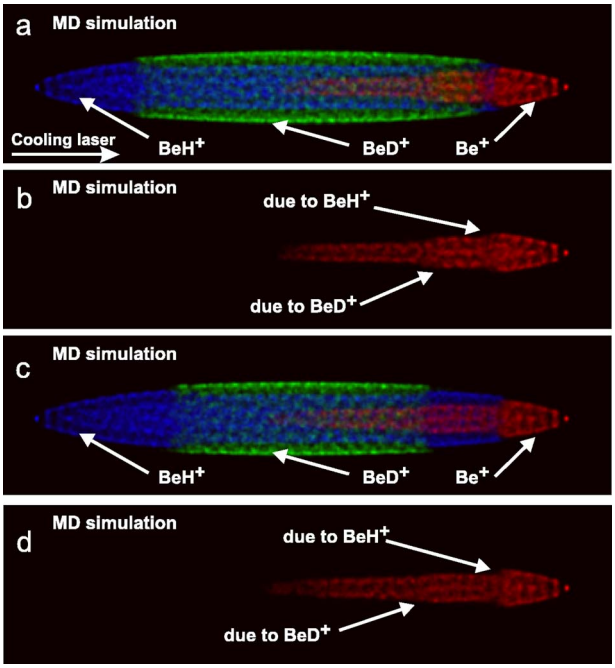


FIG. 9. (Color online) (a) Simulated $Be^+$ ion crystal containing 100 $Be^+$, 300 $BeH^+$, and 300 $BeD^+$ ions at $\approx$10 mK. (b) Same as in (a), only LC particles are displayed. $Be^+$ ions are shifted to the right by light pressure forces. The distortions in the outer $Be^+$ shell, induced by SC particles, are marked. (c, d) Simulated $Be^+$ ion crystal containing 100 $Be^+$, 400 $BeH^+$, and 200 $BeD^+$ ions at $\approx$10 mK. The difference between the distortions in (b) and (d) might allow for a species-selective estimate of SC ion numbers.

heavier than the LC ions. We find that in medium-size crystals each SC species present in the outer layers of the crystal has a detectable effect on the shape of the $Be^+$ ion crystal boundary. As an example, in Fig. 9 we compare two simulated trispecies $Be^+$ ion crystals with a different $BeH^+/BeD^+$ number ratio. The $Be^+$ ions are shifted relative to the SC particles by light pressure forces included in the simulations. The presence of the two SC species, $BeH^+$ and $BeD^+$, induces two "ridges" in the $Be^+$ structure because of the different effective trap potential for the two SC species. The position of the ridges and the details of the $Be^+$ ion crystal structure are functions of the individual SC ion numbers. Thus, a systematic experimental study of the LC crystal structure as a function of the laser light pressure force and comparison with MD simulations might allow for a species-selective estimate of SC ion numbers.

## V. SUMMARY AND OUTLOOK

The results presented in this work represent a novel example of the use of laser-manipulated particles for chemical reaction studies. Using the method described chemical reactions between ultracold ensembles of selectable initial ion number from a few up to several thousand particles can be observed as a function of time.

We have observed chemical reactions between laser-cooled, excited $Be^+$ ions and neutral $H_2$, HD, and $D_2$ molecules. Measurements of reaction rates from the study of

CCD images and laser-cooling fluorescence levels are in agreement with the Langevin ion-neutral reaction model. Furthermore, we have studied chemical reactions between ultracold triatomic hydrogen molecules, $H_3^+$, sympathetically cooled by laser-cooled $Be^+$, and molecular oxygen. In this reaction, MD simulations were an important tool, allowing us to determine the number of ions of one of the reaction partners and to deduce upper limits for the translational temperature of the particles. Thus we have shown that is is possible to study certain chemical reactions even in the case when neither one of the reactants nor the products can be directly detected.

Ultracold laser-cooled and sympathetically cooled ions in traps open up the possibility for high-precision measurements on well-localized systems and are interesting targets for the study of chemical reactions of atoms and molecules interesting to astrophysics and chemistry. The method presented has the potential to observe chemical reactions at the level of individual molecules in a cold environment.

Returning to the perspective outlined in the Introduction, the study of chemical reactions between state-prepared ultracold atomic/molecular ions and state-prepared ultracold neutral molecules, we point out that the preparation of translationally ultracold ensembles are by now established techniques both on the ion side and on the neutral side. Translationally ultracold neutral molecules can be generated by a number of techniques, such as, photoassociation, Feshbach resonances in optical traps [28,29], Stark deceleration and subsequent trapping by time-varying electric fields [30], filtering out of a thermal ensemble and storage in a electrostatic quadrupole trap [31], or cryogenic buffer gas cooling possibly followed by magnetic trapping [32]. The challenging next tasks are the combination of these and molecular ion state preparation techniques into a single apparatus.

Another interesting perspective is the generation and use of mixed-species ion strings with deterministic order. Ordering might be achieved starting with an initially pure $Be^+$ ion string, switching off the laser cooling, and subsequently illuminating only individual $Be^+$ ions by the same laser, tightly focused on the particular ion. Injection of neutral molecular hydrogen would then lead to the formation of a molecular ion at a desired position in the string. Such two-species linear ion chains could be used to implement new cooling schemes for the vibrational motion of extended linear ion chains or to prepare molecular quantum states for quantum information processing (see [33] and references therein). Furthermore, quantum logic techniques could be used to study the vibrational trap mode spectrum of mixed-species ion chains containing sympathetically cooled particles [34].

## ACKNOWLEDGMENTS

The authors thank U. Fröhlich for contribution to the initial phase of this work, the Deutsche Forschungsgemeinschaft (DFG) and the EU network HPRN-CT-2002-00290 "Ultracold Molecules" for financial support. P.B. was supported by the EU network and the Alexander-von-Humboldt Stiftung.

[1] D. Gerlich, *Advances in Chemical Physics: State-Selected and State-to-State Ion Molecule Reaction Dynamics* (Wiley, New York, 1992), Vol. LXXXII.
[2] D. Gerlich, E. Herbst, and E. Roueff, Planet. Space Sci. **50**, 1275 (2002); O. Asvany, I. Savic, S. Schlemmer, and D. Gerlich, Chem. Phys. **298**, 97 (2004).
[3] E. Herbst, Philos. Trans. R. Soc. London, Ser. A **358**, 2523 (2000).
[4] T. Glenewinkel-Meyer and D. Gerlich, Isr. J. Chem. **37**, 343 (1997).
[5] See, e.g., Philos. Trans. R. Soc. London, Ser. A **358**, Nr. 1774 (2000); J. Mikosch *et al.*, J. Chem. Phys. **121**, 11030 (2004).
[6] A. Bertelsen, I. S. Vogelius, S. Jørgensen, R. Kosloff, and M. Drewsen, Eur. Phys. J. D **31**, 403 (2004).
[7] D. J. Larson, J. C. Bergquist, J. J. Bollinger, W. M. Itano, and D.. J. Wineland, Phys. Rev. Lett. **57**, 70 (1986).
[8] P. Bowe, L. Hornekaer, C. Brodersen, M. Drewsen, J. S. Hangst, and J. P. Schiffer, Phys. Rev. Lett. **82**, 2071 (1999).
[9] B. Roth, U. Fröhlich, and S. Schiller, Phys. Rev. Lett. **94**(5), 053001 (2005).
[10] P. Blythe, B. Roth, U. Fröhlich, H. Wenz, and S. Schiller, Phys. Rev. Lett. **95**, 183002 (2005).
[11] L. Hornekær, Ph.D. thesis, Aarhus University (2000).
[12] M. Drewsen, L. Hornekaer, N. Kjaergaard, K. Molhave, A. M. Tommensen, Z. Videnseni, A. Mortensen, and F. Jensen, in *Non-Neutral Plasma Physics Conference IV*, AIP Conf. Proc. No. 606 (AIP, New York, 2002), p. 135.
[13] T. Baba and I. Waki, J. Chem. Phys. **116**, 1858 (2002).
[14] M. Raimondi and J. Gerratt, J. Chem. Phys. **79**(9), 4339 (1983).
[15] H. Schnitzler, U. Fröhlich, T. K. W. Boley, A. E. M. Clemen, J. Mlynek, A. Peters, and S. Schiller, Appl. Opt. **41**, 7000 (2002).
[16] J. B. Hasted, *Physics of Atomic Collisions* (Butterworths, London, 1964).
[17] D. A. Church, J. Mod. Opt. **39**(2), 423 (1992).
[18] J. K. Kim, L. P. Theard, and W. T. Huntress Jr., Chem. Phys. Lett. **32**, 610 (1975); A. E. Roche, M. M. Sutton, D. K. Rohme, and H. I. Schiff, J. Chem. Phys. **55**, 5840 (1971).
[19] N. G. Adams and D. Smith, Chem. Phys. Lett. **105**, 604 (1984).
[20] M. G. Raizen, J. M. Gilligan, J. C. Berquist, W. M. Itano, and D. J. Wineland, Phys. Rev. A **45**, 6493 (1992).
[21] B. Roth, A. Ostendorf, H. Wenz, and S. Schiller, J. Phys. B **38**, 3673 (2005).
[22] B. Roth, P. Blythe, and S. Schiller (unpublished).
[23] T. Baba and I. Waki, J. Appl. Phys. **89**, 4592 (2001).
[24] T. Baba and I. Waki, Jpn. J. Appl. Phys., Part 1 **92**, 4109 (2002).
[25] T. Hasegawa and T. Shimizu, Phys. Rev. A **66**, 063404 (2002).
[26] U. Fröhlich, B. Roth, and S. Schiller, Phys. Plasmas **12**, 073506 (2005).

[27] *CRC Handbook of Chemistry and Physics* (Taylor and Francis, New York, 2002), p. 82.
[28] N. Vanhaecke, W. de Souza Melo, B. Laburthe Tolra, D. Comparat, and P. Pillet, Phys. Rev. Lett. **89**, 063001 (2005).
[29] C. Regal, C. Ticknor, J. L. Bohn, and D. Jin, Nature (London) **424**, 47 (2003).
[30] H. L. Bethlem, F. M. H. Crompvoets, R. T. Jongma, S. Y. T. van de Meerakker, and G. Meijer, Phys. Rev. A **65**, 053416 (2002); M. R. Tarbutt *et al.*, Phys. Rev. Lett. **92**, 173002 (2004).
[31] T. Junglen, T. Rieger, S. A. Rangwala, P. W. H. Pinske, and G. Rempe, Phys. Rev. Lett. **92**, 223001 (2004).
[32] J. D. Weinstein *et al.*, Nature (London) **395**, 395 (1998); **395**, 148 (1998).
[33] C. Wunderlich, G. Morigi, and D. Reiss, Phys. Rev. A **72**, 023421 (2005).
[34] P. O. Schmidt *et al.*, Science **309**, 749 (2005).

# Sympathetic Cooling of Complex Molecular Ions to Millikelvin Temperatures

A. Ostendorf, C. B. Zhang, M. A. Wilson, D. Offenberg, B. Roth, and S. Schiller

*Institut für Experimentalphysik, Heinrich-Heine-Universität Düsseldorf, 40225 Düsseldorf, Germany*

(Received 14 July 2006; published 15 December 2006)

Gas-phase singly protonated organic molecules of mass 410 Da (Alexa Fluor 350) have been cooled from ambient temperature to the hundred millikelvin range by Coulomb interaction with laser-cooled barium ions. The molecules were generated by an electrospray ionization source, transferred to and stored in a radio-frequency trap together with the atomic ions. Observations are well described by molecular dynamics simulations, which are used to determine the spatial distribution and thermal energy of the molecules. In one example, an ensemble of 830 laser-cooled $^{138}Ba^{+}$ ions cooled 200 molecular ions to less than 115 mK. The demonstrated technique should allow a large variety of protonated molecules to be sympathetically cooled, including molecules of much higher mass, such as proteins.

DOI: 10.1103/PhysRevLett.97.243005 PACS numbers: 33.80.Ps, 32.80.Lg, 42.50.Vk, 47.11.Mn

One of the current themes of quantum physics is the creation of cold ($<1$ K) molecules to study molecule-molecule, molecule-atom, and molecule-radiation interactions under these novel low temperature conditions. The recent progress in this field has seen the development of methods for cooling and simultaneously confining molecules using external fields. So far, the production of cold molecules has been limited to few-atom molecules. Neutral di-, tri-, and tetra-atomic molecules can be produced by atom-to-molecule conversion methods in ultracold atomic gases [1]. Cold magnetic few-atom molecules have been produced by buffer gas cooling in a magnetic trap [2]; slow molecules with electric dipole moments have been produced by Stark deceleration [3] and by cold particle selection, and trapped in electric traps [4]. Molecules can be implanted into superfluid droplets of $^{3}$He and $^{4}$He, and acquiring the droplet temperature ($T \approx 0.38$ K) [5]. Sympathetic cooling [6,7] has been used to cool charged diatomic and triatomic molecules to tens of mK by Coulomb interaction with laser-cooled atomic ions in radio-frequency ion traps [8–10]. This approach has recently enabled high-resolution ro-vibrational spectroscopy of molecular ions at sub-Kelvin temperature [11].

There is need for methods to permit a similar control over complex, i.e., massive, molecules. Here we demonstrate a significant extension of the mass range of molecules that can be prepared at low temperatures in the gas phase, demonstrating, for the first time to our knowledge, cooling of stored polyatomic molecules (containing 42 atoms in this case) to a temperature range significantly below that reachable with conventional cryogenic techniques (buffer gas cooling, typically at $\sim$10 K) [12], or in previous sympathetic cooling ($\sim$ 14 K) [13]. Our method furthermore allows strong spatial localization of the molecules. The source type employed, electrospray ionization [14], is commonly used for mass spectroscopy of macromolecules and can be used to produce a vast variety of protonated molecular ions in various charge states and, in particular, molecular ions of biological interest (e.g., proteins). We expect that the cooling method demonstrated here can be extended to such large molecules as well, leading to new approaches for studies of biomolecular systems. Since the cooling method used is independent of the internal structure of the ions it is not limited to molecules, but could also be used with atomic or other clusters.

The apparatus consists of an electrospray molecular ion source (ESI), an octopole ion guide transporting the ions into a linear rf trap, a barium ion source, an ion counter, a fluorescence detector and an intensified CCD camera for observing the barium ions, and a laser system for Doppler cooling. Except for the last three, these parts are enclosed in a vacuum chamber, in which the pressure drops from atmospheric pressure at the ion source to $5 \times 10^{-10}$ mbar in the trap region. Molecular compounds are dissolved in a solution which is injected into the ESI source. There, charged droplets of the solvent are ejected by a needle and undergo rapid evaporation into smaller and smaller droplets until a final Coulomb explosion causes a significant fraction of single molecules to be created with varying numbers of protons attached. Molecules of a desired charge-to-mass ratio are then selected using a quadrupole mass filter (resolution 1 Da). The rf octopole ion guide channels the molecules to the trap. It is 1.9 m long and collinear with the trap axis.

The linear quadrupole trap produces an effective trap potential with radial dependence $(QV_0/\Omega r_0)^2(r/r_0)^2/4m$, where $Q$ is the ion charge, $m$ is the mass, $\Omega = 2\pi \times 2.5$ MHz is the trap rf frequency, $V_0/2 = 200$ V is the rf amplitude applied to each electrode, and $r$ is the radial distance from the trap ($z$) axis ($r_0 = 4.4$ mm is the axis-to-electrode-surface distance). Thus, heavier ions experience a shallower trapping potential. In this potential, the ions can oscillate, with a mass-to-charge-ratio-dependent characteristic frequency. This secular oscillation can be excited by applying an ac voltage to the trap electrodes.

The loading and laser-cooling of the barium ions is described in [10]. Cold barium ion ensembles are routinely produced by Doppler cooling. The final steady-state ki-

 

netic energy per particle is so low that the interparticle Coulomb repulsion energy dominates, leading to structured ensembles [15,16]. They vary in shape from linear strings to large "Coulomb crystals" composed of spheroidal shells, depending on the total ion number and the chosen trap parameters. Crystals as cold as 5 mK have been observed and typical ion-ion distances are around 25 $\mu$m. At the lowest temperatures discrete "sites" in the crystals become apparent.

We have used the molecular compound Alexa Fluor 350 ($C_{16}H_{14}N_2O_9S$) (herein denoted by AF), since its peak absorption wavelength around 350 nm makes it stable against photodissociation by the 493 and 650 nm cooling lasers [17]. The compound is dissolved in a 50:50 solution of methanol and water at a concentration of 250 pmol/ml. Formic acid is added at 1.25% concentration to protonate the AF molecules. Singly protonated $AF^+$ ions were then selected using the mass filter, as higher charge states were less abundant for this molecule.

The following procedure for producing sympathetically cooled ensembles of $AF^+$ molecules was developed. First, helium buffer gas was injected into the trap chamber via a leak valve to a pressure of $1 \times 10^{-4}$ mbar and $AF^+$ was loaded into the trap for 6 s. The room-temperature buffer gas serves to efficiently remove the high kinetic energy of the incoming molecular ions and cool them to $\sim$300 K. The buffer gas was then rapidly pumped away with the background pressure returning to the $10^{-10}$ mbar level a few minutes later. Next, a cloud of barium ions was loaded from the oven into the trap. Lighter impurity ions generated at the same time were ejected from the trap by applying a strong swept-frequency (125–500 kHz) secular excitation. In this way a cold crystal of barium ions was obtained, surrounded by heavier $AF^+$ ions [Fig. 1(a) and 1(b)]. The laser-cooled barium crystal acts to sympathetically cool the $AF^+$ ions and, conversely, the presence of the $AF^+$ slightly heats the barium ensemble. The sympathetically cooled barium isotopes lie on the right-hand side of the crystal due to light pressure forces pushing the $^{138}Ba^+$ ions to the left [Fig. 1(a)]. This particular two-species ensemble was trapped and cooled for 4 minutes, but this time could be as long as an hour.

The trap contents can be determined using a nondestructive and a destructive technique. Resonant secular excitation of a particular species leads to a drop in the $^{138}Ba^+$ fluorescence rate because the coolant ions are heated, either directly or through interspecies interactions. Radial resonances were observed at typically 102 kHz (for direct $Ba^+$ excitation) and at around 33 kHz (Fig. 2). The latter value implies a mass of the trapped molecules of 418 $\pm$ 11 amu, consistent with the value expected for $AF^+$. The excitation amplitude used heated the ensemble so strongly that the crystal melted. When scanning from high to low frequency this permitted the measurement of the single-particle secular frequency as opposed to the (shifted) frequency of a strongly coupled two-component crystal [18].

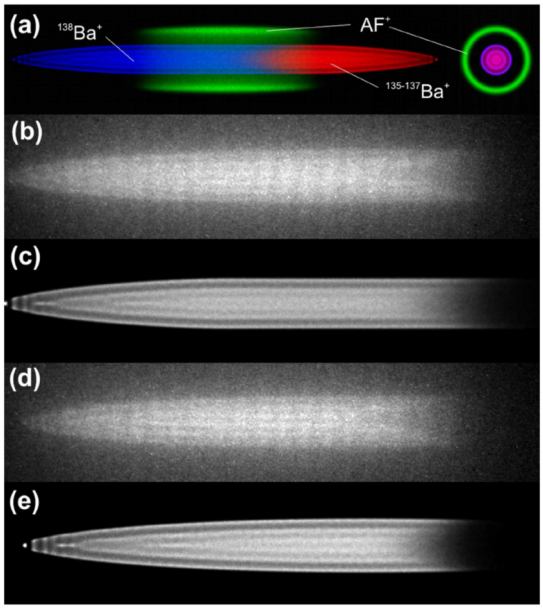


FIG. 1 (color online). (a) Simulated multispecies crystal (side- and cross-sectional views): laser-cooled $^{138}Ba^+$ ions (blue) at 25 mK, sympathetically cooled barium isotopes ($^{135-137}Ba^+$, red), $AF^+$ ions at 95 mK (green). Lasers propagate to the left. The $Ba^+$ ensemble is 1660 $\mu$m long and 130 $\mu$m in diameter. The $AF^+$ sheath is 300 $\mu$m in diameter. (b) CCD image of the barium crystal with $AF^+$ present; six distinct layers are visible corresponding to three coaxial spheroidal shells (camera exposure time: 0.5 s). (c) Simulation of the crystal in (b). (d) Barium crystal after ejection of all $AF^+$ ions. (e) Simulation of the crystal in (d), $T_{Ba,0} = 20$ mK.

The trapped ions are then extracted by reducing the rf amplitude $V_0/2$, which reduces the depth of the trap potential. Heavy and hot ions escape first. Upon leaving the trap, the ions are attracted by the cathode of the channel

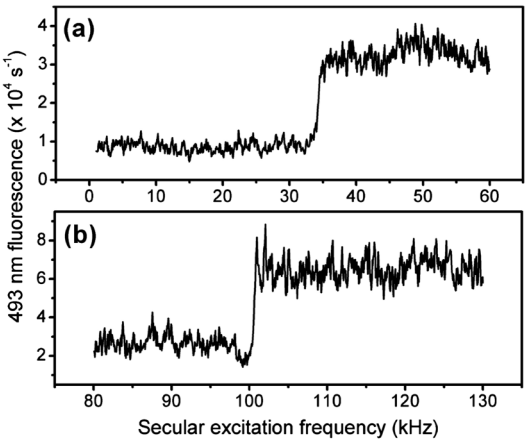


FIG. 2. Mass scan of a Coulomb crystal containing barium and $AF^+$ ions. Excitation of radial oscillations of (a) $AF^+$ ions and (b) $Ba^+$ ions. Calculated single-particle radial secular frequencies are 33.7 kHz and 102 kHz, respectively (respective axial frequencies are at 19.3 and 11.2 kHz).

electron multiplier (CEM). Reducing $V_0$ from 400 to 150 V removes only the heavy molecules, see Fig. 3. The remaining crystal consists of barium ions only [Fig. 1(d)]. By lowering $V_0$ further to 0 V this crystal is also ejected and the barium ions are detected, Fig. 3. The ion count peaks occur at clearly separate rf drive amplitudes, confirming that the mass of the trapped molecular ions was roughly 3 times that of barium (i.e., >400 Da). The ion signal sizes allow determination of the ratio of the number of barium ions to $AF^+$ ions (here 5.9:1), assuming equal detection efficiencies. The ion extraction spectrum also provides evidence that the heavier molecules are sympathetically cooled by the barium ions. Figure 3(a) (inset) shows the extraction of both ion species when laser cooling is not applied, i.e., the ensemble is at room temperature due to He buffer gas cooling, while Fig. 3(b) (inset) shows the mass spectrum of an ensemble with similar ion numbers when the barium ions have first been laser-cooled to a cold cloud. Both peaks are clearly narrower in the second case and indicate a narrowed energy distribution for the $Ba^+$ and the $AF^+$ ions. However, the ion extraction method is not accurate enough to discriminate between a crystal at 25 mK, for example, (Fig. 3), and a cold cloud at a few 100 mK [Fig. 3(b) (inset)].

The ability to image the atomic ion ensemble and the well-defined environment provided by the trap apparatus allows one to deduce further information about the two-species ensemble with the help of molecular dynamics simulations [9,10]. The simulations solve Newton's equation of motion including the effective (i.e., time-averaged), species-dependent trap quasipotential (here, micromotion is neglected), the mutual Coulomb repulsion force between all ions, a light pressure force along the $z$ direction, and a viscous damping force $F_D = -\beta v_z$ ($v_z$ is the $z$ component of the velocity) representing the laser-cooling process act-

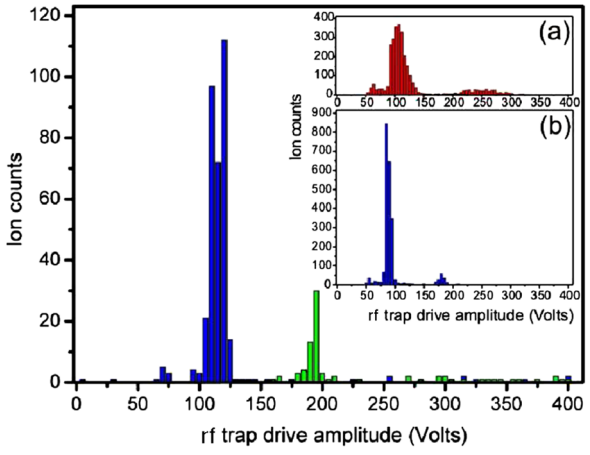


FIG. 3 (color online). Ions (of crystal in Fig. 1) detected on the CEM as the trap rf voltage is decreased. Heavier $AF^+$ ions are ejected first (right-hand peak); inset (a) extraction of a different sample of non-laser-cooled barium and $AF^+$ ions at ~300 K; inset (b) extraction of a laser-cooled cloud at a temperature of a few hundred mK for $Ba^+$ and $AF^+$ ions.

ing on the $^{138}Ba^+$ ions only. The interspecies Coulomb force is responsible for the sympathetic cooling. The damping coefficient $\beta$ is a (fixed) parameter in the simulations. Heating rates $H$ (equal for each ion of a given species) are added to the model, each representing the total of all heating effects, examples being: recoil upon photon emission, collisions with residual gas molecules, rf heating (an ion-ion interaction effect in the presence of micromotion [19]), and external electric noise. As a reasonable assumption, we set the heating rate for $^{138}Ba^+$ and for the isotopes equal in a given crystal. The heating is implemented by giving each particle a velocity kick proportional to the specified heating rate in a random direction at each time step. Time steps between 50 and 400 ns are used. The competition between the laser cooling and the specified heating rates leads to a steady-state thermal equilibrium. The secular temperature $T_i$ of each ion species subensemble is defined as $T_i = \frac{2}{3}\langle\langle E_i\rangle\rangle/k_B$, where $\langle\langle E_i\rangle\rangle$ is the time- and subensemble-averaged kinetic energy per ion. The ion velocities follow a Maxwell-Boltzmann distribution.

In addition to the secular (thermal) motion in the quasipotential, micromotion is always present. It occurs essentially in the $x$-$y$ plane and contributes to a "blurring" of the crystal images. We have checked the importance of micromotion by performing a simulation taking it fully into account, for the case of an ideal trap. We found that its effects are not dominant for our crystal dimensions and temperatures, i.e., only weakly affect the secular temperature and the image blurring. The micromotion peak-to-peak amplitude orthogonal to the viewing direction is $\approx 4$ $\mu$m for the radially outermost $Ba^+$, smaller than the resolution of the imaging system, $\approx 10$ $\mu$m. The corresponding average (radial) micromotion energy per $Ba^+$ ion is $\approx k_B(7.4\ \mathrm{K})$. For $AF^+$ the simulations give a micromotion peak-to-peak amplitude of $\approx 5$ $\mu$m, corresponding to an average micromotion energy of $\approx k_B(19\ \mathrm{K})$. Furthermore, excess micromotion due to trap imperfections could be present. While it was not possible to determine the excess micromotion amplitude, experimentally some trap imperfections were minimized by symmetrizing the crystals via dc offset potentials applied to individual trap electrodes ([10]). The micromotion simulation also indicates that for an ideal trap there is almost no "leakage" of micromotion into the $z$ direction. Hence, the $z$ axis would be the preferred laser propagation direction for spectroscopic studies.

By using the quasipotential MD simulations that ignore ion micromotion and its consequent blurring, and by ignoring the finite imaging resolution, the observed blurring of the CCD images is completely ascribed to thermal motion only. Thus, the secular temperature results given below represent upper limits.

Visual comparison of overall structure, structural details, and blurrings of CCD and simulated images permits fitting the number of ions and the heating rates, and thus obtaining the secular temperatures. First, the ion numbers can be

fitted by taking fixed, nominal values for the heating or cooling rates in the simulations, since these quantities are almost uncorrelated. The crystal with $AF^+$ present [Fig. 1(b) and 1(c)] contains $830 \pm 20$ $^{138}Ba^+$ ions, and $420 \pm 20$ other isotopes, and, inferred from the ion counter data, $200 \pm 20$ $AF^+$. After removal of $AF^+$ [Fig. 1(d) and 1(e)], the $^{138}Ba^+$ number was $770 \pm 20$, and the isotope number $410 \pm 20$, indicating a small loss of ions from the trap during the removal of the $AF^+$ ions.

In order to determine the $AF^+$ heating rate and temperature via the simulations, the damping coefficient $\beta$ must be determined directly. We consider the sum of the cooling or heating effects due to the green ($g$) and red ($r$) lasers, $\beta/m_{\mathrm{Ba}} = 2\sum_i(\hbar k_i^2/2m_{\mathrm{Ba}})\Gamma_i(\partial\rho_e/\partial\Delta_i)|_{\Delta_i}$. The barium mass $m_{\mathrm{Ba}}$, the wave numbers $k_i$, and partial decay rates $\Gamma_i$ for the green and red transitions are constants, while the change in excited state population $\rho_e$ with laser detunings $\Delta_i$ is calculated from 8-level Bloch equations using measured laser saturation parameters and detunings [20]. We find $\beta/m_{\mathrm{Ba}} \approx 760\ \mathrm{s}^{-1}$, where the dominant cooling effect comes from the green laser. At 20 mK secular temperature, this is equivalent to a cooling rate of $dT/dt = 2/3(\beta/m_{\mathrm{Ba}})T = 10\ \mathrm{K\,s}^{-1}$.

As nonoptimal laser polarizations with respect to the magnetic field and the presence of micromotion may lead to less efficient cooling, we consider a range of $\beta$ values. For an upper value $\beta/m_{\mathrm{Ba}} = 870\ \mathrm{s}^{-1}$ we determine the upper limit of the heating rates and the temperatures consistent with the CCD images, and similarly for a minimum value $\beta/m_{\mathrm{Ba}} = 440\ \mathrm{s}^{-1}$, we determine the associated lower limit for the heating rates and temperatures. First, the crystal without $AF^+$ is simulated, which yields the $Ba^+$ heating rate and temperature ($H_{\mathrm{Ba}^+}$, $T_{\mathrm{Ba}^+,0}$) upper and lower limits (7.6 K/s, 28 mK) and (2.3 K/s, 12 mK), respectively. These heating rates are next used as input to the simulation of the crystal with $AF^+$, since the crystal dimensions are similar. The results are $(H_{\mathrm{AF}^+}, T_{\mathrm{Ba}^+}, T_{\mathrm{AF}^+}) = (4.3\ \mathrm{K/s}, 35\ \mathrm{mK}, 115\ \mathrm{mK})$ and (2.5 K/s, 15 mK, 45 mK), respectively. Figure 1(a) shows the simulation result for an intermediate value $\beta/m_{\mathrm{Ba}} = 760\ \mathrm{s}^{-1}$, $H_{\mathrm{Ba}^+} = 6.6$ K/s, $H_{\mathrm{AF}^+} = 3.7$ K/s, giving $T_{\mathrm{AF}^+} = 95$ mK. Thus, we find an upper limit of the secular temperature $T_{\mathrm{AF}^+} = 115$ mK; this is a conservative estimate in view of the high $\beta$ value and the neglect of micromotion and of image resolution effects.

The temperature of the molecular ions also depends upon the total ion number. Increasing the number of ions, for example, changes the spatial distribution such that the molecular ions are situated at a larger average distance from the $Ba^+$ crystal, leading to a decrease of the sympathetic interaction strength and hence an increase in molecular temperature. Lower temperatures might therefore be possible using smaller $Ba^+$ numbers. The simulations also show that the inclusion of an additional ion species with an intermediate mass between that of $Ba^+$ and $AF^+$, which would be located radially between the two, would act as a "conducting layer," increasing the cooling efficiency and leading to a lower temperature for the heavy molecules. For example, 50 ions of mass 200 Da added to the above crystal would decrease the $AF^+$ secular temperature from 95 to 42 mK.

Our method could be extended to heavier molecular ions with multiple positive charges, which can be produced by the ESI source. For a given molecular mass, the higher the charge state, the closer the molecules are to the coolant ions and the more efficient the sympathetic cooling process is. If necessary, exposure of the molecular ions to the cooling lasers could be avoided, by focusing the beams on the atomic coolants only.

The long storage times in the near collisionless environment should permit studies of weak- or low-energy processes, e.g., triplet-singlet decay, photodissociation, vibrational dynamics, black-body-induced processes, and cold collisions. High-resolution spectroscopy could be performed using the method described in [11]. Many experiments could be enhanced by using internally cold or even quantum-state selected molecules, e.g., to allow strongly simplified spectra or quantum-state resolved collision studies. However, since the ion-ion interaction does not couple efficiently to the internal degrees of freedom of the molecules, the internal temperature is expected to be in thermal equilibrium with the vacuum chamber. Cooling the internal degrees of freedom should be possible via radiative cooling in a cryogenic environment.

This work was supported by the DFG program SP1116 and the EC network No. HPRN-CT-2002-00290. We thank H. Wenz and J. Koelemeij for discussions.

[1] J. Doyle *et al.*, Eur. Phys. J. D **31**, 149 (2004).
[2] J. D. Weinstein *et al.*, Nature (London) **395**, 148 (1998).
[3] F. M. H. Crompvoets *et al.*, Nature (London) **411**, 174 (2001).
[4] T. Rieger *et al.*, Phys. Rev. Lett. **95**, 173002 (2005).
[5] M. Wewer and F. Stienkemeier, Phys. Rev. B **67**, 125201 (2003).
[6] D. J. Larson *et al.*, Phys. Rev. Lett. **57**, 70 (1986).
[7] M. D. Barrett *et al.*, Phys. Rev. A **68**, 042302 (2003).
[8] M. Drewsen *et al.*, Phys. Rev. Lett. **93**, 243201 (2004).
[9] P. Blythe *et al.*, Phys. Rev. Lett. **95**, 183002 (2005).
[10] B. Roth *et al.*, J. Phys. B **38**, 3673 (2005).
[11] B. Roth *et al.*, Phys. Rev. A **74**, 040501(R) (2006).
[12] A. Kamariotis *et al.*, J. Am. Chem. Soc. **128**, 905 (2006).
[13] V. L. Ryjkov *et al.*, Phys. Rev. A **74**, 023401 (2006).
[14] M. Yamashita and J. B. Fenn, J. Phys. Chem. **88**, 4451 (1984).
[15] I. Waki *et al.*, Phys. Rev. Lett. **68**, 2007 (1992).
[16] M. G. Raizen *et al.*, Phys. Rev. A **45**, 6493 (1992).
[17] We also trapped rhodamine 101 and 6 G together with laser-cooled barium ions, but both were found to photodissociate in the presence of the cooling lasers.
[18] T. Baba and I. Waki, J. Appl. Phys. **92**, 4109 (2002).
[19] J. D. Prestage *et al.*, Phys. Rev. Lett. **66**, 2964 (1991).
[20] Ch. Raab *et al.*, Phys. Rev. Lett. **85**, 538 (2000).

INSTITUTE OF PHYSICS PUBLISHING JOURNAL OF PHYSICS B: ATOMIC, MOLECULAR AND OPTICAL PHYSICS

J. Phys. B: At. Mol. Opt. Phys. **39** (2006) S1241–S1258 doi:10.1088/0953-4075/39/19/S30

# Production of ultracold diatomic and triatomic molecular ions of spectroscopic and astrophysical interest

**B Roth, P Blythe, H Daerr, L Patacchini and S Schiller**

Institut für Experimentalphysik, Heinrich Heine Universität Düsseldorf, 40225 Düsseldorf, Germany

E-mail: Bernhard.Roth@uni-duesseldorf.de

Received 28 February 2006, in final form 11 April 2006
Published 25 September 2006
Online at stacks.iop.org/JPhysB/39/S1241

**Abstract**

We have produced large samples of ultracold (<20 mK) $ArH^+$, $ArD^+$, $N_2H^+$, $N_2D^+$, $H_3^+$, $D_3^+$, $D_2^+$, $H_2D^+$ and $D_2D^+$ molecular ions, by sympathetic cooling and crystallization via laser-cooled $Be^+$ ions in a linear radio-frequency trap. As technique, we used chemical reactions with sympathetically cooled noble gas atomic ions or $N_2^+$ and $O_2^+$ molecular ions. These ultracold molecules are interesting targets for high-precision measurements in fundamental physics and may open new routes for the study of state-selective chemical reactions relevant to interstellar chemistry.

## 1. Introduction

Translationally cold (in the millikelvin regime) molecular ions embedded inside Coulomb crystals are ideal targets for a large variety of investigations, including high-precision measurements of ro-vibrational transition frequencies, and state-selective studies of chemical reactions.

Heteronuclear diatomic ions, such as diatomic molecular hydrides, e.g., $ArH^+$ and $ArD^+$, are promising systems for high-precision laser spectroscopy and fundamental studies, such as tests of time independence of certain fundamental constants, namely particle mass ratios [1, 2]. For example, $ArH^+$ has several useful properties. Its electronic ground state is a $X^1\Sigma^+$ state. The nuclei have no quadrupole moment and only a single nuclear spin (1/2) is present. This yields a simple hyperfine structure of the ro-vibrational transitions [2]. Furthermore, $ArH^+$ has relatively large vibrational and rotational transition rates, but still small enough for enabling ultra-high spectral resolution [3]. One can drive the low-lying ro-vibrational transitions using commercially available continuous-wave laser sources, e.g. OPOs, in the mid-IR wavelength region, see [3] and references therein, or quantum cascade lasers. Using far-infrared laser spectroscopy the first determination of the electric dipole moment of a molecular ion, $ArD^+$,

  

was demonstrated with an accuracy at the few per cent level, by measuring the Zeeman effect in low-lying rotational transitions of $ArH^+$ and $ArD^+$, produced in a discharge source [4]. The use of ultracold $ArH^+$ ions may allow us to improve precision of such measurements. Precision measurements of one or several ro-vibrational transition frequencies over time could serve to test the constancy of the nuclear-to-electron mass ratio. A technique to perform high-precision spectroscopy on non-fluorescing ions has recently been demonstrated [5]. Another interesting perspective is to use certain ultracold heteronuclear diatomics, in $^{1,2,3}\Sigma$ or $^2\Pi$ states which are among the most frequent electronic ground states in molecules, as model systems for the implementation of schemes for internal state manipulation [3, 2]. For this purpose, molecules with a relatively simple hyperfine structure of the ro-vibrational transitions are more favourable, in order to limit the number of laser sources required for internal cooling schemes.

Being among the most abundant molecules in interstellar clouds, the chemistry of hydrogen molecular ions is relevant to astronomy. At present, the interstellar gas-phase chemistry of $H_3^+$ and its deuterated isotopomers is not completely understood [6, 7]. Measurements of state-specific reactions of $H_3^+$ via high-resolution infrared spectroscopy can provide valuable input for theories of ion–molecule gas-phase chemistry and precise calculations of molecular transition frequencies. Such measurements could so far only be performed on warm samples [8]. Ultracold ensembles of triatomic hydrogen molecular ions, possibly cooled to their ro-vibrational ground state using cryogenic techniques, could lead to improved studies. As an example, translationally ultracold molecular ions in low-lying ro-vibrational levels (populated at room temperature) could be excited to higher ro-vibrational levels (not populated at room temperature), using standard IR laser sources. Chemical reactions between state-prepared ultracold molecular ions and (state-prepared) ultracold neutral molecules, which are endothermic when the ions are in low-lying vibrational levels, but exothermic for the excited vibrational levels, could then be studied.

A powerful method for cooling molecular ions to translational temperatures in the millikelvin regime is sympathetic cooling. The translational energy of molecular ions can be reduced by interaction with directly cooled (laser-cooled) atomic ions. Under strong cooling, i.e., when the translational temperature drops to about 50 mK, the ions undergo a phase transition to an ordered state, a Coulomb crystal, characterized by well-defined sites [9–11]. Typical interparticle distances are in the range of a few tens of micrometres. This method has been applied to an increasing number of molecules (and atoms), since it overcomes the lack of closed optical transitions required for direct cooling and is independent of electric or magnetic dipole moments or the internal level structure [12, 13].

Recently, we have reported the production of ultracold molecular hydrogen ions, e.g., $H_2^+$, $H_3^+$, and their deuterated isotopomers $HD^+$, $D_2H^+$, $H_2D^+$ and $D_2^+$, via sympathetic cooling using laser-cooled $Be^+$ ions in a linear rf trap [13]. The molecular ions were produced by *in situ* ionization of neutral molecular gases ($H_2$, $D_2$ or HD) in the ion trap using low-energy electrons. Ion crystals of various sizes and ion species ratios were formed with the fraction of molecules exceeding 70%. Chemical reactions were involved in some of the molecule species production. Since the method used also leads to the formation of unwanted impurity ions purification was applied in order to remove those ions from the crystal [14, 13]. However, crystal purification usually also leads to partial loss of the molecular species of interest.

In this work, we demonstrate a novel, more efficient production method for the molecular hydrogen ions $H_3^+$, $D_3^+$, $D_2^+$, and for $D^+$. We use heavier atomic or molecular ions, e.g. $Ar^+$, $Ne^+$, $Kr^+$, $N_2^+$ or $O_2^+$, as reactants in order to produce ultracold and pure ensembles of $H_3^+$. The fraction of atomic to molecular ions can be controlled. The method was also applied to produce various ultracold deuterated hydrogen isotopomers, $D_3^+$, $D_2^+$ and $D^+$ atomic ions. Furthermore, multi-step chemical reactions were used to produce and reliably detect

heavier medium-weight diatomic and triatomic molecular hydrides, such as $ArH^+$, $ArD^+$, $N_2H^+$ and $N_2D^+$.

## 2. Apparatus and methods

A detailed description of our ion trap apparatus and the basic experimental procedure is given elsewhere [11, 14]. Here, we summarize the main aspects only. We use a linear quadrupole trap to simultaneously store laser-cooled (LC) and sympathetically cooled (SC) ions. The trap is enclosed in an ultra-high vacuum chamber kept below $5 \times 10^{-11}$ mbar. Stable trapping of ions is ensured by a Mathieu stability parameter, $q = 2QV_{RF}/m\Omega^2 r_0^2$, significantly below 0.9. Here, $Q$ and $m$ are the charge and the mass of the ions. $V_{RF}$ and $\Omega$ are the amplitude and the frequency of the rf driving field and $r_0 = 4.3$ mm is the distance from the trap centre to the electrodes. Typically, we set the stability parameter $q \simeq 0.054$ for the $Be^+$ ions. In the absence of ion–ion interactions, oscillations transverse to the $z$-axis (the trap centreline) occur with a frequency $\omega_r = \left(\omega_0^2 - \omega_z^2/2\right)^{1/2}$, with $\omega_0 = QV_{RF}/\sqrt{2}m\Omega r_0^2$. The longitudinal frequency $\omega_z = (2\kappa QV_{EC}/m)^{1/2}$ is obtained from a static potential $V_{EC}$ applied to the end sections of the trap in order to achieve particle confinement in the $z$-direction. $\kappa$ is a constant determined by the trap geometry.

For laser cooling of $Be^+$ ions we produce light resonant with the $^2S_{1/2}(F = 2) \rightarrow {}^2P_{3/2}$ transition at 313 nm by doubly resonant sum frequency generation [15]. One of the fundamental waves is frequency stabilized to a hyperfine transition of molecular iodine. Thus, absolute frequency stability is achieved for the UV laser light. An AOM allows for shifting the UV frequency within a range of 340 MHz while maintaining absolute frequency stability. Optical pumping to the metastable ground state $^2S_{1/2}(F = 1)$ is prevented using a repumper red detuned by 1.250 GHz. The cooling laser beam is along $z$.

Neutral beryllium atoms are evaporated from an oven and ionized *in situ* in the trap by an electron beam crossing the trap centre. The $Be^+$ ions are subsequently laser-cooled so that they undergo a phase transition to an ordered state, a Coulomb crystal [16]. The phase transition is monitored using a charge-coupled device (CCD) camera and a photo-multiplier tube (PMT), both located perpendicular to the trap symmetry axis. Typically, the translational temperature of the $Be^+$ ions in such crystals is in the few millikelvin range [11] (see section 3 for a description of the method used for temperature determination). Then, $Ar^+$, $Ne^+$, $Kr^+$ or $O_2^+$ ions are produced by electron-impact ionization of neutral gases introduced to the vacuum chamber at pressures of $\approx 4 \times 10^{-10}$ mbar. The loading rate is controlled by the partial pressure of the neutral gas and the electron beam intensity. A fraction of the ions is sympathetically cooled and crystallized via Coulomb interaction with the ultracold $Be^+$ ions and embedded in ordered ion shells at larger radii compared to the $Be^+$ ions, due to their larger mass-to-charge ratio. After allowing for the gas pressure to drop to the initial value, neutral molecular hydrogen gas is introduced in the vacuum chamber at partial pressures of $\approx 2 \times 10^{-10}$ mbar. As a result, $H_3^+$ molecular ions are formed via two-step ion-neutral chemical reactions. The two reaction paths are, respectively,

$$\begin{aligned} Ar^+ + H_2 &\rightarrow Ar + H_2^+ \\ &\Rightarrow H_2{}^+ + H_2 \rightarrow H_3^+ + H \end{aligned} \tag{1}$$

$$\begin{aligned} Ar^+ + H_2 &\rightarrow ArH^+ + H \\ &\Rightarrow ArH^+ + H_2 \rightarrow H_3^+ + Ar. \end{aligned} \tag{2}$$

The initial reactions in (1) and (2) are exothermic by $\approx 0.15$ eV and have a branching ratio of 0.15:0.85. They are expected to proceed with a temperature-independent Langevin reaction

rate constant $k_L = 1.9 \times 10^{-9}$ cm$^3$ s$^{-1}$; see, e.g., [17–19]. For (1), to the best of our knowledge, no measured rate constant has been reported so far. The second step in (1), being exothermic by ≈2 eV, proceeds with a large (measured) rate constant $k = 2.9 \times 10^{-9}$ cm$^3$ s$^{-1}$ [19–21].

In reaction (2), the (measured) rate constant is $k = 1.1 \times 10^{-9}$ cm$^3$ s$^{-1}$, for the first step [19], and $k = (5\text{–}9) \times 10^{-10}$ cm$^3$ s$^{-1}$ for the second step, which is exothermic by ≈1.67 eV, [19, 18]. Similar reactions occur when $Ne^+$, $Kr^+$, $N_2^+$ or $O_2^+$ are used as reactants, with smaller (by a factor of 2 for $Kr^+$) or comparable (for $N_2^+$ and $O_2^+$) rate constants for the respective reaction paths. Furthermore, for the case of $N_2^+$ and $O_2^+$, the second reaction paths in (2) proceed with rate constants smaller (by a factor of 5–10) than the rate constants for the initial reaction paths [22, 23]. For the case of $Ne^+$, the reaction should proceed at a calculated Langevin rate $k_L = 1.53 \times 10^{-9}$ cm$^3$ s$^{-1}$ (see [19] and references therein) however, no experimental results were reported to date.

The produced light diatomic and triatomic hydrogen molecular ions, $H_2^+$ and $H_3^+$, are embedded in the vicinity of the trap axis, where they displace the heavier $Be^+$ ions. A dark core is observed appearing in the crystal. Since the reaction between $H_2^+$ ions and neutral $H_2$ is relatively fast, the amount of $H_2^+$ formed (relative to $H_3^+$) can be controlled by the duration of the $H_2$ inlet. Experimentally, for sufficiently long $H_2$ inlet times (typically on the order of a few tens of seconds) one can achieve full conversion of the $H_2^+$ ions into $H_3^+$ ions.

The molecular hydrogen ions, $H_2^+$ and $H_3^+$, are identified via excitation of their trap (secular) oscillation modes and detection of the induced change in the fluorescence of the atomic coolant ions. For the measurements in this work we excited radial oscillation modes only. However, for slightly anisotropic trap potentials, leading to small mass-specific displacements of the different ion species from trap centre, a coupling between radial and axial oscillation modes is induced, as observed for some of the generated crystals. In the presence of heavier molecules outside the $Be^+$ ions, and/or in the presence of strong cooling light pressure forces on the $Be^+$ (which moves, e.g., the heavy ions to one end of the crystal) in an anisotropic trap potential, the radial excitation of the heavy ions in the outer crystal regions couples into the $z$-motion of the $Be^+$ ions in the following way: as the heavy ions are moved radially (even at small amplitudes, far away from their own radial motional frequency), the $Be^+$ ions are displaced along $z$, and so their axial motion is excited. The $Be^+z$-resonance is not present if the heavy ions are removed from the trap. This effect has to be taken into account for the analysis the motional frequency spectra obtained.

For the radial excitation of particle oscillation modes an additional rf field is applied to an external electrode parallel with the $z$-axis of the trap, located between the two uppermost trap electrodes (at 45° to the $x$- and $y$-axis of the trap). When the frequency of the excitation field is resonant with a mode of an SC ion species the $Be^+$ fluorescence level changes. This can be observed via the PMT. The change is due to the fact that the SC ion species' heating also leads to a heating of the LC ions, via Coulomb interaction, and thus, to a change of the observed atomic fluorescence [24]. The trap oscillation spectra in this work were obtained with the laser detuned to the red of the cooling transition by approximately the natural line width of $Be^+$ (≈20 MHz). For such a detuning, the excitation of a particular SC species leads to an increase of atomic fluorescence.

For a trapped SC ion with mass $m$ the radial oscillation frequency is approximately given by

$$\omega = \frac{m_{Be}}{m}\omega_{Be}, \tag{3}$$

with $\omega_{Be}(m_{Be})$ being the radial oscillation frequency (mass) of the $^9Be^+$ [25]. For the parameters used, $\omega_{Be} = 280$ kHz. Experimentally, an oscillating electric field with its

frequency scanned between 10 kHz and 2 MHz is applied to the plate electrode, with amplitudes of up to several volts to excite the collective motion of the ions.

The CCD camera images of the $Be^+$ ion fluorescence obtained are compared to the results from molecular dynamics (MD) simulations. In the simulation we solve Newton's equations of motion for LC and SC particles in an effective, time-independent harmonic potential. The simulations are performed using a simple linear viscous damping force to describe the cooling laser [26], and include light pressure forces and trap asymmetries (where required). These asymmetries, obvious from radial asymmetries of imaged ion crystals, can arise from static stray potentials leading to species-dependent displacements of the ions from trap centre. In order to allow for comparison with the observed structures the calculated ion trajectory positions are averaged over time and the obtained spatial probability distribution is plotted.

Using the MD simulations, the motional frequency spectrum for pure and mixed-species ion crystals can also be computed. In the simulation, a small (uniform) step-function perturbation is applied to all ion species in, e.g., the $x$-direction, and then the system is allowed to evolve, leading to damped oscillations of the ions around their equilibrium positions. The Fourier spectrum of the sum over all coordinates $x$ is the computed motional spectrum for the case of small excitation amplitudes [27].

## 3. Production of ultracold diatomic and triatomic hydrogen molecular ions

### *3.1. $H_3^+$ ions*

Figure 1 illustrates the production of ultracold $H_3^+$ ions using chemical reactions and sympathetic cooling. In the example given, $Ar^+$ ions were used as reactants.

First, an about 1.3 mm long Coulomb crystal containing ≈1250 $Be^+$ ions was produced, figure 1(a). The crystal displays an ordered shell structure with a typical inter-shell spacing of ≈29 $\mu$m. An upper limit for the translational temperature of the crystal of ≈10 mK was deduced from MD simulations. For this purpose, the size of the imaged ion spots was compared to the simulations. The estimated temperature agrees well with direct temperature measurements based on the determination of the spectral line shape of the spontaneous emission fluorescence; see [11, 25].

Subsequently, $Ar^+$ ions, produced *in situ* in the trap, were sympathetically crystallized and embedded in shells located at larger radii compared to the $Be^+$ ion shells, due to their larger mass-to-charge ratio. This leads to a massive radial deformation of the $Be^+$ ion shells, due to space-charge effects, figure 1(b). Since the camera images show a projection of the ion crystal perpendicular to its symmetry axis (along $z$) the deformation of the $Be^+$ shells becomes obvious on the upper and lower part of the image only. The longitudinal extension of the crystal is significantly increased, exceeding the field of view of the CCD camera. According to the MD simulations, the crystal has an estimated length of ≈3 mm and contains around 1000 $Ar^+$ ions. The crystal shape is consistent with small admixtures of lighter impurities (≈150 ions), such as $N_2^+$ and $Ar^{++}$, formed by chemical reactions or electron-impact ionization of background gas molecules during loading (see also the secular excitation spectrum in figure 2(a)). The SC ion temperature is estimated at ≈20 mK, from the simulations and assuming thermal equilibrium with the $Be^+$ ions. Usually, $Be^+$ ion losses are small during the loading of $Ar^+$. The slight asymmetry of the crystal along the $z$-axis (in longitudinal direction) is due to light pressure forces felt by the atomic coolants only.

In the next step, ultracold $H_3^+$ ions are formed via the chemical reactions (1) and (2), as evidenced by the appearance of a large dark crystal core, figure 1(c) (see below for the mass-spectroscopic analysis of the ions formed). Note that the small dark core on the left part

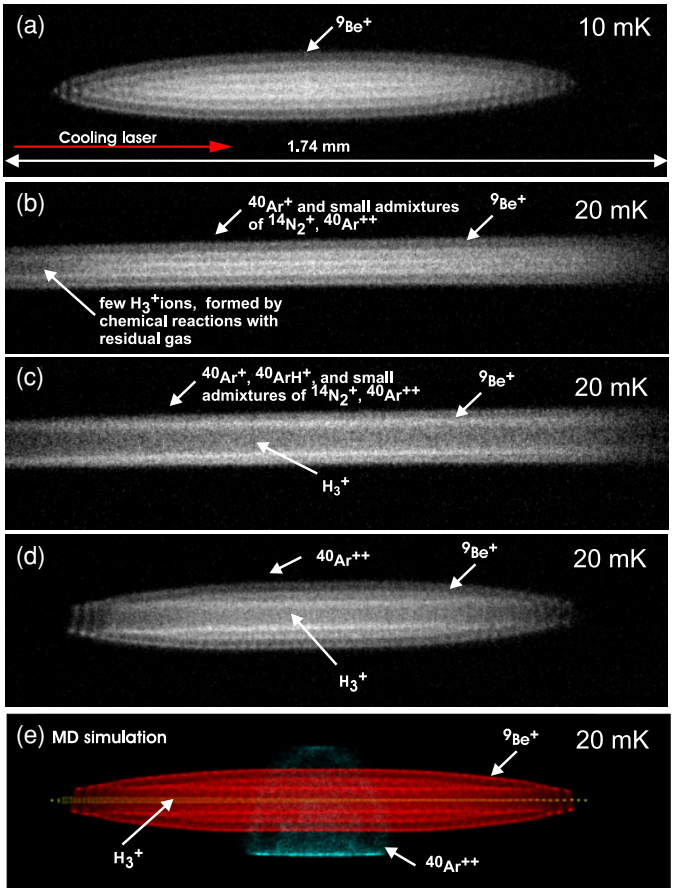


**Figure 1.** (a) Fluorescence image of a pure $Be^{+}$ ion crystal, (b) after loading with $Ar^{+}$ ions, (c) after $H_2$ inlet, showing formation of $H_3^{+}$ ions via chemical reactions, (d) after removal of $Ar^{+}$, $ArH^{+}$ and heavier contaminants, by trap opening and re-closing. We deliberately did not remove $Ar^{++}$ ions. The cooling laser beam direction is to the right. Camera integration time was 2 s. Estimates of the translational temperatures, obtained from MD simulations, are indicated. (e) MD simulation of a large multi-component ion crystal containing ≈1150 $Be^{+}$ ions, ≈100 $H_3^{+}$ ions and ≈30 $Ar^{++}$ ions at ≈20 mK. The shape of the simulated crystal is in good agreement with the crystal in (d).
(This figure is in colour only in the electronic version)

of the crystal in figure 1(b) is also due to $H_3^{+}$ ions formed via chemical reactions between $Ar^{+}$ and background hydrogen molecules, as found via secular mass-spectroscopy. Furthermore, $ArH^{+}$ was formed, as described in section 4.

Usually, chemical reactions between laser-excited $Be^{+}$ ions and neutral $H_2$ gas occur, leading to the formation of $BeH^{+}$, and thus, to loss of $Be^{+}$ ions [28]. However, this process was minimized here by reducing the population in the excited state of $Be^{+}$ by strongly detuning the laser frequency to the red of the cooling transition during exposure of the crystal to neutral $H_2$. The absence of $BeH^{+}$ is also confirmed by MD simulations [25].

The third step consists in the removal of ions with a mass-to-charge ratio larger than ≈20 from the trap. This is achieved by applying a sufficiently large static quadrupole potential to the central trap electrodes. The symmetry of the trap secular potential is broken to the point that the motion of the ions becomes unstable in one radial direction for heavy ions but

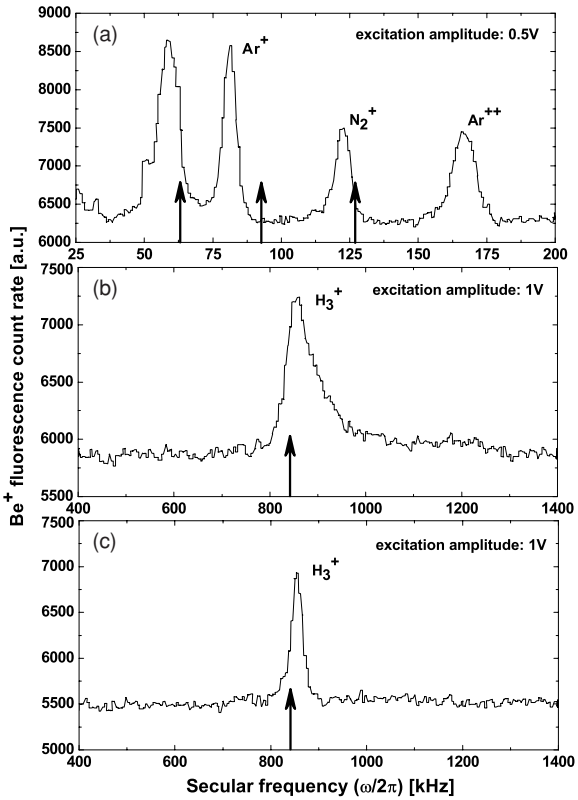


**Figure 2.** Motional frequency spectra for multi-species crystals: (a) after loading of $Ar^+$ ions (figure 1(b))—sweep direction is towards higher frequencies; (b) after inlet of $H_2$ and formation of ultracold $H_3^+$ ions (figure 1 c); (c) after the removal of ions heavier than $Ar^{++}$ (figure 1(d)). The calculated single-particle secular frequencies are marked as arrows: $Ar^+$, 63 kHz; $N_2^+$, 90 kHz; $Ar^{++}$, 126 kHz; $H_3^+$, 840 kHz. The strong deviations between observed and calculated motional frequencies occur in these (large) ion crystals, due to the Coulomb interaction between the ions.

not for the lighter SC species and the coolants [14]. In the example shown, we deliberately did not remove impurities with a mass-to-charge ratio smaller than ≈20, mostly $Ar^{++}$, from the crystal, in order to estimate their number via the MD simulations. Figure 1(d) shows the resulting ion crystal. This crystal can be well reproduced by the MD simulations, figure 1(e), if the number of $Be^+$ ions ≈1150, the number of molecular hydrogen ions ≈100, the (assumed uniform) translational temperature of the (multi-species) ion crystal is 20 mK, and the number of $Ar^{++}$ ions is 30.

In general, the number of $H_3^+$ ions can be controlled by the pressure of the neutral hydrogen gas and the loading time, and can be varied over a wide range, from a few ions embedded as a string on the crystal axis up to a few thousand ions forming a large dark core. For the production of small numbers of ultracold $H_3^+$ it is important that the residual gas partial pressure of molecular hydrogen is sufficiently low.

### *3.2. Detection via secular excitation mass spectroscopy*

Figures 2(a)–(c) show the measured secular excitation mass spectra obtained for the crystals of figures 1(b)–(d). The secular excitation spectrum of the ion crystal after loading with $Ar^+$ is

presented in figure 2(a). The spectrum shows a fairly complicated structure with pronounced features at 58 kHz, 82 kHz, 122 kHz and 166 kHz. The calculated single-particle secular frequencies for $Ar^+$, $N_2^+$ and $Ar^{++}$ are 63 kHz, 90 kHz and 126 kHz. Due to Coulomb coupling between the ions the measured frequencies deviate significantly from the calculated single-particle frequencies; see, e.g., [30, 29]. Therefore, the MD simulations are used for assigning the resonances to the various species.

The feature at 58 kHz can be attributed to the excitation of the axial $\omega_z$ $Be^+$ mode. This feature appears to be split in frequency, as indicated in figure 2(a), caused by small anisotropies of the trap secular potential. The feature at 82 kHz is due to sympathetically crystallized $Ar^+$, whereas the features at 122 kHz and 166 kHz are attributed to $N_2^+$ and $Ar^{++}$ ions, respectively. As a check, measurements in the cloud state, where coupling between ions is weak, yield secular frequencies that agree within the experimental resolution with the calculated values.

Figure 2(b) shows the secular spectrum of the crystal after exposure to neutral $H_2$ gas. It shows the low mass-to-charge region indicating the content of the produced dark crystal core. The spectrum shows an asymmetric feature with a maximum at ≈855 kHz, attributed to the production of translationally ultracold $H_3^+$ ions. After the removal of the outer (heavy) SC particles, $ArH^+$, $Ar^+$, $N_2^+$, but not $Ar^{++}$, the feature has narrowed and become symmetric (figure 2(c)). According to the MD simulations, the change in the width can be explained by space-charge effects induced by the heavier SC ions located outside the $Be^+$ shells. This interpretation is also consistent with the strong deformation of the crystal shape following the loading with neutral argon gas. In addition, an increased translational temperature of the crystal (due to the embedded SC particles) or temperature gradients in radial and axial trap direction could contribute to the broadening of the $H_3^+$ secular line shown in figure 2(b).

For comparison, the secular frequency spectrum of another $Be^+$ ion crystal of comparable size and shape after inlet and electron beam ionization of neutral $H_2$ gas is presented in figure 3(a). The corresponding secular frequency spectrum typically shows a broad feature originating from embedded $H_3^+$ and $H_2^+$ ions with their trap modes of oscillation being strongly coupled. Repeated secular excitation leads to ejection of a part of the SC particles from the trap and, thus, to weaker coupling between the different species. Then, the individual contributions of $H_3^+$ and $H_2^+$ modes can be resolved, as shown in figure 3(b). The spectrum then exhibits two broad features with maxima at ≈800 kHz and ≈1170 kHz. The width of the two features and their shift from the single-particle frequencies of 840 kHz $\left(H_3^+\right)$ and 1260 kHz $\left(H_2^+\right)$ are due to the large excitation amplitude used and, again, due to Coulomb coupling between the ions.

The computed motional frequency spectrum for the two-component ion crystal shown in figure 1(b), containing ≈1100 $Be^+$, ≈1300 $Ar^+$, and small admixtures of $N_2^+$ (≈150) and $Ar^{++}$ ions (≈150), is presented in figure 4. This spectrum shows three features at around 75 kHz, 126 kHz and 170 kHz, stemming from embedded $Ar^+$, $N_2^+$ and $Ar^{++}$ ions, respectively. The features in the simulated spectrum agree with the measured data (figure 2(a)) at the level of a few kilohertz, which is the typical level of agreement between our simulations and the measurements. However, the position of the double feature at around 40 kHz, attributed to the excitation of the axial ($\omega_z$) $Be^+$ mode and split in frequency due to the anisotropy of the trap secular potential (reproduced in the simulations), and the position of the feature at 75 kHz are shifted to lower values compared to the measured frequencies. This shift might be explained by nonlinearities in the response signal, since in the simulations the perturbation amplitude applied is small compared to the amplitude applied in experiment. Furthermore, the features at 126 kHz and at 170 kHz are shifted towards (slightly) larger values compared to the measured data, which is attributed to the different excitation amplitudes together with space-charge effects [27]. The smaller features at frequencies <25 kHz are numerical artefacts.

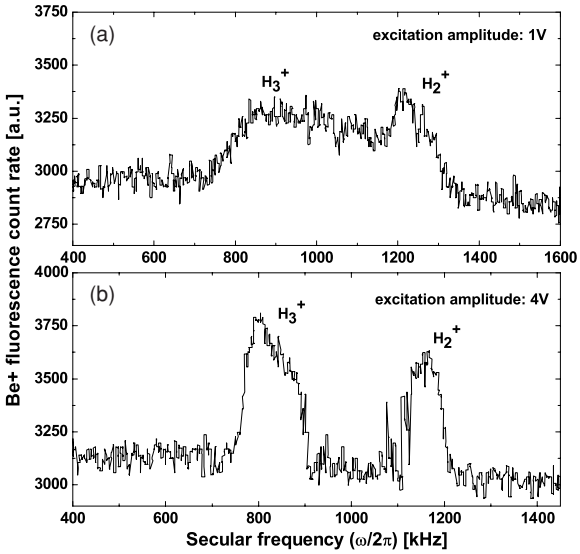


**Figure 3.** Motional frequency spectra for a $Be^+$ crystal after (a) loading of $H_2^+$ and $H_3^+$ via electron-impact ionization of neutral $H_2$. The spectrum shows a broad feature between 857 kHz and 1300 kHz, with maxima indicated around 850 kHz and 1200 kHz, originating from SC $H_3^+$ and $H_2^+$ ions, in approximately equal numbers, and the coupling between their trap modes of oscillation. This interpretation is confirmed by our MD simulations, (b) after repeated secular excitation where some of the SC particles were removed using a larger excitation amplitude (4 V).

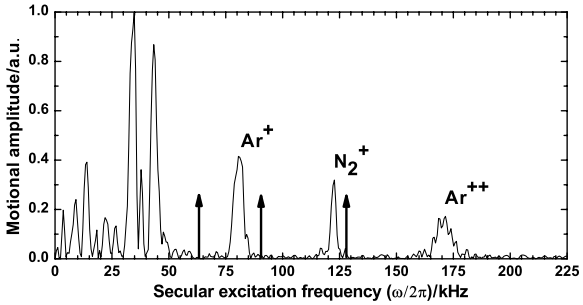


**Figure 4.** MD simulation of the motional frequency spectrum of the crystal shown in figure 1(b). The single-particle secular frequencies for $Ar^+$ (63 kHz), $N_2^+$ (90 kHz) and $Ar^{++}$ (126 kHz) are marked with arrows. The double feature at around 40 kHz originates from the excitation of the axial $\omega_z$ $Be^+$ trap mode, whereas the smaller features at frequencies <25 kHz are numerical artefacts.

### *3.3. $D_3^+$, $D_2^+$ and $D^+$ ions*

Figure 5 illustrates that the method described can also be used to produce samples of ultracold $D_3^+$, $D_2^+$ and $D^+$ ions. The relevant chemical reactions are

$$\begin{aligned} Ne^+ + D_2 &\rightarrow NeD^+ + D \\ &\Rightarrow NeD^+ + D_2 \rightarrow D_3^+ + Ne \end{aligned} \tag{4}$$

$$\begin{aligned} Ne^+ + D_2 &\rightarrow Ne + D_2^+ \\ &\Rightarrow D_2^+ + D_2 \rightarrow D_3^+ + D \\ &\Rightarrow D + D_2^+ \rightarrow D^+ + D_2. \end{aligned} \tag{5}$$

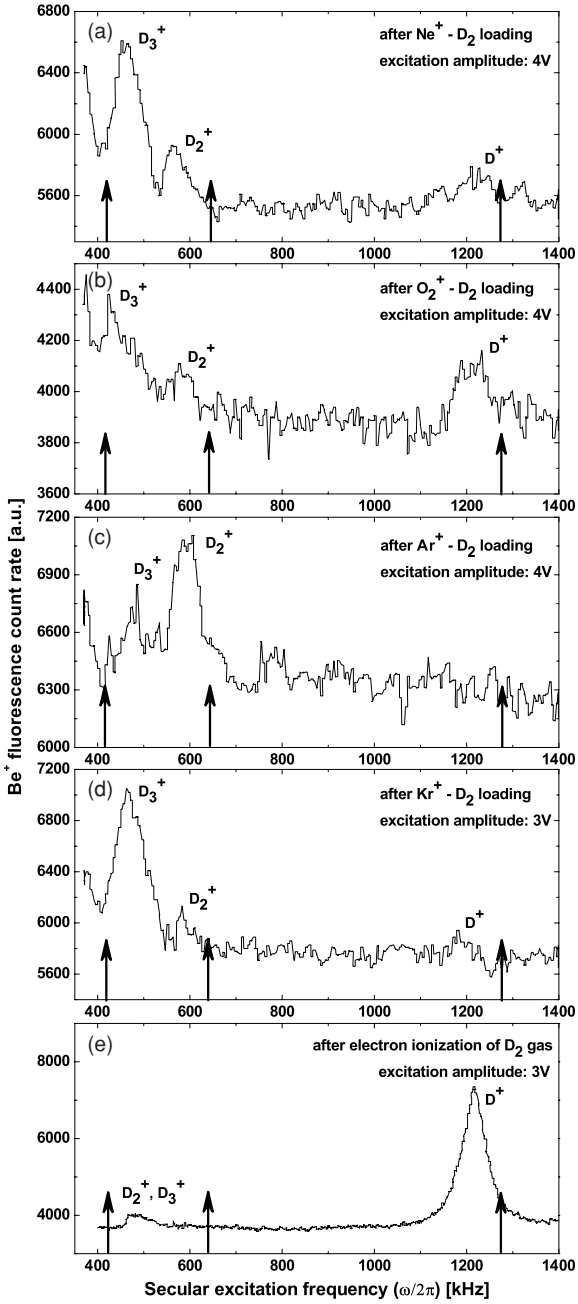


**Figure 5.** Spectrum of a $Be^+$ ion crystal after loading of (a) $Ne^+$ ions and $D_2$ inlet, (b) $O_2^+$ ions and $D_2$ inlet, (c) $Ar^+$ ions and $D_2$ inlet, (d) $Kr^+$ ions and $D_2$ inlet. Sweep direction is towards higher frequencies. (e) loading and electron-impact ionization of neutral $D_2$; excitation amplitude: 3 V. The single-particle secular frequencies are marked by arrows: $D_3^+$, 420 kHz; $D_2^+$, 640 kHz; $D^+$, 1260 kHz.

Whereas the first step of reaction (4) should proceed at a (calculated) Langevin reaction rate of $k_L = 1.53 \times 10^{-9}$ cm$^3$ s$^{-1}$, for the second step smaller values for the rate constant were

measured, $k = 2 \times 10^{-11}$ cm$^3$ s$^{-1}$ [19]. The second step in reaction (5) occurs with a rate constant $k = 1.5 \times 10^{-9}$ cm$^3$ s$^{-1}$, whereas for the third step, exothermic by ≈1.87 eV, $k = 5 \times 10^{-10}$ cm$^3$ s$^{-1}$ [31].

Figure 5(a) shows the motional frequency spectrum of a crystal after loading of $Ne^+$ ions and leaking in neutral $D_2$ gas for several seconds. The spectrum displays three features at frequencies of 460 kHz, 560 kHz and 1220 kHz. The first two features are attributed to the presence of ultracold $D_3^+$ and $D_2^+$ molecules. Again, the measured frequencies deviate significantly from the single-particle motional frequencies, 420 kHz $\left(D_3^+\right)$ and 640 kHz $\left(D_2^+\right)$, respectively, due to Coulomb coupling. The shift of the $D_2^+$ line is larger since the relative fraction of $D_3^+$ to $D_2^+$ ions is ≈3. The third (smaller) feature is attributed to the presence of small amounts of $D^+$ ions (single-particle frequency: 1260 kHz). The rise of the PMT count rate at ≈380 kHz is due to the onset of the excitation of the $Be^+$ trap oscillation mode (280 kHz).

The chemical reactions occurring differ significantly when using $O_2^+$ and $Ar^+$ as reactants, whereas when using $Kr^+$ ions they proceed similar to the case with $Ne^+$. Figure 5(b) shows a secular frequency spectrum of a $Be^+$-$O_2^+$ ion crystal after leaking in neutral $D_2$ gas. The resulting ultracold ion plasma contains three SC particle species, $D_3^+$, $D_2^+$ and $D^+$, at an approximately equal concentration. $Ar^+$ as a reactant mainly produces $D_3^+$ and $D_2^+$ ions; see figure 5(c). Finally, with $Kr^+$ the main fraction is $D_3^+$; figure 5(d). Note that for the formation of $D^+$ ions a three-step chemical reaction is required.

For comparison, figure 5(e) shows a typical secular frequency spectrum following inlet and electron-impact ionization of $D_2$ gas. The spectrum shows a large feature at 1220 kHz, originating from the $D^+$ ions formed, and a second, much smaller feature at ≈480 kHz, originating from $D_3^+$ and $D_2^+$ ions. Its frequency lies between the single-particle values for $D_3^+$ and $D_2^+$, due to the strong coupling between the two species. Typically, mixtures of $D_3^+$, $D_2^+$ and $D^+$ ions are produced, with their relative fractions varying with $D_2$ loading time and electron beam energy.

## 4. Production of nitrogen hydride and argon hydride molecular ions

### *4.1. $N_2H^+$ and $N_2D^+$ ions*

Ultracold $N_2H^+$ and $N_2D^+$ molecular ions were produced via the reactions

$$N_2^+ + H_2 \rightarrow N_2H^+ + H \tag{6}$$

$$N_2^+ + D_2 \rightarrow N_2D^+ + D. \tag{7}$$

If the $H_2$ or $D_2$ gas is removed sufficiently early multi-step reactions of the type (2) and (4) do not occur efficiently, and the molecular ions remain in the trap.

The detection of (small) amounts of nitrogen hydride (or argon hydride) molecular ions via secular excitation mass spectrometry in the crystal state is complicated mainly due to the limited experimental resolution and the coupling between LC and SC particles which depends on the number of ions involved, their translational temperature and the excitation amplitude. This can lead to combined trap modes of oscillation in the spectra, as illustrated in figure 6. There, an ensemble of $H_2^+$ and $H_3^+$ ions, with its secular spectrum shown in figure 6(a), was exposed to molecular nitrogen gas and the secular spectrum was recorded after the observed dark crystal core, stemming from embedded $H_2^+$ and $H_3^+$ ions, disappeared completely, figure 6(b). The spectrum shows two broad features at around 30 kHz and 120 kHz, attributed to the interplay between trap oscillation modes of $Be^+$ and $N_2H^+$ ions formed via chemical reactions.

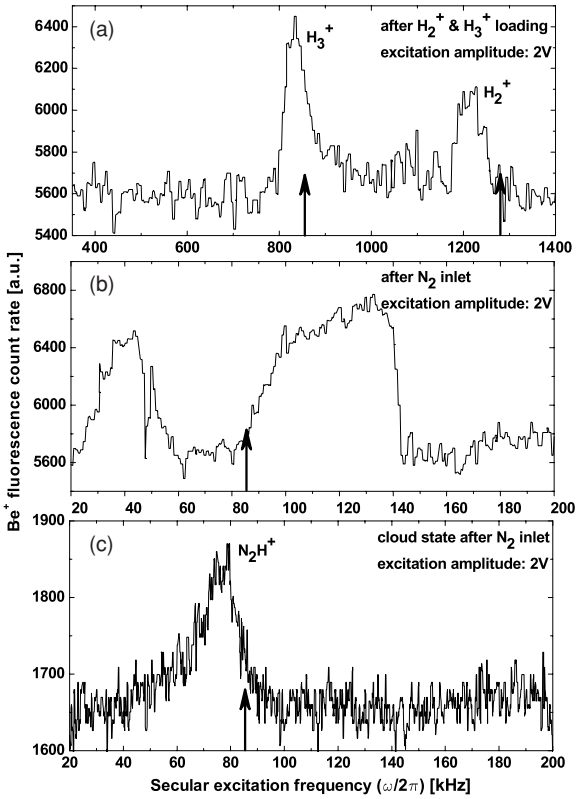


**Figure 6.** Motional frequency spectrum for a $Be^+$ ion crystal after inlet and electron-impact ionization of $H_2$ gas (a), after subsequent inlet of neutral $N_2$ in the crystal state (b), and in the cloud state (c). Arrows as before.

The $N_2H^+$ feature is hidden in the broad structure at around 120 kHz. In the cloud state secular spectrum, figure 6(c), the composite trap modes of oscillation disappear, due to a weaker coupling, and a single feature is observed, stemming from $N_2H^+$. However, it is desirable to detect the molecular ions formed in the crystal state, in order to estimate their number and their translational temperature by the simulations. For this purpose and in order to avoid complications originating from coupling effects in strongly correlated plasmas, a different detection technique was developed. An additional chemical reaction is introduced, in order to shift the resonance frequency of the reaction products formed in this step to an experimentally more favourable frequency region and still allow for an unambiguous identification of the molecular ions formed in the first step.

The production and detection of ultracold $N_2H^+$ molecular ions is shown in figure 7. First, $N_2^+$ (and smaller amounts of $N^+$ ions) were produced and embedded in the crystal. Figures 7(a) and (b) show the measured motional frequency spectra for the multi-species ion plasma in the crystal and the cloud state, respectively. Due to Coulomb coupling, the motional frequencies deviate significantly between the two states. Furthermore, the feature at around 40 kHz, originating from the excitation of the axial $Be^+$ mode, is absent in the cloud state spectrum, probably due to a weaker coupling between radial and axial trap modes of different ion species, as explained above. After inlet of neutral $H_2$ gas, hydrogen molecular ions, $H_3^+$

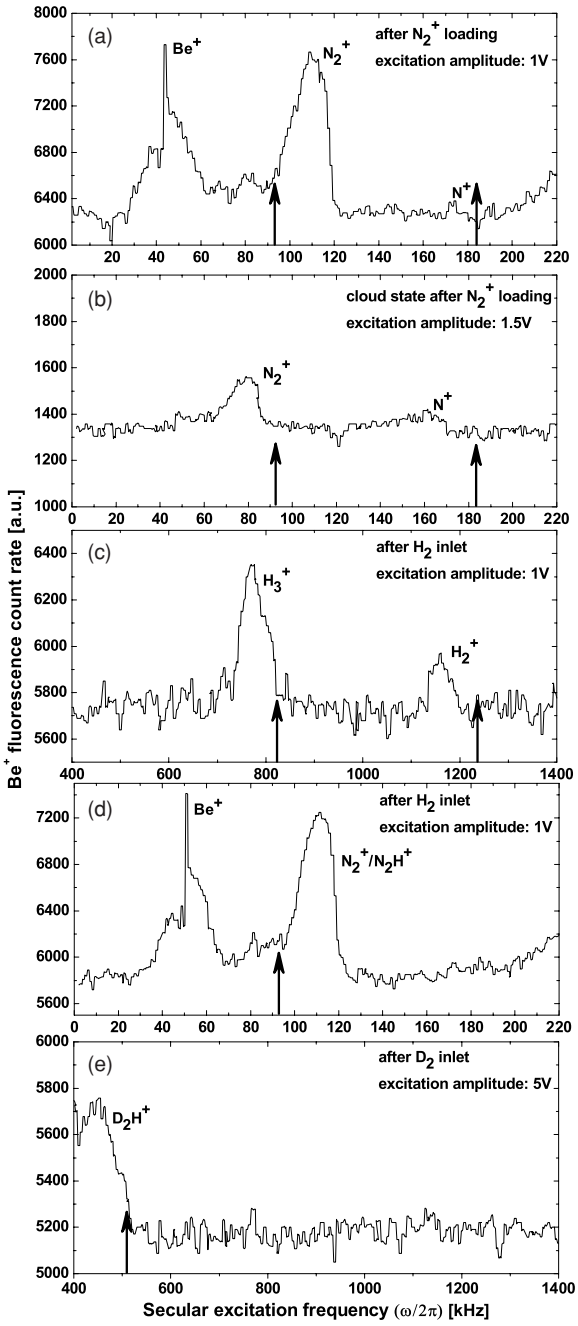


**Figure 7.** Motional frequency spectra for a $Be^+$ ion ensemble after inlet and electron-impact ionization of $N_2$ gas (a), (b), after subsequent inlet of neutral $H_2$, for the low-mass range (c) and the high-mass range (d), and followed by inlet of neutral $D_2$ (e). Part (b) is for the cloud state, and parts (a), (c)–(e) are for the crystal state. Arrows as before.

and $H_2^+$, are produced; see reactions (4) and (5). The corresponding secular spectrum is shown in figure 7(c), with the size of the $N_2^+$ feature, now containing also $N_2H^+$, reduced during the

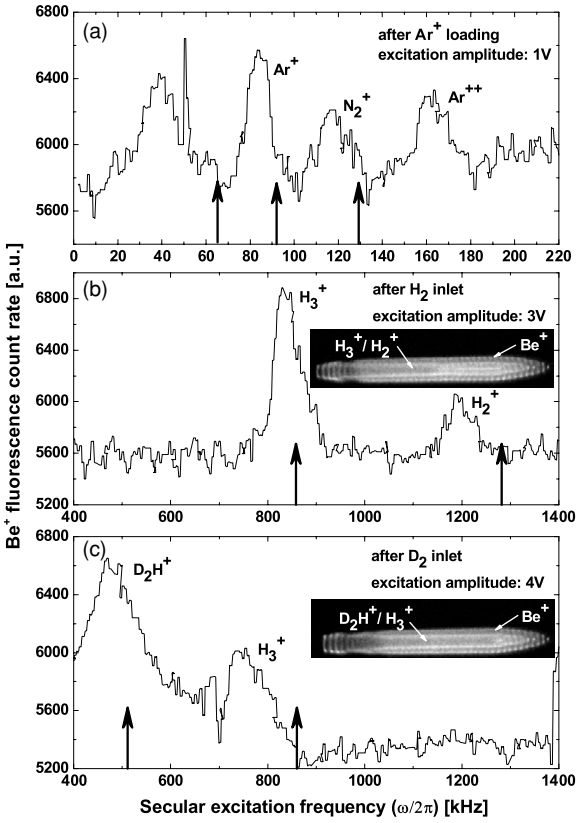


**Figure 8.** Motional frequency spectrum for a $Be^+$ ion crystal after inlet and electron-impact ionization of Ar gas (a), after subsequent inlet of neutral $H_2$ (b), and additional inlet of neutral $D_2$ (c). Arrows as before.

above reactions, figure 7(d). In the next step, exposure of the ion crystal to neutral $D_2$ leads to the appearance of a mass-5 feature in the spectrum, figure 7(e), attributed to the formation of ultracold $D_2H^+$ ions via

$$N_2H^+ + D_2 \rightarrow D_2H^+ + N_2. \tag{8}$$

The dark crystal core formed in the first step (containing $H_3^+$ and $H_2^+$) increases during the second step ($D_2$ inlet) indicating the formation of additional ultracold molecules, $D_2H^+$. The appearance of a mass-5 feature in the spectrum cannot be explained via other reaction channels, therefore, this allows for identification of the species produced as $D_2H^+$. Analogously, ensembles of ultracold $N_2D^+$ molecules were formed and detected via the appearance of a mass-4 feature in the spectrum. MD simulations were used to deduce an upper limit for the translational temperature of the nitrogen hydride molecules. The observed ion crystal structure can be reproduced in the simulations when the translational temperature of the nitrogen hydride ions is at below 20 mK. Therefore, we can conclude that the molecules formed are in the crystal state.

### *4.2. $ArH^+$ ions*

Figure 8(a) shows the motional frequency spectrum after inlet and electron-impact ionization of Ar gas. In addition to a double feature at around 40 kHz, originating from the excitation

of the axial $Be^+$ trap mode, the spectrum displays three distinct features, originating from embedded $Ar^+$ (at around 85 kHz), doubly charged $Ar^{++}$ (at around 160 kHz), and $N_2^+$ from residual gas (at around 115 kHz). After subsequent $H_2$ inlet, in the secular spectrum, the presence of $ArH^+$ produced via reaction (2) cannot be resolved. The low-mass spectrum evidences the appearance of a dark crystal core which is due to the formation of ultracold $H_3^+$ and $H_2^+$ ions via reactions (1) and (2); figure 8(b). Typically, the $H_2$ inlet is stopped after a few seconds, when the longitudinal extension of the dark crystal core is approximately half the total crystal extension; see the inset of figure 8(b) (longer exposure times would lead to larger crystals cores and thus more molecular hydrogen ions formed, an unfavourable situation for the detection method described below).

The production of $ArH^+$ in the previous step can be shown by a subsequent exposure to neutral $D_2$ gas. $ArH^+$ ions will further react via the exothermic (by $\approx$1.67 eV) reaction,

$$ArH^+ + D_2 \rightarrow D_2H^+ + Ar, \tag{9}$$

leading to the formation of mass-5 molecular ions, $D_2H^+$; see figure 8(c). During this reaction, the dark $Be^+$ crystal core, initially containing $H_3^+$ and $H_2^+$ only, increases in size showing that additional light molecules are formed and embedded around the crystal axis; see the inset of figure 8(c).

The $D_2H^+$ formation paths are

$$H_2^+ + D_2 \rightarrow D_2H^+ + H \tag{10}$$

$$H_3^+ + D_2 \rightarrow D_2H^+ + H_2, \tag{11}$$

where $H_2^+$ and $H_3^+$ are ions in the core. The rate constant for the first reaction is $k = 3.2 \times 10^{-9}$ cm$^3$ s$^{-1}$ [32], and for the second reaction $k = 1.2 \times 10^{-9}$ cm$^3$ s$^{-1}$ can be assumed; see [33]. These reactions would not increase the number of ions in the core, as the produced $D_2H^+$ would, at best, replace a $H_2^+$ or $H_3^+$ core ion. Thus, the increase of the core size can only be explained by the presence of $ArH^+$.

As reactions (1) and (2) proceed at only slightly larger Langevin rates compared to reactions (4) and (5) (see [19]) residual $Ar^+$ is still contained in the crystal after the $H_2$ inlet, so that $D_2$ inlet will then lead to the formation of mass-6 $\left(D_3^+\right)$, mass-4 $\left(D_2^+\right)$ and mass-2 ions ($D^+$) via reactions (4) and (5), but not to mass-5 ions, $D_2H^+$. These ions are not observed in the spectrum, probably because of the domination of the large $D_2H^+$ feature. Similarly, reactions between $N_2^+$ or $Ar^{++}$ contaminants and neutral $D_2$ would also not lead to the formation of mass-5 ions.

### *4.3. $ArD^+$ ions*

The formation of ultracold $ArD^+$ ions is illustrated in figure 9. Here, ultracold $Ar^+$ ions (and smaller numbers of $N_2^+$ contaminants), embedded in a $Be^+$ ion crystal, were exposed to neutral $D_2$, leading to the formation of $ArD^+$ and $D_2^+$ ions via reaction (4). The secular spectrum (figure 9(b)) shows a pronounced feature at around 580 kHz, attributed to the presence of $D_2^+$, and a smaller feature at around 800 kHz, originating from $H_3^+$ ions formed by chemical reactions of $Ar^+$ with residual $H_2$ gas via reactions (1) and (2). Subsequent exposure of the ions to $H_2$ gas leads to the formation of additional mass-4 ions, $H_2D^+$, via

$$ArD^+ + H_2 \rightarrow H_2D^+ + Ar, \tag{12}$$

as evidenced by the increase in size of the mass-4 peak and the observed increase in the size of the crystal core. The rate constant for this reaction is $k = 9.9 \times 10^{-10}$ cm$^3$ s$^{-1}$ [18]. All other competing reaction channels, see reactions (1) and (2), would lead to the

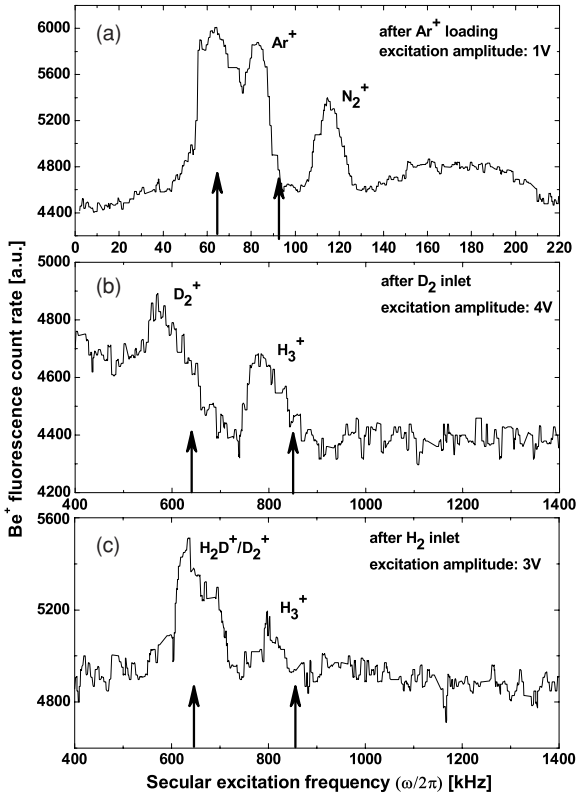


**Figure 9.** Motional frequency spectra for a $Be^+$ ion crystal after inlet and electron-impact ionization of Ar gas (a), after subsequent inlet of neutral $D_2$ (b), and followed by inlet of neutral $H_2$ (c). Arrows as before.

formation of mainly $H_3^+$ ions (in contrast to the experimental observation). The difference in the secular frequencies between the mass-4 features in figures 9(b) and (c) is due to the different excitation amplitudes, with the larger amplitude leading to a downward shift of the motional frequency [27].

## 5. Conclusion

We have demonstrated a novel production method for translationally ultracold $H_3^+$, $H_2D^+$ and $D_2H^+$ ions, based on two-step chemical reactions. The method was also used to produce samples of ultracold $D_3^+$, $D_2^+$ or $D^+$ ions. These sympathetically cooled ions were detected via excitation of their trap (secular) modes. For the interpretation of the measured secular mass spectra we used MD simulations. When the reaction chain is stopped at the first step, ultracold diatomic and triatomic molecular hydrides, e.g. $ArH^+$, $ArD^+$, $N_2H^+$ and $N_2D^+$, are obtained. The ion number in the multi-species ion crystals can be varied over a wide range from a few hundreds to several thousands, with SC particle fractions of up to 70%. Also, ion crystals containing small numbers ($<10$) of molecular hydrogen ions or their deuterated isotopomers can reliably be produced with a high degree of control. Using MD simulations we estimate the translational temperature of the crystallized molecular ions at below 20 mK.

The results described in this work could serve as systems for precision (spectroscopic) measurements on ultracold molecules. Such ultracold molecular samples in their electronic ground states could be used to perform precise tests of quantum chemical theories, to investigate chemical reactions with ultracold neutral atoms and molecules, and to implement schemes for laser manipulation of internal degrees of freedom. Reactions between cold $H_3^+$ ions and neutral molecular hydrogen isotopes are important for astrophysics. Furthermore, $ArH^+$, $ArD^+$ or $H_3^+$ ions are attractive systems for tests of time independence of particle masses. The produced two- and multi-species ion crystals could also be used to systematically study trap modes as a function of temperature and ion number.

## Acknowledgments

The authors thank H Wenz for the MD simulations and the Deutsche Forschungsgemeinschaft (DFG) and the EU network HPRN-CT-2002-00290 'Ultracold Molecules' for financial support. PB was also supported by the Alexander-von-Humboldt Stiftung.

## References

[1] Fröhlich U, Roth B, Antonini P, Lämmerzahl C, Wicht A and Schiller S 2004 Ultracold trapped molecules: novel systems for test of the time-independence of the electron-to-proton mass ratio *Lecture Notes in Physics* vol 648 (Berlin: Springer) pp 297–307

[2] Vogelius I S, Madsen L B and Drewsen M 2004 Rotational cooling of heteronuclear molecular ions $^{1,2,3}\Sigma$ and $^2\Pi$ electronic ground states *Phys. Rev.* A **70** 053412

[3] Vogelius I S, Madsen L B and Drewsen M 2002 Blackbody-radiation-assisted laser cooling of molecular ions *Phys. Rev. Lett.* **89** 173003

[4] Laughlin K B, Blake G A, Cohen R C, Hoyde D C and Saykally R J 1987 Determination of the dipole moment of $ArH^+$ from the rotational Zeeman effect by tunable far-infrared laser spectroscopy *Phys. Rev. Lett.* **58** 996–9

[5] Schmidt P O, Rosenband T, Langer C, Itano W M, Bergquist J C and Wineland D J 2005 Spectroscopy using quantum logic *Science* **309** 749–52

[6] Herbst E 2000 The astrochemistry of $H_3^+$ *Phil. Trans. R. Soc.* A **358**

[7] Glenewinkel-Meyer T and Gerlich D 1997 Single and merged beam studies of the reaction $H_2^+(v = 0, 1; j = 0, 4) + H_2 \rightarrow H_3^+ + H$ *Isr. J. Chem.* **37** 343–52

[8] See, e.g., Herbst E *et al* 2000 *Phil. Trans. R. Soc.* A **358** 1774
Mikosch J *et al* 2004 Action spectroscopy and temperature diagnostics of $H_3^+$ by chemical probing *J. Chem. Phys.* **121** 11030–7

[9] Larson D J, Bergquist J C, Bollinger J J, Itano W M and Wineland D J 1986 Sympathetic cooling of trapped ions: a laser-cooled two-species nonneutral ion plasma *Phys. Rev. Lett.* **57** 70

[10] Bowe P, Hornekaer L, Brodersen C, Drewsen M, Hangst J S and Schiffer J P 1999 Sympathetic crystallization of trapped ions *Phys. Rev. Lett.* **82** 2071

[11] Roth B *et al* 2005 Sympathetic cooling of $^4He^+$ ions in a radiofrequency trap *Phys. Rev. Lett.* **94** 053001

[12] Bertelsen A, Jorgensen S and Drewsen M 2005 The rotational temperature of molecular ions in Coulomb crystals *Preprint* physics/0504128

[13] Blythe P, Roth B and Schiller S 2005 Production of cold trapped molecular hydrogen ions *Phys. Rev. Lett.* **95** 183002

[14] Fröhlich U, Roth B and Schiller S 2005 Ellipsoidal Coulomb crystals in a linear radiofrequency trap *Phys. Plasmas* **12** 073506

[15] Schnitzler H, Fröhlich U, Boley T K W, Clemen A E M, Mlynek J, Peters A and Schiller S 2002 All-solid-state tunable continuous-wave ultraviolet source with high spectral purity and frequency stability *Appl. Opt.* **41** 7000

[16] Raizen M G, Gilligan J M, Bergquist J C, Itano W M and Wineland D J 1992 Ionic crystals in a linear Paul trap *Phys. Rev.* A **45** 6493

[17] Baer M and Beswick J A 1979 Electronic transitions in the ion–molecule reaction $(Ar^+ + H_2 \leftrightarrow ar + H_2^+) \rightarrow ArH^+ + H$ *Phys. Rev.* A **19** 1559

[18] Bedford D K and Smith D 1990 Variable-temperature selected ion flow tube studies of the reactions of $Ar^+$, $Ar_2^+$ and $ArH_n^+$ (n = 1-3) ions with $H_2$, HD and $D_2$ at 300 K and 80 K *Int. J. Mass Spectrom. Ion Process.* **98** 179–90

[19] McDaniel E W, Cermak V, Dalgarno A, Ferguson E E and Friedman L 1970 *Ion–Molecule Reactions* (New York: Wiley)
[20] Huber K P and Herzberg G 1979 *Molecular Spectra and Molecular Structure* (New York: Van Nostrand-Reinhold)
[21] Bowers M T and Elleman D E 1969 Kinetic analysis of the concurrent ion–molecule reactions in mixtures of argon and nitrogen with $H_2$, $D_2$, and HD utilizing ion-ejection-ion-cyclotron-resonance techniques *J. Chem. Phys.* **51** 4606–17
[22] Roche A E, Sutton M M, Bohme D K and Schiff H I 1971 Determination of proton affinity from the kinetics of proton transfer reactions: I. Relative proton affinities *J. Chem. Phys.* **55** 5480
[23] Adams N G and Smith D 1984 A further study of the near-thermoneutral reactions $O_2H^+ + H_2 \leftrightarrow H_3^+ + O_2$ *Chem. Phys. Lett.* **105** 604
[24] Baba T and Waki I 1996 Cooling and mass-analysis of molecules using laser-cooled atoms *Japan. J. Appl. Phys.* **35** L1134
[25] Roth B, Ostendorf A, Wenz H and Schiller S 2005 Production of large molecular ion crystals via sympathetic cooling by laser-cooled $Ba^+$ *J. Phys. B: At. Mol. Opt. Phys.* **38** 3673–85
[26] Schiller S and Lämmerzahl C 2003 Molecular dynamics simulation of sympathetic crystallization of molecular ions *Phys. Rev.* A **68** 053406
[27] Roth B, Blythe P and Schiller S 2005 Motional resonance coupling in cold multi-species Coulomb crystals, in preparation
[28] Roth B, Blythe P, Wenz H, Daerr H and Schiller S 2006 Ion-neutral chemical reactions between ultracold, localized ions and neutral molecules with single-particle resolution *Phys. Rev.* A **73** 042712
[29] Hasegawa T and Shimizu T 2002 Resonant oscillation modes of sympathetically cooled ions in a radio-frequency trap *Phys. Rev.* A **66** 063404
[30] Baba T and Waki I 2002 Sympathetic cooling rate of gas-phase ions in a radio-frequency-quadrupole ion trap *Appl. Phys.* B **74** 375
[31] Karpas Z, Anicich V G and Huntress W T 1979 An ion cyclotron resonance study of reactions of ions with hydrogen atoms *J. Chem. Phys.* **70** 2877–81
[32] Clow R P and Futrell J H 1972 Ion–molecule reactions in isotopic hydrogen by ion cyclotron resonance *Int. J. Mass Spectrom. Ion Phys.* **8** 119–42
[33] Adams N G and Smith D 1981 A laboratory study of the reaction $H_3^+ + HD \leftrightarrow H_2D^+ + H_2$: the electron densities and the temperatures in interstellar clouds *Astrophys. J.* **248** 373–9

PHYSICAL REVIEW A **74**, 040501(R) (2006)

# Rovibrational spectroscopy of trapped molecular hydrogen ions at millikelvin temperatures

B. Roth, J. C. J. Koelemeij, H. Daerr, and S. Schiller
*Institut für Experimentalphysik, Heinrich-Heine-Universität Düsseldorf, 40225 Düsseldorf, Germany*
(Received 27 June 2006; published 6 October 2006)

We report a high-resolution spectroscopic study of molecular ions at millikelvin temperatures. We measured several rovibrational infrared transitions in $HD^+$ molecular ions, stored in a radio-frequency trap and sympathetically cooled to ≈20 mK by laser-cooled $Be^+$ ions. We observed hyperfine splitting of the lines, in good agreement with theoretical predictions. The transitions were detected by monitoring the decrease in ion number after selective photodissociation of $HD^+$ ions in the upper vibrational state. The method described here is expected to be generally applicable.

DOI: 10.1103/PhysRevA.74.040501 PACS number(s): 33.20.−t, 32.80.−t, 42.50.−p

In recent years, a number of novel techniques have been developed to cool the translational energy of gas-phase molecules to the millikelvin regime, where conventional cryogenic techniques are not applicable [1]. With the availability of stored ensembles of subkelvin neutral and charged molecules, sometimes also internally cold, their use for a variety of applications is moving into focus. One wide-ranging application is high-resolution spectroscopy, which is possible because the usual line-shifting and broadening effects due to collisions, high thermal velocities, and finite transit time are strongly suppressed. Spectroscopy of rovibrational transitions in the electronic ground state can take advantage of these special conditions because the lifetime of vibrational levels of molecules is typically long (~ milliseconds or longer), and thus lifetime broadening is not an important limitation. The low translational temperature also increases the absorption rate significantly, and efficient excitation is possible even on weak overtone transitions.

Subkelvin molecular ions can be obtained by sympathetic cooling [2,3]—the molecular species and a laser-coolable atomic species, with the same sign of charge, are simultaneously stored in a radio-frequency trap. Laser cooling the atoms then also efficiently cools the molecular ions via the long-range Coulomb interaction. Temperatures below 20 mK can be reliably reached. We have recently shown that using $Be^+$ ions as coolant permits to cool sympathetically ions from mass 1 to mass 200 amu [4–6]. A heavier atomic coolant species can be used to extend the mass range. For example, using $^{138}Ba^+$ as coolant, molecular ions up to mass 410 amu have recently been cooled [7].

Here we demonstrate high-resolution spectroscopy of vibrational transitions in a localized sample of molecular ions at millikelvin temperature. We show that high spectral resolution can be achieved even with small molecular samples and standard laser systems. We apply the technique to $HD^+$ ions, but it could be used in the same way to significantly improve the precision of (ground-state) level energies of a large variety of molecular ions, which have traditionally been measured in discharges [8] or in ion beams [9] and in traps equipped with buffer gas cooling (>10 K) [10].

Our application to $HD^+$ is motivated by the fact that it is the simplest molecule after $H_2^+$, and as such is of interest as a fundamental three-body quantum system. $HD^+$ is also important for astrochemistry [11]. In particular, a comparison between measured vibrational transition frequencies and high-precision *ab initio* calculations [12–16] could lead to the first identification of QED effects in a molecular system and to a spectroscopic measurement of the fundamental constant $m_e/m_p$ [17] and of the deuteron quadrupole moment [18]. Previous spectroscopic studies of $HD^+$ and other isotopomers were performed on warm ensembles or on ion beams [9,19–21].

Vibrational spectroscopy in the electronic ground state in absence of collisions is faced with the difficulty that molecules excited to a vibrational level decay only slowly, implying very low fluorescence rates. As the fluorescence wavelengths are in the mid to far infrared, photon counting would require a sophisticated detection system. We circumvent this difficulty by applying the technique of $(1+1')$ resonance-enhanced multiphoton dissociation (REMPD): the molecules are excited by an infrared (ir) laser and then selectively photodissociated from the upper vibrational state by a second, fixed-wavelength ultraviolet (uv) laser (Fig. 1). The remaining number of molecular ions is the quantity mea-

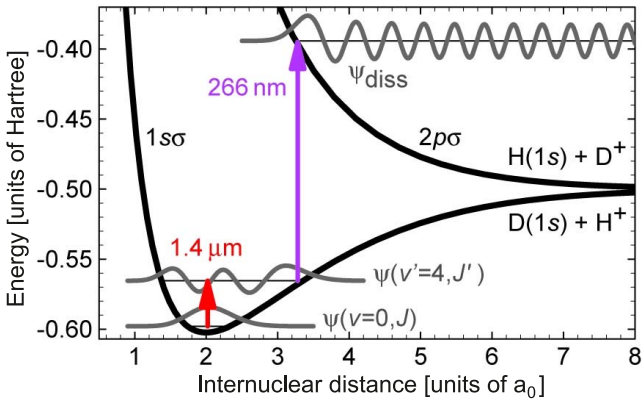


FIG. 1. (Color online) Principle of $(1+1')$ REMPD spectroscopy of $HD^+$ ions. A tunable ir diode laser excites a rovibrational overtone transition $(v'=4,J') \leftarrow (v=0,J)$. The $HD^+$ ions excited to the $v'=4$ vibrational level are dissociated using cw 266 nm laser radiation: $HD^+(v'=4)+h\nu \rightarrow H+D^+$ or $H^++D$. Due to different Franck-Condon wave function overlap, the calculated uv absorption cross section from the $v'=4$ level ($\sim 2.4\times 10^{-17}$ cm$^2$) is about seven orders of magnitude larger than from $v=0$ [25]. Energy values represent total binding energies of the molecule.

 

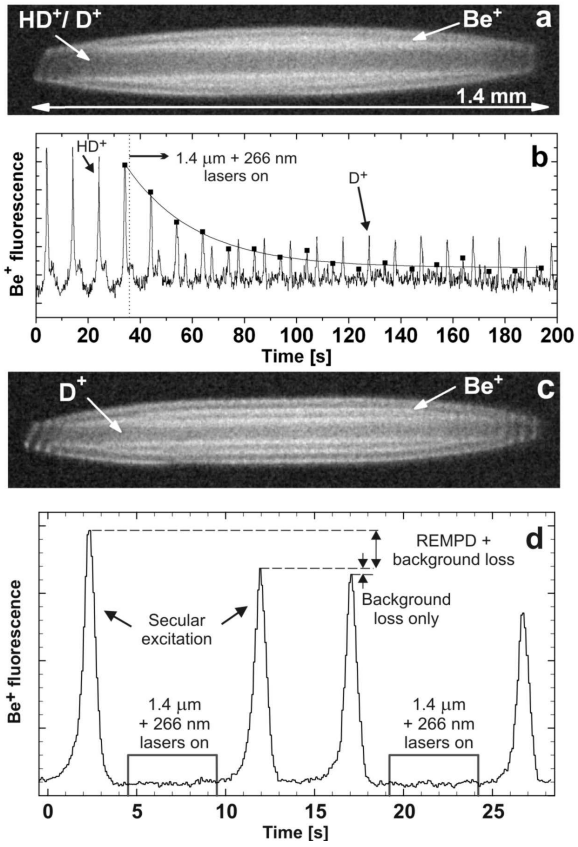


FIG. 2. (a) Initial ion crystal: ≈1100 $Be^+$, ≈100 $HD^+$, and ≈20 $D^+$ ions at ≈20 mK. The presence of cold $HD^+$ ions is obvious from the dark crystal core. (b) Repeated secular excitation of the crystal in (a) at 3 V amplitude. The excitation frequency was swept between 500 and 1500 kHz. The ir laser is tuned to the maximum of the $(v'=4,J'=1)\leftarrow(v=0,J=2)$ line. The curve is an exponential fit with a decay constant of 0.04 $s^{-1}$. (c) Ion crystal after dissociation of all $HD^+$ ions: ≈1100 $Be^+$ and ≈50 $D^+$ ions at ≈20 mK. (d) Measurement cycle consisting of repeated probing of the number of $HD^+$ ions before and after exposure to the spectroscopy lasers.

sured as a function of the frequency of the ir laser. As the molecular sample is small (typically 40–100 ions) the spectroscopy requires the spectra to be obtained by repeated molecular ion production and interrogation cycles.

For sympathetic cooling of $HD^+$ ions, we store both $Be^+$ and molecular ions in a linear radio-frequency trap [4]. The $Be^+$ ions are laser cooled and form a cluster structure around the trap center [22]. Due to the long-range electrostatic interaction between atomic coolants and molecular ions, the latter are efficiently cooled and embedded in the vicinity of the axis of the $Be^+$ ion crystals [see Fig. 2(a)]. Small numbers of $D^+$ ions, formed during loading by dissociation of neutral HD, are also present, but do not influence the subsequent measurements. The crystal in Fig. 2(a) contains ≈1100 $Be^+$, ≈100 $HD^+$, and ≈20 $D^+$ ions at a translational temperature of ≈20 mK. The $HD^+$ clusters formed have lifetimes of several minutes, limited by chemical reactions with residual gas. Inside the clusters, the ions perform a diffusive motion due to the residual thermal energy. Since the particles repel each other, the long-range collisions do not lead to significant line shifts or line broadening.

The trapped species are identified and the time evolution of their numbers is monitored by excitation of their mass-dependent radial (secular) modes, using a spatially homogenous and temporally oscillating electric field. We use molecular dynamics simulations to deduce ion numbers, spatial distributions, and upper limits for the translational temperature of the ions [4]. We excite $HD^+$ at an electric field frequency around 840 kHz. As a consequence, the atomic coolants are heated by the molecular ions, which changes the scattering rate of 313 nm cooling light by the $Be^+$ ions. The secular resonance becomes visible in the $Be^+$ fluorescence [see Fig. 2(b)], and its height is proportional to the amount of $HD^+$ in the ion crystal. Typically we use a 3 V peak-to-peak potential amplitude, applied to an electrode outside the trap, with the frequency being swept linearly from 500 to 1000 kHz at a rate of 0.2 Hz. Excitation amplitude, sweep rate, and covered frequency range were chosen so that the ion crystal had sufficient time to cool back to its initial temperature between individual excitation cycles.

Rovibrational spectroscopy is performed by continuous-wave (cw) excitation by a single-frequency, widely tunable diode laser, followed by photodissociation from the upper level by a cw ultraviolet laser (Fig. 1). The loss of $HD^+$ ions from the trap is measured. Due to the weak coupling between external and internal degrees of freedom, the internal (rotational) temperature of the $HD^+$ ions is expected to be at 300 K, in thermal equilibrium with the vacuum chamber [23], with a significant (>5%) population for rotational levels up to $J=6$. Indeed, we have observed 12 transitions between 1391 and 1471 nm, from lower rotational levels $J=0$ to 6. The linewidth of the ir laser was ~5 MHz on a 1 s time scale, and its frequency was calibrated with an accuracy of 40 MHz by absorption spectroscopy in a water vapor cell.

The loss of $HD^+$ ions depends not only on the REMPD process, but also on transitions induced by blackbody radiation (BBR). We modeled the loss of $HD^+$ by solving the rate equations for the populations of all $(v,J)$ levels interacting with the ir and uv lasers, as well as with the BBR radiation at 300 K. The theoretically obtained excitation spectrum (see Fig. 3 and text below) of the levels probed by the ir laser is included, but for the remainder of the calculation hyperfine structure, due to electron, nuclear, and rotational spins, is ignored. The rovibrational transition moments involved are taken from [24]. The rate of dissociation by uv light is obtained using cross sections from [25]. For typical uv intensities, dissociation rates of $10^2$–$10^3$ $s^{-1}$ are found. The rate equation model reveals two different time scales at which the $HD^+$ number declines during a typical experiment. A first, fast (<1 s) decay occurs when the ir laser selectively promotes $HD^+$ ions from a specific $(v=0,J)$ level to a rotational level in $v'=4$, from which they are efficiently photodissociated. This process rapidly dissociates those $(v=0,J)$ $HD^+$ ions which are in the hyperfine states probed by the ir laser. The remaining molecular ions (a significant fraction of the total initial number) are dissociated significantly slower, essentially at the rate at which the hyperfine levels of $(v=0,J)$ are repopulated by BBR and spontaneous emission. For example, for the $(v'=4,J'=1)\leftarrow(v=0,J=2)$ transition, and for typical intensities of 6 $W/cm^2$ for the ir and

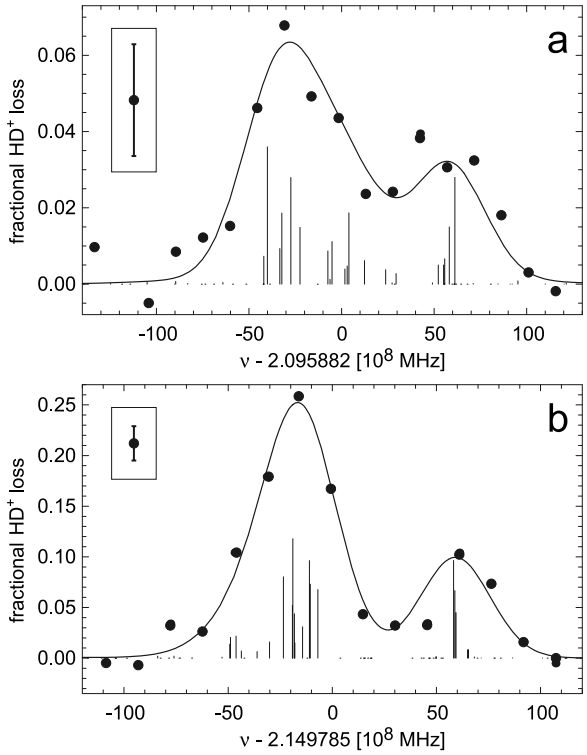


FIG. 3. Rovibrational transition spectra with partially resolved hyperfine splitting: (a) $(v'=4,J'=1)\leftarrow(v=0,J=2)$ at 1430 nm, (b) $(v'=4,J'=3)\leftarrow(v=0,J=2)$ at 1394 nm. The curves are fits to the data (●), where the theoretical stick spectra were broadened by ≈40 MHz. The theoretical spectrum exhibits a large number of very weak transitions, due to weak mixing of pure coupled angular momentum states by $H_{\text{eff}}$. The ordinate values are the molecular ion dissociation probability for a 5 s irradiation of 0.65 W/cm$^2$ ir and 10 W/cm$^2$ uv light. The insets show typical error bars.

10 W/cm$^2$ for the uv laser, the fast $HD^+$ decay takes place at a rate ~10 s$^{-1}$ (which is not resolved experimentally), whereas the decay due to BBR-induced repopulation occurs at a rate of ~0.04 s$^{-1}$. The latter rate is fairly consistent with the measured decay depicted in Fig. 2(b), but observed decay rates depend strongly on which part of the hyperfine spectrum is interrogated. This points at a shortcoming of the simple rate equation model used here, and our observations can probably be explained precisely only by a rate equation model that takes the full hyperfine structure of all involved $(v,J)$ levels into account.

As an example, Fig. 2(b) shows the time evolution of the $HD^+$ secular excitation resonance while the $HD^+$ ions are excited on the maximum of the rovibrational line $(v'=4,J'=1)\leftarrow(v=0,J=2)$ at 1430.3883 nm. The decrease of the $HD^+$ resonance in the secular excitation spectrum, induced by the REMPD process, is accompanied by a decrease of the dark crystal core containing the hydrogen molecular ions. The secular excitation spectrum also shows an increase of the number of $D^+$ ions, which result from the dissociation of excited $HD^+$ ions. These ions are sympathetically cooled and remain in the crystal core. Figure 2(c) shows the mixed-species ion crystal after all $HD^+$ was dissociated. The dark crystal core has shrunk significantly, and the crystal now contains ≈1100 $Be^+$ and ≈50 $D^+$ ions. Assuming equal probability for photodissociation to $D^+$ and $H^+$, this number indicates that most generated $D^+$ ions are sympathetically cooled and trapped. Loss rates are obtained by exponential fitting to the maxima of the $HD^+$ resonances in the secular excitation spectrum [solid line in Fig. 2(b)]. In this way, a 0.01 s$^{-1}$ background loss rate of $HD^+$ ions from the trap is obtained when both the ir and uv lasers are turned off. This loss is due to chemical reactions between $HD^+$ ions and background gases. The observed background loss rate is fitted well by a single-exponential decay, which rules out strong nonlinear dependence of the $Be^+$ fluorescence during secular excitation on the number of $HD^+$ ions.

The spectroscopic signal used to produce the spectra in Figs. 3(a) and 3(b) is the molecular ion dissociation probability, obtained as the relative change of the heights of the $HD^+$ secular resonances in the $Be^+$ fluorescence before and after the REMPD excitation [Fig. 2(d)]. For each transition, the $HD^+$ dissociation probability was measured as a function of the frequency of the ir laser, in steps of 15 MHz. Each data point was obtained by averaging over several individual measurements of the $HD^+$ dissociation probability occurring over ~5 s. Each data point requires a new loading of $HD^+$ ions in the $Be^+$ crystal. For all measurements, comparable $HD^+$ ion numbers were used, as deduced from the size of the crystal core after loading. However, during each $HD^+$ loading cycle a small fraction of the $Be^+$ is lost from the trap, due to chemical reactions with neutral HD gas [6]. The same $Be^+$ ion crystal can be used for up to 40 $HD^+$ loadings, sufficient for obtaining the spectra in Figs. 3(a) and 3(b). A typical spectrum is taken within 1–2 h.

Detailed measurements for two transitions $(v'=4,J'=1,3)\leftarrow(v=0,J=2)$ are shown in Figs. 3(a) and 3(b). Both spectra reveal a partly resolved hyperfine structure, which can be compared with the prediction from an effective spin Hamiltonian, written as $H_{\text{eff}}=b_1\mathbf{I}_p\cdot\mathbf{S}+c_1I_{pz}S_z+b_2\mathbf{I}_d\cdot\mathbf{S}+c_2I_{dz}S_z+\gamma\mathbf{S}\cdot\mathbf{J}$ [15,21]. Here, $\mathbf{I}_p$, $\mathbf{I}_d$, and $\mathbf{S}$ denote the spin of the proton, deuteron, and electron, respectively; the subscript $z$ indicates the projection on the internuclear axis. The hyperfine coefficients $b_1$, $b_2$, $c_1$, $c_2$, and $\gamma$ have been recently calculated to high accuracy [13]. The hyperfine level energies and eigenfunctions are found by diagonalization of the matrix representation of $H_{\text{eff}}$ in a suitable angular momentum coupling scheme. Terms arising from the nuclear spin-rotation and deuteron quadrupole interactions are neglected as they contribute ≪1 MHz to the hyperfine level energies [13]. The results of the diagonalization were subsequently used to calculate line strengths of the individual hyperfine components within a given rovibrational transition, leading to "stick spectra," as shown in Figs. 3(a) and 3(b). Inhomogeneous broadening of the spectra may be accounted for by convolving each line with a Gaussian line shape of a given width.

The broadened stick spectra are fitted to the experimental spectra using the linewidth, the vertical scale and the frequency offset as fit parameters [Figs. 3(a) and 3(b)]. The frequency offset corresponds to the deperturbed rovibrational transition frequency, which is thus determined to within the accuracy of the wavelength calibration of the ir laser (40 MHz) and the fit uncertainty (3 MHz). The measured

deperturbed rovibrational transition frequency is in good agreement with the *ab initio* results from [14]. The partly resolved hyperfine structure in the measured spectra agrees well with the theoretical results obtained from [13,15]. We find both theoretically and experimentally that the hyperfine structure for other transitions in the $P$ and $R$ branches is similar to that in Figs. 3(a) and 3(b).

We observe a typical line broadening of 40 MHz. This is remarkable, as the kinetic energy in the secular motion (as inferred from molecular dynamics simulations) of the $HD^+$ ions can give rise to broadening of about 10 MHz only [4]. Saturation broadening also does not play a significant role, as confirmed by comparing spectra taken at different ir and uv intensities. Using the polarization-dependent 313 nm fluorescence of the $Be^+$ ions as a magnetic field probe, the magnetic field (which is along the direction of propagation of the 313 nm laser beam) has been adjusted and verified to be 50 mT and to vary by no more than 40 mT over the extent of the crystal, which implies Zeeman broadening $<1$ MHz. This leaves Doppler broadening due to micromotion as the most probable cause for the observed line broadening. For our trap, in which the $HD^+$ ions are located at least 10 $\mu$m away from the trap axis, the (radial) micromotion energy exceeds $k_B \times (0.5\ \mathrm{K})$. Through the Coulomb interaction, this radial motion couples to the axial motion, which is along the ir laser beam direction. A linewidth of 40 MHz would be explained by $k_B \times (0.2\ \mathrm{K})$ of energy in the axial motion, and we therefore attribute the excess broadening to the Doppler effect associated with micromotion.

The results described are of significance in several respects. They demonstrate the possibility of high-resolution spectroscopy of small, trapped molecular ion samples, sympathetically cooled well into the millikelvin range. We have achieved a spectral resolution ten times higher than with any previous cold molecular ion method, and the same enhancement was obtained for the excitation rate. The observed population dynamics demonstrated the weakness of collisions. The methods used for trapping, cooling, and detection are quite general, and are applicable to a host of other molecular ion species. This includes other ions of astrophysical and cosmological interest such as $H_3^+$ and its isotopomers, which have been trapped in our setup [4,5]. Also, the spectral resolution achieved here may be further improved: for instance, first-order Doppler broadening may be circumvented by use of a tightly confining trap which holds the ions in the Lamb-Dicke regime, or by two-photon spectroscopy. Furthermore, the presence of the atomic coolant ions offers an *in situ* tool to detect possible perturbing fields. In the absence of first-order Doppler shifts, a spectroscopic accuracy well below the megahertz level should be attainable. For few-electron molecular ions, $HD^+$ in particular, this offers a realistic perspective for testing *ab initio* theoretical descriptions [12]. Finally, the present method will enable studies of internal coherence in molecules on time scales orders of magnitude longer than with conventional methods and measurements of all rovibrational levels in small ions by multistep ir excitation.

We thank H. Wenz, T. Fritsch, M. Okhapkin, S. Jorgensen, and A. Kondorskiy for helpful assistance and discussions, and the DFG and the EC network HPRN-CT-2002-00290 for support. J.K. acknowledges support from the Alexander von Humboldt foundation.

[1] J. Doyle *et al.*, Eur. Phys. J. D **31**, 149 (2004).
[2] D. J. Larson *et al.*, Phys. Rev. Lett. **57**, 70 (1986).
[3] K. Molhave and M. Drewsen, Phys. Rev. A **62**, 011401(R) (2000).
[4] P. Blythe *et al.*, Phys. Rev. Lett. **95**, 183002 (2005).
[5] B. Roth *et al.*, J. Phys. B **39**, S1241 (2006).
[6] B. Roth *et al.*, Phys. Rev. A **73**, 042712 (2006); B. Roth and S. Schiller (unpublished).
[7] A. Ostendorf *et al.* (unpublished).
[8] J. L. Gottfried, B. J. McCall, and T. Oka, J. Chem. Phys. **118**, 10890 (2003).
[9] W. H. Wing *et al.*, Phys. Rev. Lett. **36**, 1488 (1976).
[10] O. Asvany *et al.*, Science **309**, 1219 (2005).
[11] D. Gerlich and S. Schlemmer, Planet. Space Sci. **50**, 1287 (2002).
[12] V. I. Korobov, Phys. Rev. A **70**, 012505 (2004).
[13] D. Bakalov, V. Korobov, and S. Schiller (unpublished).
[14] R. E. Moss, Mol. Phys. **78**, 371 (1993).
[15] R. D. Ray and P. R. Certain, Phys. Rev. Lett. **38**, 824 (1977).
[16] L. Hilico *et al.*, Eur. Phys. J. D **12**, 449 (2000).
[17] S. Schiller and V. Korobov, Phys. Rev. A **71**, 032505 (2005).
[18] J. F. Babb, in *Current Topics in Physics*, edited by Y. M. Cho, J. B. Hong, and C. N. Yang (World Scientific, Singapore, 1998), p. 531.
[19] K. B. Jefferts, Phys. Rev. Lett. **23**, 1476 (1969).
[20] Z. W. Fu, E. A. Hessels, and S. R. Lundeen, Phys. Rev. A **46**, R5313 (1992).
[21] A. Carrington, I. McNab, and C. Montgomerie, J. Phys. B **22**, 3551 (1989).
[22] R. Blümel *et al.*, Nature (London) **334**, 309 (1988).
[23] A. Bertelsen, S. Jorgensen, and M. Drewsen, J. Phys. B **39**, 83 (2006).
[24] E. A. Colbourn and P. R. Bunker, J. Mol. Spectrosc. **63**, 155 (1976).
[25] M. Tadjeddine and G. Parlant, Mol. Phys. **33**, 1797 (1977); A. Kondorskiy (private communication).

# Motional resonance coupling in cold multispecies Coulomb crystals

B. Roth, P. Blythe, and S. Schiller
*Institut für Experimentalphysik, Heinrich-Heine-Universität Düsseldorf, 40225 Düsseldorf, Germany*
(Received 24 August 2006; published 1 February 2007)

We investigate the coupling between motional resonances of translationally cold (10 mK range) atomic and molecular ions in multispecies Coulomb crystals, stored in a linear Paul trap. The atomic and molecular ions were sympathetically cooled by laser-cooled $Be^+$ ions. The motional resonances of the different ion species were determined nondestructively with high mass-to-charge resolution upon excitation with an oscillating electric field. The experimental results show good agreement with results from molecular dynamics simulations and allow for a precise identification of sympathetically cooled particles in multispecies ion crystals.

DOI: 10.1103/PhysRevA.75.023402 PACS number(s): 32.80.Pj, 52.27.Jt, 52.27.Gr, 61.50.−f

## I. INTRODUCTION

There is a growing body of research focused on the production of dense samples of cold gas phase molecules, which are of interest in chemical physics, molecular physics, and plasma and astrophysics among other fields. Trapped ensembles of cold molecules are promising systems for the study and control of chemical reactions. High-precision measurements of fundamental constants may also be enhanced or enabled by using cold trapped molecular ions [1,2].

For neutral species, several methods for cold molecule production have been demonstrated. These include the formation of alkali-metal dimers from precooled atoms via Feshbach resonances or photoassociation [3–5], and trapping and cooling of preexisting molecules using buffer gas cooling or static electric fields [6,7]. For molecular ions, sympathetic cooling has been used to cool a large variety of molecular species via their interaction with cold atomic ions in electrostatic or electrodynamic ion traps [8,9]. In such a situation, the translational molecular motion may be reduced to a few tens of millikelvin, or less, by interaction with laser-cooled (LC) atomic ions.

The development of techniques for the production of cold molecules also requires the development of particle identification techniques. In general, fluorescence detection is not applicable due to the lack of closed transitions. Time-of-flight mass spectroscopy is a destructive method for molecular ions or after ionization of neutral molecules. Nondestructive techniques are of interest because they can increase the experimental flexibility. The excitation of the mass-dependent motional resonances of the trapped ions is one such technique, and is widely used for mass spectrometry of large and small ion clouds [10–12].

We have used excitation of motional resonances to identify the molecular species embedded in laser-cooled crystals of beryllium ions [9]. In the crystalline state mutual Coulomb interactions are dominant and, therefore, the motional resonance spectrum is more complicated than for ion clouds (fluid state). The interactions between the different ion species can perturb the observed motional frequencies by a significant amount. In this work, we analyze such perturbations both experimentally and via molecular dynamics (MD) simulations. We consider multicomponent ion crystals containing up to several thousand $Be^+$ ions with fractions of sympathetically cooled (SC) ions of up to 70%. The results obtained increase our ability to unequivocally identify the species present in the ion trap, and lead directly to increased sensitivity for spectroscopic and chemical experiments on cold, trapped molecular ions.

## II. BASIC TRAP THEORY

For a linear radio-frequency ion trap (Paul trap), the axial ($\omega_z$) and radial ($\omega_r$) secular frequencies of an ion species in the harmonic effective trap potential (pseudopotential) $U_{trap}(x,y,z)=(m/2)(\omega_r^2 r^2+\omega_z^2 z^2)$ are given by $\omega_z=(2\kappa Q V_{EC}/m)^{1/2}$ and $\omega_r=(\omega_0^2-\omega_z^2/2)^{1/2}$, respectively, with $\omega_0=QV_{rf}/\sqrt{2}m\Omega r_0^2$ and $r^2=x^2+y^2$. The $z$ axis is along the centerline of the trap and $\kappa\approx 3\times 10^{-3}$ mm$^{-2}$ is a constant determined by the trap geometry. $Q$ and $m$ are the mass and the charge of the trapped ion species, $V_{rf}$ and $\Omega$ are the amplitude and the frequency of the rf driving field (for radial confinement of the particles), and $V_{EC}$ is a dc potential giving the longitudinal confinement along the $z$ axis. $r_0$ is the distance from the electrode surfaces to the trap axis.

It can be seen from the above expressions that simple scaling laws apply for the radial oscillation frequencies of single trapped ions, namely, that $\omega_r \propto q/m$ for $|a_r|=4QV_{dc}/mr_0^2\Omega^2 \ll |q_r|=2QV_{rf}/mr_0^2\Omega^2$ and $\omega_0 \gg \omega_z$. Here, $V_{dc}$ is a static quadrupole potential on the trap electrodes. For singly charged ions, as studied here, simple ratios are expected between the motional frequencies of different trapped species, if the coupling between the species is neglected. The oscillation frequencies reflect the strength of confinement, and so lighter ions will generally be closer to the trap axis than heavier ions. This radial separation is seen clearly for multispecies ion crystals [8,9].

## III. EXPERIMENT

The trap used in these experiments is driven at 14.2 MHz, with a peak-to-peak rf amplitude of 380 V, enclosed in an ultrahigh-vacuum chamber. The chamber is equipped with a leak valve for the controlled introduction of neutral molecules.

Beryllium atoms are evaporated from an oven, and ionized in the trap center by a 750 eV electron beam, where they are laser-cooled to a few millikelvin. Experimentally,

 

we find that the relatively large value for the electron beam energy is favorable for efficient loading of beryllium ions to our trap. The cooling laser light, resonant with the $^2S_{1/2}(F=2) \rightarrow {}^2P_{3/2}$ $Be^+$ transition at 313 nm, is produced by doubly resonant sum frequency generation [13]. An acousto-optic modulator allows for tuning of the uv frequency within a range of 340 MHz. Optical pumping to the metastable $^2S_{1/2}(F=1)$ ground state is prevented by generating 1.25 GHz sidebands on the cooling light via an electro-optic modulator. The fluorescence of the $Be^+$ ions is measured with a photomultiplier tube and a charge-coupled device (CCD) camera. The camera integration time was 2 s.

The laser cooling leads to a phase transition from a disordered cloud or "cold fluid" to an ordered state, a Coulomb crystal [14,15]. Typical translational temperatures of the crystallized beryllium ions are well below 20 mK [16]. For definition of a quantization axis, a magnetic field of a few gauss is applied to the trap (along its $z$ axis). This low field does not perturb the motion of the ions at any detectable level.

## IV. TRAP LOADING

The loading of beryllium ions typically also produces ions of the residual gas in our vacuum chamber—mostly $N_2^+$. Some of these heavier ions collect outside the beryllium ion ensemble. Mass-selective cleaning of the trap is applied to eject these heavy impurity ions. To this end, we temporarily add a static quadrupole potential $V_{dc}$ to the trap electrodes, breaking the radial symmetry [17]. As $V_{dc}$ increases, heavier ions are no longer stable in the trap and are ejected. In this way we can efficiently remove all heavy impurity ions.

Subsequently, molecular ions are loaded into the trap by leaking neutral molecules into the vacuum chamber and ionizing them with the electron beam energy set to below 200 eV. The neutral gases used for the experiments detailed here are $^3He$, $^4He$, $H_2$, HD, and $D_2$. The primary ions produced from these gases are lighter than beryllium, and these ions collect in the center of the trap, forming a dark (nonfluorescing) core in the beryllium crystal. After loading the molecular ions, motional excitation scans, detailed below, are performed.

## V. METHODS

In order to identify the trapped ion species we excite the radial motion of the ions in the trap using an external plate electrode to which an oscillating electric field is applied. The electrode is placed at 45° to the $x$ and $y$ axes of the trap, perpendicular to the $z$ axis. The $z$ axis is horizontal, parallel to the cooling laser beam direction. The excitation field has an amplitude of up to several volts and its frequency is scanned between 2 kHz and 2 MHz.

When the excitation field is resonant with the oscillation mode of a crystal component, energy is pumped into the motion of that component. Via the Coulomb interaction, some of this energy is eventually distributed through the crystal as heat, increasing the temperature of the beryllium ions. This modifies the fluorescence intensity of the beryllium ions. For the motional excitation spectra presented here, the cooling laser was detuned to the red of the beryllium fluorescence line center by two to three natural linewidths (40–60 MHz). In this case, increasing the temperature of the beryllium ions leads to an increase in the observed fluorescence (and also to an increase in the cooling rate, limiting the temperature rise). Thus, the beryllium fluorescence level as a function of excitation frequency indicates the motional spectrum of all ions.

## VI. COUPLING MECHANISMS AND RESULTS

The equations given above for the motional frequencies of a single ion in a harmonic trap are also valid for the center-of-mass motion of large, single-species ion crystals, as confirmed in experiment. However, mixed-species crystals can complicate this picture. The motion of each species is then affected by the Coulomb potential of all the others. In multicomponent ion plasmas containing several different ion species, the coupling between the motional modes of the different ion species can depend strongly on the temperature of the ion plasma (and thus on its state, fluid or crystalline). In order to characterize the different coupling mechanisms we compare the spectra of multispecies ion crystals with those in the fluid state, where coupling between different ion species is much weaker due to the larger interparticle spacing.

The spatial distribution of the ion species can then also affect the motional frequencies and the strength of coupling between them. Strong effects are, for example, seen when a static offset potential is present in the trap, such that the equilibrium positions of the ions are displaced from the trap center. Finally, the motional spectra exhibit systematic shifts related to the excitation method, requiring their characterization.

### A. Systematics

#### *1. Scan amplitude*

As a simple two-component system, a $Be^+$ crystal was loaded with $^4He^+$ ions [Fig. 1(a)]. Helium ions are used here, because during the loading of helium isotopes, only small amounts of impurity ions are formed. Since these ions collect in the outer shells of the ion crystal they can easily be removed by temporary application of a dc quadrupole potential. Figure 1(a) shows the crystal used for the above measurements containing $\approx 1100$ $Be^+$ and $\approx 250$ $^4He^+$. The observed crystal structure is in good agreement with results from MD simulations, Fig. 1(b). The $Be^+$ and $He^+$ ions have a translational temperature of $\approx 15$ mK, as found by fitting an appropriate Voigt profile to the $Be^+$ line obtained by a frequency scan of the cooling laser over the atomic resonance and by the MD simulations, assuming equal heating rates for both species [9,16].

Repeated motional excitation was performed, with increasing excitation amplitude from 0.5 to 4 V. Figure 1(c) illustrates the shift of the observed motional frequencies caused by variations in the excitation amplitude. The fit to the experimental data gives a coefficient of the shift of the

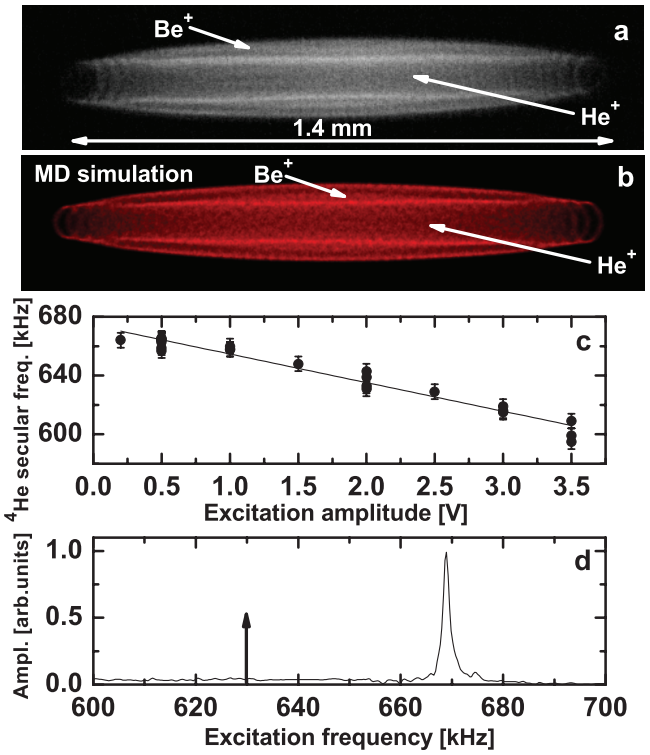


FIG. 1. (Color online) Drive-amplitude-induced resonance frequency shift. (a) Two-component $Be^+$-$^4He^+$ ion crystal underlying the measurement, containing ≈1100 $Be^+$ and ≈250 $^4He^+$ ions. Cooling laser direction is to the right. (b) MD simulation of the ion crystal in (a). (c) Motional frequencies for ultracold $^4He^+$ ions for the above ion crystal as a function of excitation amplitude. The line is a linear fit to the data. (d) Simulated secular frequency spectrum for the crystal in (b). Note that the $^4He^+$ secular frequency for zero excitation amplitude in (c), (d) is shifted to higher values compared to the calculated single-particle frequency (at 630 kHz), which is marked by a vertical arrow.

resonance frequency of ≈−20 kHz/V for $^4He^+$ (possible small nonlinear contributions to this behavior will be investigated in more detail in future studies). This shift can be explained by the interplay between two competing effects, the species-dependent cooling and heating rates present in the trap (see [18] for a detailed discussion).

Figure 1(d) shows the simulated secular frequency spectrum for the crystal shown in Fig. 1(b). The secular excitation process is simulated by instantly shifting the particles in one radial direction, e.g., the $x$ direction, which then subsequently perform oscillations around their equilibrium positions, damped by the interactions. Via MD simulations (without micromotion of the ions taken into account), the position of each particle is computed versus time. A Fourier analysis of the total kinetic energy time series gives the secular oscillation spectrum [19]. For the simulated spectrum, where a (relatively) small initial position shift is applied, the $^4He^+$ feature appears at 670 kHz. For comparison, the calculated single-particle frequency for $^4He^+$ is at 630 kHz. This shift agrees well with the extrapolated experimental value of 675 kHz from Fig. 1(c). Details on the numerical code can be found in [19]. See below for a discussion of the upward shift observed.

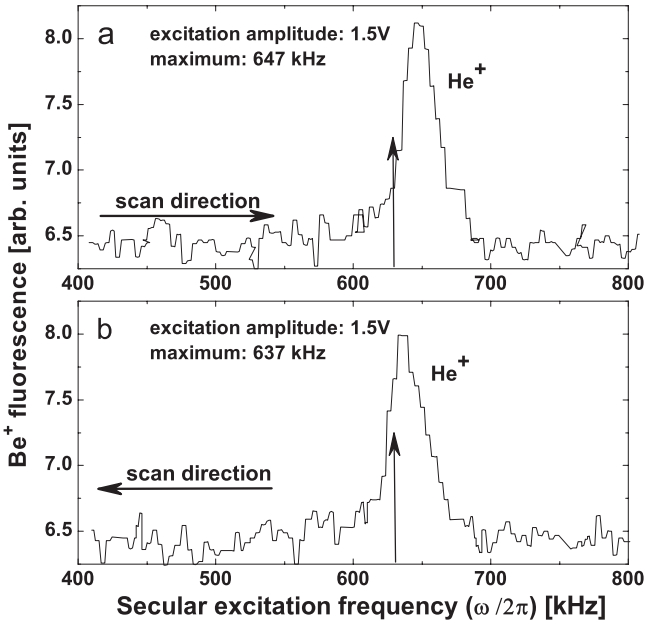


FIG. 2. Scan-direction-induced resonance frequency shift: Motional frequency spectrum of an cold $Be^+$ ion crystal (<20 mK) loaded with $He^+$ ions. Sweep direction toward higher (a) and toward lower (b) frequencies. The calculated single-particle secular frequency for $^4He^+$ ions is marked by vertical arrows.

#### 2. Scan direction

Another shift of the observed frequency is related to sweep direction of the motional excitation scan, shown in Fig. 2. An explanation for this effect can also be found in [18]. The $^4He^+$ resonance in backward direction is shifted toward smaller values compared to the forward scan by ≈10 kHz, this value being roughly constant across excitation amplitudes.

## VII. INTERACTION-INDUCED FREQUENCY SHIFTS

### A. Strong coupling

Strong coupling between trap modes of two different SC ion species contained in a $Be^+$ crystal is illustrated in Fig. 3(a). The mixed-species $Be^+$ ion crystal was formed following inlet and ionization of neutral $H_2$ gas. During the inlet phase, the neutral $H_2$ gas can react with $H_2^+$ ions to produce $H_3^+$ ions. This reaction proceeds with a large reaction rate on the order of the Langevin rate, with a rate constant $k=2.9\times10^{-9}$ $cm^3/s$ [20–22]. The inset in Fig. 3(a) shows the mixed-species ion crystal observed, with the large dark core stemming from the embedded light molecular ions. The slight asymmetry of shape of the crystal is due to small anisotropies of the effective trap potential and smaller amounts of heavier $BeH^+$ ions outside the $Be^+$ ion shells.

With large numbers of $H_3^+$ and $H_2^+$ ions, forming a multi-shelled core in the $Be^+$ crystal, their radial motions can be strongly coupled. In this situation, the ions of different species are sufficiently tightly coupled that they all oscillate at the same frequency. The situation is made more complex by the inhomogeneous environment of each ion, such as its po-

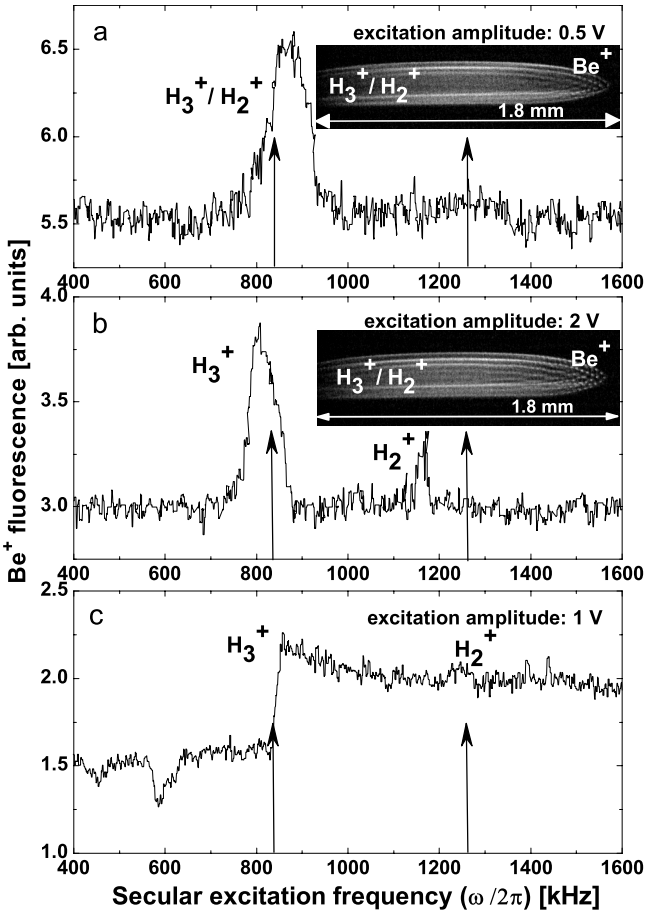


FIG. 3. Interaction-induced strong (a), (b) and weak (b) coupling, (a) Motional frequency spectrum of a $Be^+$ ion crystal following electron impact ionization of $H_2$ gas. The crystal (see inset) contains ≈1400 LC $Be^+$ ions and ≈1300 SC ions (as found by MD simulations). The SC ions consist of ≈700 $H_2^+$ and $H_3^+$ ions, located in the crystal core, and of ≈600 $BeH^+$ ions located outside the $Be^+$ shells. The latter are responsible for the slight asymmetry in the shape. The translational temperature of all species is ≈20 mK. Sweep direction toward higher frequencies. (b) Motional spectrum and ion crystal (inset) after partial removal of lighter SC ions (note the reduced size of the core), containing ≈1350 LC ions and ≈1200 SC ions: ≈450 $H_3^+$, ≈100 $H_2^+$, and ≈650 $BeH^+$. Relative fractions for the light ions were estimated from the size of the features in the spectrum. (c) Spectrum following electron impact ionization of $H_2$ gas in the cloud state. Calculated single-particle secular frequencies for the SC ions are marked by arrows: 840 kHz ($H_3^+$) and 1260 kHz ($H_2^+$). The feature at ≈580 kHz is attributed to the excitation of the second harmonic of the $Be^+$ trap mode (calculated frequency 560 kHz).

sition in the center or toward one end of the crystal. The individual positions can be strongly affected by the exact composition of the core. This leads to the spectrum seen in Fig. 3(a). The spectrum shows a broad feature between 800 and 930 kHz and was obtained with an excitation amplitude of 0.5 V. The calculated single-particle secular frequencies for pure $H_3^+$ or $H_2^+$ are at 840 and 1260 kHz, respectively.

For comparison, we also measured the secular spectrum for a mixed-species ($Be^+$, $H_3^+$, and $H_2^+$) ion plasma in the cloud (fluid) state [23], after loading and electron impact ionization of neutral $H_2$ gas, Fig. 3(c). The obtained secular frequencies for the individual species $H_3^+$ and $H_2^+$ are closer to the calculated single-particle value. This is due to the smaller coupling between the different ion species as compared to the crystalline state. At the excitation amplitude used, 1 V, a fraction of the SC ions was expelled from the trap when scanning over the $H_3^+$ secular frequency, by heating their translational motion. As a consequence of the removal of SC ions, the ion plasma becomes colder, but still remains in the cloud state, and the $Be^+$ fluorescence increases. After the scan has passed the $H_3^+$ resonance frequency, a slow decrease of the fluorescence occurs, probably, due to LC and SC ions reaching thermal equilibrium. Therefore, the secular spectrum [Fig. 3(c)] shows a steplike feature at this frequency, in contrast to the situation in the crystalline state. However, this reduction of temperature in the mixed-species ion plasma subsequently leads to a decrease of the $H_2^+$ feature in the secular spectrum, compared to the crystalline case [Fig. 3(a)]. In general, for a given ion number ratio, we found that the size of a specific spectral feature is, in first order, proportional to the excitation amplitude and inversely proportional to the ion temperature, for both the fluid and crystalline state.

The decrease in $Be^+$ fluorescence at around 580 kHz in Fig. 3(c) is attributed to the excitation of the second harmonic of the $Be^+$ trap mode of oscillation. This resonance is seen only in the cloud state and for slightly asymmetric trap potentials. The latter may also explain the shift of the $Be^+$ second harmonic frequency compared to the calculated frequency (560 kHz). According to the simulations, such an asymmetry-induced shift affects mainly the heavier ion species ($Be^+$) and is negligible for ion species closer to the trap axis ($H_3^+$ and $H_2^+$), due to their smaller mass-to-charge ratio and, consequently, the steeper trap potential.

The coupling strength between trap modes in mixed-species ion crystals can be controlled via the ion number ratio. Figure 4 shows a mixed-species ion crystal where the SC ion number ratio was varied [Figs. 4(a)–4(c)]. The crystal was obtained by loading and ionization of HD gas into a pure $Be^+$ ion ensemble. Initially, it contains ≈1000 $Be^+$ ions, ≈75 $HD^+$ ions, and ≈25 $D^+$ ions [Fig. 4(a)]. While repeated secular excitation measurements are performed [Figs. 4(d) and 4(e)], the number of $HD^+$ ions was decreased by dissociation using suitable lasers [24]. This leads to the formation of additional $D^+$ (and $H^+$) ions. Note that a part of the $HD^+$ dissociation product ions is lost from the trap, probably due to the large kinetic energy of these ions [24]. Furthermore, small background losses of both $HD^+$ and $D^+$ ions are due to chemical reaction with residual background gases. The initial $HD^+$ ion number was reduced to zero during the run, as obvious from the size reduction of the dark crystal core [Figs. 4(a)–4(c)] and the relative sizes of the individual features in the spectra [Fig. 4(e)]. At the same time, the number of $D^+$ ions is raised to ≈35. As more and more $HD^+$ ions are dissociated, the numbers and relative fractions of $HD^+$ and $D^+$ ions are varied, and thus the coupling between their trap oscillation modes is modified. Reduced coupling strength between the different $HD^+$ and $D^+$ trap modes enables their resolution in the spectra toward the middle of the run [Fig. 4(e)]. The results described also show the transition between strong (at the beginning of the run) and weak coupling of

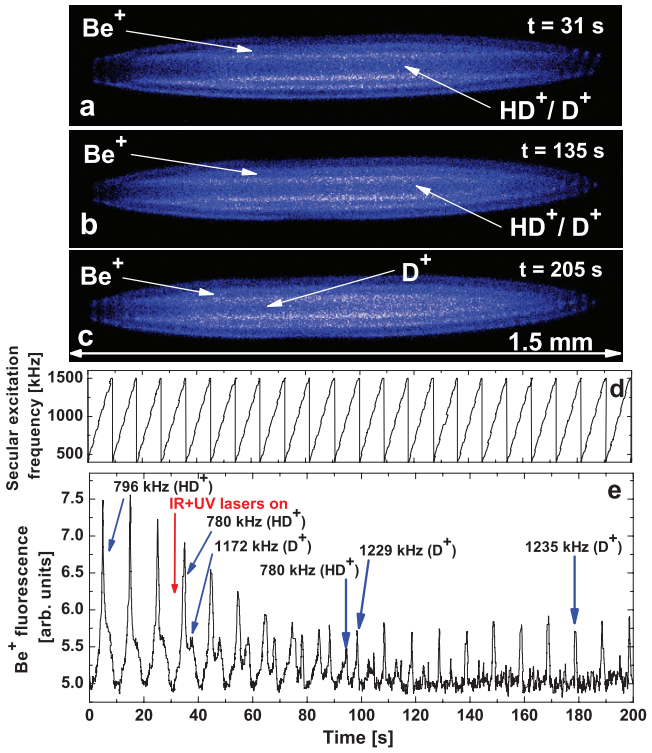


FIG. 4. (Color online) Coupling strength as a function of relative particle fractions. (a), (b), (c) Mixed-species ion crystal at three different times after the start of the secular frequency measurement, containing different ion numbers and relative particle fractions. The change of the ion numbers is obvious from the reduction in size of the crystal core (containing $HD^+$ and $D^+$ ions) with time. Ion species numbers obtained from simulations: (a) 1000 $Be^+$, 75 $HD^+$, and 25 $D^+$, (b) 1000 $Be^+$, 20 $HD^+$, and 30 $D^+$, (c) 1000 $Be^+$ and 35 $D^+$. (d) Repeated secular excitation frequency scans (scan range 400–1100 kHz). Sweep direction toward higher frequencies. Excitation amplitude 3 V. (e) Series of low-mass motional frequency spectra, illustrating the change of the strong coupling effect as a function of relative ion numbers. The measured resonance frequencies for $HD^+$ and $D^+$ ions for three times during the run are also shown.

trap modes (toward the end of the run). See below for a detailed discussion.

### B. Weak coupling

Figure 3(b) shows the secular frequency spectrum after removal of a fraction of the SC ions, via repeated secular excitation. This leads to a reduction of the size of the dark crystal core, visible in the inset. The number of $Be^+$ and $BeH^+$ ions changed slightly compared to Fig. 3(a), due to chemical reactions with residual background $H_2$ gas [25,26].

In the spectrum, two resonances are now identified, attributed to the presence of $H_3^+$ and $H_2^+$ ions. The $H_3^+$ resonance, however, is shifted toward lower frequencies (by ≈30 kHz) compared to its single-particle frequency (at 840 kHz), whereas the $H_2^+$ resonance exhibits a larger shift (by ≈90 kHz) relative to its single-particle frequency at 1260 kHz. The positions of the resonances are determined by two mechanisms, a downward frequency shift caused by the amplitude of the motional excitation combined with an upward shift which is intrinsic to the situation of more than one species being simultaneously trapped [27]. The resulting shift of the resonance frequencies is stronger for the lighter molecular ions ($H_2^+$).

The upward shift is clearly seen in Fig. 1(c), for the $Be^+$-$^4He^+$ crystal. From the experimental data we extrapolate a value of ≈675 kHz for zero excitation amplitude (calculated single-particle frequency 630 kHz). This shift is caused by the Coulomb interaction between the $Be^+$ body of the crystal and the $He^+$ core, and is confirmed by the MD simulations. The presence of the Coulomb potential of the core ions "steepens" the effective potential in which the beryllium ions move (when added to the harmonic trapping potential). Likewise, the outer beryllium shells' Coulomb potential increases the effective harmonic frequency (to a first approximation) confining the core ions. The reason this is not observed for pure crystals (inner shells altering the frequency of outer shells) is that they all oscillate coherently when driven by an external potential, and so the ion's Coulomb potential moves with them—no ion experiences significant deviation from its equilibrium position in the crystal, although the crystal as a whole is moving. When two species, with different motional frequencies, are present this is no longer true—each moves in the Coulomb potential of the other. The size of the induced secular frequency shifts is also confirmed by our MD simulations [Fig. 1(d)].

The amplitudes of the resonances in Fig. 3(b) indicate that (approximately) the number of $H_3^+$ ions exceeds the number of $H_2^+$ ions by a factor of 2. Using other loading procedures, e.g., varying the loading time or the partial pressure of the neutral $H_2$ gas, different relative fractions between the individual core constituents were achieved, and thus different coupling strengths were observed. For crystals with varying ion fractions in the core, the comparison between experimental and simulated spectra allows for an estimate of their relative fractions, even when the individual features are not resolved, whereas the total LC and SC ion numbers are determined by comparison between the CCD images observed and the simulated crystal shapes [9,19,26].

### C. Asymmetry

The axial symmetry of the effective potential is broken when a static (quadrupole) potential is applied to the trap, so that the different ion species are displaced from the trap center. The displacement is larger for heavier (less tightly bound) species. In this way one can achieve a configuration in which lighter SC ion species are located outside the beryllium ion shell ensemble.

Figure 5 shows observed secular frequency spectra [Figs. 5(b) and 5(f)] for different asymmetric mixed-species ion crystals [Figs. 5(a) and 5(c)]. In Figs. 5(d)–5(f), the results of MD simulations for the ion crystal in Fig. 5(c) together with the corresponding simulated secular frequency spectrum are presented, respectively.

For mixed-species ion crystals with at least three components in an asymmetric potential, the secular spectrum at low

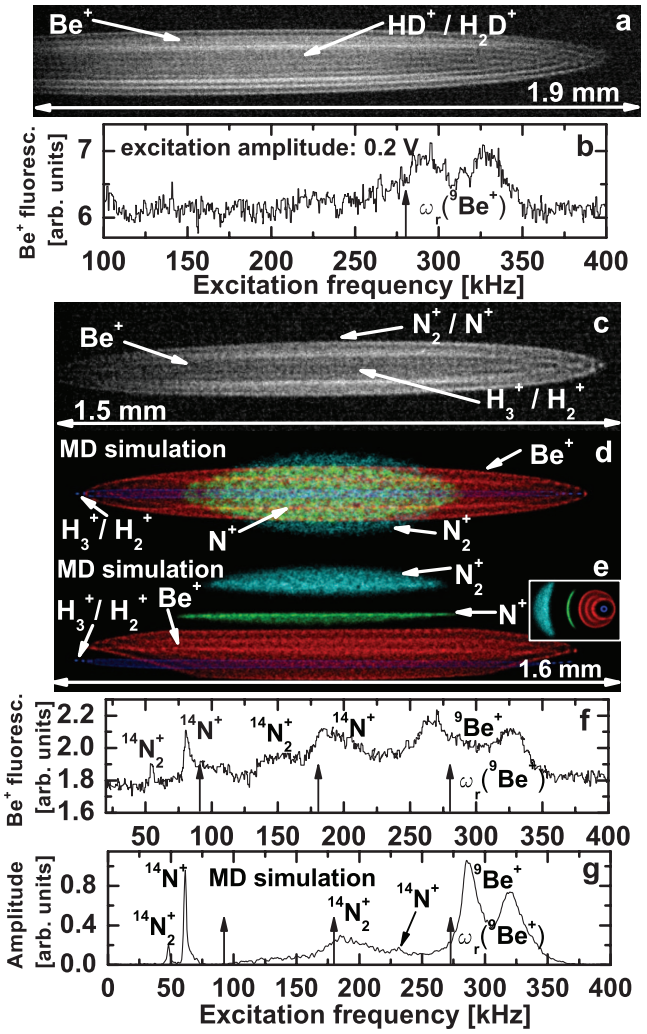


FIG. 5. (Color online) Trap-asymmetry-induced frequency shifts. (a) Asymmetric $Be^+$ ion crystal containing ≈3220 $Be^+$, ≈250 $H_2D^+$, and ≈250 $HD^+$ ions at ≈30 mK (dark core). (b) High-mass motional spectrum of the crystal in (a). (c) Asymmetric $Be^+$ ion crystal, after loading with $H_2$ gas. The crystal contains ≈900 $Be^+$, ≈90 $H_3^+$, ≈90 $H_2^+$, ≈50 $N^+$, and ≈100 $N_2^+$ at 20 mK. Relative fractions of $H_2^+$ and $H_3^+$ ions are estimated from corresponding secular spectra. (d), (e) MD simulation of the crystal in (c). The view is from the side (d), same perspective as in (c), from the top (e) (in the plane and perpendicular to the plane of observation of the camera, respectively), and along the axis of the trap, inset in (e). Individual ion species are spatially shifted relative to each other and relative to the trap center, due to trap potential anisotropy. (f) High-mass motional spectrum of the crystal in (c). (g) Simulated secular frequency spectrum for the crystal in (d). Vertical arrows mark the calculated single-particle frequencies of $N_2^+$ (90 kHz), $N^+$ (180 kHz), and $Be^+$ (280 kHz).

excitation frequencies can be complex. In the absence of heavier molecular ions, usually embedded outside the $Be^+$ ion shells, the secular frequency for the $Be^+$ ions usually is split in frequency and shifted to slightly higher frequencies, due to Coulomb coupling to the large number of light molecular species embedded in the crystal core [Figs. 5(a) and 5(b)].

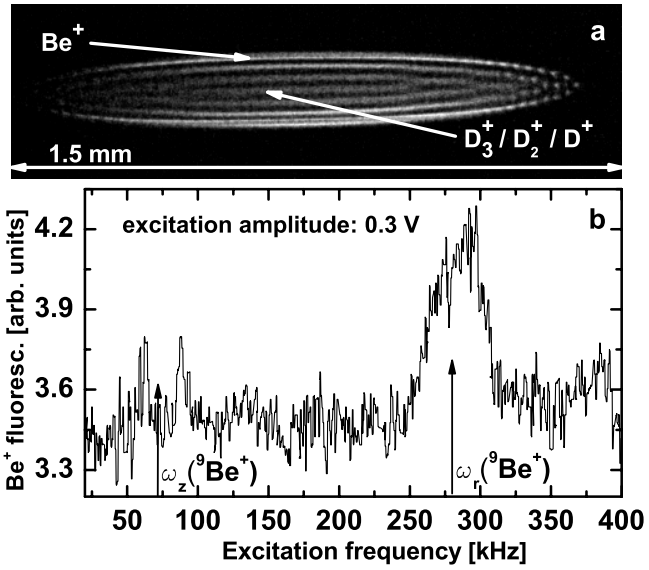


FIG. 6. Excitation of axial trap modes in an asymmetric trap potential. (a) Asymmetric mixed-species ion crystal containing 700 $Be^+$ and 550 lighter SC ions, $D_3^+$, $D_2^+$, and $D^+$, at ≈20 mK. Heavier molecular ions were removed from the trap. (b) High-mass motional spectrum of the crystal in (a). Measured resonances are attributed to the excitation of axial (at 63 and 88 kHz) and radial (at around 285 kHz) $Be^+$ trap modes. The calculated axial (71 kHz) and radial (280 kHz) single-particle frequencies for $Be^+$ are marked with arrows.

In the presence of heavier ions (and of a light core) [see Figs. 5(c) and 5(f)], the beryllium resonance is also split in frequency (peaks at 265 and 330 kHz). Its calculated single-particle frequency is at 280 kHz. Additional peaks at 190, at 150, at 81, and at 54 kHz are present. These resonances are caused by heavier contaminants present in the trap: $N^+$ ions (at 81 and 190 kHz) and $N_2^+$ ions (at 54 and 150 kHz), again split in frequency due to the anisotropy of the trap potential. The calculated single-particle frequencies are at 90 (for $N_2^+$) and 180 kHz (for $N^+$).

In addition, we observed experimentally that in the presence of a heavier or lighter species outside the beryllium crystal (possible for asymmetric crystals), and/or in the presence of a strong cooling light-pressure force on the beryllium ions (which moves the beryllium ions to one end of the crystal) in an asymmetric trap potential, the radial excitation of the heavy or light ions in the outer crystal regions can couple into the $z$ motion of the beryllium. As the outer (heavy or light) ions are moved radially, the beryllium is displaced along $z$, and so its axial motion is excited. A mixed-species ion crystal and the corresponding motional spectrum illustrating this effect are shown in Figs. 6(a) and 6(b), respectively. In the spectrum, we found that the axial $Be^+$ resonance is split in frequency (due to the trap anisotropy) and that the radial $Be^+$ resonance is broadened compared to the unperturbed situation. Furthermore, the axial and radial resonances are centered around slightly larger frequencies compared to the calculated single-particle frequencies. This is attributed to Coulomb-coupling-induced frequency shifts in the mixed-species ion crystal. The excitation of the axial

resonances is not present if the SC ions are expelled from the trap or the asymmetry of the trap potential is removed.

In the special case of the spectrum shown in Fig. 5(f) the $Be^+$ axial resonance (possibly split in frequency) is probably hidden under the larger features caused by $N_2^+$ and $N^+$ ions. We expect that a systematic study of the above axial excitation of beryllium trap modes will be necessary for better characterization of the underlying mechanisms. Note that we did not observe shifts of the secular frequencies of lighter molecular ions inside or outside the $Be^+$ crystal for anisotropic trap potentials (i.e., when the symmetry of the trap potential was broken by suitable static offset potentials) compared to the isotropic case.

Furthermore, as confirmed by our simulations, a common mode of oscillation between $Be^+$ and heavier impurity ions, e.g., $N^+$, could contribute to the resonance at around 150 kHz in Fig. 5(f), which in this case is dominated by the $N_2^+$ resonance and which is not observed when such a crystal is symmetrized, and/or after removal of the heavier ions from the trap [see also Figs. 5(a) and 5(b)]. After symmetrization of the trap potential (i.e., placing the dark core containing the molecular ions in the trap center), the frequency splitting of the axial and radial $Be^+$ resonances $\omega_z$ and $\omega_r$ is also absent.

Figures 5(d)–5(f) show results obtained from MD simulations for the crystal in 5(c) together with the corresponding simulated secular spectrum. As obvious from Figs. 5(d) and 5(e) the ion species are spatially separated, due to the trap potential anisotropy. The simulated spectrum in Fig. 5(g) is in reasonable overall agreement with the experimental result [Fig. 5(f)]. However, the detailed positions of the features in the simulated spectrum deviate from the experimental data. The individual features identified in Fig. 5(g) are at 285 and at 320 kHz ($Be^+$ ions), at 61 and at 232 kHz ($N^+$ ions), and at 48 and at 188 kHz ($N_2^+$ ions). The simulations show that the position and size of the individual features depend strongly on the ion numbers involved and the size of the electric fields causing the trap anisotropy. Using the various ion numbers as fit parameters in the simulations, the agreement between experimental and theoretical spectra could be improved. Thus, an accurate experimental determination of the ion numbers, e.g., by ion extraction and counting, would improve the accuracy of the simulated spectra.

## VIII. SUMMARY

In this work, we investigated the motional resonance spectrum of multispecies ion crystals (up to four species) in a linear Paul trap, for both isotropic and anisotropic trap potentials. The coupling between different motional resonances was studied experimentally and theoretically (by MD simulations), in order to interpret the complicated trap mode spectra measured and to reliably identify sympathetically cooled particle species, even when individual secular resonances cannot be resolved and/or direct (fluorescence) detection is prevented. We have shown that the simulations are essential for the interpretation of the experimental spectra, which are complicated by the fact that the observed resonance frequencies and their coupling are usually determined by the superposition of several, sometimes opposing, line shifting effects. In the MD simulations the different frequency shifting effects contributing to the spectra were modeled and their interplay was studied. The simulated spectra faithfully reproduce the experimental results. Quantitative agreement can be achieved using the ion numbers in the simulations as fit parameters, thus allowing for an accurate determination of relative ion species numbers contained in a given crystal. We have observed that the spectra become more complicated as the number of species increases and the lines broaden as the ion numbers increase. Further studies should explore the mode spectra of crystals containing five or more species and the mechanisms leading to the axial excitation of the beryllium ion modes.

## ACKNOWLEDGMENTS

We thank H. Wenz and C. B. Zhang for the MD simulations and the Deutsche Forschungsgemeinschaft (DFG) and the EC network HPRN-CT-2002-00290 for financial support. P. B. was also supported by the Alexander von Humboldt Stiftung.

[1] S. G. Karshenboim and V. G. Ivanov, Eur. Phys. J. D **19**, 13 (2002).
[2] S. Schiller and V. I. Korobov, Phys. Rev. A **71**, 032505 (2005).
[3] M. Greiner, C. A. Regal, and D. S. Jin, Phys. Rev. Lett. **92**, 040403 (2004).
[4] S. Dürr *et al.*, Phys. Rev. Lett. **92**, 020406 (2004).
[5] A. Fioretti *et al.*, Phys. Rev. Lett. **80**, 4402 (1998).
[6] J. D. Weinstein *et al.*, Nature (London) **395**, 148 (1998).
[7] S. A. Rangwala *et al.*, Phys. Rev. A **67**, 043406 (2003).
[8] K. Molhave and M. Drewsen, Phys. Rev. A **62**, 011401(R) (2000).
[9] P. Blythe, B. Roth, U. Fröhlich, H. Wenz, and S. Schiller, Phys. Rev. Lett. **95**, 183002 (2005).
[10] M. Welling *et al.*, Int. J. Mass Spectrom. Ion Process. **172**, 95 (1998).
[11] T. Baba and I. Waki, J. Appl. Phys. **89**, 4592 (2001).
[12] M. Drewsen *et al.*, Phys. Rev. Lett. **93**, 243201 (2004).
[13] H. Schnitzler *et al.*, Appl. Opt. **41**, 7000 (2002).
[14] D. J. Larson *et al.*, Phys. Rev. Lett. **57**, 70 (1986).
[15] F. Diedrich *et al.*, Phys. Rev. Lett. **59**, 2931 (1987).
[16] B. Roth, U. Fröhlich, and S. Schiller, Phys. Rev. Lett. **94**, 053001 (2005).
[17] U. Fröhlich, B. Roth, and S. Schiller, Phys. Plasmas **12**, 073506 (2005).
[18] T. Baba and I. Waki, Jpn. J. Appl. Phys., Part 1 **92**, 4109 (2002).
[19] B. Roth, A. Ostendorf, H. Wenz, and S. Schiller, J. Phys. B **38**, 3673 (2005).
[20] E. W. McDaniel, V. Cermak, A. Dalgarno, E. E. Ferguson, and

L. Friedman, *Ion-Molecule Reactions* (John Wiley & Sons, New York, 1970).
[21] K. P. Huber and G. Herzberg, *Molecular Spectra and Molecular Structure* (Van Nostrand–Reinhold, New York, 1979).
[22] M. T. Bowers and D. E. Elleman, J. Chem. Phys. **51**, 4606 (1969).
[23] D. H. E. Dubin and T. M. O'Neil, Rev. Mod. Phys. **71**, 87 (1999).
[24] B. Roth, J. Koelemeij, H. Daerr, and S. Schiller, Phys. Rev. A **74**, 040501(R) (2006).
[25] B. Roth, P. Blythe, H. Wenz, H. Daerr, and S. Schiller, Phys. Rev. A **73**, 042712 (2006).
[26] B. Roth, H. Daerr, P. Blythe, L. Patacchini, and S. Schiller, J. Phys. B **39**, S1241 (2006).
[27] T. Hasegawa and T. Shimizu, Phys. Rev. A **66**, 063404 (2002).

# Vibrational spectroscopy of cold $HD^+$ with 2 ppb accuracy

Jeroen C. J. Koelemeij,[1*] Bernhard Roth,[1] Andreas Wicht,[1]
Ingo Ernsting,[1] Stephan Schiller[1]

[1]Institute for Experimental Physics, Heinrich-Heine-Universität Düsseldorf, Germany

*To whom correspondence should be addressed; E-mail: jeroen.koelemeij@uni-duesseldorf.de.

**By measurement of the frequency of a vibrational overtone transition in the molecular hydrogen ion $HD^+$ , we demonstrate optical spectroscopy of trapped molecular ions with submegahertz accuracy. The achieved 2 ppb relative accuracy is a factor of 150 higher than previous results for $HD^+$ , and the measured transition frequency agrees well with recent high-accuracy *ab initio* calculations, which include high-order quantum electrodynamic effects. The key ingredients for achieving this level of accuracy are sympathetic cooling of $HD^+$ to 50 mK via laser-cooled $Be^+$ ions, which substantially reduces Doppler broadening, and spectroscopy at 1395 nm with a diode laser locked to a stable frequency comb. As indicated by an comprehensive analysis of systematic errors, our method bears potential for achieving considerably higher accuracy, and may, when combined with slightly improved theoretical calculations, provide a new method to determine the electron-proton mass ratio with greater accuracy.**

The molecular hydrogen ion and its isotopomers play a fundamental role in molecular physics

because of their simple three-body nature, making them a benchmark system for quantum theoretical calculations (*1*). Past precision spectroscopic measurements of molecular hydrogen ions and theoretical results have been in general agreement at the level of the dominant (of third order in the fine-structure constant $\alpha$) quantum electrodynamic contributions (*2–4*). Recently, the accuracy of *ab initio* calculations of the energy levels of the molecular hydrogen ion has been strongly improved (*5, 6*), and is now approaching the limits set by the uncertainty in the values of the fundamental constants which enter the calculations. The largest contributor to this type of uncertainty is the electron-proton mass ratio, $m_e/m_p$, which is known to within 0.46 ppb (*7*). If the uncertainty due to the theoretical formalism becomes smaller than that caused by $m_e/m_p$, the theoretical functional dependence of the energy levels on $m_e/m_p$ may be combined with results from high-resolution spectroscopy to infer an improved value for $m_e/m_p$ (*2*). Both this perspective and the theoretical advances call for improved measurements of the energy levels of $HD^+$ In view of the recently found indication of a variation of $m_e/m_p$ over $\sim$ Gyr timescales (*8*), which would signify a violation of the Einstein equivalence principle (*9*), it is also important to develop high-precision molecular spectroscopic techniques allowing laboratory spectroscopic searches for a present temporal variation of $m_e/m_p$ (*10*). Molecular hydrogen ions appear as promising systems because their accurate theoretical description is possible.

High-accuracy spectroscopy is best implemented using cold and confined particles. This has been achieved at a very high level with laser-cooled, trapped atomic ions, as exemplified by single-ion atomic clocks; see, for example, Ref. (*11*) and references to other work therein. Molecular ions, however, have not seen such a development, which is primarily due to a lack of transitions that can be used for laser cooling and for internal-state detection, as required for the spectroscopy. Several schemes to overcome this limitation have been proposed (*12*) and, as far as it concerns cooling, realized (*13, 14*). Recently, we have demonstrated a complete method

for molecular ion spectroscopy, which relies on sympathetic cooling of the molecular ions by storing them with laser-cooled atomic ions. Detection of a laser-induced transition is done by selective dissociation of the excited molecules and mass-spectroscopic measurement of the number of remaining molecular ions. Using this method, we previously obtained spectra of the $(v, N) : (4, 1) \leftarrow (0, 2)$ and $(4, 3) \leftarrow (0, 2)$ transitions in the $X\ ^2\Sigma^+$ electronic ground state of $\mathrm{HD}^+$ (*15*). In this work we describe a precision frequency measurement of the $(v, N) : (4, 3) \leftarrow (0, 2)$ transition, which is, to our knowledge, the most accurate optical frequency measurement performed on any molecular ion to date. We also present a comprehensive theoretical analysis of the systematic effects that contribute to the frequency uncertainty.

In the experimental procedure, we load $\sim 2000\ \mathrm{Be}^+$ ions and $\sim 150\ \mathrm{HD}^+$ ions in a linear rf trap by *in situ* electron impact ionization of their neutral counterparts (*14*). The ions are kept under ultrahigh vacuum conditions to virtually eliminate the effect of collisions with background gas constituents. The $\mathrm{Be}^+$ ions are cooled by a single 313 nm laser beam, leading to the formation of a so-called ellipsoidal Coulomb crystal, in which the ions have a translational (secular) temperature of $\sim 50$ mK in all three dimensions (Fig. 1). A measure for the number of trapped $\mathrm{HD}^+$ ions is obtained by applying an ac electric field which drives the motion of the $\mathrm{HD}^+$ ions. For a specific mass-dependent frequency, driving takes place resonantly and causes heating of the entire Coulomb crystal, which manifests itself as a change in the 313 nm fluorescence emitted by the $\mathrm{Be}^+$ ions. Using this mass-spectroscopic detection method, the molecular spectroscopy is performed by (1+1') resonance enhanced multiphoton dissociation (REMPD) of the $\mathrm{HD}^+$ ions as follows: the first photon at $1.4\ \mu$m populates the $v = 4$ level (which is otherwise unpopulated under the conditions in our apparatus, as spontaneous decay is possible through the $\mathrm{HD}^+$ permanent dipole moment), from which the $\mathrm{HD}^+$ ions are selectively dissociated by an additional 266 nm photon (Fig. 2A). The consequent loss of $\mathrm{HD}^+$ ions is interpreted as a signature of resonance of the first photon. We note that upper-state lifetimes are about 10 ms,

which would make spectroscopy by infrared fluorescence detection a challenging task. The laser system used is referenced to a GPS-disciplined hydrogen maser. It is based on a grating-enhanced diode laser with resonant optical feedback, which combines the good tunability of regular grating diode lasers with the good short-term stability of diode lasers with resonant optical feedback (*16*). This laser is frequency-locked to a titanium:sapphire-based, self-referenced fs-frequency comb, which itself is phase locked to the hydrogen maser. To frequency-lock the diode laser to the frequency comb we preprocess the beat note signal between diode laser and comb by a tracking oscillator. We subsequently use a frequency-to-voltage scheme (*17*) to derive an error signal for the diode laser frequency stabilization from the tracking oscillator output signal. This locking scheme limits the diode laser frequency inaccuracy to a few kHz over the 6 s duration of one measurement cycle, and to less than 25 kHz on longer time scales ($\sim$ days). The resolution of the laser system is currently limited to $\sim 300$ kHz, which is primarily due to the short-term instability of the frequency comb.

The spectrum of the $(v, N) : (4, 3) \leftarrow (0, 2)$ transition at 1395 nm measured with this laser system is displayed in Fig. 3. Each data point shown in the graph is the average of seven individual points, each of which equals the fractional loss of $\mathrm{HD}^+$ ions induced by a 6 s period of REMPD. The signal due to loss of $\mathrm{HD}^+$ by processes other than the REMPD process (*e.g.* chemical reactions during collisions with background gas molecules) is independently measured and eliminated from the data. The spectrum shown in Fig. 3 was taken in three runs lasting five to eight hours each. Care was taken to reproduce the same conditions (most importantly the $\mathrm{HD}^+$ ion number and temperature (*18*), the intensities of all lasers involved, and the magnetic field settings) during each run. The spectrum in Fig. 3 shows two resolved hyperfine components around the deperturbed frequency, $\nu_d$, of the $(v, N) : (4, 3) \leftarrow (0, 2)$ rovibrational transition. The value of $\nu_d$ is of interest as it contains the dependence on $m_e/m_p$ . To separate off the hyperfine contribution to the spectrum, we fit the spectrum to a model line function ob-

tained using the theoretical effective hyperfine hamiltonian given by Bakalov *et al.* (*19*). We neglect contributions arising from nucleon-rotation interactions, the deuteron quadrupole moment, and finite-size effects of the proton and deuteron. The omitted terms contribute less than 100 kHz to the hyperfine level energies. A schematic of the hyperfine levels in the upper and lower rovibrational states, as well as the strongest electric dipole transitions between them, are shown in Fig. 2B. The theoretical spectrum in the absence of any broadening or micromotion effects is represented by the stick spectrum in Fig. 3. The model line function includes Doppler broadening, as well as the sidebands of each line in the spectrum due to excess micromotion of the $HD^+$ ions at the $14.2$ MHz drive frequency of the trap. This micromotion is driven by electric fields that stem from imperfections in the ion trap design, and has an amplitude of $0.3$ $\mu$m along the propagation direction of the infrared laser beam. We independently confirmed the presence of micromotion by performing a time-to-amplitude correlation measurement on the 313 nm fluorescence (*20*). As Doppler broadening gives a width of $\Gamma \sim 20$ MHz to each spectral component, the carrier and sidebands of each feature merge together to yield an overall broadening to $\sim$ $40$ MHz. Several of the model parameters ($\nu_d$, a vertical scaling factor, and $\Gamma$) of the spectrum are fitted to all individual data points simultaneously. The fitted spectrum is indicated by the smooth continuous curve through the data in Fig. 3. A fit to the averaged data points gives the same result. From the fitted value for the Doppler width, $\Gamma = 20.3(1.4)$ MHz, we deduce an $HD^+$ temperature of 53(8) mK, which agrees with results from molecular dynamics simulations of the crystal images observed with a CCD camera (*14*). The most important of all fitted parameters, the value for $\nu_d$, is sensitive to changes in the other parameters of the model. Uncertainties in parameters of the model line function which are not fitted but determined independently, are translated to an additional uncertainty in $\nu_d$, yielding a total $1\sigma$ statistical uncertainty of 0.45 MHz. We note that the measurement of the laser frequency does not contribute significantly to this uncertainty. The fit also indicates that the hyperfine structure

observed in our experiment agrees with the calculated hyperfine structure at the same level of uncertainty.

Table 1: Systematic shifts and uncertainties

| Origin | Shift (MHz) | Uncertainty (MHz) |
|---|---|---|
| Measurement uncertainty | 0 | 0.45 |
| Hyperfine Hamiltonian | 0 | 0.14 |
| Zeeman effect | 0 | 0.06 |
| ac Stark shifts[a] | 0 | 0.017 |
| $2^{\mathrm{nd}}$-order Doppler shift[a] | 0 | 0.01 |
| Collisional shift[a] | 0 | 0.001 |
| Final result for $\nu_d$ | 214 978 560.6 | 0.5 |
| Theory (*5, 6*) | 214 978 560.88 | 0.07 |

[a]Shift does not contribute significantly and is set to zero here

Besides the statistical uncertainty, the value of $\nu_d$ has an uncertainty due to systematic shifts. An overview of systematic shifts and their uncertainties is shown in Table 1. The largest contribution to the inaccuracy comes from the terms which were omitted from the hyperfine hamiltonian. The second largest uncertainty stems from the Zeeman effect, which we evaluate as follows. First, we determine the magnetic field in our ion trap from the spatial intensity distribution of the 313 nm fluorescence, as seen on a camera image of the $\mathrm{Be}^+$ ion crystal. From the behavior of this distribution as a function of the magnetic field vector, which can be controlled through three mutually perpendicular sets of Helmholtz coils, we retrieve the magnetic field and its gradient. Next, we theoretically investigate the effect of the measured magnetic field (which varies between 0 and 1 G over the trap volume) on the observed spectrum using the Zeeman Hamiltonian given by Hegstrom (*21*); see methods in the supporting online material. Our analysis yields a zero Zeeman shift with a statistical uncertainty margin of 60 kHz. This value is

taken as an upper limit on the uncertainty of the Zeeman shift to $\nu_d$, and should be compared with the expected magnitude of rotational Zeeman shifts of $\nu_d \sim g_R \mu_n \times (1\ \mathrm{Gauss}) \approx 500$ Hz, where $g_R$ is the $g$ value for the rotation of the molecule, and $\mu_n$ stands for the nuclear magneton.

Other systematic shifts include ac Stark shifts due to the various optical fields at the position of the ions. The infrared laser itself causes a shift as it probes a multilevel system, consisting of various transitions at different frequencies which are all addressed by the infrared laser. Taking three mutually connected levels at a time, we solve the optical Bloch equations to obtain an upper bound to the shift. The 266 nm dissociation laser and the 313 nm cooling laser also cause a shift as they couple bound states to the dissociation continuum. We obtain the strength of the bound-continuum state coupling from the wavelength-dependent dissociation rate given in Ref. (*22*), and use Fano theory to estimate the total shift caused by the 266 nm and 313 nm lasers (*23*). Both ultraviolet lasers have an intensity corresponding to about 1 mW focused to a $100$ $\mu$m spot size at the position of the ions, whereas the infrared laser has $170$ $\mu$W of power focused to a $200$ $\mu$m spot size. We estimate that each of these lasers causes an ac Stark shift of much less than 10 kHz to $\nu_d$. Other ac Stark shifts are due to the presence of blackbody radiation (BBR) and the rf trap potential. To estimate the magnitude of these shifts, we use the scalar polarizability $\alpha(\omega)$ for the levels probed by our laser. $\alpha(\omega)$ is found employing the $\mathrm{HD}^+$ rovibrational wavefunctions and the dipole moment function for the $X\ ^2\Sigma^+$ state obtained using the *ab initio* data from Ref. (*24*). We find that both the BBR shift and the shift by the trap potential are smaller than 1 kHz. Other small systematic shifts are due to collisions with background gas constituents and the second-order Doppler effect, for which we take into account both the trap (secular) motion and the (excessive) micromotion. We estimate that these shifts affect $\nu_d$ by less than 1 kHz and 10 kHz, respectively.

Our final result for $\nu_d$ is $214\,978\,560.6(5)$ MHz. The 2.3 ppb relative uncertainty in our result represents an improvement over previous spectroscopic results for $\mathrm{HD}^+$ by a factor of 150 (*3,*

*25*). Our value agrees well with the most recent theoretical value of $214\,978\,560.88(7)$ MHz by Korobov, who considered relativistic and radiative corrections up to order $m_e\alpha^6$ (*5,6*). Thus, our value for $\nu_d$ is consistent with the 2002 CODATA recommended value for $m_e/m_p$ , which was used in the calculations, to within 5 ppb. To obtain this margin, we used the partial derivatives with respect to $m_e/m_p$ of the energies of the $(v, N) : (0, 2)$ and $(4, 3)$ levels, given in Ref. (*10*).

The error budget in Table 1 shows that there are no obvious limitations for improvement of the experimental accuracy by one order of magnitude, other than the statistical uncertainty and the uncertainty in the hyperfine Hamiltonian. The former is closely related to the width of the lines which constitute the spectrum. With relatively straightforward modifications to the apparatus, it will be possible to eliminate the micromotion sidebands. Furthermore, resolution in the kHz range (and possibly lower) will result if the confinement by the trap is increased so that Doppler-free spectroscopy in the Lamb-Dicke regime becomes possible, thereby removing the Doppler broadening (*26*). In addition, the hyperfine Hamiltonian and the Zeeman effect may be determined experimentally with sufficient accuracy by rf spin flip spectroscopy in combination with the REMPD method used here (*3*). When the experimental accuracy improves by one order of magnitude, and provided the uncertainty in the theoretical level energies improves by a factor of two, a competitive new value for $m_e/m_p$ could be inferred already. In addition, the combined theoretical and experimental results for the $HD^+$ energy levels would establish an accurate link between the value of $m_e/m_p$ and that of other fundamental constants, such as $\alpha$ and the proton-deuteron mass ratio. Finally, we point out that the relative accuracy achieved in the spectroscopy here is considerably better than obtained with methods based on buffer gas cooled trapped molecular ions (*27*) and obtained with ion beams, buffer gas cooled by a supersonic jet (*28*), where Doppler broadening due to $\geq 10$ K temperatures limits the resolution achievable with single-photon spectroscopy. The main ingredients of the method, sympathetic cooling by laser-cooled ions and a destructive spectroscopic scheme in combination with mass-

specific detection, lend themselves for extension of this form of high-resolution spectroscopy to other ionic species such as, for example, the astronomically relevant $H_3^+$ ion (*29*), and complex molecules (*30*). Therefore, it could lead to a vast improvement of the accuracy of spectroscopic constants for many molecular ions, and give an impetus to developments in molecular theory.

# References and Notes


1. C. A. Leach, R. E. Moss, *Annu. Rev. Phys. Chem.* **46**, 55 (1995).
2. W. H. Wing, G. A. Ruff, W. E. Lamb, Jr., J. J. Spezeski, *Phys. Rev. Lett.* **36**, 1488 (1976).
3. K. B. Jefferts, *Phys. Rev. Lett.* **23**, 1476 (1969).
4. A. Carrington, I. R. McNab, C. A. Montgomerie, *Mol. Phys.* **66**, 519 (1989).
5. V. I. Korobov, *Phys. Rev. A* **74**, 052506 (2006).
6. V. I. Korobov (private communication).
7. P. J. Mohr, B. N. Taylor, *Rev. Mod. Phys.* **77**, 1 (2005).
8. E. Reinhold, *et al.*, *Phys. Rev. Lett.* **96**, 151101 (2006).
9. C. Will, *Theory and Experiment in Gravitational Physics*, revised ed. (Cambridge University Press, Cambridge, UK, 1993).
10. S. Schiller, V. Korobov, *Phys. Rev. A* **71**, 032505 (2005).
11. W. H. Oskay, *et al.*, *Phys. Rev. Lett.* **97**, 020801 (2006).
12. P. O. Schmidt, *et al.*, *Proc. 2006 Non-Neutral Plasma VI Workshop* p. 305 (2006).
13. K. Mølhave, M. Drewsen, *Phys. Rev. A* **62**, 011401 (2000).

14. P. Blythe, B. Roth, U. Fröhlich, H. Wenz, S. Schiller, *Phys. Rev. Lett.* **95**, 183002 (2005).

15. B. Roth, J. C. J. Koelemeij, H. Daerr, S. Schiller, *Phys. Rev. A* **74**, 040501 (2006).

16. A. Wicht, M. Rudolf, P. Huke, R. Rinkleff, K. Danzmann, *Appl. Phys. B* **78**, 137 (2004).

17. A. Wicht *et al.*, in preparation.

18. In our setup, $HD^+$ temperatures as low as 20 mK can be achieved, which imply a Doppler width of 12–13 MHz and would allow partial resolution of the micromotion sidebands. However, this would also introduce a sensitivity of the shape of the spectrum to temperature differences between different runs, thereby causing additional noise. Measuring at 50 mK (estimated reproducibility $\pm 10$ mK), for which sidebands are completely unresolved, reduces this temperature dependence.

19. D. Bakalov, V. I. Korobov, S. Schiller, *Phys. Rev. Lett.* **97**, 243001 (2006).

20. D. J. Berkeland, J. D. Miller, J. C. Bergquist, W. M. Itano, D. J. Wineland, *J. Appl. Phys.* **83**, 5025 (1998).

21. R. A. Hegstrom, *Phys. Rev. A* **19**, 17 (1979).

22. M. Tadjeddine, G. Parlant, *Mol. Phys.* **33**, 1797 (1977).

23. U. Fano, *Phys. Rev.* **124**, 1866 (1961).

24. B. D. Esry, H. R. Sadeghpour, *Phys. Rev. A* **60**, 3604 (1999).

25. J.J. Spezeski, Ph.D. thesis, Yale University (1977).

26. J. C. Bergquist, W. M. Itano, D. J. Wineland, *Phys. Rev. A* **36**, 428 (1987).

27. O. Asvany, *et al.*, *Science* **309**, 1219 (2005).

28. O. V. Boyarkin, T. R. Rizzo, *J. Comp. Phys.* **103**, 1985 (1995).

29. T. R. Geballe, T. Oka, *Science* **312**, 1610 (2006).

30. A. Ostendorf, *et al.*, *Phys. Rev. Lett.* **97**, 243005 (2006).

31. We thank C. B. Zhang for performing molecular dynamics simulations, and V. Korobov for helpful discussions. We acknowledge support from DFG and the EC network "Cold Molecules" HPRN-CT-2002-00290. J.K. acknowledges support from the Alexander von Humboldt Foundation.

**Fig. 1.** Simplified view of the ion trap and related intra-vacuum tools. Three laser beams (with wavelengths 313 nm, 266 nm and 1395 nm) propagate along the symmetry axis of the linear rf trap. To load $\mathrm{Be}^+$ ions into the trap, the oven is used to create an effusive beam of neutral beryllium atoms traversing the trap, after which they become ionized *in situ* by impact of electrons fired from the electron gun. An imaging lens with large numerical aperture is used to image 313 nm $\mathrm{Be}^+$ fluorescence onto a CCD camera and a photomultiplier tube (not shown). Laser cooling of $\mathrm{Be}^+$ at 313 nm results in the formation of a Coulomb crystal, as shown on the CCD image of the 313 nm fluorescence (inset). The width of the image corresponds to 2 mm. A leak valve is used to admit small quantities of neutral HD gas to the trap volume, which are ionized using the electron gun. The formed $\mathrm{HD}^+$ ions are sympathetically cooled via the Coulomb interaction with the $\mathrm{Be}^+$ ions, and accumulate in the center of the Coulomb crystal (dark core in the CCD image).

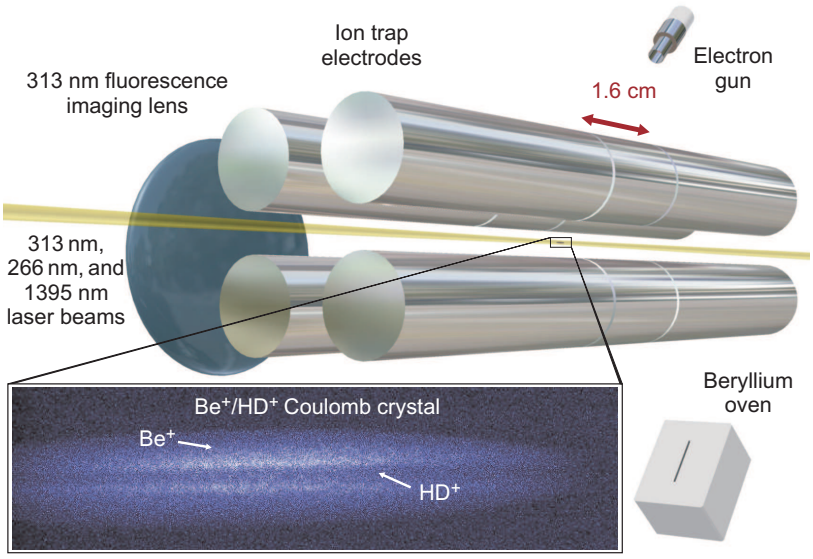
Ion trap
electrodes
Electron
gun
313 nm fluorescence
imaging lens
1.6 cm
313 nm,
266 nm, and
1395 nm
laser beams
Be+/HD+ Coulomb crystal
Be+
HD+
Beryllium
oven

**Fig. 2.** (A) Potential energy curves and rovibrational wavefunctions for the states involved in the (1+1') REMPD scheme (see text). Franck-Condon overlap prevents dissociation of $v = 0$ population by the 266 nm laser, but ensures efficient dissociation of any population in $v' = 4$. (B) Hyperfine levels of the $(v, N) : (0, 2)$ and $(4, 3)$ rovibrational states. The quantum numbers refer to the following coupling scheme for the electron spin $\mathbf{s}_e$, proton spin $\mathbf{I}_p$, deuteron spin $\mathbf{I}_d$, and molecular rotation $\mathbf{N}$: $\mathbf{J} = \mathbf{S} + \mathbf{N}$, where $\mathbf{S} = \mathbf{F} + \mathbf{I}_d$, and $\mathbf{F} = \mathbf{s}_e + \mathbf{I}_p$. The labels for the quantum number $J$ are not shown. As the 1395 nm radiation does not couple to the various spins, the strongest transitions can be grouped by their spin configurations, as indicated by the different colors used in the graph.

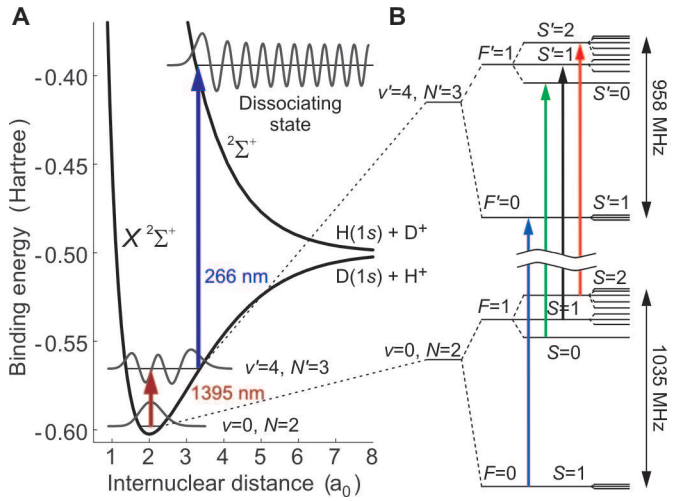
A
B
Binding energy (Hartree)
-0.40
-0.45
-0.50
-0.55
-0.60
1 2 3 4 5 6 7 8
Internuclear distance (a0)
Dissociating state
2Σ+
X 2Σ+
266 nm
1395 nm
H(1s) + D+
D(1s) + H+
v'=4, N'=3
v=0, N=2
S'=2
S'=1
S'=0
F'=1
F'=0
S'=1
958 MHz
S=2
S=1
S=0
F=1
F=0
S=1
1035 MHz

**Fig. 3.** Spectrum of the $(v, N) : (4, 3) \leftarrow (0, 2)$ transition in the $X\ ^2\Sigma^+$ electronic ground state of $HD^+$ , obtained by (1+1') REMPD spectroscopy. The offset frequency in the abscissa label is our measured result for the deperturbed frequency $\nu_d$ and is accurate to within 0.5 MHz. The smooth curve in the upper panel represents a fit with a reduced $\chi^2$ value of 1.1 of the model line function to the data. Underneath the data and the fit, the theoretical hyperfine line spectrum, calculated using the hyperfine hamiltonian given in Ref. (*19*), is shown. The same color coding as in Fig. 2 is used to classify the individual hyperfine transitions. For clarity, the data points in the upper panel are joined by line segments; the lower panel shows the differences between the individual data points (black dots) and the fitted curve. Each data point is an average of seven individual measurements of the fractional loss of trapped $HD^+$ ions induced by a 6 s period of REMPD. Frequency error bars are not shown as they are smaller than the dots representing the data points.

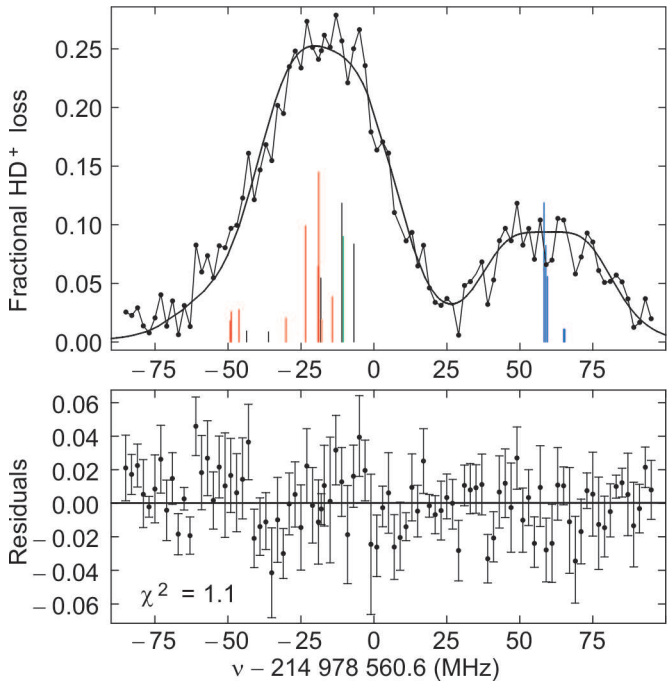
Fractional HD+ loss
0.25
0.20
0.15
0.10
0.05
0.00
−75
−50
−25
0
25
50
75
Residuals
0.06
0.04
0.02
0.00
−0.02
−0.04
−0.06
χ2 = 1.1
ν − 214 978 560.6 (MHz)

# Supporting Online Material

## Methods

The Zeeman effect of the $(v, N) : (4, 3) \leftarrow (0, 2)$ transition is expected to have a marginal (sub-kilohertz) effect on the deperturbed transition frequency $\nu_d$, since this depends on the small rotational magnetic moment of the molecule. However, the presence of the electron spin, having a magnetic moment which is three orders of magnitude larger, may have a visible effect on the shape of the hyperfine spectrum and therefore affect the model line function. To find an upper limit on the magnitude of the Zeeman shift, we theoretically investigated the Zeeman effect on the spectrum as follows. We add the Zeeman Hamiltonian given by Hegstrom (1) to the effective hyperfine Hamiltonian. The resulting Hamiltonian is diagonalized, and the eigenstates are used in the calculation of line strengths. This procedure gives us the model line function as a function of the magnetic field. We take into account the magnetic field orientation as measured in our apparatus, but assume a homogenous field value of 1 G. The polarization state of the infrared laser has equal amounts of $\sigma^+$ and $\sigma^-$ polarization; however, to find an upper limit we assume $\sigma^+$ transitions only. With these assumptions, we use the model line function to simulate a total of 100 spectra. To each spectrum, we add random random noise similar to that in our experimental spectrum, and fit the zero-field model line function as done for the experimental spectrum. For each spectrum $i$, this gives a theoretical value $\nu_{d,B}(i)$, and the average over all spectra is written $\nu_{d,B}$. Another set of 100 spectra is generated in a similar way, but for a zero magnetic field. Fitting all spectra from this set again with the zero-field line model function, we obtain an average value $\nu_{d,0}$. We find no significant frequency difference between $\nu_{d,0}$ and $\nu_{d,B}$, within a statistical uncertainty margin of 60 kHz. We note that the presence of a magnetic field gradient in our apparatus (causing the field to vary roughly between 0 and 1 G over the trap volume) would require a complicated model line function to be fitted to the experimental

spectrum directly, which we circumvent by the upper-limit estimation above.

1. R. A. Hegstrom, *Phys. Rev. A* **19**, 17 (1979).

# Molecular dynamics simulations of cold multi-species ion ensembles in a linear Paul trap

C. B. Zhang, D. Offenberg, B. Roth, M. A. Wilson, S. Schiller
*Institut für Experimentalphysik, Heinrich-Heine-Universität Düsseldorf, 40225 Düsseldorf, Germany*

The properties of cold multi-species ion plasmas with large ($> 200$) ion numbers are modelled in detail using molecular dynamics simulations. The implementation of heating effects is discussed. We describe how to extract temperatures and ion numbers of laser-cooled and sympathetically cooled ion species from experimental CCD images. A method to identify trapped ion species non-destructively by the excitation of their oscillation modes is presented. The sympathetic cooling process and effects of the rf micromotion are analyzed.

## I. Introduction

Sympathetic cooling by laser-cooled atomic ions has been established as a powerful method to produce a vast variety of trapped, cold ($\ll$1 K) atomic and molecular species [1–4]. These samples with temperatures from tens of mK to sub-mK are well suited for studies of chemical reactions [5–8] and spectroscopy [9], including high-resolution spectroscopy [10, 11].

In order to understand and characterize such cold ion plasmas, molecular dynamics (MD) simulations were carried out [12, 13]. Simulations can be performed for ion clusters containing several ion species with ion numbers from a single ion up to several thousand ions. In previous studies of one-component (species) plasmas the particle arrangement [14], the ion crystal structure [15], and rf heating [16] were investigated, in order to understand the basic properties of the systems. Simulations of sympathetically cooled multi-species ion ensembles include, for example, studies of the ion mass range which can be sympathetically cooled [17], or interactions between a few highly charged ions and large numbers of laser-cooled atomic ions [18]. However, this kind of studies are still rare and specialized. There is need for simulations closer to the experiments to better understand the interaction of different ion species, to predict the time dependent behaviors of the trapped ions, and to assist in the interpretation of new results. Conversely, the simulation models can also be verified and improved by comparing their results with experimental data.

In our experiments with sympathetically cooled ions in linear Paul traps, the time evolution of the laser-cooled ions' fluorescence offers a possibility to analyze the properties of the trapped ion ensembles. A resonant excitation of ion oscillations, for example, leads to changes in the fluorescence and can be used for non-destructive mass spectrometry of the confined ions [19]. If the temperature of the laser cooled ion ensemble is low enough, structured ensembles form [20], denoted as Coulomb or ion crystals, which can be imaged by a CCD camera. Fig. 1 shows a CCD image of a $^9Be^+$ ion crystal taken perpendicularly to the trap axis [7]. From the crystal's shape and structure properties such as ion numbers and temperatures can be deduced by comparison with simulated images.

In this article, we present our simulation model for cold multi-species ion crystals. The implementation of heating effects and laser cooling is discussed in detail. We introduce our method to extract ion numbers and temperatures of laser-cooled and sympathetically cooled ions from CCD images of ion crystals via simulations. The process of sympathetic cooling as well as the effects of rf micromotion are studied. We also simulate aspects of secular excitation of ions for the purpose of species identification.

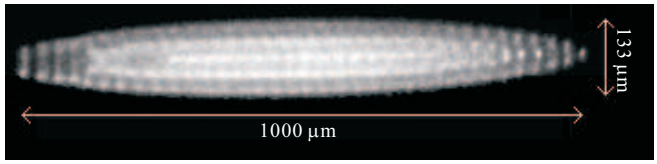


FIG. 1: CCD image of a typical laser-cooled $^9Be^+$ ion crystal in a linear Paul trap. The cooling laser propagates to the right, the crystal is at $\approx$ 6 mK and consists of (435$\pm$10) $^9Be^+$ and 7 $H_2^+$ ions.

## II. The simulation model

### A. Equations of motion and forces

Our simulations of multi-species ion crystals in linear Paul traps are based on solving Newton's equations of motion for all laser-cooled and sympathetically cooled ions

$$\begin{aligned} m_i\ddot{\boldsymbol{r}} &= \boldsymbol{F}_i(\boldsymbol{r}_1,\dots\boldsymbol{r}_{N_{LC}+N_{SC}},\boldsymbol{v}_1,\dots\boldsymbol{v}_{N_{LC}+N_{SC}},t) \\ &= \boldsymbol{F}_i^{trap} + \boldsymbol{F}_i^{Coulomb} + \boldsymbol{F}_i^{stochastic} + \boldsymbol{F}_i^{laser} \end{aligned} \quad (1)$$

where $i = 1,\dots,N_{LC}+N_{SC}$ ($N_{LC}$ and $N_{SC}$ are the numbers of laser-cooled and sympathetically cooled ions, respectively). Masses, positions and velocities are $m_i$, $\boldsymbol{r}_i$ and $\boldsymbol{v}_i$. $\boldsymbol{F}_i(\boldsymbol{r}_1,\dots\boldsymbol{r}_{N_{LC}+N_{SC}},\boldsymbol{v}_1,\dots\boldsymbol{v}_{N_{LC}+N_{SC}},t)$ is the total force acting on the ion $i$, which depends on the positions and velocities of all other ions, and the time $t$. There are several contributions to this force: the conservative trap potential force $\boldsymbol{F}_i^{trap}$, the Coulomb interaction force due to all other ions $\boldsymbol{F}_i^{Coulomb}$, the stochastic force $\boldsymbol{F}_i^{stochastic}$ [21] resulting from the random interactions of ions with surroundings such as collisions with

residual gas, scattered light, electric field noise, rf heating, and the laser cooling force $\boldsymbol{F}_i^{laser}$, which acts on the laser-cooled ions only.

The linear trap provides a rf oscillating saddle-shaped potential which confines the ions in the radial plane ($x$-$y$) with voltage amplitude $V_0$ and angular frequency $\Omega$, while the ions in the axial ($z$) direction are confined by a dc trapping field $V_{ec}$. Near the center of the trap, the trap potential is described by [22]

$$V(x,y,z,t) = \frac{2V_0}{r_0^2}\left(x^2-y^2\right)\cos(\Omega t) + \frac{\kappa V_{ec}}{2z_0^2}\left(2z^2-x^2-y^2\right), \quad (2)$$

where $r_0$ and $z_0$ are the radial and axial dimensions of the trap. In this potential ions perform a dominant motion of low frequency (secular motion) with a superimposed fast jitter motion (micromotion) of small amplitude. Their time-averaged motion is the secular motion which can be described as a motion in the harmonic pseudopotential well

$$\psi(x,y,z) = \frac{eV_0^2}{m\Omega^2 r_0^4}(x^2+y^2) + \frac{\kappa V_{ec}}{2z_0^2}\left(2z^2-x^2-y^2\right), \quad (3)$$

with secular frequencies in radial $(x,y)$ and axial directions:

$$\omega_r := \omega_x = \omega_y = \sqrt{\frac{Q}{m}\left(\frac{qV_0}{4r_0^2} - \frac{\kappa V_{ec}}{z_0^2}\right)}, \quad \omega_z = \sqrt{\frac{Q}{m}\frac{2\kappa V_{ec}}{z_0^2}}. \quad (4)$$

Here, $q \equiv 2QV_0/mr_0^2\Omega^2$ and $Q$ is the ion charge. A necessary condition for stable trapping of non-interacting ions is $q < 0.908$.

The Coulomb force $\boldsymbol{F}_i^{Coulomb}$ is the repulsive force from all other ions confined in the trap, and has the form

$$\boldsymbol{F}_i^{Coulomb} = \frac{Q_i Q_j}{4\pi\varepsilon_0} \bigtriangledown \sum_{j=1, j\neq i}^{N} \frac{\boldsymbol{r}_{ij}}{r_{ij}}, \quad (5)$$

where $r_{ij}$ and $\boldsymbol{r}_{ij}$ are the distance and the unit vector between ion $i$ and ion $j$, respectively. $\varepsilon_0$ is the permittivity of free space.

In our work, Newton's equations of motion for the trapped ions are numerically solved using the leapfrog algorithm. If the simulations are performed in the pseudopotential approximation ($\boldsymbol{F}_i^{trap} = -Q_i\nabla\psi$), the integration time step $\Delta t$ can be much longer and the computing time is much shorter compared to the case when micromotion is considered (where $\boldsymbol{F}_i^{trap} = -Q_i\nabla V$). The specific time steps used for simulations depend on the rf frequency $\Omega$ of the considered ion trap. We operate two traps – one for experiments with laser-cooled $^{138}Ba^+$ ions ($\Omega = 2\pi(2.5$ MHz)), another for $^9Be^+$ ions ($\Omega = 2\pi(14.2$ MHz)). For simulations of ion crystals in the barium trap the time steps typically are 2 or 10 ns when micromotion is included, and 400 or 500 ns in the pseudopotential case. For the beryllium trap, the time steps have to be shorter, 1 ns and 50 ns for the micromotion and the pseudopotential cases, respectively. Typical simulated time intervals are in the order of milliseconds, leading to computing times up to weeks for the largest systems (3000 particles). Note that the computing time scales approximately as $N_{tot}^2$, since the calculation of $\boldsymbol{F}_i^{Coulomb}$ is the most time-consuming part of the simulation.

Our simulation program "SOSC" (Simulation Of Sympathetic Cooling) is implemented in Delphi, runs on ordinary Windows PCs and comes with a graphical user interface.

### B. Heating effects

In order to characterize the temperature of an ion crystal one has to distinguish between the energy contributions of the micromotion and the secular motion. The secular energy, where the micromotion oscillation is averaged out, can be taken as an indication of the temperature of the ion crystal, since it arises from the disordered motion of the interacting ions in the time-averaged trap potential. In contrast, the micromotion contribution to the total energy arises from a driven motion, which is limited to the radial direction in the linear ion traps considered here.

Fig. 2 shows the root-mean-square (RMS) and the rf period-averaged velocity distributions in axial ($v_z$) and radial ($v_x$ or $v_y$) directions for an ion ensemble where micromotion was included in the simulation. The period-averaged velocities show a Gaussian distribution corresponding to that of a gas in thermal equilibrium, and the variances of the axial and radial velocities are equal. Thus a unique secular temperature of an ion ensemble can be introduced as $T_{sec} = (Nk_B)^{-1}\sum_i mJ^{-1}\langle(\sum_j v_{ixj})^2 + (\sum_j v_{iyj})^2\rangle$ ($j$ and $J$ are the time step number and the number of time steps in one rf period, respectively, $\langle\ldots\rangle$ denotes an average over many rf periods). The micromotion "temperature" is defined via the total kinetic energy as $T_{micro} = (Nk_B)^{-1}\langle\sum_i mJ^{-1}\sum_j(v_{ixj}^2 + v_{iyj}^2)\rangle$.

If the ion ensemble is not aligned in a string along the trap axis (where the micromotion would be zero) and for secular temperatures in the mK regime, the micromotion temperature is several orders of magnitude higher than the secular temperature (Fig. 2(b)). The micromotion leads to rf heating - an ion-ion interaction during which micromotion energy is transferred to secular energy [16, 23–25]. Fig. 3 shows how the secular temperature of an ion ensemble rises due to rf heating only. In this simulation, where micromotion is included, an ensemble of 1250 $^{138}Ba^+$ ions was set to 600 mK, then all cooling and heating sources were switched off and the ensemble was left evolving. As rf heating rises with temperature [16], the temperature increase is slow in the beginning with a rf heating rate $dT_{sec}/dt \approx k_B(2.93$ K/s) at 600 mK, and much faster at higher temperatures with

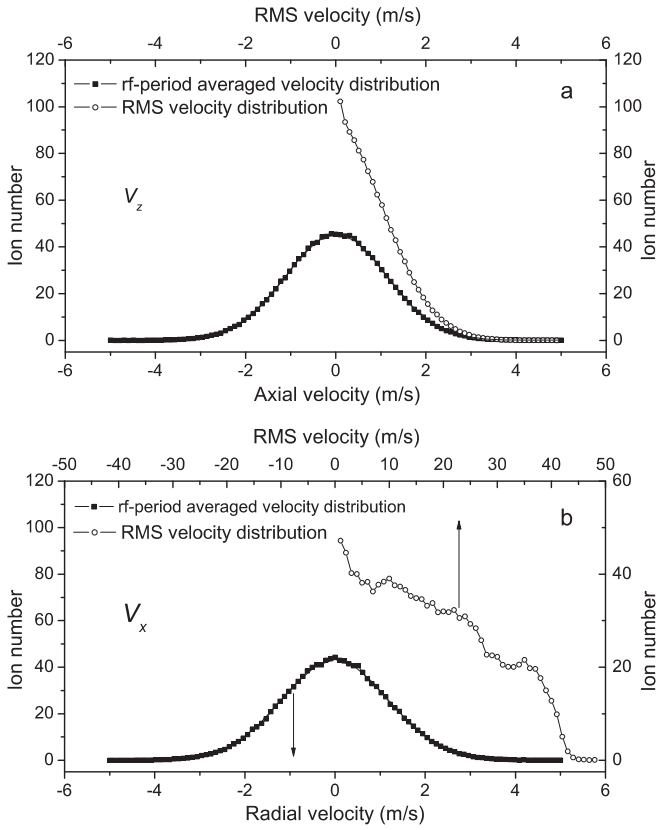


FIG. 2: Velocity distributions for an ion ensemble containing 1250 $^{138}Ba^{+}$ ions at $\approx$ 13 mK. The rf averaged and RMS velocity distributions are shown for (a) the axial and (b) a radial directions. The simulation included micromotion.

a rate of $\approx k_B(39.29\ \mathrm{K/s})$ at 10 K. In our experiments, the ion ensembles are generally in the crystal state at temperatures from 5 to 100 mK with small $q$ parameters and low ion numbers (less than 3000 ions). Under these conditions, rf heating is almost negligible ($\ll k_B(1\ \mathrm{K/s})$).

However, trap imperfections as a result of rf phase shifts or stray fields can lead to an increased rf heating [23]. To obtain an upper limit of this effect, we implemented an additional rf phase shift of 0.1 rad between neighboring electrodes and a DC offset of 5 V in $x$-direction applied to the central electrodes in our simulations. An ensemble of 1250 $^{138}Ba^{+}$ions was set to 36.5 mK, and then let evolve with cooling and heating sources switched off. As Fig. 4 shows, the rf heating is very low ($\approx 0.00234$ K/s) in this typical temperature regime, even in the case of a strongly imperfect trap.

Another heating source which can be substantial also at low temperatures is due to residual gas collisions. For example, in a background gas of $N_2$ at 300 K and a pressure of $1 \times 10^{-9}$ mbar the average $^{138}Ba^{+}$-$N_2$ elastic collision rate is $\gamma_{\mathrm{elastic}} \approx 0.017\ \mathrm{s}^{-1}$ [26]. In each collision the average energy transfer is $\approx k_B$ (128 K), leading to a heating rate $h_{coll} = k_B(2.2\ \mathrm{K/s})$, which increases linearly with the residual gas pressure (as discussed below, see Eq. (10, 11)).

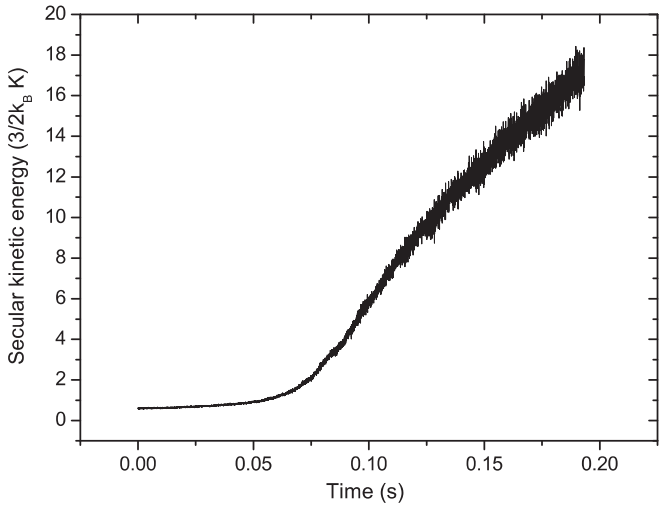


FIG. 3: Rf heating. After the laser cooling is switched off (at $t = 0$) the secular energy of an ion ensemble (1250 $^{138}Ba^{+}$ions, $q = 0.119$) rises quickly from $\approx$ 600 mK to $\approx$ 17 K in about 0.2 s only due to rf heating.

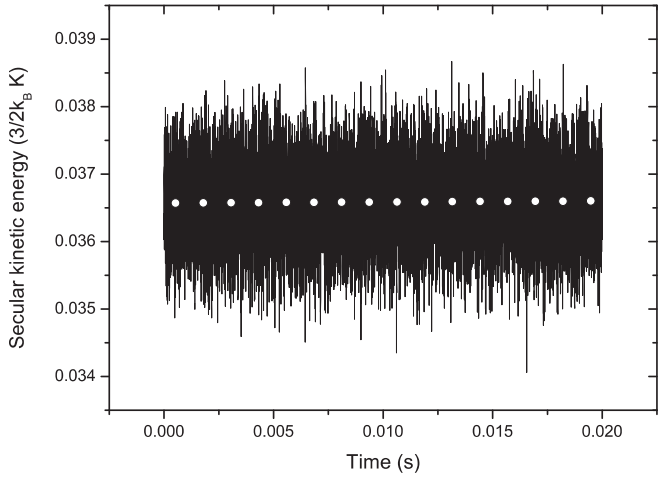


FIG. 4: Rf heating in an imperfect trap. The simulation includes an additional rf phase shift of 0.1 rad between neighboring electrodes and a DC offset of 5 V in $x$-direction applied to the central electrodes. The plot shows the temperature of an ion ensemble (1250 $^{138}Ba^{+}$ions, $q = 0.083$) in absence of laser cooling and other heating. A linear fit (open circles) yields a heating rate of $\approx 0.00234$ K/s.

This collision heating effect can be modelled by giving each ion a velocity kick at each integration step with a fixed magnitude in a random direction. It is described by the function

$$\boldsymbol{w}_k(t) = v_{i,0}\boldsymbol{v}_{k,0}(t). \tag{6}$$

Here, $v_{i,0}$ is a constant velocity kick magnitude that in general may differ from species to species, $\boldsymbol{v}_{k,0}(t)$ is a unit vector whose direction is chosen randomly for each ion at each integration step. The average change in kinetic energy per ion for a particular species from one integration

step (duration $\Delta t$) to the next is

$$\langle \Delta E_i \rangle = \frac{m_i}{2} \left( \langle \boldsymbol{v}_k^2(t+\Delta t) \rangle - \langle \boldsymbol{v}_k^2(t) \rangle \right) = \frac{m_i}{2} \langle 2\boldsymbol{v}_k(t)\boldsymbol{w}_k(t) + \boldsymbol{w}_k^2(t) \rangle = \frac{m_i}{2} \langle \boldsymbol{w}_k^2(t) \rangle, \quad (7)$$

since the ion velocities and the velocity kicks are uncorrelated. The kinetic energy increase rate per ion (heating rate) is therefore

$$h_i = \frac{\langle \Delta E_i \rangle}{\Delta t} = \frac{1}{2} m_i v_{i,0}^2 / \Delta t. \quad (8)$$

In another way, at each integration step we choose randomly $N_{i,kick}$ ions of each species and give them random velocity kicks. Then, the heating rate is

$$h_i = \frac{1}{2} m_i \frac{N_{i,kick}}{N_{i,total}} \widetilde{v}_{i,0}^2 / \Delta t. \quad (9)$$

Here, $N_{i,total}$ is the total ion number of ions of species $i$, and $\widetilde{v}_{i,0}$ are $v_{i,0}$ determined by requiring $h_i$ to be equal to $h_{coll}$.

Thus, a given heating rate can be implemented in two ways - by frequent kicks with low velocity kick amplitudes $v_{i,0}$ or by rare ones with high amplitudes. Considering the case of an ion colliding with a residual gas atom or molecule, the velocity magnitude change can be bigger than 100 m/s. This is so strong that the ion leaves the ion crystal and moves in the whole trap volume. Each time the ion passes through the ion cluster, it transfers some energy to it, with the energy loss rate being the lower, the faster the ion is [18]. Fig. 5 shows the kinetic energy of an ion ensemble of 1249 barium ions and a single ion after the latter has suffered a head-on collision with a helium atom of $\frac{3}{2}k_B(300\text{ K})$ kinetic energy. The colliding barium ion suddenly gains a large velocity (76.8 m/s) and starts to oscillate in the trap. Its kinetic energy is periodically transformed into potential energy and back, and gradually leaks to other ions until the whole ensemble reaches an equilibrium state. For a typical crystal, as considered here, the thermalization time is $\tau \approx 0.2$ ms.

The collision heating of an ensemble of $N$ ions will be essentially continuous if the time between two collisions in the whole ensemble, $N\gamma_{elastic}$, is smaller than the thermalization time $\tau$, i.e. for ion numbers $N > 1/(\gamma_{elastic}\tau)$. For a typical value of $\gamma_{elastic} = 0.02\ \text{s}^{-1}$, this condition is fulfilled for $N > 250000$ ions. Thus, much smaller ensembles can appear significantly colder in a single CCD image than the actual time-averaged temperature, if the CCD exposure time is less than $1/(N\gamma_{elastic})$. With a typical exposure time of 2 s this is the case for $N < 25$ ions. Indeed, our experience is that small clusters show a lower temperature (as found from the CCD images) than larger ones.

Ion ensembles considered here are usually large ($N > 2000$) and the CCD camera exposure times are long enough, so that collision heating due to the relatively rare collision events can be implemented by a more continuous heating in the simulations. Choosing more frequent

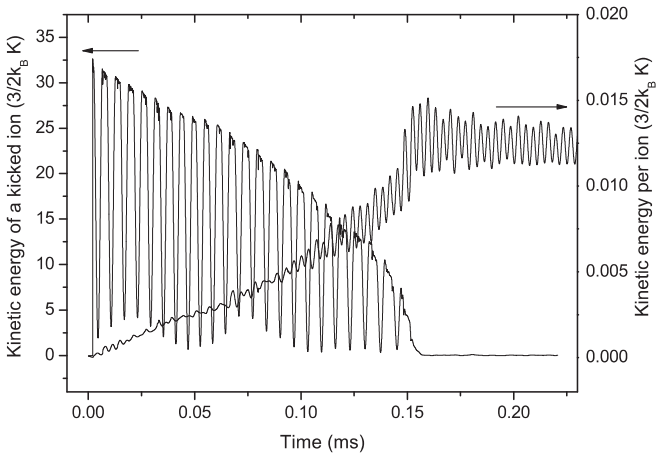


FIG. 5: Ion-neutral head-on collision. After its collision with a neutral helium atom a barium ion gradually transfers its gained kinetic energy (left scale) to the whole ion ensemble, whereupon the potential and the kinetic energy per ion (right scale) increase.

velocity kicks with appropriately low velocity kick magnitudes, computing time can be saved because equilibrium states are reached much faster (within a few ms). Fig. 6 illustrates that one specific heating rate can be realized with different parameter sets, according to Eq. (9). Here, an ensemble of 1250 barium ions was set to 0 K and then let evolve without any cooling and with a heating rate $h = k_B(11.95\text{ K/s})$. In the first case all ions were kicked after each time step ($\Delta t = 500$ ns) with kick magnitude $v_0 = 2.68 \times 10^{-2}$ m/s and in the second case just one ion ($N_{i,kick} = 1$) was kicked every time step with an adequately higher magnitude of $\widetilde{v}_0 = 0.949$ m/s. As expected, in both cases the increase of the kinetic energy per ion is the same.

The heating rate used in Fig. 6 obviously does not lead to a linear increase of the kinetic energy per ion, as expected from Eq. (8). This is due to the fact, that the definition considers an equilibrium state of heating and cooling effects, whereas Fig. 6 shows a dynamic process with heating only. Here, the rising temperature leads to an increase of the ion ensemble's volume whereupon the potential energy of the ensemble increases non-linearly. Due to energy conservation it is the total energy of the ensemble which increases linearly with time when applying a certain heating rate. Both, the kinetic energy and the potential energy increase non-linearly. This is shown in Fig. 7 for an ensemble of 1250 barium ions heated with $h = k_B(11.95\text{ K/s})$ without any cooling. The black (middle) curve shows the nonlinear change of the kinetic energy, and the red (lower) curve the one of the potential energy. Here, the ground potential energy (the mutual Coulomb-energy of the ions at zero temperature and the trap potential energy), $k_B(70.75\text{ K})$, was set as reference energy. The green (upper) curve is the total energy change due to the velocity kicks. It is linear with a slope of $k_B(11.6\text{ K/s})$, which agrees well with the applied heat-

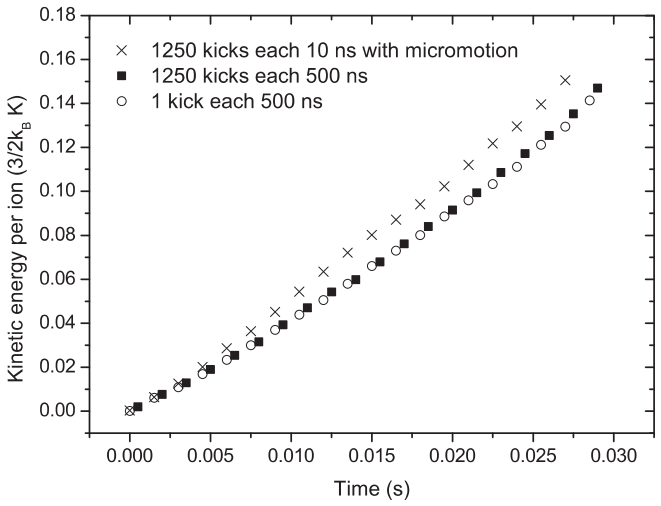


FIG. 6: Heating with velocity kicks. A specific heating rate was realized with different velocity kick frequencies $N_{i,kick}/(N_{i,total}\Delta t)$ by adjusting kick magnitudes accordingly (circle and square curve). The crosses show the heating with micromotion (see Section III.G).

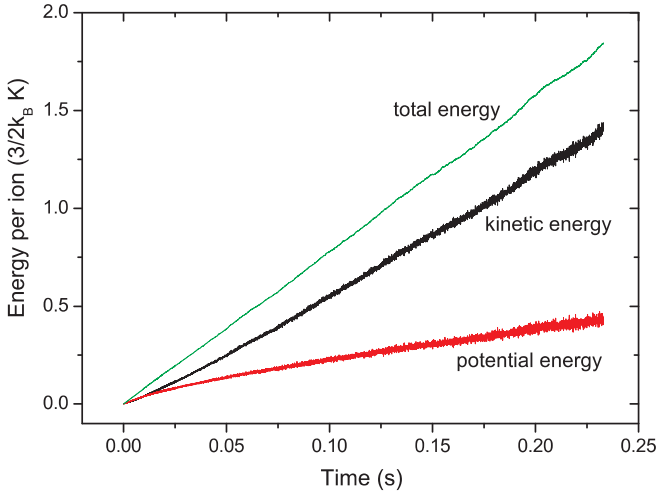


FIG. 7: (color online) Energy distribution. The total energy per ion (green, upper curve) increases linearly according to the implemented heating rate in the velocity kick model. However, the kinetic (black, middle curve) and the potential (red, lower curve) energy grow non-linearly due to a growth of the ion ensemble's volume.

ing rate $h$.

The validity of the kick model can also be verified experimentally by comparing theoretical collision heating rates with those extracted from experimental data via simulations. At low temperatures ($T < 300$ K) the most important ion-neutral interaction arises from an induced dipole attraction which has a potential $\varphi = -\alpha e^2/2r^4$ [26]. Here $\alpha$ is the polarizability of the neutral atom or molecule, $e$ the electron charge, and $r$ the radial separation. Using classical collision theory one can derive an

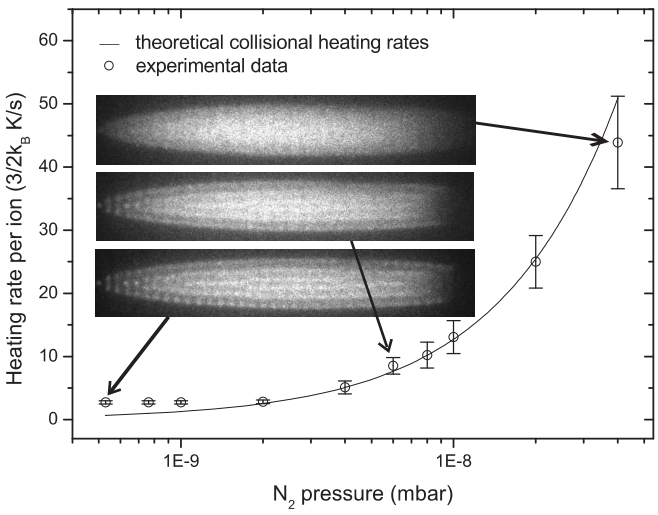


FIG. 8: Collision heating. The black curve shows the theoretical collision heating rates for collisions of $^{138}Ba^+$ ions and $N_2$ molecules. They well agree with the heating rates extracted from the experiment via simulations (dots).

expression for the ion-neutral collision heating rate as

$$h_{collision} = 3n_n \frac{2.21\pi}{m_n + m_c}\sqrt{\frac{\alpha\mu e^2}{4\pi\varepsilon_0}}k_B(T_n - T_c), \qquad (10)$$

and the average elastic collision rate

$$\gamma_{elastic} = 2.21\pi n_n \sqrt{\frac{\alpha e^2}{4\pi\epsilon_0\mu}}, \qquad (11)$$

where $n_n$ is the particle density of the neutral gas, $m_n$ ($m_c$) and $T_n$ ($T_c$) are the masses and temperatures of the neutrals (charged particles), $\mu = m_n m_c/(m_n + m_c)$ is the reduced mass and 2.21 is the numerical value of a certain Fresnel integral [27]. Experimentally, CCD images of an ensemble of $^{138}Ba^+$ ions at different $N_2$ pressures were taken. Assuming a realistic cooling rate $\beta = 2 \times 10^{-22}$ kg/s (see Section II.C), we obtained the heating rate at each pressure from simulations by adjusting the heating rate to a value which yields the best agreement of simulated and experimental image. Fig. 8 shows the collision heating rate (black, circle curve) for $^{138}Ba^+$ ions and $N_2$ molecules, rising linearly with the $N_2$ pressure. The experimental values agree well with these theoretical heating rates.

However, higher heating rates are required to reproduce the experimental images at low pressures. Apparently there are other heating sources besides rf and collision heating, such as scattered light and electric field noise acting on the trapped ions. As we cannot quantify them, they are not implemented in our simulations directly, but their effect can be included in the velocity kick model as a pressure-independent contribution to $v_0$.

### C. Cooling model

As laser cooling force $\boldsymbol{F}_i^{laser}$ we consider a linear viscous damping force plus a constant light pressure force

$$\boldsymbol{F}_i^{laser} = -\beta \dot{\boldsymbol{r}}_i + \boldsymbol{F}_{light}. \tag{12}$$

The light pressure force $\boldsymbol{F}_{light}$ pushes the laser cooled ion ensemble in the laser beam direction and gives a spatial offset from the potential well center. The cooling force reduces the velocity magnitude of the laser cooled ions, so the kinetic energy change rate per ion is

$$\begin{aligned}\Delta E_i &= \frac{1}{2}m_i v_i^2(t+\Delta t) - \frac{1}{2}m_i v_i^2(t) \\ &= \frac{1}{2}m_i \left(1 - \frac{\beta \Delta t}{m_i}\right)^2 v_i^2(t) - \frac{1}{2}m_i v_i^2(t) \\ &= \frac{1}{2}m_i v_i^2(t) \left( \left(\frac{\beta \Delta t}{m_i}\right)^2 - 2\frac{\beta \Delta t}{m_i}\right). \end{aligned} \tag{13}$$

Because the friction coefficient $\beta$ is very small ($\beta_{max} \approx \pi^2\hbar/\lambda^2 \approx 4 \times 10^{-21}$ kg/s for transitions at optical wavelengths $\lambda$ [17]), the first term in the parenthesis can be neglected. Thus, the kinetic energy decrease rate per ion ("cooling rate") is

$$c_i = \frac{\langle \Delta E_i \rangle}{\Delta t} = -\frac{2\beta}{m_i}\langle \frac{1}{2} m_i v_i^2(t) \rangle = -\frac{2\beta}{m_i}\langle E_i \rangle. \tag{14}$$

The temperature of the ion species $j$, $T_j$, is obtained from $\frac{3}{2}k_B T_j = \langle E_j \rangle$, where $\langle E_j \rangle$ is the time- and ensemble-averaged kinetic energy. The temperature decrease rate of an ion ensemble $j$ is

$$\frac{dT_j}{dt} = -\frac{2\beta}{m_j} T_j \tag{15}$$

This holds when the cooling is along all three spatial directions simultaneously. If the ion ensemble is cooled by only one laser beam along the axial direction $z$, then in Eq. (14) $v_i$ is $v_{i,z}$, and $E_i$ is $E_{i,z}$. Thus, the temperature reduction rate should be divided by 3 to get

$$\frac{dT_j}{dt} = -\frac{2}{3}\frac{\beta}{m_j} T_j. \tag{16}$$

Indeed, cooling with only one laser beam is sufficient to reduce the secular motion of the ions in all dimensions, because their mutual Coulomb interaction leads to a fast thermalization. This is also conventionally implemented in experiments. Fig. 9 shows an ensemble of 1250 barium ions cooled with a friction coefficient $\beta = 2 \times 10^{-22}$ kg/s along the axial direction without applying any heating. The secular kinetic energy per ion in radial ($x$ or $y$) and axial ($z$) direction decreases by two orders of magnitude within less than 10 ms. As the radial secular motion is reduced indirectly, its decrease is slightly slower than that of the axial secular motion which is most obvious in the mK regime.

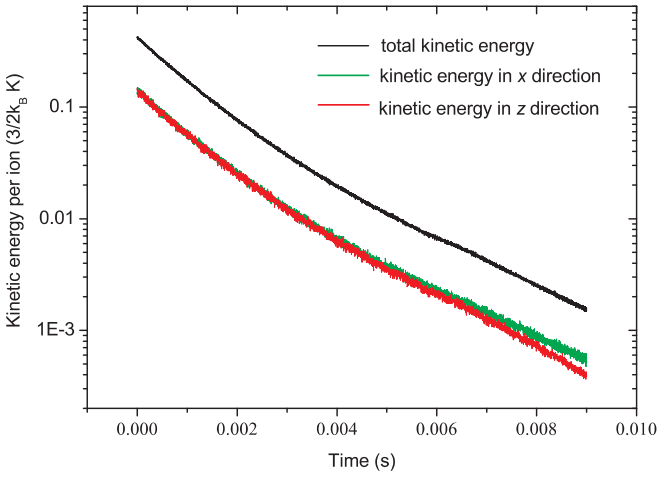


FIG. 9: (color online) Simulation of viscous cooling of an ion ensemble. 1250 barium ions are cooled by only one laser beam along the trap axis ($\beta = 2 \times 10^{-22}$ kg/s, no heating applied). The secular kinetic energy is effectively reduced in all dimensions.

### D. Simulation of CCD images

When taking CCD images of laser-cooled ion ensembles our typical exposure times are in the order of 0.5 to 2 s. During that time the ions' trajectories span several meters due to their residual secular kinetic energy (see Fig. 10). As a result, the images appear blurred and can be considered as probability density plots, rather than images of individual particles.

To reproduce these CCD images by simulations, the positions of all ions for every time step of the simulation are projected to a plane perpendicular to the desired line of sight. (In our setups, the line of sight is radial, i.e. perpendicular to the $z$-axis and at 45° to the $x$- and $y$-axis.) A density plot of this plane corresponds to a CCD image observed.

A completely realistic simulation of the CCD images would require simulation times as long as the exposure times and a more accurate implementation of the ions' collisions with the background gas, i.e. rare and strong collisions (compare Section II.B), leading to long computing times. With our more continuous velocity kick model equilibrium states are reached after simulation times of a few ms and the experimental CCD images can be reproduced with good agreement. The reason for this are the CCD exposure time, which is much longer than the thermalization time, and the inter-site diffusion time for the temperatures considered here.

In contrast to the experiment, simulations can also visualize ions which are not laser-cooled and therefore do not fluoresce. Fig. 11 shows a multi-species ion crystal [4] consisting of 830 laser-cooled $^{138}Ba^+$ ions, 420 singly charged barium isotopes ($m$ = 137 amu), and 200 singly protonated AlexaFluor350 molecules ($m$ = 410 amu). Because the radial confinement for ions with a higher mass-to-charge ratio is weaker, the

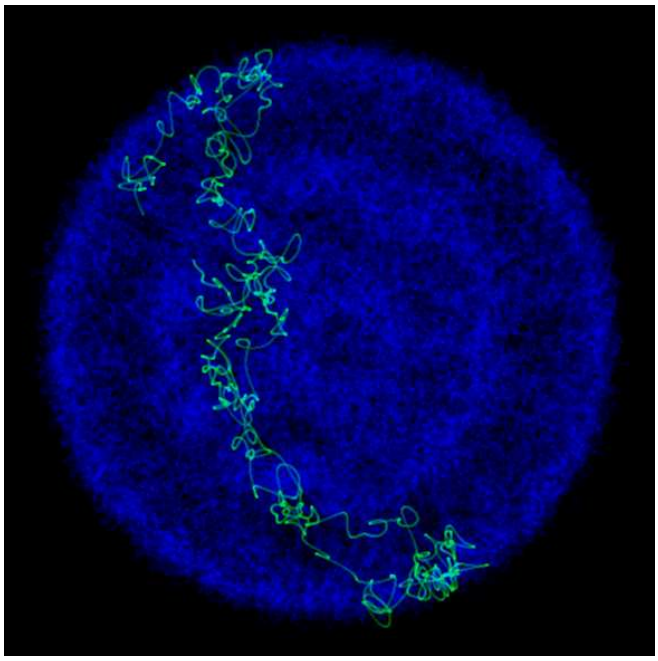

FIG. 10: (color online) Diffusion in an ion crystal. In this axial view of an ion crystal at 6 mK the trajectory of a single ion is shown in green. During the exposure time of 5 ms the ion diffuses through the whole ensemble.

heavier $^{410}AF^+$ ions are located around the $^{138}Ba^+$ ions, as shown in the axial view on the right-hand side of Fig. 11. The lighter barium isotope ions would arrange inside the $^{138}Ba^+$ crystal and form a core (see Fig. 16 for the much lighter $CO_2{}^+$ ions), but as the mass difference is small and the light pressure pushes the $^{138}Ba^+$ ions to the left, they arrange on the right side of the crystal and only slightly leak into the $^{138}Ba^+$ crystal.

## III. Applications

### A. Sympathetic heating and cooling

If other ion species are confined in the trap simultaneously with laser cooled ions, they can be sympathetically (indirectly) heated or cooled via their mutual long range Coulomb interaction.

To quantify this interaction, Fig. 12 shows a step-by-step simulation of the multi-species ion ensemble from Fig. 11. Initially, all species were set to a (secular) temperature of 0 K and in the spatial configuration of the lowest potential energy. Then a heating rate of $h_{^{138}Ba} = k_B(11.55\ \mathrm{K/s})$ is applied to the $^{138}Ba^+$ ions. Their temperature increases (black curve), and due to the sympathetic interaction the temperatures of the other two ion species increase as well. Because the mass-to-charge ratio of the barium isotope ions is very close to that of the $^{138}Ba^+$ ions, these two species couple very well and the energy transfer efficiency is high. Thus, the temperature of the barium isotope ions (red curve) closely follows that of the $^{138}Ba^+$ ions. However, for the $^{410}AF^+$ ions the coupling to the $^{138}Ba^+$ ions is lower due to their larger radial separation caused by their higher mass-to-charge ratio difference. So, their temperature increase is weaker (green curve). After 40 ms the laser cooling is switched on with a friction coefficient $\beta = 2 \times 10^{-22}$ kg/s. As the cooling of the $^{138}Ba^+$ ions is higher than the heating $h_{^{138}Ba}$, their temperature starts to decrease. When their temperature gets lower than that of the other species, these start to be cooled sympathetically until all species reach an equilibrium state with nearly equal temperatures. Finally (at $t = 100$ ms), realistic conditions are established by switching on the heating for the barium isotopes and the $^{410}AF^+$ ions (with heating rates of $k_B(11.47\ \mathrm{K/s})$ and $k_B(25.14\ \mathrm{K/s})$, respectively). Their temperatures increase above the $^{138}Ba^+$ temperature, which in turn causes a sympathetic heating of the $^{138}Ba^+$ ions. Finally, the whole ensemble reaches an equilibrium state with stable, but species-dependent temperatures, i.e. temperature gradients are present.

### B. Temperature determination of laser-cooled ions

Shape and structure of an ion crystal are determined by the trap potentials applied, the number of ions, the ion species, the light pressure force, and the temperatures. Ion numbers and temperatures can be obtained from comparison of experimental and simulated images of the ion crystals.

Firstly, the number of the trapped ions are determined. For ion crystals consisting of laser-cooled ions only the procedure is as follows: As the magnification of the imaging system is known, one just needs to adjust the number of ions until the simulated crystal has the same dimensions as the observed one. Here (mK regime), the volume of the crystal is not significantly influenced by the temperature of the ions. Therefore, the ion number can be fit without considering the temperature.

For ion crystals containing sympathetically cooled ion species in addition, the determination of ion numbers is more complicated. Ions with higher mass-to-charge ratios arrange around the laser-cooled ion ensemble and therefore modify its shape. If the species is known and the mass-to-charge ratio is still close to that of the laser-cooled ions, one can find its number by reproducing the observed deformation. However, for a species with a much higher mass-to-charge ratio, the deformation induced is not sufficient (see Fig. 11 and 16) and the ion numbers can only be determined destructively by extraction from the trap and counting [4]. As ions with a lower mass-to-charge ratio are located inside the laser-cooled ensemble and form a core, their number can be determined much easier from the size of the core.

In both cases it is essential to consider the light pressure force which shifts the laser-cooled ions out of the

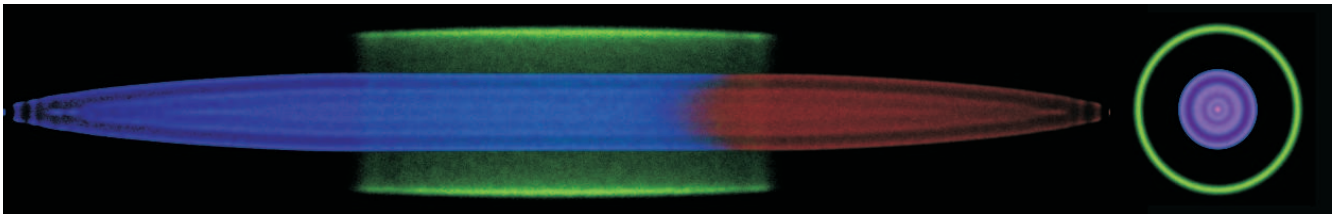

FIG. 11: (color online) Spatial structure of a multi-species ion crystal. The ion crystal consists of 830 laser-cooled $^{138}Ba^+$ ions (blue), 420 singly charged barium isotopes (red), and 200 protonated AlexaFluor350 molecules (blue). The left image is a radial view, the right an axial view.

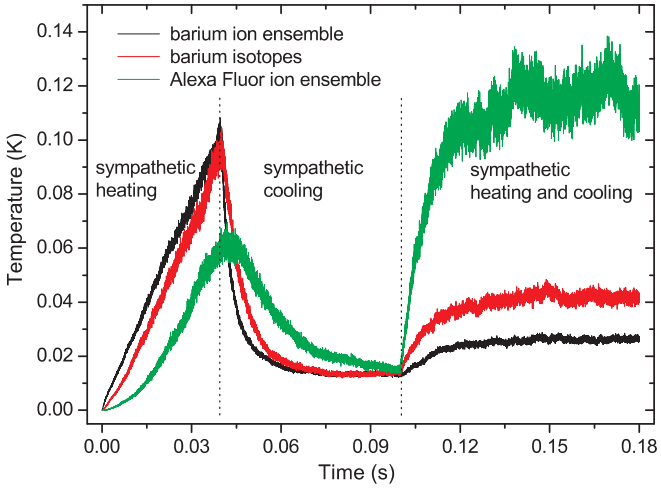


FIG. 12: (color online) Sympathetic heating and cooling in a multi-species ion ensemble. The ion composition is the same as in Fig. 11. After all species were set to a temperature of 0 K, heating is implemented for the $^{138}Ba^+$ ions only at $t = 0$ s, the other ions are sympathetically heated. At $t = 0.04$ s the laser cooling is added, and the $^{138}Ba^+$ temperature decreases. The $^{138}Ba^+$ ions now sympathetically cool the other ions. Finally at $t = 0.1$ s, heating is implemented for the barium isotopes and the $^{410}AF^+$ ions, which increases the temperatures of all species until they reach the equilibrium state.

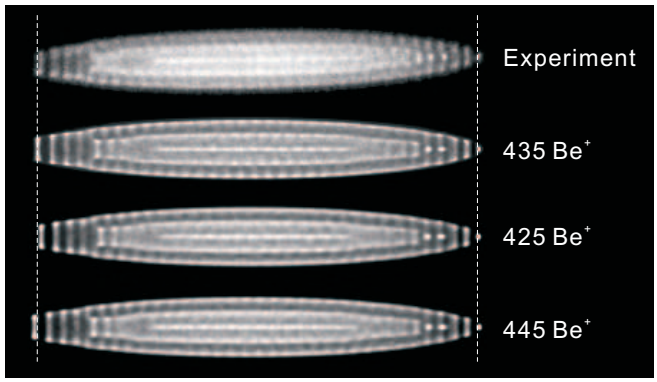


FIG. 13: Determination of ion numbers. The experimental image of a beryllium ion crystal is compared with simulated images with different ion numbers. The best fit is achieved for a number of 435 $^9Be^+$ ions.

trap center and causes strong asymmetries. For example, the beryllium ion crystal shown in Fig. 1 contains $H_2^+$ ions that are located on the left side of the crystal, the beryllium ions are shifted to the right. To determine the ion numbers in this crystal we simulated crystals with different ion numbers and compared them with the experimental CCD image (see Fig. 13). The best fit is achieved for 435±10 $^9Be^+$ and 7 $H_2^+$ ions, when a light pressure force of $8 \times 10^{-21}$ N is assumed.

In order to determine the temperature of the laser-cooled ions, a series of ion crystals at different temperatures is simulated and visually compared with the experimental CCD image. Due to scattered light and the limited resolution of our imaging system the experimental CCD images look blurred. Thus, the crystals appear warmer than they actually are. There are, however, details in the crystal structure, which are used to find the closest temperature. In Fig. 14, for example, the experimental image of a beryllium crystal (lowermost image) shows two concentric ellipsoidal shells with a string in the middle. The string displays discrete spots which are, comparing with the simulated images above, only visible for temperatures lower than 8 mK. But, these spots are not as distinct as in the simulated image at 5 mK. Thus, the best fit is achieved for a temperature of 6 mK.

Note, that these discrete spots do not correspond to single ions. Due to their residual secular kinetic energy the ions move around equilibrium positions, can jump to other positions and can even diffuse through the whole crystal. A spot in simulated or experimental CCD images shows a high probability density for ions at a certain location during the exposure time. In contrast to the experiment, in the simulations one can image ion crystals from any direction and with arbitrary magnification. Even specific sites of the crystals can be studied in detail. For example, Fig. 15(a) shows the spatial radial distribution of the spot at the right end of the beryllium crystal shown in Fig. 1. The spatial distribution has a Gaussian shape and a full width at half maximum of 6 $\mu$m. Fig. 15(b) shows the spatial distribution of the neighboring two spots. They cannot be ascribed to two ions, but to three ions which move on a circle in the $x$-$y$-plane.

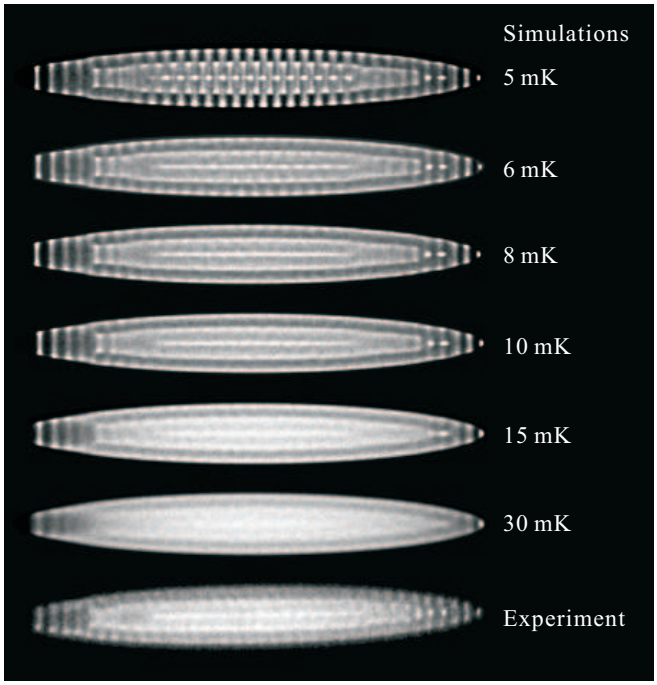


FIG. 14: Temperature determination of laser-cooled ions. A series of simulated ion crystals at different temperatures is compared to the experimental CCD image (bottom, same as Fig. 1). The best agreement is achieved for a temperature of about 6 mK.

### C. Temperature determination of sympathetically cooled ions

The temperature of sympathetically cooled ions cannot be determined as described above, because they do not fluoresce and are therefore invisible to the CCD camera. In order to find their temperature, two CCD images are required. One is taken when the laser-cooled and the sympathetically cooled ions are trapped together, the other is taken when there are only the laser-cooled ions, i. e. before loading or after extracting the sympathetically cooled ions. The temperature of both ion ensembles is different, as the heating rate $h_{sc}$ of the sympathetically cooled ions acts as an additional heating source. By simulating the CCD image of the pure laser-cooled ion ensemble its heating rate $h_{lc}$ is found. In the simulation of the whole ensemble $h_{lc}$ is kept constant for the laser-cooled species. Then, the heating rate for the sympathetically cooled species is varied in order to heat the laser-cooled ion ensemble to the observed temperature. When the right parameters are found, the temperature of the sympathetically cooled ions can be obtained from the simulation data (an example is shown in [4]).

In principle, a specific temperature of a laser-cooled ion ensemble can be achieved with a continuous set of pairs of appropriate laser-cooling and heating rates. The simulated temperature of the sympathetically cooled ion ensemble strongly depends on the implemented laser-cooling rate. When a higher laser-cooling rate is applied,

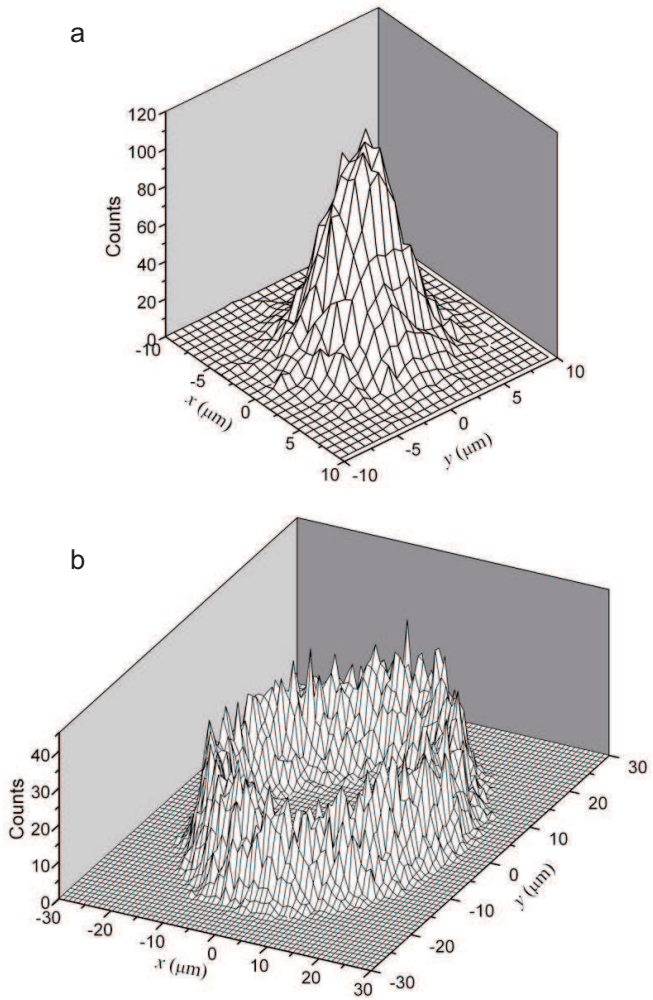


FIG. 15: Time-averaged ion trajectories. Probability density of the right end spot (a) and of the two neighboring spots (b) of the beryllium crystal in Fig. 1 ($T_{sec} = 6$ mK). The view is in axial direction, the simulation time is 200000 time steps of 50 ns.

the heating rates for all involved species need to be increased in order to keep the temperature of the laser-cooled ion ensemble constant. However, this leads to a higher temperature of the sympathetically cooled ions as illustrated in the following example: Fig. 16 shows a four-species ion crystal consisting of 700 laser-cooled barium ions (blue, 138 amu), 300 barium isotope ions (red, 137 amu), 100 $CO_2^+$ ions (pink, 44 amu), and 200 singly protonated glycyrrhetinic acid molecules (denoted as $GA^+$, green, 470 amu). In case (a), the friction coefficient $\beta$ is set to $1 \times 10^{-22}$ kg/s. To keep the crystal at 20 mK, the corresponding heating rate for barium ions and isotopes is $\approx k_B(5.94$ K/s). After loading the $GA^+$ ions, we set their heating rate to $\approx k_B(8.25$ K/s), which heats the barium ion ensemble to 25.6 mK. The temperature of the $GA^+$ ion ensemble in this equilibrium state is $\approx 130$ mK. In case (b), a higher friction coefficient $\beta = 4 \times 10^{-22}$ kg/s is set. To heat the barium

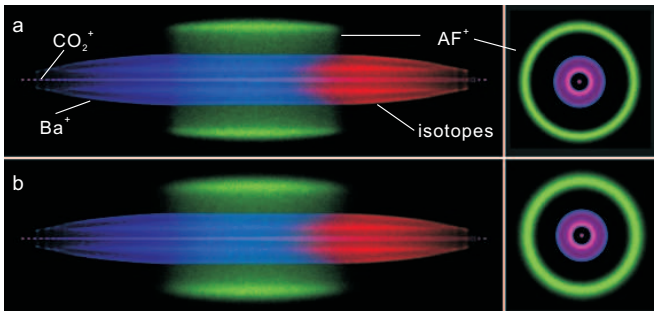


FIG. 16: (color online) Temperature determination of sympathetically cooled ions. If a higher laser-cooling rate is used in the simulations (b), one obtains higher temperatures for the sympathetically cooled species (green).

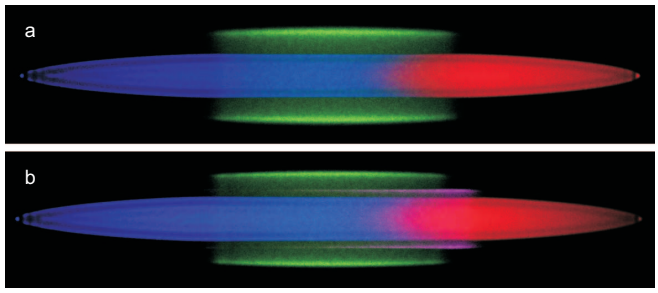


FIG. 17: (color online) Intermediate layer. The images show a multi-species ion ensemble consisting of barium ions (blue, 138 amu), AlexaFluor ions (green, 410 amu) and barium isotope ions (red, 137 amu) - (a) without and (b) with an intermediate species layer (pink, 200 amu), which helps to cool the AlexaFluor ions more efficiently.

ion ensemble to the same 20 mK and 25.6 mK values, higher heating rates are required: $\approx k_B(23.88$ K/s) for the barium ions and $\approx k_B(33.58$ K/s) for the $GA^+$ ions. Here, the final equilibrium temperature of the $GA^+$ ions ensemble is $\approx 300$ mK.

Thus, in order to obtain a concrete temperature value for the sympathetically cooled ion ensemble, the friction coefficient needs to be determined independently. From laser cooling theory

$$\beta = 2\sum_i \frac{\hbar k_i^2}{2}\Gamma_i \frac{\partial \rho_e}{\partial \Delta_i}|_{\Delta_i}. \qquad (17)$$

The wavenumbers $k_i$ and partial decay rates $\Gamma_i$ for the laser transitions are constants, whilst the change in the excited state population $\rho_e$ with laser detunings $\Delta_i$ is calculated from 8-level Bloch equations using measured laser saturation parameters and detunings [28]. The value for $^{138}Ba^+$ is in our experiments was $\approx 1.75$ kg/s [29].

### D. Advanced cooling of complex molecular ions

Sympathetic cooling in a Paul trap is most efficient for species with similar mass-to-charge ratio, as their radial separation is small.

In one of our experiments, we used laser-cooled $^{138}Ba^+$ ions to sympathetically cool complex molecular ions with masses of several hundred amu and more produced with an electrospray ion source [30]. Here, the efficiency of sympathetic cooling is relatively low due to the high radial separation of the ion species. A possibility to enhance the sympathetic cooling is the reduction of the mass-to-charge ratio difference, which can be realized by using multiply protonated molecules which are created during the electrospray process. In further experimental and theoretical studies we will investigate the sympathetic cooling of such molecules, e.g. 15 –20 fold protonated apomyoglobin (mass $\approx 16000$ amu). Another way is to raise the trap voltage to increase the radial confinement of all ions. However, higher trap voltages also cause a higher rf heating [16]. Yet another possibility is a reduction of the total ion number, in order to reduce the repulsive forces between the ion species.

A different approach is to add a (sympathetically cooled) intermediate species layer between the laser-cooled and the sympathetically cooled ions, see Fig. 17. This layer acts as a "conducting layer" and helps to transfer the energy from the sympathetically cooled ions of interest to the laser-cooled ions. Such ions of intermediate mass may be loaded into the trap deliberately or they may be produced by photodissociation of the molecular ions. Fig. 18 shows an example for the sympathetic cooling process, in which 200 $^{410}AF^+$ ions are sympathetically cooled from about 490 to 8 mK by 1250 $^{138}Ba^+$ ions – with and without intermediate layer. Initially, the barium ions are kept at very low temperature ($< 3$ mK) by applying a high cooling rate ($\beta = 200\times10^{-22}$ kg/s), while the $^{410}AF^+$ ions are kept at about 490 mK. Then, the heating for the $^{410}AF^+$ ions is turned off and their temperature decreases due to sympathetic cooling. It takes about 40.6 ms to cool them to $\approx 8$ mK, but only 8.8 ms when 50 ions with an intermediate mass (200 amu) are added. Thus, the sympathetic cooling rate can be increased by a factor of 4.6, in this example.

The final temperature of the sympathetically cooled ions can be significantly lower with the intermediate species layer. For the case shown in Fig. 17, 200 $^{410}AF^+$ ions are sympathetically cooled by 830 $^{138}Ba^+$ions. With an intermediate layer (50 ions, 200 amu), the final temperature of the AlexaFluor ions can be reduced from $\approx 114$ mK to $\approx 58$ mK.

### F. Simulation of secular excitation spectra

Experimentally, trapped ion species can be identified by a resonant excitation of their radial secular motion. For this purpose, an additional ac field is applied either to the trap electrodes or an external electrode. When the excitation field is resonant with the oscillation mode of an ion species, these ions start to strongly oscillate.

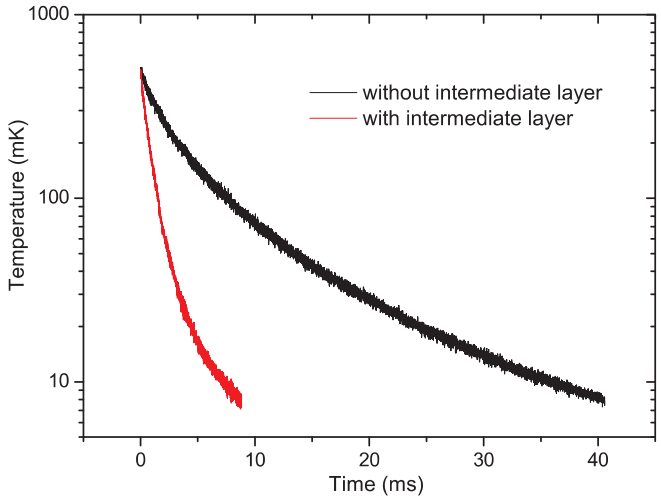


FIG. 18: Sympathetic cooling with an intermediate layer. With an additional intermediate ion species (compare Fig. 17) the sympathetic cooling of the AlexaFluor ions is much faster (red) than without (black).

Consequently, the whole ion ensemble heats up, which causes a change in the laser-cooled ions' fluorescence. By recording the fluorescence during a frequency scan one can obtain a mass spectrum of the trapped ions.

However, the observed frequencies can differ strongly from the calculated values for single ions $\omega_r$ (see Eq. (4)). This is due to the fact that the space charge of all ions and a coupling between trapped species lead to significant shifts of the oscillation frequencies [19, 31]. In a simplified picture, this can be illustrated by comparing the ideal harmonic pseudopotential (see Eq. (3)) with that modified by the space charge of the trapped ions.

In Fig. 19, for example, we consider a cold ion crystal containing 1200 $^{138}Ba^+$ ions and 500 $GA^+$ ions. The effect of the of the $GA^+$ ions on the barium ions is shown in Fig. 19(a). The shape of the potential well for a barium ion is almost unchanged, there is only an offset to higher potential energies which does not influence the barium ions' secular frequency. However, as shown in Fig. 19(b), the presence of the barium ions causes a drastic change of the potential well for $GA^+$ ions. The harmonic pseudopotential is modified to a double well potential. These potential wells are steeper, so that the $GA^+$ ions have a higher secular frequency than calculated by the single ion formula (see Eq. (3)). To quantify this, we performed fits with harmonic functions to the wells and found that the asymmetric double wells can be described by the functions $y = 11.5 \times 10^{-8}(x-160)^2 + 0.006$ and $y = 6.3 \times 10^{-8}(x-160)^2 + 0.006$ for the outer part, while the potential for a single trapped $GA^+$ ion is described by $y = 3.9 \times 10^{-8}x^2$. Thus, the radial frequency of a $GA^+$ ion can be up to $\sqrt{11.5/3.9} = 1.7$ times higher than the one calculated with the single ion formula.

For a more realistic description of the oscillation of an ion species it is necessary to include not only the

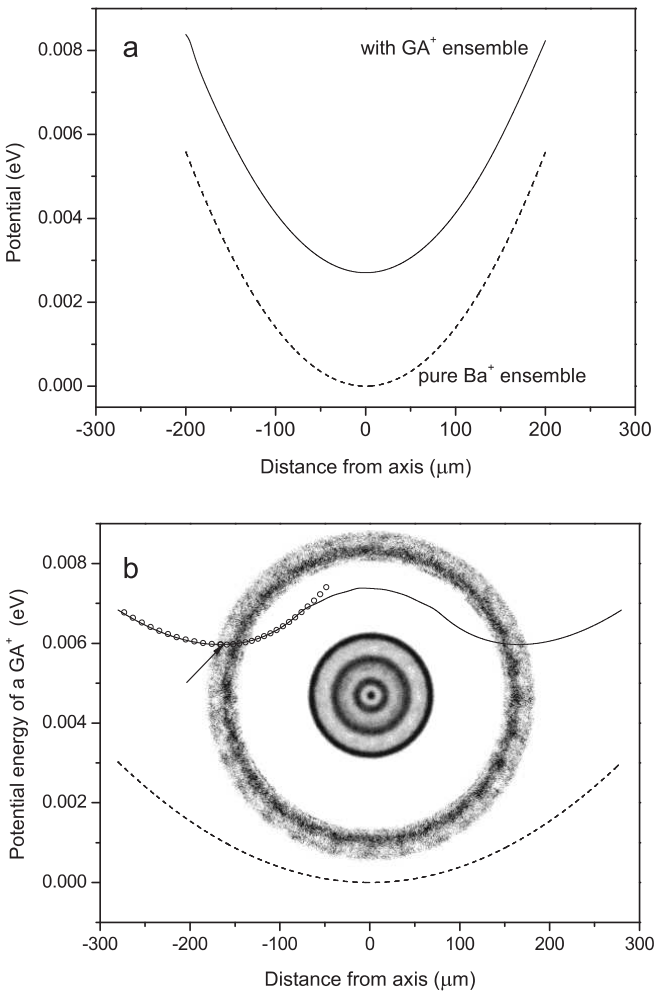


FIG. 19: Space charge effects and trap potentials. Here, we consider a cold ion crystal containing 1200 $^{138}Ba^+$ ions and 500 $GA^+$. (a) Potential wells for a single barium ion in the ideal harmonic trap potential (dashed curve) and influenced by the space charge of heavier $GA^+$ ions (solid curve). (b) Potential well for a single $GA^+$ ion in the ideal harmonic trap potential (dashed curve) and double well potential caused by the barium ions (solid curve). The gray shaded rings show an axial view of the considered ion crystal.

space charge of the other ion species, but also the space charge of the considered ion species itself. Therefore, in our simulations radial secular excitation spectra are simulated as follows: the whole ion ensemble is displaced by several $\mu$m in a radial direction. Then it is released and the center-of-mass positions of all ions are recorded for some time. Finally, a Fourier analysis of these data yields the oscillation modes of the ion ensemble components. Such spectra are shown in Fig. 20 for different ion crystals at equal trap settings ($q(^{138}Ba^+)$=0.091). For a pure $^{138}Ba^+$ ion crystal (Fig. 20(a)) the simulated frequency $\nu_{sim} = 79.3$ kHz is slightly higher than the calculated single-ion frequency $\nu_r = 79.2$ kHz as the barium ions make their potential well steeper. In comparison, the spectrum of a crystal consisting of $^{138}Ba^+$ ions

and isotopes (Fig. 20(b)) is not much different because the ion masses are quite similar. However, due to the coupling of the ions' oscillation modes there are additional small peaks beside the main peak, which is slightly shifted to a higher frequency of 77.5 kHz. Fig. 20(c) shows the excitation spectrum of an ion crystal containing barium ions with isotopes and $GA^+$ ions. The experimentally determined secular frequency for the $GA^+$ ions $\nu_{exp} = 29.3 \pm 1.3$ kHz is far away from the single-ion frequency $\nu_r = 22.4$ kHz, but can be verified by the simulated value $\nu_{sim} = 32.2$ kHz. The difference of the simulated and the experimental value depends, for example, on the excitation amplitude in the experiment or the ion numbers included in the simulation (a more detailed description can be found in [19]).

The small peaks below 10 kHz in Fig. 20(c) can be explained as follows: Fig. 21 shows the effective trap potential in the $x$-$y$-plane for the ion ensemble considered in Fig. 19 with the barium ions creating a potential hill in the center (the small spots besides are due to $GA^+$ ions). Supposed, the ac field for secular excitation is applied along the $x$-axis, $GA^+$ ions at different positions oscillate in different potential wells. Further away from the $x$ axis the potential hill is lower, so that the potential well is much shallower, leading to smaller oscillation frequencies. However, these frequencies cannot be detected experimentally because they are in the range of the axial oscillation frequencies $\omega_z$. As the radial excitation electrodes are much longer than the ion crystals, there is always an axial component in the excitation field, which causes complicated overlapping at these frequencies.

### G. Micromotion

Our simulations are a useful tool for the interpretation of experiments with sympathetically cooled molecules. For the determination of ion numbers and temperatures or the simulation of ion crystal structures and secular excitation spectra it is not necessary to include the micromotion in the simulations. To save computing time we solve Newton's equations of motion in the pseudopotential approximation. However, there are some aspects based on micromotion, which cannot be neglected and are considered in the following.

Rf heating, for example, is rather low in the mK regime but can be quite substantial at higher temperatures (see Fig. 3) [16]. Fig. 6 shows, how an ensemble of 1250 barium ions is heated from 0 to $\approx$ 160 mK with a velocity kick heating rate of $k_B(11.95$ K/s) when no cooling is applied. For the simulation including micromotion (crossed curve) the temperature rises faster than in the case of the simulation in the pseudopotential (other curves) due to the additional rf heating here. When simulating ion crystals in equilibrium, rf heating can be considered by an appropriately higher velocity kick heating rate, so that there is no need for performing the simulations in the time-dependent trap potential.

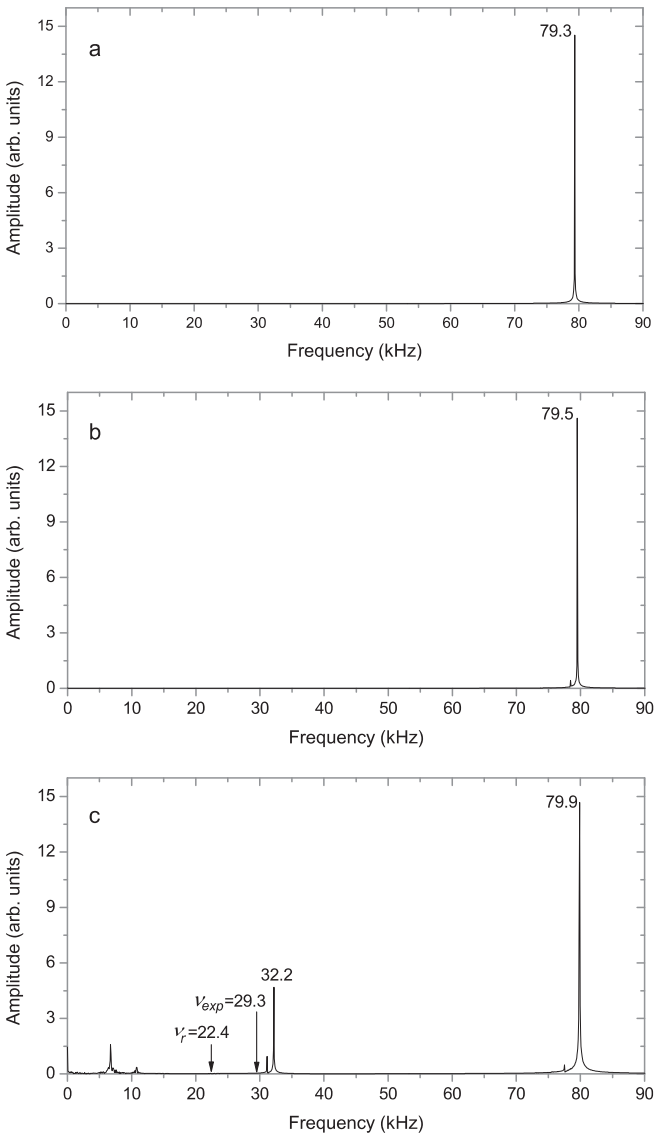


FIG. 20: Simulated radial secular excitation spectra. For equal trap parameters ($q(^{138}Ba^+)$=0.091) different crystal compositions were considered: (a) only $^{138}Ba^+$ ions, (b) $^{138}Ba^+$ ions and isotopes, (c) $^{138}Ba^+$ ions, isotopes and $GA^+$ ions. In (c) $\nu_r$ indicates the calculated single-ion frequency for a $GA^+$ ion and $\nu_{exp}$ the experimentally determined value.

Another aspect is a possible direct coupling of radial micromotion to the axial direction which would lead to an additional heating. To study this effect, a barium ion from a cold ion ensemble (830 $^{138}Ba^+$ ions, 420 barium isotope ions, and 200 $^{410}AF^+$ ions) was randomly selected and its axial position $z(t)$, one component of the radial position $x(t)$, and its axial velocity $v_z(t)$ were recorded (see Fig. 22). The solid curve $x(t)$ clearly shows the slow radial secular oscillation ($\approx$ 40 kHz) with the superimposed fast micromotion at the rf driving frequency of 2.5 MHz (see inset). As there is no apparent rf oscillation in the axial motion $z(t)$ (dashed curve) and the axial velocity $v_z(t)$ (dotted curve), one can conclude that in an ideal

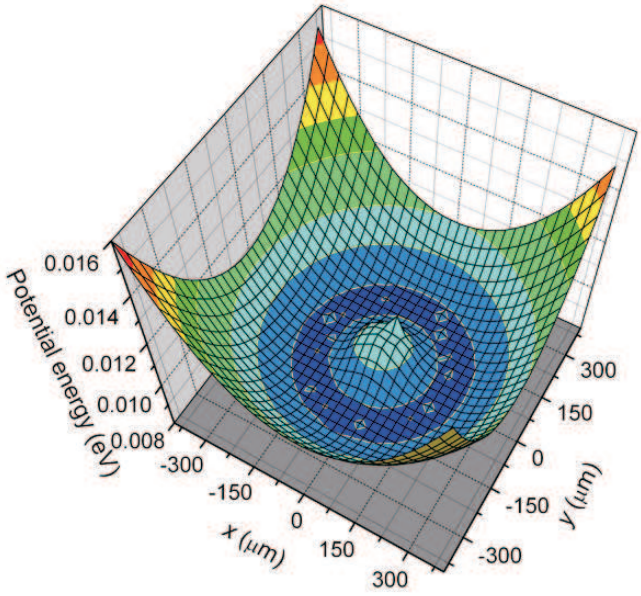


FIG. 21: (color online) Effective trap potential. Three-dimensional view of the potential in the $x$-$y$-plane for the ion ensemble considered in Fig. 19.

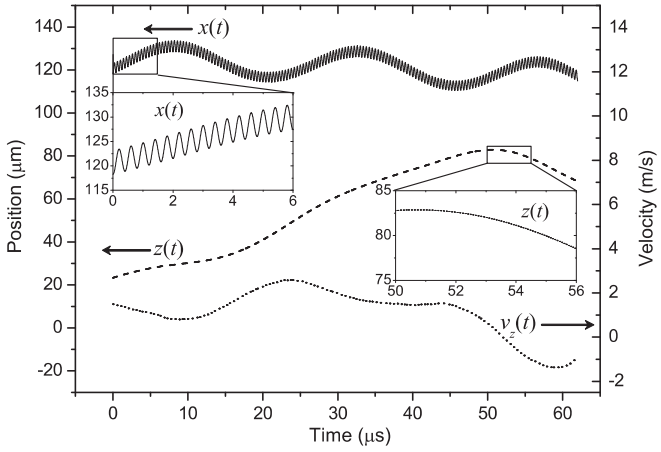


FIG. 22: Micromotion in detail. In a simulation including micromotion the $x$-component of the motion clearly shows the fast micromotion (solid curve, the inset is a magnification). The $z$-components of the motion and the velocity (dashed and spotted curve) do not show any effect of micromotion, so there is no indication of coupling between the radial and axial directions. The secular temperature of the barium ion ensemble was *approx*30 mK.

linear Paul trap, the micromotion in radial direction does not couple to the axial direction. The only possibility for an energy transfer of micromotion to the axial motion is an indirect coupling via rf heated ions which distribute their kinetic energy to the axial direction through the thermalization process.

Furthermore, we have studied the influence of the micromotion on the simulated images. Fig. 23 compares structural details of an ion ensemble consisting of 500

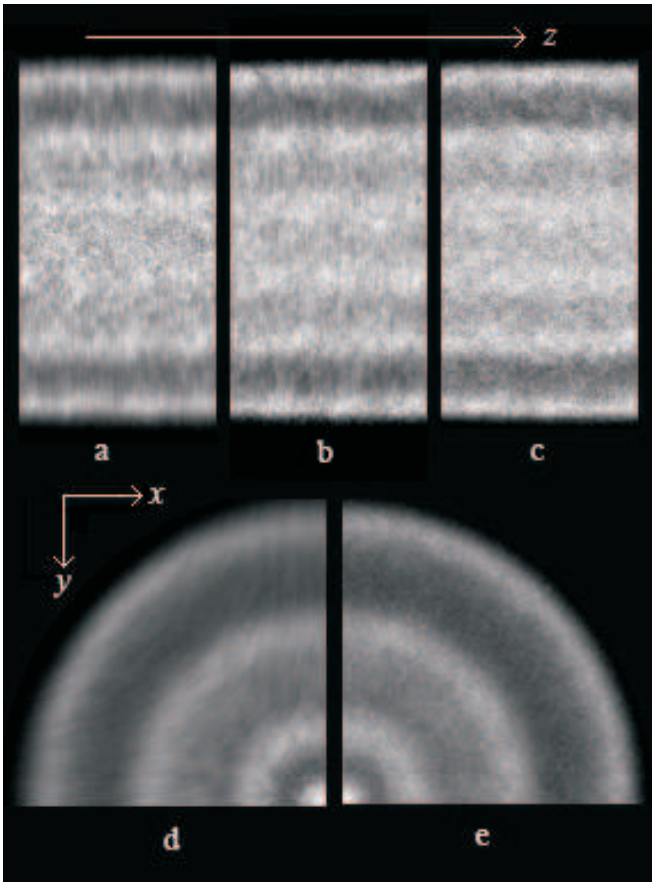


FIG. 23: Micromotion in simulated images. Here, sections from simulated images of a cold ensemble consisting of 500 barium ions are shown - simulated including micromotion (a, b, and d) and in the pseudopotential (c and e).

$^{138}Ba^{+}$ ions at $T_{sec} = 12$ mK – simulated in the pseudopotential approximation (c and e) and when including the micromotion (a, b, d). (d) and (e) show sections of axial views, (a), (b) and (c) sections of radial views, while (a) is a view along the $x$-axis and (b) and (c) correspond to the line of sight of the CCD camera (at 45° to the $x$- and $y$-axis). In fact, as the pseudopotential is radially symmetric, (c) shows the view along any angle perpendicular to the axial direction.

If the ions are close to the $x$- or $y$-axis, their micromotion is parallel to the corresponding axis, which is shown in (d). Thereby, their motional amplitude is larger, the further away they are from trap center ($z$-axis). Image (a) is taken along the $x$-axis, so the center is dominated by ions moving perpendicular to the image plane without a visible effect. The outer two shells are dominated by ions moving up and down in the image plane, so they appear blurred. However, the only possible radial line of sight for the CCD camera is between the electrodes as shown in (b). Here, the blurring is weaker and homogeneous as it can be understood comparing with image (d).

In general, the images from simulations including

micromotion appear more blurred then those from simulations in the pseudopotential. But due to the limited resolution of our imaging systems, this weak effect is not visible in the CCD images. Thus, in order to simulate experimental CCD images, the pseudopotential approach is sufficient.

## IV. Conclusion

In this work, we describe a model for the simulation of cold multi-species ion ensembles in linear Paul traps. Newton's equations of motion for all trapped ions were solved for the exact rf trap potential as well as in the rf averaged pseudopotential approximation. Studies of the influence of rf micromotion on the simulated (long time exposure) images of ion crystals and rf heating effects showed, that micromotion is of little importance for ion crystals at temperatures below 100 mK. Here, simulations in the pseudopotential approximation with their much lower computing times can be used to reproduce and interpret experimental data. Various heating effects (including rf heating) can be modelled by implementing additional velocity kicks with appropriate magnitudes and frequencies. We showed several applications of our simulation model. It can be used to extract temperatures and numbers of laser-cooled and sympathetically cooled ions from experimental CCD images of ion crystals. It also allows detailed studies of the sympathetic cooling process which help to understand and improve our experimental work. Furthermore, simulations of radial secular excitation spectra help to identify trapped ion species.

## V. Acknowledgments

We thank H. Wenz and J. Koelemeij for helpful discussions. We gratefully acknowledge funding from the EC network HPRN-CT-2002-00290 "Cold Molecules" and the DFG program SP1116.

[1] D. J. Larson et al., Phys. Rev. Lett. **57**, 70 (1986).
[2] M. D. Barrett et al., Phys. Rev. A **68**, 042302 (2003).
[3] B. Roth et al., J. Phys. B. **38**, 3673 (2005).
[4] A. Ostendorf et al., Phys. Rev. Lett. **97**, 243005 (2006).
[5] K. Molhave and M. Drewsen, Phys. Rev. A **62**, 011401 (2000).
[6] T. Baba and I. Waki, J. Chem. Phys. **116**, 1858 (2002).
[7] P. Blythe et al., Phys. Rev. Lett. **95**, 183002 (2005).
[8] B. Roth et al., Phys. Rev. A **73**, 042712 (2006).
[9] J. Mikosch et al., J. Chem. Phys. **121**, 11030 (2004).
[10] P. O. Schmidt et al., Science **309**, 749 (2005).
[11] J. Koelemeij et al., submitted (2007).
[12] J. M. Haile, *Molecular Dynamics: Elementary Methods* (John Wiley and Sons, New York, 1997).
[13] M. P. Allen and D. J. Tildesley, *Computer Simulation of liquids* (Clarendon Press, Oxford, 1987).
[14] A. Rahman and J. P. Schiffer, Phys. Rev. Lett. **57**, 1133 (1986).
[15] J. P. Schiffer, Phys. Rev. Lett. **61**, 1843 (1988).
[16] V. L. Ryjkov, X. Z. Zhao, and H. A. Schuessler, Phys. Rev. A **71**, 033414 (2005).
[17] S. Schiller and C. Lämmerzahl, Phys. Rev. A **68**, 053406 (2003).
[18] M. Bussmann et al., Int. J. Mass. Spectrom. **251**, 179 (2005).
[19] B. Roth, P. Blythe, and S. Schiller, Phys. Rev. A **75**, 023402 (2007).
[20] M. J. Jensen, T. Hasegawa, J. J. Bollinger, and D. H. E. Dubin, Phys. Rev. Lett, **94**, 025001 (2005).
[21] In fact, the stochastic force $\boldsymbol{F}_i^{stochastic}$ is implemented by the velocity kick model (see Section II.B).
[22] P. K. Gosh, *Ion traps* (Clarendon Press, Oxford, 1995).
[23] D. J. Berkeland et al., J. Appl. Phys. **83**, 5025(1998).
[24] R. Blümel, C, Kappler, W, Quint, and H. Walther, Phys. Rev. A **40**, 808 (1989).
[25] J. Prestage et al., Phys. Rev. Lett. **66**, 2964 (1991).
[26] P. Banks, Planet Space Sci. **14**, 1105 (1966).
[27] A. Dalgarno, M. R. C. McDowell, and A. Williams, Phil. Trans. Roy. Soc. A **250**, 411 (1957).
[28] C. Raab et al., Phys. Rev. Lett. **85**, 538 (2000).
[29] P. Bushev et al, Phys. Rev. Lett. **92**, 223602 (2004).
[30] J. B. Fenn et al., Science **246**, 4926 (1989).
[31] K. Okada et al., Jpn. J. Appl. Phys. **45**, 951 (2006).

# Blackbody thermometry with cold molecular ions and possible application to ion-based frequency standards

J.C.J. Koelemeij,* B. Roth, and S. Schiller
*Institute for experimental physics, Heinrich Heine University Düsseldorf, Germany*
(Dated: March 12, 2007)

We have used laser spectroscopy to measure the rotational level distribution of trapped molecular $HD^+$ ions at translational temperatures in the millikelvin range. Under our experimental conditions, the internal (rotational) degrees of freedom turn out to be independent of the translational degrees of freedom, and an effective rotational temperature close to room temperature is found. The near absence of background-gas collisions allows to relate the rotational temperature directly to the temperature of the ambient blackbody radiation (BBR). This feature suggests the use of molecular ions for BBR thermometry, which may help to improve the accuracy of frequency standards based on trapped atomic ions. We propose BBR thermometry in ion optical clocks, based on a novel scheme for nondestructive detection of rotational states of $CO^+$.

PACS numbers: Valid PACS appear here

## I. INTRODUCTION

Blackbody radiation (BBR) is ubiquitous in the physical world. In particular for spectroscopy of atoms and molecules, the presence of BBR has a significant influence on measurement and analysis. For polar molecules, room-temperature BBR has a strong effect on the population distribution of rotational and vibrational states. This affects the shape and resolution of molecular spectra to a large extent. For atoms, BBR-induced shifts to transition frequencies are often very small; however, they contribute significantly to the inaccuracy of atomic frequency standards [1–3].

Measurement of the rotational distribution of an ensemble of molecules is a common method to obtain information on the internal temperature. The internal (rovibrational) degrees of freedom of diatomic, polar molecules couple strongly to the electric component of the BBR field. In the absence of inelastic collisions with background gas constituents, the internal temperature of a polar molecule is determined completely by BBR, and polar molecules thus might be used to probe the BBR field. Such conditions may be achieved achieved with cold molecular ions stored under ultrahigh vacuum conditions. For typical ion traps, trapping frequencies are of order 1 MHz or less, whereas rotational and vibrational frequencies are much larger than 1 GHz. Therefore, no strong couplings of the translational degrees of freedom to the internal degrees of freedom are expected to exist, as indicated by the experimental work of Bertelsen *et al.* [4]. Thus, for an isolated polar molecular ion, any method to measure the populations of those internal states which interact with BBR might be used to find the temperature of the BBR field.

In this article, we demonstrate how trapped molecular ions can be used as a probe of the BBR field. We will first describe an experiment in which we determined the BBR temperature via spectroscopy of $HD^+$ molecules (Sec. II). Having established the possibility of using cold, trapped molecular ions as BBR thermometers, we propose the use molecular ions for BBR thermometry in ion traps for optical clocks in Sec. III. A novel, nondestructive method for detecting rotational state populations is proposed in Sec. III A. The detrimental effect of BBR on atomic clock transitions is discussed briefly in Sec. III B, as well as several candidate molecular ions for BBR thermometry. The results of this work are summarized in Sec. IV. In Appendix A, we address the issue of non-isothermal BBR fields, which may occur in realistic situations.

## II. EXPERIMENTAL DETERMINATION OF THE BLACKBODY TEMPERATURE USING $HD^+$

### A. Theoretical background

At room temperature, the nuclear vibration of $HD^+$ is virtually frozen out. On account of its small reduced nuclear mass, $HD^+$ has a large rotational constant, $B_0 \approx 22\ \mathrm{cm}^{-1}$. Consequently, only the seven first rotational levels are significantly populated at room temperature, where the fractional populations $f_{v,J}(T)$ are given by

$$f_{v,J}(T) = f_{0,0}(T)(2J+1)\exp\left(-E_{v,J}/k_{\mathrm{B}}T\right). \quad (1)$$

The rovibrational energies $E_{v,J}$ have been calculated to high accuracy for $HD^+$ [5]. However, the energies used in the present analysis are those obtained by solving the radial Schrödinger equation for the *ab initio* potential energy curve given by Esry and Sadeghpour [6]. The resulting rovibrational wavefunctions were subsequently used to find the expectation values $\mu_{v'J',vJ}$ of the dipole moment function, also given in Ref. [6]. Good agreement with previous values for $\mu_{v'J',vJ}$ is found [7]. The interaction of BBR with the rotational degrees of freedom is

*Electronic address: Jeroen.Koelemeij@uni-duesseldorf.de

described by Einstein rate equations, where the Einstein coefficients are given by their usual definitions:

$$A_{v'J',v''J''} = \frac{\omega^3}{3\pi\epsilon_0\hbar c^3}\frac{S_{J',J''}}{2J'+1}\mu^2_{v'J',v''J''}, \quad (2a)$$

$$B_{v'J',v''J''} = \frac{\pi^2 c^3}{\hbar\omega^3}A_{v'J',v''J''}, \quad (2b)$$

$$B_{v''J'',v'J'} = \frac{2J'+1}{2J''+1}B_{v'J',v''J''}. \quad (2c)$$

Here, the primed (double-primed) quantities refer to the the upper (lower) state of the transition, and $\omega$ is the angular frequency of the transition. $S_{J',J''}$ is given by the Hönl-London formulae [8]. The BBR spectral density, for a given temperature $T$, used in the rate equations is

$$\rho_T(\omega) = \frac{\hbar\omega^3}{\pi^2 c^3\left[\exp(\hbar\omega/k_BT)-1\right]}. \quad (3)$$

The rate equations can be modified to include the interaction with laser radiation inducing rovibrational transitions in $HD^+$, as is the case in our experiment.

### B. Experimental setup

#### 1. *Trapping, sympathetic cooling and detection of $HD^+$*

Details of the setup and the method to obtain trapped, sympathetically cooled $HD^+$ ions were described in previous publications [9, 10]. In brief, we trap $\sim 2000$ $Be^+$ ions in a linear radiofrequency trap, which are brought to temperatures of $\sim 10$ mK by means of (Doppler) laser cooling at 313 nm. We monitor the fluorescence level at 313 nm with a photomultiplier tube (PMT). At these temperatures, the beryllium ions arrange themselves in an ordered state referred to as Coulomb crystals. $HD^+$ ions are loaded into the trap by electron impact ionization of neutral HD gas, after which they are sympathetically cooled to $\sim 20$ mK by the $Be^+$ ions and become embedded inside the Coulomb crystal. The presence of $HD^+$ manifests itself as a change in the 313 nm $Be^+$ fluorescence when the $HD^+$ radial (secular) motion in the ion trap is resonantly driven by an ac electric field. For typical intensities and detunings below resonance of the 313 nm laser, the fluorescence rises if the $HD^+$ motion is excited. The rise in fluorescence is approximately linearly proportional to the number of trapped $HD^+$ ions.

#### 2. *Rovibrational spectroscopy of $HD^+$*

Recently, we have demonstrated rovibrational spectroscopy of $HD^+$ through (1+1') resonance enhanced multiphoton disscociation (REMPD) [10]. The REMPD process is depicted schematically in Fig. 1. The first photon (with wavelength 1.4 $\mu$m) drives a $(v'=4,J') \leftarrow (v=0,J)$ overtone transition within the electronic

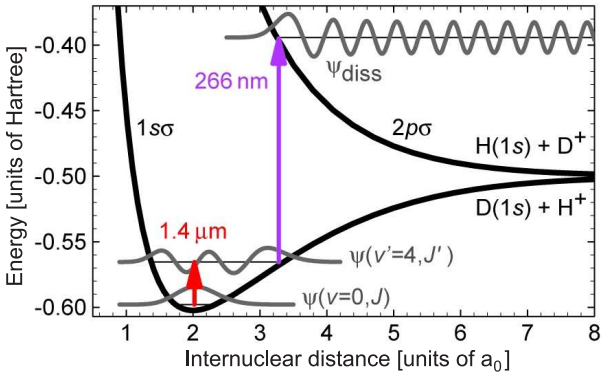


FIG. 1: (Color online) Principle of (1+1') REMPD spectroscopy of $HD^+$ ions. A tunable infrared diode laser excites a rovibrational overtone transition $(v'=4,J') \leftarrow (v=0,J)$. The $HD^+$ ions excited to the $v'=4$ vibrational level are dissociated using 266 nm laser radiation: $HD^+(v'=4)+h\nu_{266} =$ $H+D^+$ or $H^+$+D. Due to different Franck-Condon wave function overlap, the calculated uv absorption cross section from the (v=4) level ($\sim 2.4\times10^{-17}$ cm$^2$) is about seven orders of magnitude larger than from $v=0$ [11, 12]. Energy values represent total binding energies of the molecule

ground state of $HD^+$. Population in the $v=4$ state is consecutively dissociated by the second photon at 266 nm. This leads to loss of $HD^+$ ions from the trap, which is monitored with the secular excitation method described above. In our previous work we used this method aiming at high resolution of the $(v'=4,J') \leftarrow (v=0,J)$ spectra, which show hyperfine structure spanning roughly 180 MHz about the deperturbed transition frequency. Here, we will be merely interested in driving "pure" rovibrational transitions in order to infer the rotational populations $f_{0,J}(T)$ in the vibrational ground state. To this end, we dither our laser, thereby broadening it to 200 MHz (FWHM). Tuning the laser to the deperturbed frequency then ensures that all hyperfine components are simultaneously addressed.

### C. Method and results

Our experiment aims at the determination of the rotational temperature $T$ from experimentally determined populations $f_{0,J}(T)$. This is accomplished as follows. We tune the 1.4 $\mu$m laser to a specific transition $(v'=4,J+1) \leftarrow (v''=0,J)$ within the $R$ branch, where $J=0,1,...,7$. The transition frequencies used here are the *ab initio* results given by Balint-Kurti *et al.* [13]. The expected accuracy of these results is 6 MHz, which is in agreement with a recent precision measurement of the $(v'=4,3) \leftarrow (v''=0,2)$ transition [14]. Next, we execute a cycle consisting of quasicontinuous secular excitation (QSE) of the $HD^+$ trap motion for a 5 s time interval, followed by a 0.4 s period of REMPD, and ending with another 5 s of QSE (see Fig. 2). For an optimum signal-to-noise (S/N) ratio, we use the 1.4 $\mu$m laser at its

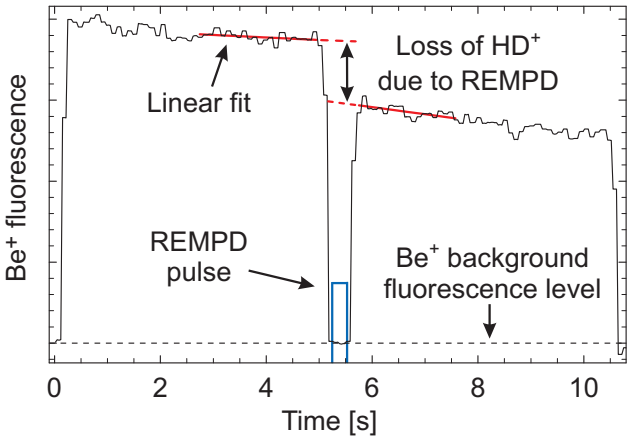


FIG. 2: (Color online) Experimental cycle of REMPD and detection of loss of $HD^+$ using the method of quasicontinuous secular excitation. Linear segments are fitted to the fluorescence during secular excitation, the slope of which is determined by all loss processes other than the REMPD. The discontinuity between the extrapolated fitted segments thus gives a measure for the loss of $HD^+$ duo to the REMPD process only.

maximum power (1.3 mW). The duration of the REMPD pulse is kept as short as possible to minimize the effect of repopulation of the lower level via BBR, which sets in on a timescale of seconds, without compromising the S/N ratio. We record the 313 nm fluorescence and fit linear segments to the fluorescence levels during the QSE. The slope of each segment takes into account slow drifts of the fluorescence level, which are caused by the loss of $HD^+$ in collisions with background gas, and by slow variations in the laser power and frequency. The discontinuity between the two segments at time $t_h$, at the end of the REMPD pulse, gives the fractional loss of $HD^+$ due to the REMPD process only (Fig. 2). To reduce the effect of possible slow drifts occurring on the timescale of the entire experiment (2.5 hours), we apply only 10 consecutive cycles per transition before moving on to another transition. Once all eight transitions have been addressed, the procedure is repeated until each transition has been subject to 30 cycles. During the procedure, some of the $Be^+$ ions are lost from the trap, mostly through chemical reactions with neutral HD gas during the loading of $HD^+$ ($HD^+$ needs to be reloaded every 3–9 cycles). To compensate the gradual loss of $Be^+$, we load extra $Be^+$ into the trap every $\sim 100$ cycles. Let $p_J(T)$ be the measured fractional loss of $HD^+$, sustained during a single cycle due to the REMPD process only, where $T$ is the true internal temperature of the molecules. The fractional populations $f_{0,J}(T)$ are related to the $p_J(T)$ in a nontrivial way, since the REMPD process (which depletes the lower rotational level $J$) competes with the repopulation of level $J$ mediated by BBR and which involves all populations within the rotational manifold. To infer $f_{0,J}(T)$ from the measured $p_J(T)$, we simulate the experimental cycle using the Einstein rate equations and obtain a theoretical value for the ratio $\tilde{f}_{0,J}(T)/\tilde{p}_J(T)$ (the tilde indicates results from the simulation). This value depends only weakly on the used laser intensities, and the uncertainty in the measured intensities has a marginal effect on the final measurement uncertainty. However, this approach forces us to assume a certain value $T_0$ for the BBR temperature, which affects the simulation through $\rho_T$ and the initial state populations given by Eq. (1). As an initial guess, we assume $T_0 = 300$ K to find $\tilde{f}_{0,J}(T_0)/\tilde{p}_J(T_0)$. For each $J$, we multiply this ratio with the measured value $p_J(T)$ to find intermediate values $f_{0,J}(T_1)$, where $T_1$ is found by fitting the distribution in Eq. (1) to the intermediate values $f_{0,J}(T_1)$. We subsequently run the simulation again, this time with $T_1$ as input temperature. This gives improved ratios $\tilde{f}_{0,J}(T_1)/\tilde{p}_J(T_1)$. Multiplying again with $p_J(T)$ gives $f_{0,J}(T_2)$, where $T_2$ is again found by fitting the rotational distribution. It should be noted that this approach directly yields the fractional populations, *i.e.* no overall scaling factors are involved. Two consecutive iterations give a final rotational temperature of 340 K, which is convergent to within a few Kelvin. This is much smaller than the 30 K uncertainty in the fitted temperature, which stems primarily from random fluctuations in the decay values, and possible unidentified $J$-dependent systematic offsets. The final fitted rotational distribution function is plotted in Fig. 3, together with several distribution functions at other temperatures. Our result clearly indicates that sympathetic cooling of molecular ions to millikelvin temperatures in an ion trap has a negligible effect on the internal (rotational and vibrational) degrees of freedom. This contrasts other cooling methods for trapped molecular ions via collisions with a buffer gas [15]. The independence of the translational and internal degrees of freedom observed in our experiment can be attributed to the fact that internal transitions have frequencies exceeding 1 THz, whereas typical trap frequencies are on the order of 1 MHz or less. As a consequence, couplings between the different degrees of freedom must be either highly non-resonant, or of very high order, and therefore weak. We note that hyperfine populations may be influenced by the trap motion in the presence of magnetic field gradients, as magnetic hyperfine transition frequencies and trap frequencies are of the same order of magnitude. However, such effects are eliminated by dithering our probe laser over the entire hyperfine spectrum.

The rotational temperature might be affected by inelastic collisions with background-gas constituents. Assuming collisions with neutral $H_2$, which is likely the most abundant background gas constituent, we can put an upper limit on the collision rate using the total cross section for collisions of a charged ion with $H_2$ [16]

$$\sigma_T = \pi\Gamma(1/3)\left(\frac{\alpha q^2}{16\epsilon_0\hbar v}\right)^{2/3}. \qquad (4)$$

Here, $v$ is the relative velocity between $HD^+$ and $H_2$ at 300 K, and $\alpha$ stands for the polarizability of $H_2$. In our

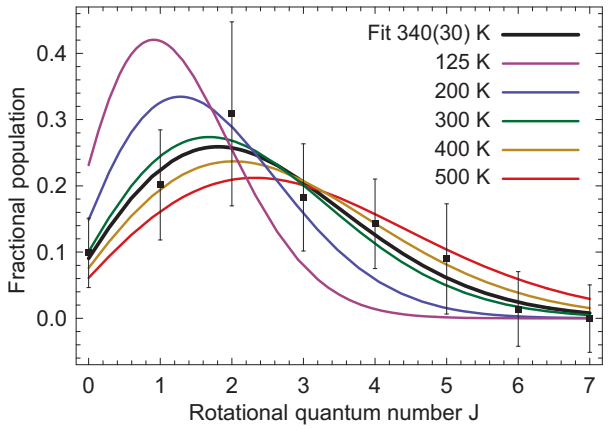


FIG. 3: (Color online) Solid curves are $HD^+$ rotational distributions (in the vibrational ground state $v = 0$) at various temperatures. The data points are the average rotational populations inferred using REMPD spectroscopy of $(v' = 4, J + 1) \leftarrow (v'' = 0, J)$ transitions in $HD^+$, where the error bars represent the standard deviation of the set of individual data points for each $J$. The black curve represents an unweighted fit of the rotational distribution to the data, resulting in $T = 340(30)$ K.

apparatus, the total pressure is smaller than $10^{-8}$ Pa. Averaging Eq. (4) over the Maxwell-Boltzmann distribution of $H_2$, and assuming collisions with $H_2$ at 300 K and $10^{-8}$ Pa, we find a total collision rate of 0.033 $s^{-1}$. A considerable fraction of these collisions is elastic, so the rate of collisional rotational relaxation will be even smaller. For comparison, the total BBR-induced transition rate (at 300 K) is larger than 0.44 $s^{-1}$ for rotational levels $J > 0$, and equals 0.11 $s^{-1}$ for $J = 0$. Thus, we can ignore the effect of collisional relaxation, and we interpret the found rotational temperature as an effective BBR temperature. It should be noted, however, that the actual BBR field may be a superposition of several BBR fields at different temperatures.

## III. NONDESTRUCTIVE SPECTROSCOPY AND BBR THERMOMETRY WITH MOLECULAR IONS

### A. Nondestructive and state-selective detection of molecular ions

The experiment described in Sec. II shows that trapped molecular ions can be used to determine the temperature of the BBR field. The $\sim 30$ K inaccuracy of the temperature measurement could, in principle, be improved by including more data points. Since the procedure for reloading $HD^+$ ions into the trap takes much longer ($\sim 60$ s) than the $\sim 15$ s for rethermalization by the BBR, an additional speed-up in the data taking rate would result if the spectroscopy would be done nondestructively. Such a scheme would also remove the need for a suitable transition for dissociation of the molecule. Furthermore, it would be more suitable for spectroscopy and manipulation of single molecular ions: high resolution spectroscopy and quantum information of single atomic ions typically relies on nondestructive detection [17].

With the application of BBR thermometry in ion-based optical clocks (Sec. III B) in mind, we propose a novel nondestructive scheme for molecular spectroscopy using an ion crystal containing one or several molecular ions, and one typical clock ion. The molecular ions could be used for BBR thermometry. For simplicity, we assume a linear ion crystal consisting of one typical clock ion, and one molecular ion. This does not preclude the application of this method to larger ion ensembles, as we will show below. The harmonically bound ions resemble a system of oscillators which are coupled through their mutual Coulomb repulsion [18], and the ion crystal thus possess a corresponding set of normal modes. The clock ion is assumed to have a strong cycling transition which allows laser cooling of all modes of the ion crystal, whereas the narrow clock transition permits resolved observation of sideband transitions on any of the modes. These features allow the determination of the mean number of motional quanta in a specific normal mode after laser cooling to $\sim 1$ mK temperature [19]. The spectroscopy can now be realized by introducing a mechanism which significantly heats a particular normal mode (here designated as the "bus" mode), but which is present only when the molecular ion is in a specific rotational state. To realize such a mechanism, we propose to use an optical dipole force, modulated at the frequency of the bus mode. Previously, this technique was used to realize a geometric phase gate for trapped atomic ion qubits [16, 20]. State-selective detection is accomplished by tuning the wavelength of the optical dipole laser near the rotational level of interest, meanwhile maintaining a considerably larger detuning from other levels. As will be shown below, near unit detection efficiency of a single rotational state might be achieved, depending on the strength of the heating mechanism compared to other heating mechanism occurring in the trap. Then, for each level out of a given set of rotational levels, measurement of the frequency of heating events would allow the determination of its time-averaged population. The populations, in turn, reveal the rotational temperature of the molecule.

As a numerical example, we consider spectroscopy of $CO^+$. The modulated optical dipole force (MODF) is realized using the $(3 - 0)$ band of the A $^2\Pi \leftarrow X\ ^2\Sigma^+$ electronic transition. This electronic transition has been subject to many studies in relation with its appearance in the emission spectrum of comet tails. The $(3 - 0)$ band origin corresponds to a wavelength of 401 nm, and experimental molecular constants are available allowing the prediction of level energies with $\sim$ GHz accuracy [21]. The electronic part of dipole transition matrix element has been calculated by Rosmus and Werner [22], and the Franck-Condon factor for the $(3 - 0)$ band is 0.18 [21].

This leads to a transition dipole moment of about 0.1 $ea_0$. The lifetime of the A $^2\Pi$ upper state has been measured and calculated by several authors and amounts to roughly $\sim 3$ $\mu$s (see [22] and references therein).

The MODF can be realized by overlapping two laser beams such that their respective wavevectors $k_i$ add up to an effective wavevector $\Delta k \geq ki$ along the axis of ion crystal. The frequency of both laser beams is detuned by $\sim 1$ GHz from a particular line $J' - J$ in the $(3-0)$ band, while the mutual detuning between the beams is near the frequency of the axial stretch mode (which acts as the bus mode here). For traps in operating in the Lamb-Dicke regime for optical wavelengths, the mode frequencies are typically 1–10 MHz. This configuration of laser beams creates a running standing wave, which exerts a force on the $CO^+$ ion only. If this force is synchronous with the stretch mode motion, it will resonantly excite its amplitude. We will assume that the stretch mode of the ion crystal has been cooled to the motional ground state using the narrow optical clock transition [23]. From the Schrödinger equation for this system (see *e.g.* [16]), it can be shown that two beams with a power of 8 mW per beam, focused to an 80 $\mu$m waist at the position of the ions, can heat the the stretch mode out of the ground state within 30 $\mu$s. This is much shorter than the lifetime due to off-resonant spontaneous emission from the A $^2\Pi$ state, which we estimate to be $\sim 50$ ms. The heating time is also much faster than the motional heating time caused by fluctuating electric fields at the location of the ion, which generally takes place on time scales longer than 1 ms [24]. It is noteworthy that such fluctuating fields are rather uniform since they stem from fluctuations of the potentials of the trap electrodes; therefore, the stretch mode is relatively insensitive to this kind of trap heating as compared to the center-of-mass mode [25]. The heating event can be detected by probing the red sideband of the stretch mode on the clock transition: only if heating occurred the red sideband will become visible, and therefore near unit efficiency in the detection might be feasible.

### B. Application of BBR thermometry to ion-based optical clocks

The presence of BBR in atomic frequency standards gives rise to a frequency shift of the clock transition which is known only to within a certain accuracy. For frequency standards based on a magnetic clock transition, the ac-Zeeman shift caused by the BBR field adds to the uncertainty in the clock frequency. Besides the limited accuracy to which Zeeman Hamiltonians are known, the uncertainty stems from inadequate knowledge of exact form of the BBR spectrum. The latter depends on the temperature distribution of the structure surrounding the atomic ensemble being interrogated, as well as on its geometry and emissivity. (Spectral) emissivities are generally not accurately known, and the spatial temperature distribution can be nontrivial in systems in which local heating due to dissipation of electric currents occurs. For example, in cesium fountain frequency standards the BBR shift gives rise to the largest systematic uncertainty in the clock accuracy ($\approx 3 \times 10^{-16}$ relative uncertainty), which is almost entirely due to the uncertainty in the BBR temperature.

Also in optical atomic clocks BBR is a source of inaccuracy; in this case it causes a (quadratic) Stark shift to the optical clock transition. Again, the uncertainty has two origins: the differential electric polarizability $\sigma_S$ (which is known from atomic structure calculations [3] or measurement [26]), and the unknown exact shape of the BBR spectrum. Typical room temperature (relative) BBR shifts are of the order $10^{-15}$ causing $\sim 1 \times 10^{-16}$ inaccuracy [27–32]. Two ion-based optical clocks have considerably smaller shifts: the liquid-helium cooled $^{199}Hg^+$ clock, which has a shift which is reduced by $10^7$ from the room temperature value [26, 33], and the $^{27}Al^+$ clock, having a relative shift of $8(3) \times 10^{-18}$ [26] due to nearly cancelling polarizabilities of the upper and lower levels of the clock transition. In view of the search for a temporal variation of the fine structure constant, $\alpha$, it will be desirable to compare variety of atomic clocks based on different species [34]. Such a comparison might therefore benefit from reduction of the inaccuracy caused by BBR in all involved atomic clocks.

Although we anticipate that nondestructive spectroscopy of $CO^+$ is well feasible, it is likely not the most suited candidate for BBR thermometry. The main reason is that every measurement of the thermal state causes a collapse of the rotational wavefunction into a nonthermal state, so that the next measurement cannot take place before the rotational state of the molecule has rethermalized. The rotational constant of $CO^+$, however, is relatively small compared to that of $HD^+$ and other diatomic hydride ions. This reduces the magnitude of the Einstein-$B$ coefficients, and makes the rethermalization process rather slow (about 200 s at room temperature). Diatomic hydride ions, on the other hand, rethermalize about as fast as $HD^+$, and are more promising candidates for BBR thermometry. In laser-cooled ion experiments, hydrides of the laser-cooled species are a frequently encountered byproduct: collisions of background gas molecules (mostly neutral $H_2$) with laser-cooled ions in their excited state are often exothermic. Morse potential molecular constants for several common metal-hydride ions are available [35–37]; however, spectroscopic accuracy for the vibrational level energies has not yet been reported. Even so, BBR thermometry using ensembles of $HD^+$ as demonstrated above remains a possibility.

## IV. SUMMARY

We have, for the first time, measured the rotational temperature of trapped molecular ions at millikelvin temperatures. Our result shows that the coupling be-

tween rotational and vibrational degrees of freedom of the molecules to translational degrees of freedom is negligible compared to the coupling with blackbody radiation. The virtual absence of inelastic collisions allows to directly relate the rotational temperature to the temperature of the BBR radiation field. The use of trapped molecular ions for BBR thermometry may find application inside trapped-ion optical clocks, as part of the determination of the BBR frequency shift to the clock transition. This may be useful especially in rf traps, where dissipation of the ac trap-drive current can lead to significant local heating of the trap electrode surfaces, and estimating the effective *in situ* BBR temperature may be problematic. In addition to the demonstrated thermometry based on $HD^+$, we propose a novel spectroscopic method to infer the rotational distribution in diatomic molecules, which are trapped simultaneously with a typical clock ion. The method relies on state-dependent observation of heating of the molecular motion by a modulated optical dipole force, similar to that used for geometric phase gates performed on trapped ion qubits [20].

### Acknowledgments

We thank H. Daerr for assistance during early stages of the experiment. J.K. acknowledges support from the Alexander von Humboldt Foundation.

[1] W. M. Itano, L. Lewis, and D. Wineland, Phys. Rev. A **45**, 1233 (1982).
[2] W. M. Itano, J. Res. Natl. Inst. Stand. Technol. **105**, 829 (2000).
[3] E. J. Angstmann, V. A. Dzuba, and V. V. Flambaum, Phys. Rev. A **74**, 023405 (2006).
[4] A. Bertelsen, S. Jørgensen, and M. Drewsen, J. Phys. B: At. Mol. Opt. Phys. **39**, L83 (2006).
[5] V. I. Korobov, Phys. Rev. A **74**, 052506 (2006).
[6] B. D. Esry and H. R. Sadeghpour, Phys. Rev. A **60**, 3604 (1999).
[7] E. A. Colbourn and P. R. Bunker, J. Mol. Spectrosc. **63**, 155 (1976).
[8] G. Herzberg, *Spectra of Diatomic Molecules*, (Van Nostrand, New York, 1950).
[9] P. Blythe, B. Roth, U. Fröhlich, H. Wenz, and S. Schiller, Phys. Rev. Lett. **95**, 183002 (2005).
[10] B. Roth, J. C. J. Koelemeij, H. Daerr, and S. Schiller, Phys. Rev. A **74**, 040501 (2006).
[11] M. Tadjeddine and G. Parlant, Mol. Phys. **33**, 1797 (1977).
[12] A. Kondorskiy (private communication).
[13] G. G. Balint-Kurti, R. E. Moss, I. A. Sadler, and M. Shapiro, Phys. Rev. A **41**, 4913 (1990).
[14] J. C. J. Koelemeij, B. Roth, A. Wicht, I. Ernsting, and S. Schiller, *submitted*.
[15] D. Gerlich, in *Advances in Chemical Physics Series, Vol. LXXXII*, C.-Y. Ng and M. Baer, Eds. (John Wiley and Sons, Inc. New York, 1992), pp. 1.
[16] D. J. Wineland, C. Monroe, W. M. Itano, D. Leibfried, B. E. King, and D. M. Meekhof, J. Res. Natl. Inst. Stand. Technol. **103**, 259 (1998).
[17] P. O. Schmidt, T. Rosenband, C. Langer, W. M. Itano, J. C. Bergquist, and D. J. Wineland, Science **309**, 749 (2005).
[18] G. Morigi and H. Walther, Eur. Phys. J. D **13**, 261 (2001).
[19] M. Barrett, B. L. DeMarco, T. Schaetz, V. Meyer, D. Leibfried, J. Britton, J. Chiaverini, W. M. Itano, B. M. Jelenkovic, J. D. Jost, et al., Phys. Rev. A **68**, 042302 (2003).
[20] D. Leibfried *et al.*, Nature **422**, 412 (2003).
[21] R. Kepa, A. Kocan, M. Ostrowska-Kopec, I. Piotrowska-Domagala, and M. Zachwieja, J. Mol. Spectrosc. **228**, 66 (2004).
[22] P. Rosmus and H. Werner, Mol. Phys. **47**, 661 (1982).
[23] F. Diedrich, J. C. Bergquist, W. M. Itano, and D. J. Wineland, Phys. Rev. Lett. **62**, 403 (1989).
[24] L. Deslauriers, S. Olmschenk, D. Stick, W. K. Hensinger, J. Sterk, and C. Monroe, Phys. Rev. Lett. **97**, 103007 (2006).
[25] D. Kielpinski, B. E. King, C. J. Myatt, C. A. Sackett, Q. A. Turchette, W. M. Itano, C. Monroe, D. J. Wineland, and W. H. Zurek, Phys. Rev. A **61**, 032310 (2000).
[26] T. Rosenband and W. M. Itano and P. O. Schmidt and D. B. Hume and J. C. J. Koelemeij and J. C. Bergquist and D. J. Wineland, arXiv:physics/0611125 (v1 14 Nov 2006).
[27] T. Becker, J. von Zanthier, A. Y. Nevsky, C. Schwedes, M. N. Skvortsov, H. Walther, and E. Peik, Phys. Rev. Lett. **63**, 051802 (2001).
[28] T. Schneider, E. Peik, and C. Tamm, Phys. Rev. Lett. **94**, 230801 (2005).
[29] X. B. R. Le Targat, M. Fouché, A. Brusch, O. Tcherbakoff, G. D. Rovera, , and P. Lemonde, Phys. Rev. Lett. **97**, 130801 (2006).
[30] U. Sterr, C. Degenhardt, H. Stoehr, C. Lisdat, H. Schnatz, J. Helmcke, F. Riehle, G. Wilpers, C. W. Oates, and L. Hollberg, Comp. Rend. Physique **5**, 845 (2004).
[31] M. M. Boyd, A. D. Ludlow, S. Blatt, S. M. Foreman, T. Ido, T. Zelevinsky, and J. Ye, Phys. Rev. Lett. **98**, 083002 (2007).
[32] H. S. Margolis, G. P. Barwood, G. Huang, H. A. Klein, S. N. Lea, K. Szymaniec, and P. Gill, Science **306**, 1355 (2004).
[33] W. H. Oskay *et al.*, Phys. Rev. Lett. **97**, 020801 (2006).
[34] J. Uzan, Rev. Mod. Phys. **75**, 403 (2003).
[35] J. B. Schilling, W. A. Goddard III, and J. L. Beauchamp, J. Am. Chem. Soc. **109**, 5565 (1987).
[36] G. Ohanessian, M. J. Brusich, and W. A. Goddard III, J. Am. Chem. Soc. **112**, 7179 (1990).
[37] K. Sugiyama and J. Yoda, Phys. Rev. A **55**, 10(R) (2004).

# Appendix C

# Conference proceedings

U. Fröhlich, B. Roth, P. Antonini, C. Lämmerzahl, A. Wicht, and S. Schiller, "Ultracold Trapped Molecules: Novel Systems for Tests of the Time-Independence of the Electron-to-Proton Mass Ratio", Lect. Notes Phys. **648**, 297 (2004).

B. Roth, J. Koelemeij, H. Daerr, I. Ernsting, S. Jorgensen, M. Okhapkin, A. Wicht, A. Nevsky, and S. Schiller, "Trapped Ultracold Molecular Ions: Candidates for an Optical Molecular Clock for a Fundamental Physics Mission in Space", in *Proc. of the 6th Internat. Conf. on Space Optics*, ESTEC, Noordwijk, The Netherlands, ESA-SP 621 (2006).

B. Roth, H. Daerr, J. Koelemeij, A. Nevsky, and S. Schiller, "Ultracold Molecular Hydrogen Ions in a Linear Radiofrequency Trap: Novel Systems for Molecular Frequency Metrology", Proc. '20th European Frequency an Time Forum EFTF', Braunschweig, Germany (2006).

B. Roth, J. Koelemeij, S. Schiller, L. Hilico, J.-P. Karr, V. Korobov, and D. Bakalov, "Precision Spectroscopy of Molecular Hydrogen Ions: Towards Frequency Metrology of Particle Masses", in *Precision Physics of Simple Atoms and Molecules*, Lect. Notes Phys. **745**, 205, Springer (2008).

# Ultracold Trapped Molecules: Novel Systems for Tests of the Time-Independence of the Electron-to-Proton Mass Ratio

U. Fröhlich, B. Roth, P. Antonini, C. Lämmerzahl*, A. Wicht, and S. Schiller

Institut für Experimentalphysik, Heinrich-Heine-Universität Düsseldorf,
40225 Düsseldorf, Germany, www.exphy.uni-duesseldorf.de

**Abstract.** The vibrational and rotational transition frequencies in molecules are functions of the electron-to-nucleon mass ratio. They can therefore be used for experiments searching for a time-dependence of the electron-to-proton and nucleon-to-nucleon mass ratios. We propose to to perform such tests with very high precision using ultracold molecular ions trapped in a radio-frequency trap and sympathetically cooled by atomic ions. The current status of an experiment using $Be^+$-ions as a coolant medium to cool light diatomic molecular ions is described. An interesting perspective is to perform high-precision spectroscopy on single ultracold molecules. We sketch an approach towards this goal.

## 1 Introduction

A large experimental effort is currently under way to test the foundation of metric theories of gravity, the Einstein Equivalence Principle (EP) [1]. This effort is motivated in part by the difficulties in unifying the theory of gravity with quantum theory. The EP includes the principle of Local Position Invariance, which states that the fundamental constants of nature, such as the fine structure constant $\alpha$, the mass ratios of the elementary particles, etc. are independent of time and position.

Tests of the time-independence of the fundamental constants can be performed by laboratory experiments or astronomical observations [2]. In laboratory tests, the frequencies of dissimilar types of oscillators are compared as a function of time, while in astronomical tests, the frequencies of the electromagnetic waves emitted in the far past by oscillators located in distant sources are compared with the current frequency values of the *same* type of oscillators as obtained in the laboratory. Table 1 gives an overview of some microscopic and macroscopic systems that define transition or oscillation frequencies.

Analysis of astronomical observations claims a variation of $\alpha$ on the order of 5 ppm over billions of years [7]. This claim provides increased stimulus for laboratory experiments. These have entered a new era, where use is made of the development of atomic clocks based on ultracold atoms and atomic ions, and new methods of precise comparison of optical and microwave frequencies. An improvement by more than an order of magnitude in the most stringent laboratory limits has already been achieved.

* Present address: ZARM, Universität Bremen, Germany.

U. Fröhlich et al., Ultracold Trapped Molecules: Novel Systems for Tests of the Time-Independence of the Electron-to-Proton Mass Ratio, Lect. Notes Phys. **648**, 297–307 (2004)
http://www.springerlink.com/ 

**Table 1.** Dependence of the transition energy or cavity photon energy (in units of the Rydberg energy $E_R$) of various oscillators on fundamental constants. For the function $F$, see [3]. The function $G(\alpha)$ is a relativistic correction factor for principal transitions; it reduces to unity in the non-relativistic limit (small-$Z$ atoms) [4]. The dependencies for molecular vibrational and rotational transitions are given for diatomic molecules, where $\mu$ is the reduced mass. For vibrational transitions between low-lying levels $H(m_e/\mu) \simeq \sqrt{m_e/\mu}$. The resonance frequency of a cavity is proportional to the size and thus to the interatomic spacing, resulting in $h\nu \propto E_R/\alpha$. Here, propagation of the electromagnetic wave in vacuum is assumed. For the case of monolithic cavities, see [5]. The last entry refers to the weak interaction-induced splitting between molecular levels of mirror molecules (enantiomers) [6] and to the parity non-conservation light shift in atoms. $G_F$ is the Fermi constant, $\theta_W$ is the Weinberg angle.

| Type | dependence |
|---|---|
| Hyperfine splitting | $g\,\alpha^2 F(\alpha Z) m_e/m_p$ |
| Fine-structure splitting | $\alpha^2$ |
| Electronic transitions | $G(\alpha)$ |
| Rotational transitions | $m_e/\mu$ |
| Vibrational transitions | $H(m_e/\mu)$ |
| Cavity frequencies | $\alpha^{-1}$ |
| Parity violation splitting | $G_F$ , $\sin^2\theta_W$ |

The best laboratory limits produced thus far constrain certain *combinations* of fundamental constants. For example, the recent high-precision tests concerned a comparison of hyperfine transition frequencies of ultracold atoms that yielded a test of the time-independence of $g_{Cs}/g_{Rb}\,\alpha^{0.44}$ at the level of $7 \cdot 10^{-16}$/yr [8]. A comparison of an optical transition in $Hg^+$ and the hyperfine frequency of Cs gave a limit of $7 \cdot 10^{-15}$/yr for the combination $g_{Cs}\alpha^6 m_e/m_p$ [9]. Vibrational transition frequencies in room-temperature molecular gases have also been investigated: a comparison of a vibration frequency of methane ($CH_4$) and the hyperfine frequency of Cs has led to an upper limit on the order $10^{-12}$/yr for the time dependence of the ratio [11]. A similar test using the molecule $OsO_4$ led to a limit $2 \cdot 10^{-13}$/yr [10]. Taking these two results together, the ratio of the two vibrational frequencies is found to be constant at the level of $10^{-12}$/yr. This may be interpreted as a limit for the time-dependence of the ratio of the characteristic nuclear masses corresponding to the vibrational modes studied.

From astronomical observations limits for individual fundamental constants have been derived. For example, concerning $\alpha$ the relativistic and spin-orbit energies of various atomic ions in quasars have been compared to laboratory values [4,7]. Concerning $m_e/m_p$, the ratio of energy differences of ro-vibrational levels in a given electronic state of molecules in distant interstellar clouds can be compared to present-day laboratory values. Based on observation of neutral $H_2$ absorption lines, constancy within 40 ppm was found [12,13].

## 2 Molecular Tests of Constancy of Electron-to-Nucleon Mass Ratios

Laboratory tests sensitive to the electron-to-nucleon mass ratio, and insensitive to other fundamental constants to lowest order, can be performed by one of the following methods [14]:

**(i)** Comparison of a vibrational or rotational molecular frequency and a non-relativistic electronic transition in an atom;
**(ii)** Comparison of a (ro-)vibrational frequency and a rotational frequency, in the same molecule or in different molecules;
**(iii)** Comparison of vibrational frequencies of different transitions in the same molecule or in different molecules;
**(iv)** Comparison of vibrational frequencies of different molecules.

The approach (iii) is based on the fact that the interatomic molecular potential is not harmonic and therefore the energy spacing between adjacent vibrational levels is not constant. The decrease in spacing for a diatomic molecule is itself a function of $m_e/\mu$, where $\mu$ is the reduced mass of the oscillating nuclei, and of the particular molecule.

If the comparisons are performed using hydrogen molecules ($H_2$, $H_2^+$, $H_3^+$), the ratio $m_e/m_p$ is accessed directly. If an arbitrary molecule is used, the ratio $m_e/\mu$ is accessed. A limit for the time-independence of $m_e/m_p$ can only be given under the assumption that the ratios of nuclear masses are time-independent, i.e. $\mu/m_p = const.$ However, if rotational or vibrational transitions of *different* molecules are compared (approach (iv)) then the ratio of nuclear masses can be probed [15]. An example is the comparison of $H_2^+$ and $D_2^+$ or $H_2^+$ and $HD^+$. Such tests would probe the time-independence of the strong interaction [16].

Referring to Fig. 1, we can describe the approaches (ii) and (iii) by

$$\frac{\mathrm{d}\,\ln\left(\frac{\nu_a-\nu_b}{\nu_a}\right)}{\mathrm{d}t} = (1-s)\frac{\mathrm{d}\,\ln(m_e/m_p)}{\mathrm{d}t}\ , \tag{1}$$

$$\frac{\mathrm{d}\,\ln\left(\frac{\nu_1}{\nu_2}\right)}{\mathrm{d}t} = (s_1-s_2)\frac{\mathrm{d}\,\ln(m_e/m_p)}{\mathrm{d}t}\ . \tag{2}$$

Here the coefficients $s_k$ are defined by the derivative of the relevant transition frequencies $\nu_k$ with respect to the electron-to-proton mass ratio,

$$\frac{m_e/m_p}{\nu_k}\frac{\mathrm{d}\nu_k}{\mathrm{d}(m_e/m_p)} \equiv s_k. \tag{3}$$

The coefficients $s_k$ can be calculated using quantum chemical algorithms. For example, Hilico et al. have performed such calculations for the vibrational levels of the $H_2^+$ and $D_2^+$ molecules [17].

To reach an interesting level of sensitivity and open up a direction for future progress, it is certainly necessary to use ultracold molecules. Since the approaches (i-iv) can be applied to essentially any molecule, molecular ions can

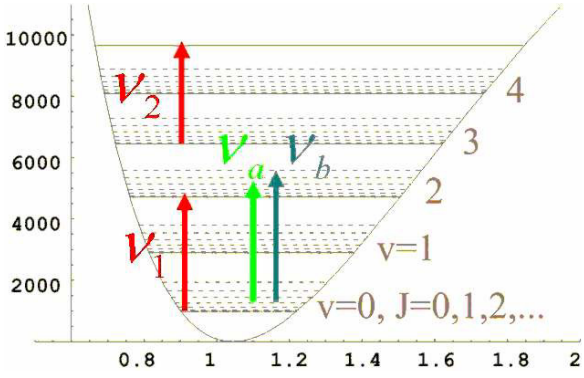


**Fig. 1.** Principle of the test of the time-independence of $m_e/m_p$. The relative difference of two ro-vibrational transition frequencies $\nu_a$, $\nu_b$ sharing a common level (method (ii)) or the ratio of two vibrational transition frequencies $\nu_1$, $\nu_2$ (method (iii)) is measured over the course of time.

be considered. These are favorable, since they can be (translationally) cooled using sympathetic cooling by laser cooled atomic ions [18]. When crystallized, the molecular ions are in the Lamb-Dicke regime, and the ro-vibrational transitions will exhibit resolved sidebands. The linewidths are expected to be equal to their natural linewidth, on the order of tens of Hz for dipole-allowed vibrational transitions in the ground electronic state, and below 1 Hz for pure rotational transitions in the lowest vibrational state. The quality factors of the transitions are therefore in the range of $10^{11}$ or larger.

On the experimental side, laser sources for performing fundamental or overtone vibrational or stimulated Raman spectroscopy with such resolution can be implemented. For example, continuous-wave optical parametric oscillators (OPO) currently can provide radiation at wavelengths up to 4 µm with free-running linewidths below 100 kHz. Diode lasers of similar linewidth are available in the telecom wavelength range. Alternatively, difference frequency generation can be used if low power levels are sufficient. The linewidth of the sources can be reduced by frequency-stabilization to cavities. Such laser sources can be used to excite fundamental or overtone vibrational transitions.

The detection of excitation to vibrational or rotational states within the electronic ground state in cold molecular ion ensembles is not straightforward, since the number of molecules will be limited and fluorescence detection is impractical (fluorescence decay rates are small and fluorescence wavelengths lie in the mid-infrared). Destructive detection of excitation is one approach and will be described in the next section. A proposal for nondestructive detection of molecular excitation is presented in the last section.

Rotational transition frequencies can be determined from a frequency difference $\nu_a - \nu_b$ between two ro-vibrational excitations, as shown in Fig. 1, or from the frequency difference of two waves used for a stimulated Raman transition within the same vibrational state, or by direct microwave spectroscopy.

Since the frequencies of the various transitions to be compared will typically be very different (except if method (iv) is used with molecules appropriately selected to have accidental degeneracies), frequency comb techniques will have to be used.

In order to reach interesting sensitivities for time-independence, the evaluation of systematic shifts will be of central importance. The experience gained from work on cold atomic ion frequency standards will certainly be of significance.

## 3 Sympathetic Cooling of Molecular Ions and Spectroscopy

In our laboratory, two experiments dedicated to translational cooling of molecular ions are under way. The first experiment uses $^9Be^+$ as a coolant ion, the second uses $^{137}Ba^+$. The choice of Beryllium was made in order to be able to efficiently trap light molecular ions, in particular molecular hydrogen ions. The much heavier Barium ions can be used to trap heavier molecular ions, even proteins, provided they are sufficiently highly charged [19]. The issue here is the requirement of stable trapping, which constrains the allowed charge-to-mass ratio of the molecular ions compared to that of the coolant ions.

One of our goals in studying molecular hydrogen ions is to measure the proton and deuteron masses spectroscopically. Besides containing the most fundamental nuclei, the diatomic molecular hydrogen ions $H_2^+$, $D_2^+$, $HD^+$, and $HT^+$, being relatively simple three-body quantum systems, are also the only ones for which ab-initio theory has the potential of reaching sufficient accuracy in the near future. The Schrödinger equation for such systems can be solved with essentially arbitrary accuracy ($10^{-14}$) as a function of the masses of the three particles. The required relativistic and QED corrections have so far been worked out to a relative accuracy on the order of $10^{-7}$, but with potential for future improvements. Precision measurements on these ions could eventually lead to highly accurate values for $m_e/m_p$ and the nuclear mass ratios $m_p/m_d$ as well as $m_p/m_T$. Among the above ions, the heteronuclear ion $HD^+$ is of particular interest from an experimental point of view since dipole-allowed vibrational transitions can be excited. We stress that even at the current stage of theoretical accuracy tests of the time independence of essentially any nuclear-to-electron mass ratio, as opposed to a measurement thereof, can be performed using corresponding molecular ions.

In the $Be^+$-experiment, we use a four-rod linear radio-frequency trap with end caps. The central electrode length is 16 mm, rod diameter is 9.9 mm, rod-to-trap-axis distance is 4.3 mm. The 313 nm cooling radiation is generated using doubly-resonant sum frequency generation (SFG) of a resonantly doubled Nd:YAG laser, and a Ti:Sapphire laser at 760 nm [20]. The Nd:YAG laser is frequency-stabilized to a hyperfine transition in molecular iodine; since the cavity used for SFG is locked to the Nd:YAG laser and the Ti:Sapphire laser is locked to the cavity, the sum frequency wave is then also frequency stabilized. An AOM placed before

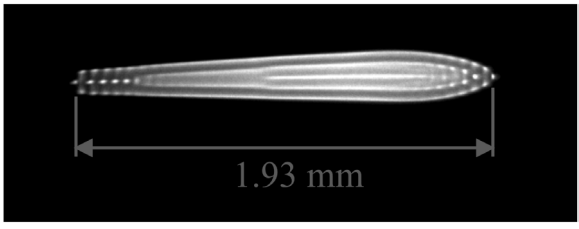


**Fig. 2.** Stable Beryllium Coulomb crystal. Cooling laser frequency was locked approx. 35 MHz red-detuned from resonance.

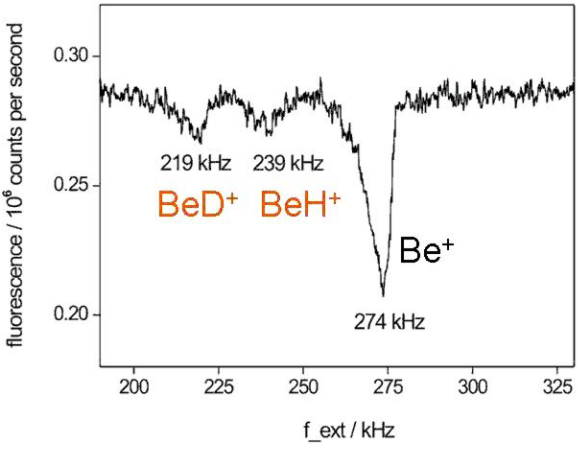


**Fig. 3.** Secular oscillation mass spectrum showing presence of beryllium hydride and deuteride ions produced by chemical reactions. Shown is fluorescence rate of the $Be^+$ ions as a function of frequency of the ac voltage applied to a 2 cm wide plate electrode at a distance 9.5 mm from the trap axis. Ac amplitude was 0.5 V.

the iodine stabilization setup allows to shift the stable UV frequency within a range of 340 MHz. UV output powers up to 80 mW were obtained.

$Be^+$-Coulomb crystals of various sizes and shapes were obtained by varying the trap and loading parameters. Figure 2 is an example of a small crystal.

We have produced molecular ions in situ by leaking HD gas into the UHV chamber for 1–2 min with pressure of $4 \cdot 10^{-10}$ mbar. Chemical reactions between HD and the crystallized $Be^+$-ions resulted in $BeH^+$ and $BeD^+$. Their presence is proven by excitation of the secular oscillation in radial direction. The excitation heats the $Be^+$ ion ensemble by Coulomb interaction and results in a decrease in $Be^+$ fluorescence. Figure 3 shows the mass spectrum of the ions contained in the trap. The secular frequencies lie within 1 % of the expected values. The crystal remains stable during excitation, but experiences a small $Be^+$ ion loss. Beryllium hydride and deuteride are heavier than the coolant ion. It is therefore expected that they are located outside the $Be^+$-crystal. Indeed, no significant dark regions are visible within the $Be^+$-crystal. We expect that the molecular

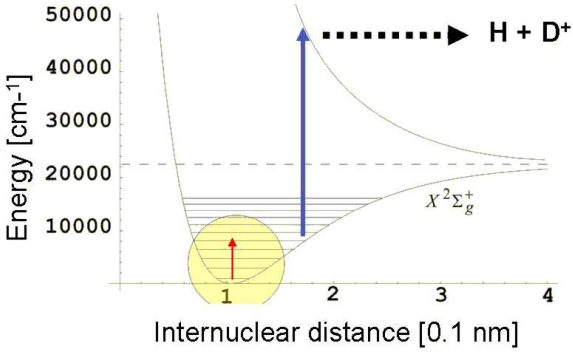


**Fig. 4.** Detection of molecular excitation by 1+1 REMPI. A vibrational transition can be detected since molecules in an excited vibrational state can be selectively dissociated with UV radiation of appropriate wavelength. The method is also applicable to selectively detect population in any particular rotational state of the lowest vibrational state if first a vibrational excitation laser is used to transfer population from the rotational state to an appropriate vibrational level

ions were sympathetically cooled and crystallized; to prove this statement, we would need to perform molecular spectroscopy or add another fluorescent atomic ion ensemble of greater mass so that the molecular ions would become "visible" as a dark shell between the added atomic ions and the $Be^+$-crystal [18].

As mentioned above, the detection of population in a long-lived ro-vibrational or rotational state poses a problem. A destructive detection method is possible by means of 1+1 resonance multi-photon ionization (REMPI). We plan to implement this for spectroscopy of $HD^+$, see Fig. 4.

Since for sympathetically cooled molecular ions in equilibrium with the laser-cooled atomic ions the internal temperature will at most be 300 K (the temperature of the vacuum chamber), in diatomic molecular ions only the lowest vibrational level will be populated initially. A vibrational excitation to be detected will transfer a fraction of these ions into another vibrational level. If a pure rotational transition (e.g. by stimulated Raman transition) is to be detected, it can be followed by a one-photon laser vibrational excitation to an excited vibrational level. The task then is to dissociate molecules preferentially from such an excited vibrational level. At least for $HD^+$ this is indeed possible, as shown in Fig. 5. A large ratio between the dissociation probabilities from a state $v' \neq 0$ and from $v = 0$ can be achieved for any $v'$ by appropriate choice of dissociation wavelength. A good choice of target vibrational level and dissociation wavelength are $v' = 4$ (corresponding to a $0 \rightarrow 4$ transition wavelength around 1.4 $\mu$m) and 266 nm (obtainable by frequency-quadrupling a Nd:YAG laser). The required photodissociation energy densities can be obtained from pulsed or cw lasers. For the $v' = 5$ target level one might be able to use the 313 nm cooling radiation as dissociation light, if it is sufficiently intense. A suitable ion optics and ion counter to extract and detect the dissociation products is required.

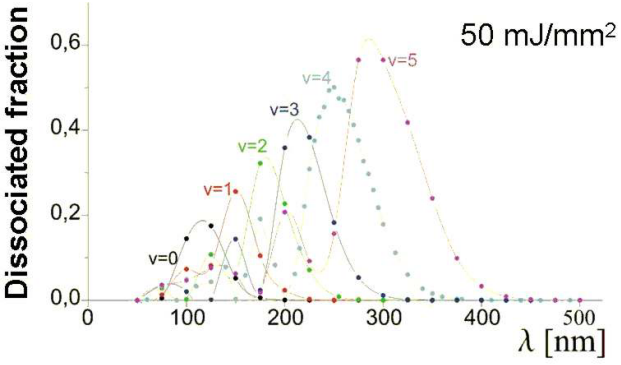


**Fig. 5.** Theoretical photodissociation probability of $HD^+$ ions in various vibrational states vs. excitation wavelength for an energy density of 50 mW/mm$^2$ and 1 s duration. [21,22].

## 4 Quantum Jump Spectroscopy

Obviously, a destructive detection method is not favourable, because of the need to reload the trap and possibly the need to reestablish a sufficiently similar configuration of the molecular/atomic ion ensemble. Various types of non-destructive detection of molecular excitation can be envisaged. Here we consider one method that is of interest if one seeks to perform spectroscopy on a single molecule. This might be the ultimate goal in precision molecular spectroscopy, since the spatial state of the molecule is then well-defined, and the determination of systematic effects is simpler. The method we propose is related to the concepts of implementing quantum gates [23] and of performing high resolution spectroscopy of atomic ions that do not have laser cooling transitions [24]. Basically, an appropriate atomic ion is used as a monitor of the internal state of the test ion (here a molecule).

Figure 6 sketches a simplified view of the procedure. A single molecular ion and a single coolant atomic ion are prepared in the trap. The atomic ion level scheme must have an accessible long-lived state. This can be an electronic state connected to the ground state by a dipole-forbidden transition, or a hyperfine state in the ground electronic state [24]. Here we consider the first case for simplicity, but the latter case would be relevant if the coolant ion is $Be^+$. The two-ion crystal is cooled by resolved sideband cooling to the motional ground state of e.g. the axial crystal mode [25]. In our model scheme this requires the P-state linewidth to be smaller than the phonon frequency. However, in practice resolved sideband cooling would be performed on a dipole-forbidden atomic transition, so that this condition can be satisfied. Note that there is no need to focus the sideband cooling radiation selectively onto the atomic ion.

The atomic ion is then transferred to the metastable state (here a D state). Now the internal vibration of the molecule is excited, with the laser tuned to the blue motional sideband. The ion crystal motional oscillation is thereby simultaneously excited. The figure shows a fundamental vibrational excitation ($v, J =$

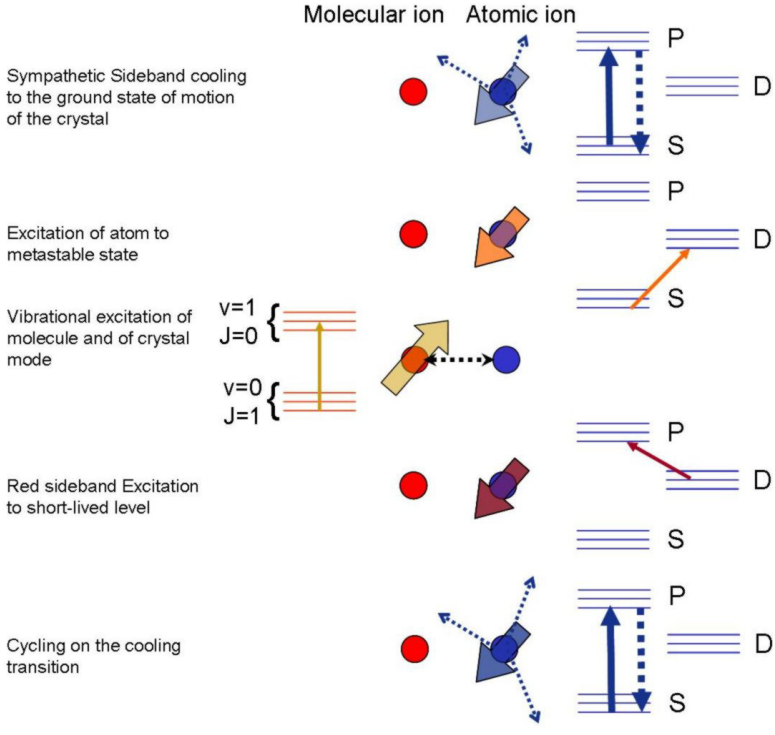


**Fig. 6.** Schematic of a method for detecting quantum jumps in molecules with high signal-to-noise ratio. The sublevels shown in the level diagrams of molecule (left) and atom (right) are the vibrational states of the crystal oscillation along the trap axis.

$1) \rightarrow (v+1, J=0)$ of the molecule and the excitation of one crystal phonon. The analogue can be done with a pure rotational excitation $(v, J) \rightarrow (v, J \pm 2)$ by using stimulated Raman scattering.

The next step consists in detecting whether a crystal phonon is present or not. To this end, the atomic ion is transferred to one of the levels of the cooling transition, using red-detuned light. This ensures that if no phonon is present, the atomic ion remains in the metastable state.

As a result, the atomic ion has been brought into a level from which the cycling can be driven, resulting in a high fluorescence rate. Thus, if the internal excitation of the molecule has taken place, this results in fluorescence from the atomic ion; the molecular quantum jump has thereby been detected. The fluorescence continues even when the molecule decays back into the ground state. Note that a ro-vibrational molecular transition $(v=0, J=1) \rightarrow (v=1, J=0)$ is a cycling transition, albeit one with a small decay rate, due to the small transition frequency.

For a spectroscopic measurement, the outlined procedure would be repeated for different values of the molecular excitation frequency.

This method, albeit technically difficult, would allow to perform spectroscopy on narrow molecular transitions with similar sensitivity as in the electron shelving method of single atomic ion spectroscopy.

## 5 Conclusion

In this paper we have pointed out that ultracold molecular ions have the potential for being used for measurements of very high spectroscopic precision, similar to what has already been demonstrated with atomic ions. Vibrational and rotational transitions limited only by the narrow natural linewidth are in principle accessible. Some approaches on how to perform the spectroscopy of molecular transitions in practice have been mentioned.

This opens up fascinating possibilities for the metrology of the electron-to-proton and proton-to-deuteron mass ratios (both absolute determination as well as time-independence tests). Measurements of parity violation, tests of the symmetrization postulate, and of the electron dipole moment in molecules are further perspectives on the use of molecular ions for fundamental physics studies. Of course, on the physical chemistry side, precision molecular structure studies will represent a huge new domain of activity, which is likely to challenge quantum chemical theory significantly.

## Acknowledgments

This work has been performed in the framework of DFG Project Schi 431/4-1 and the Gerhard-Hess Program. U.F. was supported by a fellowship of the Düsseldorf Entrepreneurs Foundation. We are grateful to H. Schnitzler, T. Boley, and A. Peters for their essential contributions in the initial phase of the work described in Sect. 3. We thank P. Zoller for mentioning quantum gates in the context of molecular quantum jumps.

## References

1. C. Will: *Theory and experiment in gravitational physics*, rev. edn. (Cambridge Univ. Press, Cambridge, 1993)
2. J.P. Uzan, Rev. Mod. Phys. **75**, 403 (2003)
3. J.D. Prestage, R. L. Tjoelker, L. Maleki, Phys. Rev. Lett. **74**, 3511 (1995)
4. V.A. Dzuba, V.V. Flambaum, J.K. Webb, Phys. Rev. A **59**, 230 (1999)
5. C. Braxmaier et al., Phys. Rev. D **64**, 042001 (2001)
6. M. Ziskind et al., Eur. J. Phys. D **20**, 219 (2002)
7. M.T. Murphy, J.K. Webb, V.V. Flambaum, Mon. Not. Roy. Astr. Soc. **365**, 609 (2003)
8. H. Marion et al., Phys. Rev. Lett. **90**, 150801 (2003)
9. S. Bize et al., Phys. Rev. Lett. **90**, 150802 (2003)
10. G.D. Rovera, IEEE Trans. Instrum. Meas. **48**, 571 (1999)
11. Y.S. Domnin et al., Quant. Elec. **26**, 1081 (1996)

12. A.Y. Potekhin et al., Astrophy. J. **505**, 523 (1998)
13. S.A. Levshakov et al., Mon. Not. Roy. Astr. Soc. **333**, 373 (2002)
14. Only molecular tests are considered here. Of course, mass spectrometry in Penning traps is an alternative approach.
15. T. Wiklind and F. Combes, Astron. Astrophys. **328**, 48 (1997)
16. H. Fritzsch, Fundamental Constants and Their Possible Time Dependence, Lect. Notes Phys. **648**, 107–113 (2004)
17. L. Hilico et al., Eur. Phys. J. D **12**, 449 (2000)
18. K. Molhave, M. Drewsen, Phys. Rev. A **62**, 011401 (2000)
19. S. Schiller, C. Lämmerzahl, Phys. Rev. A **68**, 053406 (2003)
20. H. Schnitzler et al., Appl. Opt. **41**, 7000 (2001)
21. M. Tadjeddine, G. Parlant, Mol. Phys. **33**, 1797 (1977)
22. H. Schnitzler, Ph.D. thesis, Univ. Konstanz (2001)
23. I. Cirac, P. Zoller, Phys. Rev. Lett. **74**, 4091 (1995)
24. D.J. Wineland et al.: 'Quantum Computers and Atomic Clocks'. In: *Proc. of the 6th Symp. on Frequency Standards and Metrology.* ed. by P. Gill (World Scientific, New Jersey, 2002) pp. 361–368
25. H. Rhode et al., J. Opt. B **3**, S34 (2001)

# TRAPPED ULTRACOLD MOLECULAR IONS: CANDIDATES FOR AN OPTICAL MOLECULAR CLOCK FOR A FUNDAMENTAL PHYSICS MISSION IN SPACE

**B. Roth**,* **J. Koelemeij**, **H. Daerr**, **I. Ernsting**, **S. Jorgensen**,†
**M. Okhapkin**, **A. Wicht**, **A. Nevsky**, and **S. Schiller**
*Institut für Experimentalphysik, Heinrich–Heine–Universität Düsseldorf, 40225 Düsseldorf, Germany*

Narrow ro-vibrational transitions in ultracold molecules are excellent candidates for frequency references in the near-IR to visible spectral domain and interesting systems for fundamental tests of physics, in particular for a satellite test of the gravitational redshift of clocks. We have performed laser spectroscopy of several ro-vibrational overtone transitions $v = 0 \rightarrow v = 4$ in $HD^+$ ions at around 1.4 $\mu$m. 1+1 REMPD was used as a detection method, followed by measurement of the number of remaining molecules. The molecular ions were stored in a linear radiofrequency trap and cooled to millikelvin temperatures, by sympathetic cooling using laser-cooled $Be^+$ ions simultaneously stored in the same trap.

For more than a century, spectroscopy of atoms and molecules has given insight into many aspects of nature, ranging from the very small (nuclear, atomic and particle physics) to the very large (astronomy and cosmology). Ongoing developments in precision spectroscopy are partly motivated by the possibility to perform stringent tests of fundamental laws and postulates of physics, which form the framework of contemporary theoretical models such as the standard model and general relativity. Alternatively, precision spectroscopy may be used to determine the value of fundamental constants of nature. Predictions by theoretical models need to be combined with spectroscopic data to achieve both of these goals.

Precision spectroscopy has been used once in a space experiment, the 1976 Gravity Probe A rocket mission, which carried a hydrogen maser into space. The hyperfine transition frequency of the maser (1.4 GHz) was compared with ground clocks as a function of the rocket height. The results were analyzed in the framework of General Relativity (GR) and it was found that the gravitational redshift agreed with the GR prediction at a level of 70 ppm [1].

Present state-of-the-art precision spectroscopy is performed with ultrastable lasers which probe narrow, optical transitions between energy levels in atoms and molecules. The most accurate spectroscopic results to date have been achieved with laser spectroscopy of single, ultracold trapped atomic ions [2, 3, 4]. The strong suppression of Doppler shifts, their good isolation from the environment and their long storage times make single trapped ions ideally suited for prolonged interrogation of narrow transitions. Very recently, it has been shown that the ratio of the transition frequencies of two dissimilar trapped atomic ions can be measured with a precision exceeding 1 part in $10^{16}$ [5]. For similar reasons as for atomic ions, the hitherto unexplored option of precision spectroscopy of trapped ultracold *molecular* ions is of great interest. The more complex structure of the molecules offers unique possibilities to test additional theoretical models and/or to determine the value of fundamental constants.

Based on the outstanding progress in precision spectroscopy in the optical domain, it is expected that a satellite test of General Relativity using optical clocks could search for deviations from the gravitational redshift result of GR at a level at least 10 000 times more precise than the Gravity Probe A mission [6]. By flying both atomic and molecular clocks, the scope of the test would be significantly widened, since these two clock types are dissimilar: the frequency of an atomic clock depends on the fine structure constant, and that of a molecular clock on the ratio of electron to nuclear mass. Thus, two types of tests can be performed: a test of redshift universality (Local Position Invariance) by comparing the two dissimilar clock types directly on-board, and an absolute redshift measurement by comparing the two satellite clocks with ground clocks.

Promising candidates for precision molecular spectroscopy are the molecular hydrogen ion ($H_2^+$) and its isotopomers ($HD^+$ $D_2^+$, etc.), which are the simplest of all molecules. As such, they represent the ultimate quantum-mechanical model for ab-initio molecular structure calculations, including higher order corrections, such as non-adiabatic, relativistic, and QED contributions [7, 8, 9, 10, 11, 12, 13, 14]. The relative inaccuracy of such calculations is currently at the level of $10^{-8}$ [8], and efforts are underway towards $10^{-10}$–$10^{-11}$ inaccuracy [11]. Precise measurements on these systems can therefore test quantum chemical calculations at their current state of accuracy or better and stimulate the development of more advanced theoretical models [15, 16].

Apart from being a candidate for a test of the universality of the gravitational redshift, another interesting possibility offered by the molecular hydrogen ion is the search for a temporal variation of $m_e/m_p$ [9, 17, 18]. Theories which have recently been developed in an attempt to unify the standard model with general relativity allow for or even predict such a variation. In case that $m_e/m_p$ varies in time, repeated spectroscopic measurements on a limited set of lines in the molecular hydrogen

*Proc. '6th Internat. Conf. on Space Optics', ESTEC, Noordwijk, The Netherlands, 27-30 June 2006 (ESA SP-621, June 2006)*

ion should eventually reveal a change of the transition frequencies with time [9]. Furthermore, even when an experimental result consistent with zero variation is found it still provides an upper limit on the possible variation (given by the uncertainty of the measurement), and it may serve as input for theory.

In particular, comparison of frequencies of two vibrational transitions of $HD^+$ would allow setting limits on the time dependence of both the electron-to-proton ($m_e/m_p$) and the proton-to-deuteron mass ratio ($m_p/m_d$). A comparison between transition frequencies in $HD^+$ and $H_2^+$ could be used to determine the individual contributions [9]. Apart from such measurements, high-precision spectroscopy on ultracold $HD^+$ ions could allow determining molecular physics effects such as (i) the dependence of the hyperfine coupling constants on the rotational quantum number [12, 19, 20], (ii) identification of the nuclear spin rotation interaction effect [21], (iii) measurement of the electric quadrupole interaction contribution [22], and (iv) identification of the effects of the anapole magnetic moment of the molecule [23, 24].

The molecular hydrogen cation has been subject of several experimental studies in the past. The main work has been on the hyperfine structure in several low-lying vibrational states, by Dehmelt and others [25, 26, 27], and on vibrational transitions between states close to the dissociation limit [28]. There has been only a single study of laser-induced transitions of low-lying vibrational levels, performed by Wing and coworkers almost thirty years ago [29]. All studies were performed on warm samples or on ion beams.

The extension of such measurements to the ultracold temperature regime offers the potential to increase the spectroscopic accuracy, possibly by several orders of magnitude, due to the reduction of first-order Doppler broadening and of systematic effects. Molecular hydrogen ion ensembles at $< 20\,\mathrm{mK}$ translational energy were recently produced by sympathetic cooling using laser-cooled atomic ions stored in a linear radiofrequency trap [30]. In this environment, the molecular ions are well-localized inside ordered structures, denoted as Coulomb crystals, where they can be stored on the time scale of several minutes, favorable for long interrogation times in spectroscopic measurements. Within such crystals, the particles are in an isolated, nearly collision-less regime. Typical interparticle distances are in the range of several tens of micrometers, hence collisional or pressure broadening of the transition lines is insignificant.

We have demonstrated high-resolution laser spectroscopy on ultracold molecular hydrogen ions, $HD^+$, in traps. Using the method developed, we have performed a first measurement of the ro-vibrational transitions $(v = 0, J = 0, 1, 2) \rightarrow (v = 4, J = 1, 0, 1)$, respectively, where $v$ and $J$ are the vibrational and rotational quantum numbers in the $HD^+$ electronic ground state. The above transitions span the frequency range 6991.1091 to 7122.486 $\mathrm{cm}^{-1}$, corresponding to wavelengths between 1.430 and 1.404 $\mu$m. The method developed can be applied to a huge number of other molecular ion systems.

We simultaneously store both $Be^+$ ions and molecular ions in a linear radiofrequency trap, enclosed in a UHV chamber, kept below $10^{-10}$ mbar. The trap is driven at 14.2 MHz, with a peak-to-peak amplitude of 380 V. This leads to a radial Mathieu stability parameter $q_r \simeq 0.04$, [31], and a (single-particle) radial secular oscillation frequency of 280 kHz for the $Be^+$. For the deuterium hydride ions ($HD^+$) $q_r \simeq 0.12$ and the (single-particle) radial oscillation frequency is at 840 kHz.

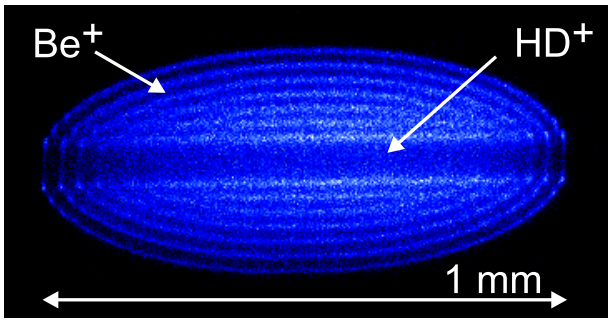


FIG. 1: Two-species ion crystal used for 1+1 REMPD spectroscopy of $HD^+$. The crystal contains $\approx 3150$ $Be^+$ and $\approx 95$ $HD^+$ ions at a translational temperature of $\approx 12$ mK. Crystal structure, ion numbers and upper limits for the translational temperature were deduced via MD simulations.

The $Be^+$ ions are laser-cooled to millikelvin temperatures using a 313 nm UV laser [32]. For strong cooling, the ions are nearly localized in ordered structures (Coulomb crystals) [33]. Due to the long-range electrostatic interaction between atomic coolants and molecular ions, the latter are efficiently cooled to translational temperatures $< 20\,\mathrm{mK}$ and embedded around the axis of the $Be^+$ ion crystals, which is energetically more favorable. Fig.1 shows a typical two-species ion crystal containing $\approx 95$ ultracold $HD^+$ ions used for our measurements. The presence of the $HD^+$ ions is obvious from the dark core of the ion crystal. Due to the weak coupling between external and internal degrees of freedom, the internal temperature of the $HD^+$ ions is expected to be at 300 K [34], in thermal equilibrium with the vacuum chamber. We use molecular dynamics (MD) simulations to deduce ion numbers, three-dimensional spatial distributions, and upper limits for the translational temperature of each species contained in the crystal. The simulations include full Coulomb interaction, light pressure forces, anisotropies of the effective trap potential, and species-dependent heating rates. We identify the trapped species by excitation of their mass-dependent motional (secular) frequencies. For individual ions in a radiofrequency trap, the motional frequencies are inversely proportional to their mass (see [30, 35, 36, 37] for a detailed

description of our procedure).

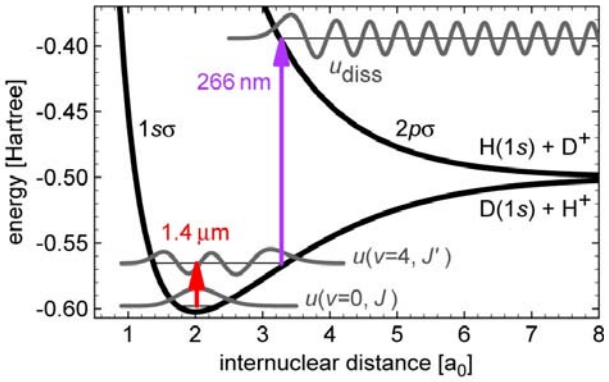


FIG. 2: Scheme of 1+1 REMPD of $HD^+$ molecular ions.

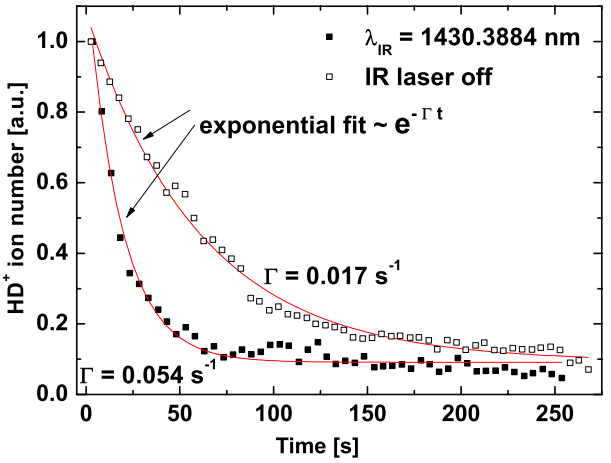


FIG. 3: Observed decrease of the number of $HD^+$ ions when the IR laser is tuned close to the $(v = 0, J = 2) \rightarrow (v = 4, J = 1)$ transition (solid squares). Background $HD^+$ losses when both lasers are off (open squares) are mainly due to chemical reactions with residual nitrogen gas present in the trap.

We perform 1+1 resonance enhanced multiphoton dissociations (REMPD) spectroscopy using a tunable infrared (IR) diode laser with a maximum output power of 4 mW to excite the ro-vibrational overtone transitions at around 1.4 $\mu$m. The diode laser has a jitter limited linewidth $< 5$ MHz. The excited $HD^+$ ions in the $v = 4$ vibrational level are state-selectively dissociated, [38], using a continuous wave 266 nm UV laser source: $HD^+(v = 4) + h\nu \rightarrow H + D^+$ or $H^+ + D$. Fig.2 shows a schematic of the spectroscopic technique used.

For detection, we observe the loss rate of ultracold $HD^+$ ions from the trap, while scanning the frequency of the IR excitation laser in a range of several 100 MHz around the (calculated) ro-vibrational transition frequency [7]. The above loss rate is determined by repeated excitation of the $HD^+$ secular motion in the trap, after turning on the excitation and dissociation lasers,

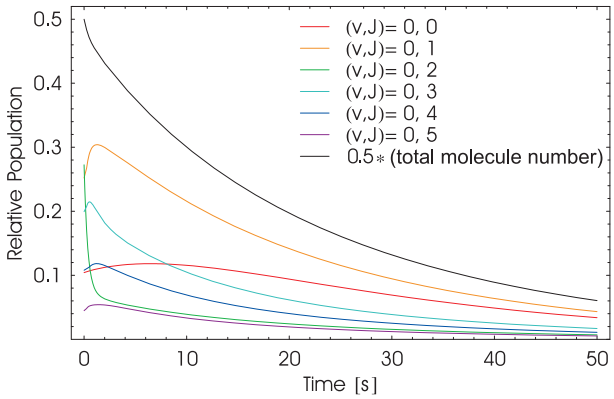


FIG. 4: Simulated population dynamics for a translationally ultracold (20 mK) collision-free ensemble of $HD^+$ ions, with the IR laser set to the maximum of the $(v = 0, J = 2) \rightarrow (v = 4, J = 1)$ transition. The intensities of the lasers are $I(\nu_{IR}) = 0.32\,\mathrm{W/cm^2}$, $I(266nm) = 0.57\,\mathrm{W/cm^2}$.

and observation of the change induced in the $Be^+$ fluorescence, due to heating of the atomic coolants by the molecular ions. This change in the atomic fluorescence is proportional to the number of $HD^+$ ions contained in the crystal.

The $HD^+$ decay rate was measured as a function of the frequency of the IR laser, by scanning the latter in discrete 15 MHz steps, Fig.3. Prior to each measurement, the frequency of the IR laser was calibrated, via absorption spectroscopy in a water vapor cell. The accuracy of the calibration is $\pm 30$ MHz. We have fitted a Gaussian to the lines obtained, in order to determine the line center. We find good agreement of the value for the line center measured with the calculated transition frequencies from [7]. The width of the lines is in the range of 100 MHz.

The observed time evolution of the $HD^+$ ion number under laser irradiation is well described by a rate equation model, see Fig.4. The model takes into account spontaneous emission and absorption of black-body radiation as well as absorption of the IR and UV light, and stimulated emission by the IR light. Transition moments are taken from [39]. The lifetimes for the excited ro-vibrational states are from [40].

As an example, Fig.4 shows the evolution when the $(v = 0, J = 2) \rightarrow (v = 4, J = 1)$ transition is driven. For the intensities shown, there is a rapid decrease of the population of the initial state due to prompt photo dissociation and, dominantly, decay from the upper vibrational state to other rotational levels of the ground vibrational state.

Due to coupling between neighboring levels via black-body radiation absorption or spontaneous emission, the $J = 2$ level population remains significant so that photo dissociation continues. On a time scale of several tens of seconds, all $HD^+$ ions contained in the crystal are photo dissociated. This time scale is in good agreement with

the experimental observation. Furthermore, the time evolution of the total population can be reasonably well described by a single exponential.

Several effects contribute to the observed line widths, e.g., hyperfine splitting of the ro-vibrational transitions [20], residual Doppler broadening, saturation broadening, and Zeeman splitting by the 10 G bias magnetic field used for $Be^+$ cooling.

In summary, we have observed a total of 12 ro-vibrational overtone transitions between 1391 nm and 1471 nm, on ultracold trapped $HD^+$ molecular ions, cooled to approximately 20 mK via laser-cooled $Be^+$ ions [41]. After excitation to the $v = 4$ vibrational level, using a tunable diode laser at 1.4 $\mu$m, the molecules were state-selectively disscociated via a 266 nm UV laser. We used secular excitation mass-spectroscopy to monitor the $HD^+$ loss rate from the trap, as a function of the frequency of the IR laser, calibrated using water absorption spectroscopy. A first measurement of the transition frequencies using a femtosecond frequency comb has been performed, and will be reported elsewhere.

The method demonstrated represents a promising route towards the application of ultracold, trapped molecules for high-precision measurements of ro-vibrational transitions, possibly leading to an improvement of the spectroscopic accuracy by several orders of magnitude. Furthermore, narrow ro-vibrational transitions in ultracold molecules are candidates for frequency references in the near-IR to visible spectral domain. They are especially interesting for fundamental tests of physics, such as a test of the time-independence of the electron-to-nuclear mass ratio, a test of Local Position Invariance, and a test of isotropy of space. Such tests could advantageously be performed in space [6].

Large ion crystals containing several hundred ultracold $HD^+$ ions may limit the spectroscopic accuracy, due to spatially varying Doppler shifts of the transition frequency. The spatial extent also introduces a sensitivity to field gradients, and the resulting spread of frequency shifts might limit the spectral resolution. Finally, even at a temperature of 10 mK, first-order Doppler shifts will limit the achievable accuracy of the 1.4 $\mu$m spectroscopy to about $10^{-9}$.

Most of the problems anticipated for trapped clouds of $HD^+$ will be virtually absent, or may be substantially alleviated otherwise, by turning to quantum-logic-enabled spectroscopy (QLES) as proposed [42] and recently demonstrated by the Wineland and coworkers for atomic ions [43]. The method would involve using a single ultracold $HD^+$ molecular ion in the Lamb-Dicke regime, coupled to a single $Be^+$ atomic ion, which is used for both cooling the translational energy of the $HD^+$ and state-selective detection of the molecular state.

*Acknowledgements* We thank the Deutsche Forschungsgemeinschaft (DFG) and the EC network HPRN-CT-2002-00290 for support. We thank C.B. Zhang for helpful assistance with the MD simulations.

---

* Electronic address: Bernhard.Roth@uni-duesseldorf.de
† S.J. is with the Department of Chemistry, University of Copenhagen, Denmark.

[1] R.F.C. Vessot et al., Phys. Rev. Lett. **45**, 2081 (1980).
[2] S.A. Diddams et al., Science **293**, 825 (2001).
[3] H.S. Margolis et al., Science **306**, 1355 (2004).
[4] E. Peik et al., Atomic Physics 19, Proceedings of the 19th ICAP, Eds.: L. G. Marcassa, V. S. Bagnato, K. Helmerson, AIP Conf. Proc. Vol. 770, AIP, New York, p. 103-111 (2005).
[5] T. Rosenband et al., Europ. Time and Frequency Forum, Braunschweig (2006).
[6] S. Schiller et al., Proc. of the 39th ESLAB Symposium "Trends in Space Science and Cosmic Vision 2020", pp.39-42, F. Favata, J. Sanz-Forcada, A. Gimenez, eds., ESA SP-588 (2005).
[7] G.G. Balint-Kurti et al., Phys. Rev. **A 41**, 4913 (1990).
[8] R.E. Moss Mol. Phys. **78**, 371 (1993).
[9] S. Schiller and V. Korobov, Phys. Rev. **A 71**, 032505 (2005).
[10] J. F. Babb et al. Current Topics in Physics, vol. 2, 531, World Scientific, Singapore (1998).
[11] V. I. Korobov, Phys. Rev. **A 70**, 012505 (2004).
[12] R. D. Ray and P. R. Certain, Phys. Rev. Lett. **38**, 824 (1977).
[13] C. A. Leach and R. E. Moss, Annual Review of Physical Chemistry **46**, 55 (1995).
[14] Z.-C. Yan, J.-Y. Zhang, and Y. Li, Phys. Rev. **A 67**, 062504 (2003).
[15] Z. Amitay et al., Science **281**, 75 (1998).
[16] A. D. J. Critchley, A. N. Hughes, and I. R. McNab, Phys. Rev. Lett. **86**, 1725 (2001).
[17] L. Hilico et al., Eur. Phys. J. D **12**, 449 (2000).
[18] U. Fröhlich. et al., Lect. Notes. Phys. **648**, 297 (2004).
[19] A. Carrington et al., Mol. Phys. **72**, 735 (1991).
[20] D. Bakalov, V. Korobov, and S. Schiller, subm. to Phys. Rev. Lett. (2006).
[21] J.F. Babb, Phys. Rev. Lett. **75**, 4377 (1995).
[22] J.F. Babb, arXiv:physics/9701007.
[23] I.B. Khriplovich and M.E. Pospelov, Z. Phys. D **17**, 81 (1990); R.R. Lewis, Phys. Rev. **A 49**, 3376 (1994).
[24] R. Alheit, Ph.D. dissertation, Univ. Mainz (1997).
[25] C. B. Richardson, K. B. Jefferts, and H. G. Dehmelt, Phys. Rev. **165**, 80 (1968).
[26] K. B. Jefferts, Phys. Rev. Lett. **23**, 1476 (1969).
[27] Z. W. Fu, E. A. Hessels, and S. R. Lundeen, Phys. Rev. **A 46**, 5313 (1992).
[28] A. Carrington, I. McNab, and C. Montgomerie, J. Phys. B: At. Mol. Opt. Phys. **22**, 3551 (1989).
[29] W. H. Wing et al., Phys. Rev. Lett. **36**, 1488 (1976).
[30] P. Blythe, B. Roth, U. Fröhlich, H. Wenz, and S. Schiller, Phys. Rev. Lett. **95**, 183002 (2005).
[31] D. J. Berkeland et al., J. Appl. Phys. **83**, 5025 (1998).
[32] H. Schnitzler et al., Applied Optics **41**, 7000 (2002).
[33] R. Blümel et al., Nature **334**, 309 (1988).
[34] A. Bertelsen, S. Jorgensen, and M. Drewsen, J. Phys. B: At. Mol. Opt. Phys. **39** 83 (2006).
[35] B. Roth, U. Fröhlich, and S. Schiller, Phys. Rev. Lett.

**94**, 053001 (2005).
[36] B. Roth, P. Blythe, and S. Schiller, "Motional Resonance Coupling in Cold Multi-Species Coulomb Crystals", in prep. (2006).
[37] U. Fröhlich, B. Roth, and S. Schiller, Phys. Plasmas **12**, 073506 (2005).
[38] M. Tadjeddine and G. Parlant, Mol. Phys. **33**, 1797 (1977).
[39] E.A. Colbourn and P.R. Bunker, J. Mol. Spect. **63**, 155 (1976).
[40] Z. Amitay, D. Zajfman, and P. Forck, Phys. Rev. **A 50**, 2304 (1994).
[41] B. Roth, J. Koelemeij, H. Daerr, and S. Schiller, "Rovibrational spectroscopy of trapped molecular hydrogen ions at millikelvin temperatures", subm. to Nature (2006).
[42] D.J. Wineland et al., in *Proceedings of the 6th Symposium on Frequency Standards and Metrology*, edited by P. Gill, World Scientific, Singapore, p. 361 (2002).
[43] P.O. Schmidt et al., Science **309**, 749 (2005).

# Ultracold Molecular Hydrogen Ions in a Linear Radiofrequency Trap: Novel systems for Molecular Frequency Metrology

**B. Roth, H. Daerr, J. Koelemeij, A. Nevsky, and S. Schiller**
*Institut für Experimentalphysik, Heinrich–Heine–Universität Düsseldorf, 40225 Düsseldorf, Germany**

We have measured the ro-vibrational infrared transition $(v = 0, J = 2) \rightarrow (v = 4, J = 1)$ in ultracold $HD^+$ molecular ions embedded inside $Be^+$ Coulomb crystals, by 1+1 REMPI spectroscopy. The molecular ions, trapped in a linear radiofrequency trap, were cooled to temperatures of few tens of mK, via sympathetic cooling using laser-cooled $Be^+$ ions. For detection, we have used secular excitation of the $HD^+$ ions to monitor their loss rate. The transition frequency agrees with a theoretical prediction.

Diatomic molecular hydrogen ions are of fundamental importance in nature. They are three-particle systems, with only a single electron, and as such among the simplest molecules. This makes them accessible to ab-initio high-precision theoretical calculations, including higher order corrections, such as non-adiabatic, relativistic, and QED corrections [1, 2, 3, 4, 5, 6, 7, 8]. Precise measurements on these systems can therefore test quantum chemical calculations at their current state of accuracy or better and stimulate the development of more advanced theoretical models [9, 10]. Furthermore, these simple molecular systems have the potential to be used for measurements of electron to nuclear mass ratios and their time variation or for a test of the universality of the coupling of gravitation to matter [3, 11, 12].

In particular, comparison of frequencies of two vibrational transitions of $HD^+$ would allow setting limits on the time dependence of both the electron-to-proton $(m_e/m_p)$ and the proton-to-deuteron mass ratio $m_p/m_d$. A comparison between transition frequencies in $HD^+$ and $H_2^+$ could be used to determine the individual contributions [3]. Apart from such measurements, high-precision spectroscopy on ultracold $HD^+$ ions could allow determining molecular physics effects such as (i) the dependence of the hyperfine coupling constants on the rotational quantum number [6, 13, 14], (ii) identification of the nuclear spin rotation interaction effect [15], (iii) measurement of the electric quadrupole interaction contribution [16], and (iv) identification of the effects of the anapole magnetic moment of the molecule [17, 18].

The molecular hydrogen cation has been subject of several experimental studies in the past. The main work has been on the hyperfine structure in several low-lying vibrational states, by Dehmelt and others [19, 20, 21], and on vibrational transitions between states close to the dissociation limit, by Carrington and coworkers [22]. To our knowledge, there has been only a single study of laser-induced transitions of low-lying vibrational levels, performed by Wing and coworkers thirty years ago [23]. These studies were performed on uncooled samples or ion beams.

The extension of such measurements to the ultracold temperature regime could increase the spectroscopic accuracy, possibly by several orders of magnitude, due to the reduction of first-order Doppler broadening and of systematic effects. Molecular hydrogen ion ensembles at $< 20\,\mathrm{mK}$ were recently produced by sympathetic cooling using laser-cooled atomic ions stored in a linear radiofrequency trap [24]. In this unique environment, the molecular ions are well-localized inside ordered structures, Coulomb crystals, where they can be stored on the time scale of several minutes, favorable for long interrogation times in spectroscopic measurements. Within the crystals, the particles are in an isolated, nearly collisionless regime (typical interparticle distances are in the range of several tens of micrometers), hence collisional or pressure broadening of the transition lines is insignificant.

We have demonstrated a novel technique for high-resolution laser spectroscopy on ultracold molecular hydrogen ions, $HD^+$, in traps. Using the method developed, we have performed a first measurement of the ro-vibrational transition $(v = 0, J = 2) \rightarrow (v = 4, J = 1)$ at 6991.1 $\mathrm{cm}^{-1}$ $(1.430\,\mu\mathrm{m})$. Here, $v$ and $J$ are the vibrational and rotational quantum numbers in the $HD^+$ electronic ground state. The method developed can be applied to a vast number of other molecular ion species.

We simultaneously store both $Be^+$ ions and molecular ions in a linear radiofrequency trap, enclosed in a UHV chamber kept below $10^{-10}$ mbar, driven at 14 MHz, with a peak-to-peak amplitude of 380 V. This leads to a radial Mathieu stability parameter $q_r \simeq 0.04$, [25], and a (single-particle) radial secular oscillation frequency of 280 kHz for the $Be^+$. For the deuterium hydride ions, $HD^+$, $q_r \simeq 0.12$ and the (single-particle) radial oscillation frequency is 840 kHz.

The $Be^+$ ions are laser-cooled to millikelvin temperatures using a 313 nm UV laser [26]. For strong cooling, the ions are nearly localized in ordered structures, denoted as Coulomb crystals [27]. Due to the long-range electrostatic interaction between atomic coolants and molecular ions, the latter are efficiently cooled to translational temperatures $< 20\,\mathrm{mK}$ and embedded around the axis of the $Be^+$ ion crystals, due to their smaller mass-to-charge ratio. Due to the weak coupling between external and internal degrees of freedom, the in-

ternal temperature of the $HD^+$ ions is expected to be at 300 K [28], in thermal equilibrium with the vacuum chamber. We use molecular dynamics (MD) simulations to deduce ion numbers, three-dimensional spatial distributions, and upper limits for the translational temperature of each species contained in the crystal. The simulations include full Coulomb interaction, light pressure forces, anisotropies of the effective trap potential, and species-dependent heating rates. We identify the trapped species by excitation of their mass-dependent motional (secular) frequencies. For individual ions in a radiofrequency trap, the motional frequencies are inversely proportional to their mass. A detailed description of our procedure can be found in [24, 29, 30, 31].

We perform 1+1 REMPI spectroscopy, using a tunable infrared (IR) diode laser with a maximum output power of 4 mW to excite the ro-vibrational overtone transition $(v = 0, J = 2) \rightarrow (v = 4, J = 1)$ at around 1430 nm. The diode laser has a jitter limited linewidth $< 5$ MHz. Its wavelength was calibrated using a water absorption cell. Subsequently, the excited $HD^+$ ions in the $v = 4$ vibrational level are state-selectively dissociated, [32], using a continuous wave 266 nm UV laser source: $HD^+(v = 4) + h\nu \rightarrow H + D^+$ or $H^+ + D$.

For detection, we observe the loss rate of ultracold $HD^+$ ions from the trap, while scanning the frequency of the IR excitation laser in a range of several 100 MHz around the (calculated) ro-vibrational transition frequency [1]. The above loss rate is determined by repeated excitation of the $HD^+$ secular motion in the trap, after turning on the excitation and dissociation lasers, and observation of the change induced in the $Be^+$ fluorescence, due to heating of the atomic coolants by the molecular ions.

The $HD^+$ decay rate was measured as a function of the frequency of the IR laser, by scanning the latter in discrete 15 MHz steps. Prior to each measurement, the frequency of the IR laser was calibrated, via absorption spectroscopy in a water vapor cell. The accuracy of the calibration is $\pm 30$ MHz. We have fitted a Gaussian to the line, in order to determine the line center. We find good agreement of the value for the line center obtained with the calculated transition frequency $6991.1092\,\mathrm{cm}^{-1}$ from Ref. [1]. The width of the line was $0.0032\,\mathrm{cm}^{-1}$, corresponding to 96 MHz.

Several effects contribute to the observed line widths, e.g., hyperfine splitting of the ro-vibrational transitions [14], residual Doppler broadening, saturation broadening, and Zeeman splitting by the 10 G bias magnetic field used for $Be^+$ cooling.

In summary, we have measured a ro-vibrational overtone transition, on ultracold trapped $HD^+$ molecular ions, cooled to approximately 20 mK via laser-cooled $Be^+$ ions. After excitation to the $v = 4$ vibrational level, using a tunable diode laser at 1.4 $\mu$m, the molecules were state-selectively disscociated via a 266 nm UV laser. We used secular excitation mass-spectroscopy to monitor the $HD^+$ loss rate from the trap, as a function of the frequency of the IR laser, calibrated using water absorption spectroscopy.

The method demonstrated represents a promising route towards the application of ultracold, trapped molecules for high-precision measurements of ro-vibrational transitions, possibly leading to an improvement of the spectroscopic accuracy by several orders of magnitude.

For Doppler-free spectroscopy and mimization of systematic effects, it appears feasible to use a single ultracold $HD^+$ molecular ion in the Lamb-Dicke regime, coupled to a single $Be^+$ atomic ion, which is used for both cooling the translational energy of the $HD^+$ and state-selective detection of the molecular state [33].

*Acknowledgements* We thank the Deutsche Forschungsgemeinschaft (DFG) and the EC network HPRN-CT-2002-00290 for support. We thank H. Wenz, T. Fritsch, and M. Okhapkin for helpful assistance and discussions.

* Electronic address: Bernhard.Roth@uni-duesseldorf.de

[1] G.G. Balint-Kurti et al., Phys. Rev. **A 41**, 4913 (1990).
[2] R.E. Moss Mol. Phys. **78**, 371 (1993).
[3] S. Schiller and V. Korobov, Phys. Rev. **A 71**, 032505 (2005).
[4] J. F. Babb et al. Current Topics in Physics, vol. 2, 531, World Scientific, Singapore (1998).
[5] V. I. Korobov, Phys. Rev. **A 70**, 012505 (2004).
[6] R. D. Ray and P. R. Certain, Phys. Rev. Lett. **38**, 824 (1977).
[7] C. A. Leach and R. E. Moss, Annual Review of Physical Chemistry **46**, 55 (1995).
[8] Z.-C. Yan, J.-Y. Zhang, and Y. Li, Phys. Rev. **A 67**, 062504 (2003).
[9] Z. Amitay et al., Science **281**, 75 (1998).
[10] A. D. J. Critchley, A. N. Hughes, and I. R. McNab, Phys. Rev. Lett. **86**, 1725 (2001).
[11] L. Hilico et al., Eur. Phys. J. D **12**, 449 (2000).
[12] U. Fröhlich. et al., Lect. Notes. Phys. **648**, 297 (2004).
[13] A. Carrington et al., Mol. Phys. **72**, 735 (1991).
[14] D. Bakalov, V. Korobov, priv. comm. (2005).
[15] J.F. Babb, Phys. Rev. Lett. **75**, 4377 (1995).
[16] J.F. Babb, arXiv:physics/9701007.
[17] I.B. Khriplovich and M.E. Pospelov, Z. Phys. D **17**, 81 (1990); R.R. Lewis, Phys. Rev. **A 49**, 3376 (1994).
[18] R. Alheit, Ph.D. dissertation, Univ. Mainz (1997).
[19] C. B. Richardson, K. B. Jefferts, and H. G. Dehmelt, Phys. Rev. **165**, 80 (1968).
[20] K. B. Jefferts, Phys. Rev. Lett. **23**, 1476 (1969).
[21] Z. W. Fu, E. A. Hessels, and S. R. Lundeen, Phys. Rev. **A 46**, 5313 (1992).
[22] A. Carrington, I. McNab, and C. Montgomerie, J. Phys. B: At. Mol. Opt. Phys. **22**, 3551 (1989).
[23] W. H. Wing et al., Phys. Rev. Lett. **36**, 1488 (1976).
[24] P. Blythe, B. Roth, U. Fröhlich, H. Wenz, and S. Schiller, Phys. Rev. Lett. **95**, 183002 (2005).
[25] D. J. Berkeland et al., J. Appl. Phys. **83**, 5025 (1998).

[26] H. Schnitzler et al., Applied Optics **41**, 7000 (2002).
[27] R. Blümel et al., Nature **334**, 309 (1988).
[28] A. Bertelsen, S. Jorgensen, and M. Drewsen, J. Phys. B: At. Mol. Opt. Phys. **39** 83 (2006).
[29] B. Roth, U. Fröhlich, and S. Schiller, Phys. Rev. Lett. **94**, 053001 (2005).
[30] B. Roth, P. Blythe, and S. Schiller, "Motional Resonance Coupling in Cold Multi-Species Coulomb Crystals", in prep. (2006).
[31] U. Fröhlich, B. Roth, and S. Schiller, Phys. Plasmas **12**, 073506 (2005).
[32] M. Tadjeddine and G. Parlant, Mol. Phys. **33**, 1797 (1977).
[33] P.O. Schmidt et al., Science 309, 749 (2005).

# Precision Spectroscopy of Molecular Hydrogen Ions: Towards Frequency Metrology of Particle Masses*

Bernhard Roth[1], Jeroen Koelemeij[1], Stephan Schiller[1], Laurent Hilico[2,3], Jean-Philippe Karr[2,3], Vladimir Korobov[4], and Dimitar Bakalov[5]

[1] Institut für Experimentalphysik, Heinrich-Heine-Universität Düsseldorf 40225 Düsseldorf, Germany
[2] Département de Physique et Modélisation, Université d'Evry Val d'Essonne Boulevard F. Mitterrand, 91025 Evry cedex
[3] Laboratoire Kastler Brossel, Université Pierre et Marie Curie T12, Case 74, 4 place Jussieu, 75252 Paris, France
[4] Joint Institute for Nuclear Research, 141980 Dubna, Russia
[5] Institute for Nuclear Research and Nuclear Energy, Sofia 1784, Bulgaria

**Abstract.** We describe the current status of high-precision ab initio calculations of the spectra of molecular hydrogen ions ($H_2^+$ and $HD^+$) and of two experiments for vibrational spectroscopy. The perspectives for a comparison between theory and experiment at a level of 1 ppb are considered.

## 1 Introduction

The molecular hydrogen ion (MHI) is the simplest stable molecule, containing just two nuclei and a single electron. Since the birth of the field of molecular physics it has played an important role: it is on one hand an important benchmark system for detailed studies of energy levels [1], for collisions and chemical reactions between charged molecules and neutral atoms/molecules, of interactions with laser radiation and energetic charged particles, and for testing the respective theoretical descriptions. On the other hand, the MHI is also an astrophysically important molecule, involved in reaction chains leading to the production of polyatomic molecules. Over 800 publications have been written on this molecule in the last 35 years [2]. The large majority are theoretical studies.

Concerning high-resolution spectroscopy of MHIs, only a limited number of investigations have been carried out, most of which a long time ago. Radiofrequency spectroscopy of the hyperfine structure in several vibrational levels has been performed on $H_2^+$ trapped in a Paul trap [3]; several low-lying fundamental ro-vibrational transitions of $HD^+$ have been measured using laser spectroscopy on an ion beam [4], while rotational and ro-vibrational transitions of $H_2^+$, $D_2^+$ and $HD^+$ close to the dissociation limit were investigated using microwave and laser spectroscopy, also on an ion beam [5,6]. The highest spectroscopic accuracies reported so far were achieved in the experiments of Jefferts and of Wing *et*

* This text will appear in "Precision Physics of Simple Atomic Systems", *Lecture Notes in Physics*, Springer, 2007

*al.* [4,7], $\simeq 1 \cdot 10^{-6}$ in relative units. Recently, also the dissociation energies have been obtained with accuracies $\simeq 1 \cdot 10^{-6}$ [8]. Thus, the experimental accuracies have been far less than those achieved in hydrogen or helium spectroscopy.

In the late 1990s, it was recognized that there are attractive reasons and many opportunities to study MHIs in novel ways and to achieve a much higher precision than previously possible [9]. Several techniques, not used before on MHIs, appeared to be applicable, including translational cooling, internal cooling, spectroscopy with reduced Doppler broadening, Doppler-free spectroscopy, high sensitivity ion detection. Novel laser systems not available at the time of the last precision spectroscopic studies can be used advantageously, among them diode lasers, quantum cascade lasers and the femtosecond frequency comb. The prospect of significantly improved experimental precision has also motivated us to develop more extended theoretical treatments of the MHI; in the course of these efforts, the accuracy of the energy levels has been increased by approximately two orders of magnitude compared to previous work.

Some of the above techniques have by now been implemented, and are reported here; the remaining appear to be feasible in the near future. These recent developments open up a number of novel applications of MHIs:

**(i)** test advanced *ab initio* molecular calculations (in particular, QED contributions)
**(ii)** measure certain fundamental constants
**(iii)** test concepts for the manipulation of molecules (state preparation, alignment)
**(iv)** sense fields (blackbody radiation [10])
**(v)** probe fundamental physics laws (e.g. Lorentz Invariance [11], time invariance of fundamental constants [12,13])
**(vi)** study electric dipole interactions between molecules [14]
**(vii)** explore elastic, reactive and charge exchange collisions with neutral atoms and molecules at ultralow collision energies

The successful demonstration of manipulation of MHIs at the quantum state level could also open up the possibility to study collisions with quantum-state resolution, i.e. where all parent particles are in specific quantum states.

An attractive perspective of our work pursued under (i) is to eventually determine the ratios of electron-to-proton mass ($m_e/m_p$), proton-to-deuteron mass ($m_p/m_d$) and proton-to-triton mass ($m_p/m_t$) from a comparison between accurate experimental and theoretical energy level data. The basis for this possibility is the dependence of the vibrational and rotational transition frequencies on the fundamental constants. For fundamental vibrational and rotational transitions, the frequencies scale approximately as

$$h\,\nu_{vib} \sim \sqrt{m_e/\mu}\,R_\infty\,, \qquad h\,\nu_{rot} \sim (m_e/\mu)R_\infty\,, \tag{1}$$

where $\mu = M_1 M_2/(M_1 + M_2)$ is the reduced mass of the two nuclei and $R_\infty$ is the Rydberg energy. The precise dependencies have been computed in refs.

[12,15,16]. The mass ratios $m_p/m_d$, $m_p/m_t$ and $m_e/m_p$ are conventionally determined by Penning ion trap mass spectrometry on single particles or by electron spin resonance of single hydrogen-like ions in a Penning ion trap. Relative accuracies are currently $2.0 \cdot 10^{-10}$ [17], $2 \cdot 10^{-9}$, and $4.6 \cdot 10^{-10}$ [17,18], respectively. Note that in case of $m_e/m_p$, the determination involves the use of QED [19]. Clearly, the corresponding accuracies of $\nu_{vib}$, $\nu_{rot}$ represent the goal levels for our ongoing experimental and theoretical efforts on $H_2^+$ and $HD^+$.

Several aspects support the expectation that such accuracies can be reached in the near future. First, the lifetimes of vibrational levels are long, the shortest ones occurring for low-lying levels in $HD^+$, $\simeq$ 10 ms. The relative linewidth due to spontaneous decay is thus of the order or smaller than $10^{-13}$. Second, Doppler broadening can be strongly reduced or eliminated by either cooling the molecular ions or by performing two-photon Doppler-free spectroscopy. Finally, collision broadening and time-of-flight broadening can also be minimized by both cooling and providing a good ultra-high vacuum environment. Systematic shifts due to light fields, trap electric fields, and trap and environmental magnetic fields will need to be considered; hereby it will be helpful that these influences be calculated accurately, using the relative simplicity of the MHI. The theoretical determination of the energy levels at the goal accuracy level will need as input nuclear properties such as the proton and deuteron nuclear radii, which may be obtained e.g. from hydrogen spectroscopy or nuclear scattering experiments.

In this contribution we present an overview of our theoretical and experimental results achieved recently on MHIs. Chapter 2 describes the theoretical approaches for a precise computation of energy levels, including hyperfine and QED effects and the computation of one- and two-photon spectra. Chapter 3 presents the development and results from an experiment for trapping and spectroscopy of $H_2^+$ performed at the Université d'Evry Val d'Essonne. Chapter 4 summarizes an experiment on $HD^+$ at the University of Düsseldorf.

## 2 *Ab initio* theory of $H_2^+$ and $HD^+$

The dissociation energies of 462 states in $H_2^+$ and 619 in $HD^+$ in a wide range of $v$ and $L$, vibrational and rotational quantum numbers, have been calculated some time ago by R.E. Moss [20,21] with a relative accuracy of $\sim 5 \cdot 10^{-9}$ (including the leading order relativistic and radiative corrections). Later the numerical precision of the nonrelativistic energies have been improved up to $10^{-15} - 10^{-24}$ a.u. [12,15,22–26] by using variational methods. The ultimate accuracy of $\sim 10^{-24}$ a.u. has been obtained for the $H_2^+$ ground state [26]. These calculations demonstrate that at least the nonrelativistic ro-vibrational transition frequencies can be determined with an uncertainty well below the 1 kHz level. In this section we describe the calculation of QED corrections as an expansion in terms of $\alpha$, the fine structure constant. The numerical method exploits a variational approach based on the Slater-type exponents as basis functions. We demonstrate that the frequencies of ro-vibrational transitions can be obtained in this way with a precision better than 1 part per billion (ppb).

### 2.1 Variational expansion

The variational bound state wave functions are calculated by solving the three-body Schrödinger equation with Coulomb interaction using the variational approach based on the exponential expansion with randomly chosen exponents. Details and the particular strategy of choice of the variational nonlinear parameters and basis structure that have been adopted in the present work can be found in [23].

Briefly, the wave function for a state with a total orbital angular momentum $L$ and of a total spatial parity $\pi = (-1)^L$ is expanded as follows:

$$\begin{aligned} \Psi^{\pi}_{LM}(\mathbf{R},\mathbf{r}_1) &= \sum_{l_1+l_2=L} \mathcal{Y}^{l_1 l_2}_{LM}(\hat{\mathbf{R}},\hat{\mathbf{r}}_1) G^{L\pi}_{l_1 l_2}(R,r_1,r_2), \\ G^{L\pi}_{l_1 l_2}(R,r_1,r_2) &= \sum_{n=1}^{N} \Big\{ C_n \,\mathrm{Re}\big[e^{-\alpha_n R-\beta_n r_1-\gamma_n r_2}\big] \\ &\qquad + D_n \,\mathrm{Im}\big[e^{-\alpha_n R-\beta_n r_1-\gamma_n r_2}\big] \Big\}. \end{aligned} \tag{2}$$

Here $\mathcal{Y}^{l_1 l_2}_{LM}(\hat{\mathbf{R}},\hat{\mathbf{r}}_1) = R^{l_1} r_1^{l_2} \{Y_{l_1} \otimes Y_{l_2}\}_{LM}$ are the solid bipolar harmonics, $\mathbf{R}$ is the position vector of nucleus 2 relative to nucleus 1, and $\mathbf{r}_1$, $\mathbf{r}_2$ are positions of an electron relative to nuclei 1 and 2, respectively. The complex exponents, $\alpha$, $\beta$, $\gamma$, are generated in a pseudorandom way.

When the exponents $\alpha_n$, $\beta_n$, and $\gamma_n$ are real, the method reveals slow convergence for molecular type Coulomb systems. The use of complex exponents allows to reproduce the oscillatory behaviour of the vibrational part of the wave function and to improve convergence [27,23].

The advantage of choice (2) is the simplicity of the basis functions. It allows evaluating analytically matrix elements of the Breit-Pauli Hamiltonian and the leading-order radiative corrections and, more importantly, to treat in a systematic way the singular integrations encountered in higher-order contributions [28].

### 2.2 Leading-order relativistic and radiative corrections

Relativistic corrections of the leading $R_\infty \alpha^2$ order, the Breit-Pauli Hamiltonian, are well known and can be found in many textbooks [29,30]. The nuclear finite size effects are considered as contributions to this order. Details, relevant particularly to the case of the MHIs, can be found in [31].

In what follows we assume that the nuclear charges are $Z_1 = Z_2 = Z = 1$ and nuclear masses are denoted by capital $M$. The units adopted are ($\hbar = e = m_e = 1$).

The radiative corrections of an order $R_\infty \alpha^3$ for a one electron molecular system can be expressed by the following set of equations (see Refs. [32–34]).

The one-loop self-energy correction (orders $R_\infty\alpha^3$ and $R_\infty\alpha^3(m/M)$) is:

$$\begin{aligned} E^{(3)}_{se} = {} & \frac{4\alpha^3 Z}{3}\left(\ln\frac{1}{\alpha^2} - \beta(L,v) + \frac{5}{6} - \frac{3}{8}\right)\langle\delta(\mathbf{r}_1)+\delta(\mathbf{r}_2)\rangle\,, \\ & +\alpha^3 Z^2 \sum_{i=1,2}\left[\frac{2}{3M_i}\left(-\ln\alpha - 4\,\beta(L,v) + \frac{31}{3}\right)\langle\delta(\mathbf{r}_i)\rangle - \frac{14}{3M_i}Q(r_i)\right], \end{aligned} \tag{3}$$

where

$$\beta(L,v) = \frac{\langle \mathbf{J}(H_0 - E_0)\ln\left((H_0-E_0)/R_\infty\right)\mathbf{J}\rangle}{\langle[\mathbf{J},[H_0,\,\mathbf{J}]]/2\rangle} \tag{4}$$

is the Bethe logarithm. The latter quantity presents the most difficult numerical problem in computation of QED corrections for the three-body bound states. In [34,35] the calculations for a wide range of ro-vibrational states in $H_2^+$ and $HD^+$ have been performed to an accuracy of about 7 significant digits. The operator $\mathbf{J}$ in (4) is the electric current density operator of the system[1]. The last term, $Q(r)$, in Eq. (3) is the mean value of a regularized operator introduced by Araki and Sucher [36] for the $1/(4\pi r^3)$ potential:

$$Q(r) = \lim_{\rho\to 0}\left\langle \frac{\Theta(r-\rho)}{4\pi r^3} + (\ln\rho + \gamma_E)\delta(\mathbf{r})\right\rangle. \tag{5}$$

The values of this matrix element for ro-vibrational states are calculated in [31].

The remaining contributions in this order can be obtained from the Pauli form factor of an electron (anomalous magnetic moment):

$$E^{(3)}_{anom} = \pi\alpha^2 Z\left[\frac{1}{2}\left(\frac{\alpha}{\pi}\right)\right]\langle\delta(\mathbf{r}_1)+\delta(\mathbf{r}_2)\rangle\,. \tag{6}$$

and from the one-loop vacuum polarization:

$$E^{(3)}_{vp} = \frac{4\alpha^3 Z}{3}\left[-\frac{1}{5}\right]\langle\delta(\mathbf{r}_1)+\delta(\mathbf{r}_2)\rangle\,. \tag{7}$$

### 2.3 $R_\infty\alpha^4$ order corrections in the nonrecoil limit

The contribution of recoil corrections, proportional to $(m/M)$, in the $R_\infty\alpha^4$ order are too small for our present consideration and may be neglected. Radiative corrections for a bound electron in an external field are known analytically

[1] $\mathbf{J} = \sum_a z_a\mathbf{p}_a/m_a$, where $z_a$, $\mathbf{p}_a$, $m_a$ are the charge, impulse, and mass of a particle $a$. The sum is performed over all particles of the system.

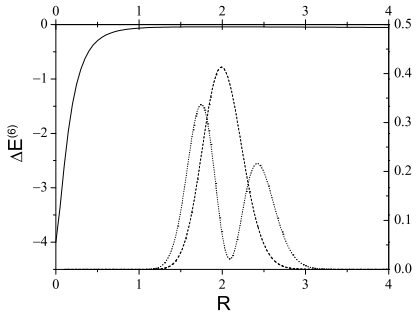


**Fig. 1.** Adiabatic potential of the $m\alpha^6$ order contribution to the Dirac energy of the two-center problem ($Z_1 = Z_2 = 1$). Dashed curves are the squared densities of the ground and first vibrational state wave functions of $H_2^+$ ion.

[38,39]:

$$
\begin{aligned}
E^{(4)}_{se} &= \alpha^4 Z^2 \left[4\pi \left(\frac{139}{128} - \frac{1}{2}\ln 2\right)\right] \langle \delta(\mathbf{r}_1) + \delta(\mathbf{r}_2)\rangle \,, \\
E^{(4)}_{vp} &= \alpha^4 Z^2 \left[\frac{5\pi}{48}\right] \langle \delta(\mathbf{r}_1) + \delta(\mathbf{r}_2)\rangle \,, \\
E^{(4)}_{anom} &= \alpha^2 Z\pi \left[\left(\frac{\alpha}{\pi}\right)^2 \left(\frac{197}{144} + \frac{\pi^2}{12} - \frac{\pi^2}{2}\ln 2 + \frac{3}{4}\zeta(3)\right)\right] \langle \delta(\mathbf{r}_1) + \delta(\mathbf{r}_2)\rangle \,, \\
E^{(4)}_{2loop} &= \alpha^2 Z\pi \left[\left(\frac{\alpha}{\pi}\right)^2 \left(-\frac{6131}{1296} - \frac{49\pi^2}{108} + 2\pi^2 \ln 2 - 3\zeta(3)\right)\right] \langle \delta(\mathbf{r}_1) + \delta(\mathbf{r}_2)\rangle \,.
\end{aligned}
\tag{8}
$$

The last equation includes both the Dirac form factor and polarization operator contributions.

The $R_\infty \alpha^4$ relativistic correction is obtained using the adiabatic "effective" potential for an $m\alpha^6$ term in the $\alpha$ expansion of the two-center Dirac energy (see Fig. 1). Averaging over the squared wave function density of a state one gets $E^{(4)}_{rc}$. The adiabatic potentials have been obtained recently with about 5 significant digits [37], and the Born-Oppenheimer solution yields approximate wave functions at the $(m/M) \approx 10^{-4}$ level, which allows to claim that $E^{(4)}_{rc}$ is now known to 4 digits.

Some higher order radiative corrections for a bound electron in an external field are also known in an analytic form [38,39] and can be included into consideration:

$$
E^{(5)}_{se} = \alpha^5 Z^3 \, \ln^2 (Z\alpha)^{-2} \big[-1\big] \, \langle \delta(\mathbf{r}_1) + \delta(\mathbf{r}_2)\rangle \,. \tag{9}
$$

The electron ground state wave function may be approximated by $\psi_e(\mathbf{r}_e) = C[\psi_{1s}(\mathbf{r}_1) + \psi_{1s}(\mathbf{r}_2)]$, where $\psi_{1s}$ is the hydrogen ground state wave function and $C$ is a normalization coefficient. Thus, one may use this approximation to

evaluate other contributions in the $R_\infty\alpha^5$ order:

$$
\begin{aligned}
E^{(5')}_{se} &= \alpha^5 Z^3 \Big[A_{61}\ln(Z\alpha)^{-2} + A_{60}\Big]\,\langle\delta(\mathbf{r}_1)+\delta(\mathbf{r}_2)\rangle\,,\\
E^{(5)}_{2loop} &= \frac{\alpha^5}{\pi} Z^2 \big[B_{50}\big]\,\langle\delta(\mathbf{r}_1)+\delta(\mathbf{r}_2)\rangle\,,
\end{aligned}
\tag{10}
$$

where the constants $A_{61}$, $A_{60}$, and $B_{50}$ are taken equal to the constants of the $1s$ state of the hydrogen atom $A_{61} = 5.419\ldots$ [40], $A_{60} = -30.924\ldots$ [41], and $B_{50} = -21.556\ldots$ [42] (see also Ref. [39] and references therein). The final theoretical uncertainty in the transition frequency (see Table 1) is determined by the total contribution of the last two equations.

### 2.4 Hyperfine structure of states

The leading order contribution to the hyperfine splitting of the ro-vibrational states is calculated using the spin-dependent part of the Breit-Pauli interaction Hamiltonian, with phenomenological values for the nuclear magnetic moments and the electron anomalous magnetic moment. The hyperfine levels of $HD^+$, $E_{vLFSJ}$, are labelled with the quantum numbers $F$, $S$ and $J$ of the intermediate angular momenta $\mathbf{F} = \mathbf{I}_p + \mathbf{s}_e$, $\mathbf{S} = \mathbf{F} + \mathbf{I}_d$ and of the total angular momentum $\mathbf{J} = \mathbf{L} + \mathbf{S}$ [43]. In case of $H_2^+$ due to Pauli exclusion principle the total nuclear spin $I$ is uniquely defined by $L$ and parity of the electronic state. The following coupling scheme is adopted: $\mathbf{F} = \mathbf{I} + \mathbf{s}_e$ and $\mathbf{J} = \mathbf{L} + \mathbf{F}$ [44]. The hyperfine structure (HFS) of the ro-vibrational states of $HD^+$ consists of 4, 10 or 12 hyperfine sub-levels for $L=0$, $L=1$ and $L\geq 2$, respectively (see Fig. 2). The multiplicity of the HFS of $H_2^+$ is reduced to 1 for $L=0$, 5 for $L=1$, 2 for even, and 6 for odd $L$ states. Typically, the hyperfine splitting of the lower ro-vibrational states of $HD^+$ and $H_2^+$ is about 1 GHz. The uncertainty in the hyperfine spectrum is related to the unknown contribution of the spin interaction terms of orders $O(R_\infty\alpha^4(m/M))$ and higher, which have not yet been taken into consideration, and is estimated not to exceed 100 kHz.

Each transition line between ro-vibrational states is split into a multiplet of hyperfine components, corresponding to the allowed transitions $i \to f$ between

**Table 1.** Summary of contributions to the $(v=0, L=0) \to (v'=1, L'=0)$ transition frequency (in MHz).

| | $H_2^+$ | $HD^+$ |
|---|---|---|
| $\Delta E_{nr}$ | 65 687 511.0686 | 57 349 439.9717 |
| $\Delta E_{\alpha^2}$ | 1091.041(03) | 958.152(03) |
| $\Delta E_{\alpha^3}$ | −276.544(02) | −242.118(02) |
| $\Delta E_{\alpha^4}$ | −1.997 | −1.748 |
| $\Delta E_{\alpha^5}$ | 0.120(23) | 0.106(19) |
| $\Delta E_{tot}$ | 65 688 323.688(25) | 57 350 154.368(21) |

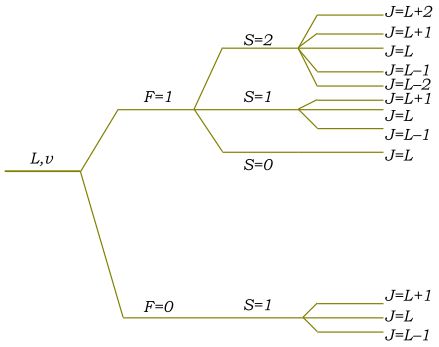


**Fig. 2.** Hyperfine structure of a ro-vibrational state of $HD^+$ with $L \geq 2$.

the states of the hyperfine structure of the initial and final states. Whether these hyperfine components will be resolved or the spectrum profile depends on the initial and final state lifetime and on the experimental conditions (transition linewidth $\Gamma_f$, laser intensity $I$, temperature, interaction time etc.) Examples of spectral data are presented in experimental sections of our review (see Fig. 13). The shape of the profile also depends on the population of the initial hyperfine states. The general expressions for the probability per unit time for one- and two-photon transitions between ro-vibrational states of the MHIs with account of the hyperfine structure are given in Ref. [45].

The probability per unit time for the hyperfine transition $i \to f$ at resonance (averaged over the magnetic numbers of initial and final states), $\Gamma_{f,i}$, may be represented in the form:

$$\Gamma_{f,i} = T_{f,i}^2 \, \Gamma_{v'L',vL}, \qquad \Gamma_{v'L',vL} = \frac{2\pi\alpha}{3\hbar} \, \frac{I}{\Gamma_f} \, \frac{\langle v'L' || \, \mathbf{d} \, || vL \rangle^2}{2L+1}. \tag{11}$$

Here $\Gamma_{v'L',vL}$ is the probability per unit time of laser-stimulated dipole transitions between ro-vibrational states, $\langle v'L' || \, \mathbf{d} \, || vL \rangle$ is the reduced matrix element of the electric dipole moment of the $HD^+$ ion $\mathbf{d} = \sum_a z_a \mathbf{r}_a$, and

$$T_{f,i} = \sqrt{(2J'+1)(2L+1)} \sum_{F''S''} (-1)^{S''+J+L'} \left\{ \begin{array}{ccc} L & 1 & L' \\ J' & S'' & J \end{array} \right\} \beta^f_{F''S''} \beta^i_{F''S''}, \tag{12}$$

where $\beta^{vLFSJ}_{F''S''}$ are constant amplitudes of the state vectors of the hyperfine states:

$$|vLFSJ, J_z\rangle = \sum_{F''S''} \beta^{vLFSJ}_{F''S''} \sum_{M\zeta} C^{JJ_z}_{LM,S''\zeta} \Psi_{vLM}(\mathbf{R}, \mathbf{r}_1) \chi(F''S'', \zeta), \tag{13}$$

determined from the effective Hamiltonian of spin interaction. Here $\chi(FS, \zeta)$ are basis spinors of definite values of $F$, $S$ and $S_z$ in the space of the spin variables. The relative intensity of the hyperfine components of a transition line

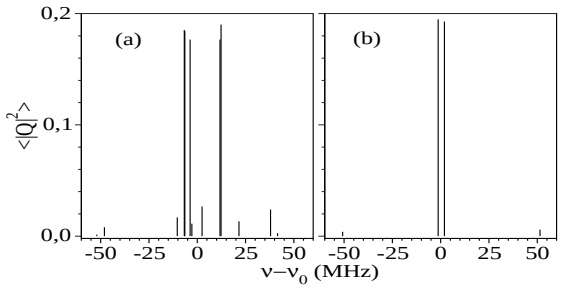


**Fig. 3.** Hyperfine splitting and intensities of the two-photon ro-vibrational transition line for the $H_2^+$ ion: (a) $(v=0, L=1) \to (v'=1, L'=1)$, (b) $(v=0, L=2) \to (v'=1, L'=2)$.

between ro-vibrational states is thus determined by the amplitudes $T_{f,i}$. In case the individual hyperfine components cannot be resolved, the observable intensity is reduced to the intensity of the dipole ro-vibrational transition $\Gamma_{v'L',vL}$, in agreement with the identity $\sum_f T_{f,i}^2 = 1$.

The hyperfine structure of the one- and two-photon transition lines includes a large number of components, most of which, however, are suppressed. There are as well dominant (or "*favoured*") transitions between states with similar spin structure, such as $(vLFJ) \to (v'L'FJ')$ with $\Delta J = \Delta L$ (for $H_2^+$). In such pairs of homologous hyperfine states the spin-dependent corrections to the ro-vibrational energies $E_{v'L'FJ'}$ and $E_{vLFJ}$ have close values, which partially cancel each other when evaluating the spin correction to the resonance transition frequency $(E_{v'L'FJ'} - E_{vLFJ})/h$. Indeed, the *favoured* hyperfine transitions span over a frequency interval less than 25 MHz (see Fig 3). It is natural to expect that the unknown contributions to the frequency of the favoured transitions from the spin interactions of order $R_\infty \alpha^4 (m/M)$ and higher also tend to cancel each other; therefore, the theoretical uncertainty of the resonance frequency of the *favoured* hyperfine sublines will be less than $\sim 5$ kHz.

### 2.5 Two-photon transition probabilities

In order to assess the feasibility of Doppler-free two-photon spectroscopy in $H_2^+$ or $HD^+$, it is essential to evaluate transition probabilities between ro-vibrational states. This can be done using the formula from second-order perturbation theory [46], and the accurate wavefunctions provided by variational calculations. Assuming that magnetic sublevels are equally populated, the two-photon transition probability at resonance between states $v, L$ and $v', L'$ is

$$\Gamma_{v,L,v',L'} = \left(\frac{4\pi a_0^3}{\hbar c}\right)^2 \frac{4I^2}{\Gamma_f} \overline{Q}_{v,L,v',L'} \tag{14}$$

where $I$ is the excitation intensity, $\Gamma_f$ the transition linewidth, and

$$\overline{Q}_{v,L,v',L'} = \frac{1}{2L+1} \sum_{k=0,2} \frac{\left|\langle vL \| Q^{(k)} \| v'L' \rangle\right|^2}{2k+1}. \tag{15}$$

$Q^{(0)}$, $Q^{(2)}$ are respectively the scalar and tensor parts of the two-photon transition operator

$$Q = \frac{1}{4\pi\epsilon_0 a_0^3}\,\mathbf{d}\cdot\boldsymbol{\epsilon}\,\frac{1}{E-H}\,\mathbf{d}\cdot\boldsymbol{\epsilon} \tag{16}$$

Here, $E = [E(v,L) + E(v',L')]/2$ is the one-photon resonance energy and $\boldsymbol{\epsilon}$ the exciting field polarization. The two-photon transition probabilities were calculated in [22,47].

For the $H_2^+$ case [47] there exists a quasi-selection rule $\Delta v = \pm 1$, and the dimensionless transition probabilities $\overline{Q}_{v,L,v',L'}$ are rather small, of the order of 1, which is due to the level structure of $H_2^+$. If we consider the example of transitions between $L = 0$ states, these states are of ${}^1S^e$ symmetry, and there is no resonant intermediate level of ${}^1P^o$ symmetry that could enhance the transition probability.

The situation is different in the $HD^+$ case [22], since there is no splitting between singlet and triplet state due to the loss of exchange symmetry between the nuclei. As a result, for a transition between $L = 0$ ($S^e$) states, there exist intermediate bound $P^o$ levels which can be very close in energy and efficiently enhance the transition probability. This is most likely to happen if the difference between $v$ and $v'$ (the initial and final vibrational quantum numbers) is an even number. In this case, the state $(v'' = (v+v')/2, L'' = L \pm 1)$ is often close to the middle energy $E = [E(v,L) + E(v',L')]/2$, because of the quasi-harmonic structure of vibrational levels. As a result, some of the most intense two-photon lines are $\Delta v = 2$ transitions in the 5-6 $\mu$m range or $\Delta v = 4$ transitions in the 2.5-3 $\mu$m range, accessible e.g. with continuous-wave optical parametric oscillator or quantum cascade lasers. The dimensionless transition probabilities $\overline{Q}_{v,L,v',L'}$ can reach values as high as 300 for the $(v=0, L=1) \to (v=2, L=1)$ transition at 5.366 $\mu$m. Thus, the $HD^+$ molecular ion is a promising candidate for precise two-photon spectroscopy.

The next step is to consider the hyperfine structure of two-photon transition lines. The representation of the hyperfine state vectors in the $H_2^+$ case is

$$|vLFJJ_z\rangle = \sum_{F'} \beta_{F'}^{vLFJ} \sum_{M\zeta} C_{LM,F'\zeta}^{JJ_z}\,\psi_{vLM}(\mathbf{R},\mathbf{r_1})\,\chi(F',\zeta). \tag{17}$$

The definitions for $\chi(F',\zeta)$ and $\beta_{F'}^{vLFJ}$ are similar to those in (13). Assuming equal populations for hyperfine magnetic sublevels, the dimensionless transition probability between levels $|i\rangle = |vLFJ\rangle$ and $|f\rangle = |v'L'F'J'\rangle$ is:

$$\overline{Q}_{i,f} = (2J'+1) \sum_{k=0,2} \frac{\left| \langle vL\|Q^{(k)}\|v'L'\rangle \sum_{F''} (-1)^{J'+L+F''} \begin{Bmatrix} L & k & L' \\ J' & F'' & J \end{Bmatrix} \beta_{F''}^{f} \beta_{F''}^{i} \right|^2}{2k+1} \tag{18}$$

The hyperfine structure of two different transitions for linear polarization is shown in Fig. 3. Transitions between odd $L$ states (Fig. 3(a)) comprise between 25 to 34 components, 5 or 6 of which are favoured. Transitions between even

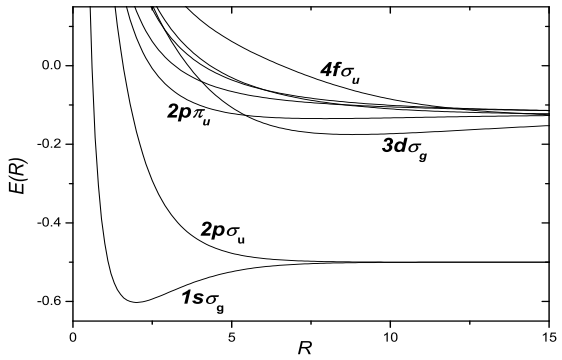


**Fig. 4.** Born-Oppenheimer electronic energies (in a.u.) of the adiabatic potential terms.

$L$ states (Fig. 3(b)) have a much simpler structure, the total nuclear spin being zero. The non zero even $L$ spectrum comprises only two main components (verifying $\Delta J = 0$) together with two weak satellites. Transitions between $L = 0$ states are structureless, which makes them especially attractive from a metrological point of view.

## 3 Two-photon spectroscopy of $H_2^+$

A two-photon vibrational spectroscopy experiment aimed at the determination of the electron to proton mass ratio is being setup at the Kastler Brossel Laboratory. We begin by recalling the basic spectral features of the MHI, and discuss the planned experimental sequence. In the second part, we report on the present status of the experimental setup. It is composed of a hyperbolic Paul trap in which a few thousand $H_2^+$ ions can be confined, a UV laser for ion preparation and detection by state-selective photodissociation, and a narrow-line, tunable laser system that will excite the two-photon transition.

### 3.1 $H_2^+$ level structure

Although the Born Oppenheimer (BO) approximation is not relevant for highly accurate calculations, it remains a very convenient tool to get a useful insight into the $H_2^+$ level structure. In order to understand the processes discussed here, it is enough to consider the first two BO electronic curves: the ground state $1s\sigma_g$ and first excited state $2p\sigma_u$, which are depicted in Fig. 4.

The exact symmetries of the system are the total spatial parity $\pi$ and the exchange of nuclei $P_{12}$; the $g/u$ electronic parity $\pi_e$ used in the BO approach is related to them by $\pi_e = \pi P_{12}$. The bound levels of $H_2^+$ can be labelled $v, (^{2I+1}L^{e,o})$ where $v$ and $L$ are the vibrational and orbital quantum numbers, $I$ is the total nuclear spin quantum number and $(e, o)$ stands for the total parity. Since the total spatial parity is $\pi = (-1)^L$, the $1s\sigma_g$ curve only supports $^1S^e$, $^3P^o$, $^1D^e \ldots$ levels.

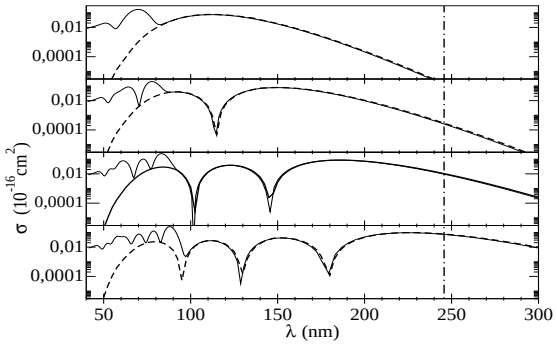


**Fig. 5.** Photodissociation cross sections of the $L=0$, $v$ levels of $H_2^+$. The dashed lines are the result of a Born Oppenheimer calculation [50], which takes the $1s\sigma_g$ and $2p\sigma_u$ electronic curves into account. The nodal structure of the cross section reflects that of the vibrational wavefunction. The solid lines are obtained from an exact variational method which fully takes into account the three body dynamics [51]. The additional nodal structure appearing in the short wavelength domain can be interpreted as the photodissociation to higher excited electronic states ($3d\sigma_g$, $2p\pi_u$, $4f\sigma_u$, ...). The dot-dashed vertical line corresponds to the KrF laser wavelength of 248 nm.

The $2p\sigma_u$ electronic curve presents at large internuclear distances a weak attractive potential that supports two bound $L = 0$ energy levels [20,48]. Some of those states have been observed by microwave or laser spectroscopy experiments [49]. At higher $L$ the $2p\sigma_u$ potential supports bound or dissociative $^1P^o$, $^3D^e$ $^1F^o$ ... states that can be calculated numerically using either the variational, or the complex coordinate rotation method.

### 3.2 One-photon transitions: photodissociation

The selection rules for one-photon dipole transitions are $\Delta L = \pm 1$ and $\Delta I = 0$. As a consequence, transitions between bound ro-vibrational states of $H_2^+$ are forbidden (in contrast with the $HD^+$ case), resulting in very long-lived states. On the other hand, one-photon photodissociation transitions from $1s\sigma_g$ to $2p\sigma_u$ electronic states are allowed. The photodissociation cross sections $\sigma_v$ of the $(^1S^e, v)$ states have been first computed by Dunn [50] in the Born-Oppenheimer approximation, and then using the perimetric coordinate variational method in [51]. The results are given in Fig. 5. They show that a laser source in the 250 nm range can be used to selectively photodissociate the $v = 1, 2, 3, \ldots$ vibrational states while keeping the ions in the $v = 0$ level since the successive cross section ratios $\sigma_{v+1}/\sigma_v$ are 214, 40, 10, for $v = 0, 1, 2$, respectively.

### 3.3 Two-photon transitions: choice of the transition

One-photon transitions between bound states being forbidden, a high resolution study of the vibrational structure of $H_2^+$ is only possible using Doppler-free two-photon spectroscopy. Two-photon transitions obey the selection rule $\Delta L = 0, \pm 2$

as well as the quasi selection rule $\Delta v = \pm 1$, as discussed in section 2.5. The corresponding $(v, L) \rightarrow (v' = v+1, L')$ transition frequencies lie in the 8-12 $\mu$m range. Among them, we have chosen to probe the $v=0 \rightarrow v=1$ transitions, for $L$ and $L'$ equal to 0 or 2 and eventually 1 or 3. We now give the arguments that explain this choice.

The first condition to fulfill is that it should be possible to prepare a large enough number of $H_2^+$ in the initial state of the transition. The ro-vibrational populations of $H_2^+$ ions, after creation by electron impact ionization of a low pressure $H_2$ gas, have been studied both theoretically and experimentally [52]. The vibrational populations are linked to the overlap of the $H_2$ and $H_2^+$ vibrational wave functions (Franck-Condon principle); they are found to be of the order of 12, 18, 18, 15, 11, 8, 5, 4% for the first few levels. The rotational populations of the $H_2^+$ ions are those of the $H_2$ mother molecules, i.e. 12, 28, 28, 18, 8% at 300 K. Moreover, we have shown in the previous paragraph that UV photodissociation provides a convenient way to prepare ions in the ground vibrational state; it is then desirable to choose a $v=0$ state as initial state of the transition, with $L$ between 0 and 3, $L=1$ or 2 being the best choices with respect to the number of ions. The same photodissociation process can be used to detect the ions in the excited $v=1$ state.

The hyperfine structure of two-photon lines should also be considered; it is apparent from Fig. 3 that it is simpler for transitions between even $L$ states. Interpretation of experimental data is likely to be easier in this case.

The intensities of the various $(v = 0, L) \rightarrow (v' = 1, L')$ (with low $L$) two-photon lines are of the same magnitude; the choice of a particular transition depends mostly on the availability and characteristics of laser sources at the required wavelength. The whole mid-infrared range is accessible by the recently developed quantum cascade lasers (QCL); $L' = L$ transitions are especially attractive, because they lie within the spectrum of $CO_2$ lasers ($\lambda \simeq$ 9-10 $\mu$m). Also, a number of frequency reference molecular absorption lines are known in this range [53]. The first transition that is going to be probed in our experiment is the $(v = 0, L = 2) \rightarrow (v' = 1, L' = 2)$ line at 9.166 nm. The details of coincidences with $CO_2$ lines and molecular reference lines, which make this transition favorable, are explained below.

### 3.4 Experimental sequence

The two-photon transition matrix elements $|Q_{v,L,v',L'}|^2$ of the "favoured" hyperfine components of two-photon transitions are of the order of 0.2 (see Fig. 3). A typical QCL can deliver about 50 mW of single-mode optical power. Assuming a perfect coupling to a build-up cavity of finesse 1000 with a waist of 1 mm, one obtains a laser flux of 15 W/mm$^2$. Assuming an instrumental width $\Gamma_f \approx$10 kHz, equation (14) yields transition rates of about 70/s. This order of magnitude shows that long interaction times are needed and that one has to work with a cloud of trapped ions, having a radius of the order of the beam waist.

The considerations of the previous paragraph show that vibrational two-photon spectroscopy of $H_2^+$ can be performed by $(2+1')$ resonance enhanced

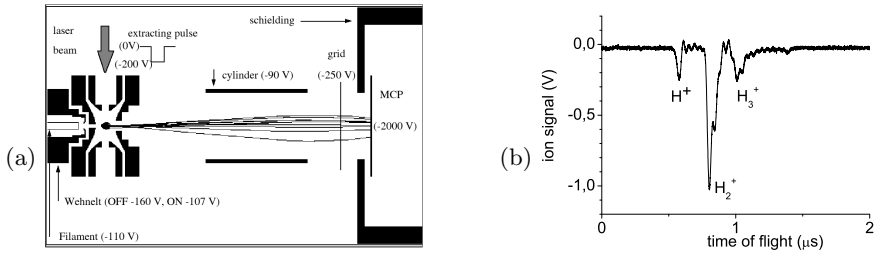


**Fig. 6.** (a) Simulation of the experimental setup for ion creation, trapping and detection using the SIMION7 software. MCP is a multichannel plate detector. (b) Time of flight spectrum showing the $H^+$, $H_2^+$ and $H_3^+$ species confined in the Paul trap.

multiphoton dissociation (REMPD). This process is very similar to that implemented for $HD^+$ vibrational spectroscopy and described in more detail in Section 4.

The experiment will be conducted in the following stages:

- simultaneous creation, trapping and selection of $(L, v = 0)$ $H_2^+$ ions.
- excitation of the $(L, v=0) \rightarrow (L', v'=1)$ two-photon transition.
- photodissociation of the $(L, v=1)$ $H_2^+$ ions.
- time of flight detection of $H^+$ and $H_2^+$ ions.

### 3.5 Experimental setup

The ion trap is depicted in Fig. 6(a). It is a hyperbolic Paul trap with a ring of inner radius $r_0 = 8.2$ mm and two end caps separated by $2z_0 = 6$ mm. Two pairs of holes (2 mm in diameter) are drilled in the ring along two orthogonal axes to shine the ion cloud with the UV and IR light. Both end cap electrodes are AC grounded. A RF voltage (about 200 V peak to peak amplitude at 10.3 MHz) and a continuous voltage of a few Volts are applied to the ring electrode, resulting in trapping well depths of a few eV.

The $H_2^+$ ions are produced by electron impact ionisation from the residual $H_2$ gas. The electron gun is made of a tungsten wire and a Wehnelt cylinder; it is typically turned on for 100-200 ms. A 1 mm hole in one of the end cap electrodes allows access to the trap.

The contents of the trap are analyzed by applying a short negative high voltage pulse to the second end cap, thus extracting the ions from the trap through a 2 mm hole. The extracted ions are accelerated and focused onto a multi-channel plate (MCP) detector located 7 cm away, a long enough distance to separate by time of flight the $H^+$, $H_2^+$ and $H_3^+$ ions that are simultaneously produced and trapped. A typical time of flight spectrum is shown in Fig. 6(b). Up to a few thousand $H_2^+$ ions can be stored in the trap. The ion lifetime is of a few seconds and is limited by the residual pressure in the vacuum chamber.

The undesirable $H^+$ and $H_3^+$ ions are eliminated using the parametric excitation of their secular motion, by applying RF voltage in the MHz range on one

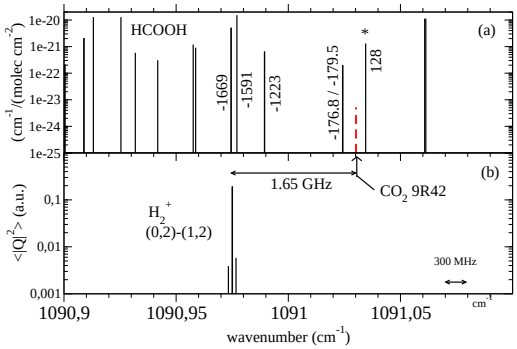


**Fig. 7.** (a) Absorption spectrum of formic acid (HCOOH) [53]. The line intensities are given in $\mathrm{cm}^{-1}/(\mathrm{molecule\ cm}^{-2})$. (b) Two-photon transition probabilities in atomic units. The central peak is made of two close components (see Fig. 3). The dashed line is the 9R(42) $CO_2$ emission line. The detunings between the 9R(42) $CO_2$ line and the HCOOH lines are indicated in MHz. The $CO_2$ laser is locked to the HCOOH line indicated by the star.

of the end cap electrodes during the ionisation process. A KrF excimer laser at 248 nm is used to photodissociate the $v \geq 1$ states in order to produce a $(L, v=0)$ ions cloud. The ions are shined by 20 mJ pulses during the filling of the trap. The characterization of ro-vibrational populations of the resulting ion cloud is now in progress.

Since all the bound states of $H_2^+$ are metastable, the natural widths of the two-photon transitions are extremely small. In Paul traps, the ion cloud temperature is of the order of magnitude of the potential depth expressed in K, i.e. $\approx 10^4$ K in our trap. Under those conditions, the two-photon linewidth $\Gamma_f$ (appearing in Eq. (14)) is expected to be limited by the second-order Doppler effect, i.e. of the order 10 kHz. It will limit the ultimate frequency resolution of the experiment at the $3 \cdot 10^{-10}$ level, and the mass ratio resolution at the $6 \cdot 10^{-10}$ level.

Ion cooling will thus be necessary in order to reach the metrological objective of the experiment at the $10^{-10}$ level. Nevertheless, the first step of the experiment is the observation of a two-photon transition, which is feasible with hot ions using a kHz linewidth laser source.

### 3.6 Two-photon excitation laser source

The laser system we have built is aimed at exciting the $(L = 2, v = 0) \rightarrow (L' = 2, v' = 1)$ two-photon transition at 9.166 $\mu$m. In this range, two kinds of laser sources are available. Single-mode $CO_2$ lasers have high output power and sub-kHz linewidths, but are hardly tunable on ranges exceeding 100 MHz, i.e. much smaller than the 1.65 GHz gap between the closest $CO_2$ emission line (9R(42)) and the $H_2^+$ line (see Fig. 7(b)). Recently, single mode quantum cascade laser (QCL) became commercially available. They can be tuned over about 10 $\mathrm{cm}^{-1}$ (300 GHz) through their temperature and injection current, but have

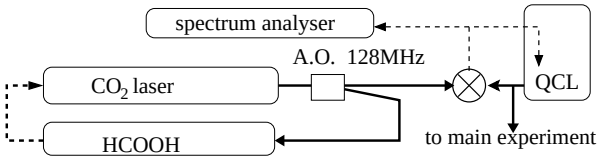


**Fig. 8.** Simplified setup of the $CO_2$/HCOOH phase-locked quantum cascade laser source. The QCL is mounted in a liquid nitrogen optical cryostat. The mixer is a room temperature HgCdZnTe detector. Solid lines are optical paths. Dashed lines are electrical paths and servo loops. A.O. is an acousto-optic modulator.

large linewidths of the order of a few MHz. Several experiments have shown that the linewidth can be reduced well below the kHz level by injection-current locking the QCL to a molecular line [54] or to a high finesse Fabry-Perot cavity resonance [55]. We have developed a laser source that takes advantage of both the narrow linewidth of the $CO_2$ laser and the tunability of the QCL [56].

The setup is shown in Fig. 8. A $CO_2$ laser oscillating on the 9R(42) line is frequency shifted by 128 MHz and stabilized on the intracavity saturated absorption signal of the $(21, 3, 19) \rightarrow (21, 2, 20)$ line of the $\nu_6$ band of formic acid (HCOOH) (see Fig. 7(a)). The absolute frequency of that transition (32 708 263 980.5 kHz) has recently be determined with an uncertainty of 1 kHz [57] by sum frequency mixing with a 30 THz wide visible femtosecond frequency comb [58]. The QCL is operated in a liquid nitrogen optical cryostat. The output power is 50 mW with a 700 mA injection current and a temperature of 80K. The QCL is phase-locked to the $CO_2$ laser with a tunable frequency offset in the 500-2000 MHz range [56]. The analysis of the beat note spectrum under locked conditions (see Fig. 9) shows that we have realized a narrow-line tunable laser source well suited to probe the $H_2^+$ two-photon lines, and also the ro-vibrationnal

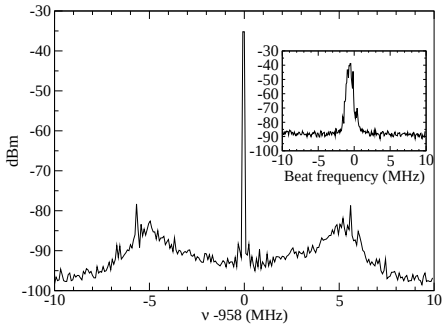


**Fig. 9.** Phase-locked beat note between the QCL and the $CO_2$/HCOOH frequency reference. RBW 10 kHz, VBW 1 kHz. The spectrum shows a loop bandwidth of the order of 6 MHz. The central peak is extremely narrow, with a -3dB width smaller than the 200 Hz resolution of the spectrum analyser. The inset shows the free running beat note with the same scale and a 500 kHz RBW.

spectrum of HCOOH [58] or other molecules ($NH_3$, ...) of atmospheric or astrophysical interest.

## 4 Cooling and Spectroscopy of $HD^+$

In experiments performed at the University of Düsseldorf, the MHIs $H_2^+$, $D_2^+$, and $HD^+$ were cooled to temperatures of $\simeq 10$ mK in a radiofrequency trap, by sympathetic cooling with laser-cooled beryllium ions. High-resolution spectroscopic studies of several rovibrational infrared transitions in $HD^+$ were performed. Hyperfine splitting of the lines was observed, and is in good agreement with theoretical predictions. The transitions were detected by monitoring the decrease in ion number after selective photodissociation of $HD^+$ ions in the upper vibrational state.

### 4.1 Preparation and characterization of cold MHI ensembles

MHIs are just a few of a multitude of species that can be cooled to mK temperatures, by sympathetic cooling [59,60] - the molecular species and a laser-coolable atomic species, with the same sign of charge, are simultaneously stored in a radiofrequency trap. Laser cooling the atoms then also efficiently cools the molecular ions via the long-range Coulomb interaction. Temperatures below 20 mK can be reliably reached. We have shown that using $Be^+$ ions as coolant permits to cool sympathetically ions from mass 1 to mass 200 amu [61–63]. A heavier atomic coolant species can be used to extend the mass range. For example, using $^{138}Ba^+$ as coolant molecular ions up to mass 410 amu have recently been cooled [64].

We use a linear quadrupole trap to simultaneously store both $Be^+$ and MHIs. The radiofrequency trap is driven at 14 MHz, with a peak-to-peak amplitude of 380 V. This results in a radial Mathieu stability parameter $q_r \simeq 0.13$ for $HD^+$. The trap is enclosed in a UHV chamber kept below $10^{-10}$ mbar. The chamber is equipped with a leak valve for the controlled introduction of gases. An all-solid-state 313 nm laser system is used for cooling $Be^+$ [65].

To load $Be^+$ ions into the trap, atoms are thermally evaporated from a beryllium wire, and ionised by an electron beam. The molecular loading is achieved by leaking in neutral gas at a pressure of $\sim(1\text{–}3)\cdot10^{-10}$ mbar, ionised by an electron beam with an energy of 200 eV, and a current of $\sim 30$ $\mu$A, for a loading time of 2 s. This produces mixed-species crystals like those shown in Figs. 10(a,b). The ions with a higher charge-to-mass ratio (in this case the molecular ions) experience a stronger trap pseudopotential, and thus form a dark (non-fluorescing) core to the crystal. The asymmetric distribution of species along the $z$-axis observed in Fig. 10(b) is caused by the light pressure of the cooling laser on the beryllium ions.

The observed crystals are reproduced by molecular dynamics (MD) simulations [61,66]. Visual matching of overall structure, structural details and blurrings of CCD and simulated images allows fitting the ion numbers and temperatures of the different species. The number of ions of different species given

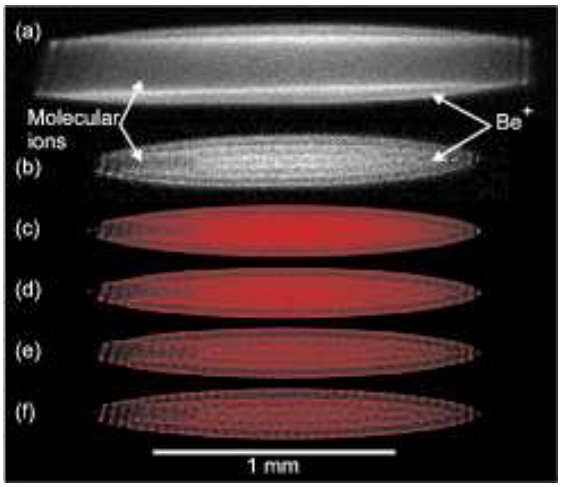


**Fig. 10.** Fluorescence images of (a) a large ion crystal with a high fraction of sympathetically cooled ions (approximately 1200 light ions and 800 $Be^+$ ions) (b) a smaller crystal containing approx. 690 $Be^+$ ions, and 12 (exactly) $HD^+$ ions, and simulated images of this crystal at (c) 20 mK, (d) 12 mK, (e) 8 mK and (f) 6 mK. In the simulations, the beryllium ions are shown in red and the $HD^+$ ions in blue. Laser cooling beam propagation is to the right, along the $z$-axis [61].

in Fig. 10(b) were found in this way. In the simulations we assume an ideal linear trap, use the quasipotential approximation and model heating effects by stochastic forces on the ions. The obtained temperatures are thus effective secular temperatures. Fig. 10 shows a determination of the temperature; agreement is found for a $Be^+$ temperature of appox. 10 mK. This sets an upper limit, as our experimental images are also limited in sharpness by our detection optics, CCD resolution, and sensor noise, which are not considered. The temperature varies depending on crystal size and cooling parameters, and is typically in the range 5 mK to 15 mK, with smaller crystals generally colder. These temperatures are consistent with measurements of the fluorescence lineshape of the $Be^+$ ions.

For all species of molecular ions studied here, our MD simulations show that the sympathetically cooled molecular ion ensemble is also crystalline, i.e. its time-averaged ion distribution is strongly inhomogeneous, and that it is strongly thermally coupled to the $Be^+$ ions. Assuming similar heating effects for the molecular ions and the $Be^+$ ions, the simulations show that the moleculars ions have a temperature similar to that of $Be^+$, due to the strong Coulomb coupling.

The trapped species are identified and the time evolution of their numbers is monitored by excitation of their mass-dependent radial (secular) modes, using a spatially homogenous and temporally oscillating electric field. For $HD^+$ ions the measured secular frequency was $\approx$770 kHz, significantly shifted from the calculated single-particle frequency, due to Coulomb coupling between different species in the trap [67]. Excitation amplitude, sweep rate, and covered frequency

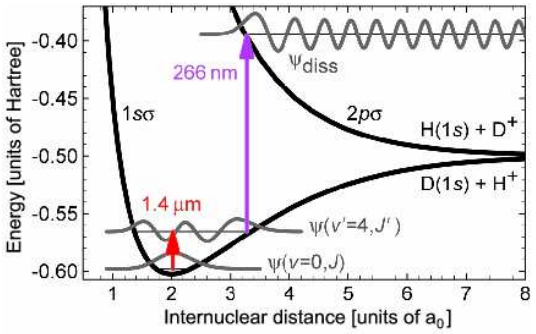


**Fig. 11.** Principle of $(1+1')$ REMPD spectroscopy of $HD^+$ ions. A tunable IR diode laser excites a rovibrational overtone transition $(v=0, L) \rightarrow (v'=4, L')$. The $HD^+$ ions excited to the $v'=4$ vibrational level are dissociated using cw 266 nm laser radiation: $HD^+(v'=4)+h\nu \rightarrow H+D^+$, or $H^+ + D$. Due to different Franck-Condon wavefunction overlap, the calculated UV absorption cross section from the $v'=4$ level ($\sim 2.4\times 10^{-17}$ $cm^2$) is about 7 orders of magnitude larger than from $v=0$ [68]. Energy values represent total binding energies of the molecule [69].

range were chosen so that the ion crystal had sufficient time to cool back to its initial temperature between individual excitation cycles. The excitation heats both the molecular ions and the atomic coolants, which changes the scattering rate of 313 nm cooling light by the $Be^+$ ions. The $HD^+$ secular resonance becomes visible in the $Be^+$ fluorescence, and its strength is proportional to the amount of $HD^+$ ions in the ion crystal.

### 4.2 Spectroscopy of $HD^+$

The choice of $HD^+$ for spectroscopic studies was made because of the availability of dipole-allowed ro-vibrational transitions which simplify the spectroscopic techniques. Nevertheless, vibrational spectroscopy in the electronic ground state in near-absence of collisions, as is the case for the present molecular ions ensembles, is faced with the difficulty that molecules excited to a vibrational level decay only slowly, implying very low fluorescence rates. As the fluorescence wavelengths are in the mid to far infrared, photon counting would require a sophisticated detection system. We circumvent this difficulty by applying the technique of $(1+1')$ resonance enhanced multiphoton dissociation (REMPD): the molecules are excited by an infrared (IR) laser and then selectively photodissociated from the upper vibrational state by a second, fixed-wavelength ultraviolet (UV) laser (Fig.11). The remaining number of molecular ions is the quantity measured as a function of the frequency of the IR laser. As the molecular sample is small (typ. 40-100 ions) the spectroscopy requires the spectra to be obtained by repeated molecular ion production and interrogation cycles. The lasers employed are a single-frequency, widely tunable diode laser at 1.4 $\mu$m (Agilent 81480A), and a resonantly frequency-doubled Yb:YAG laser at 266 nm. The IR laser linewidth

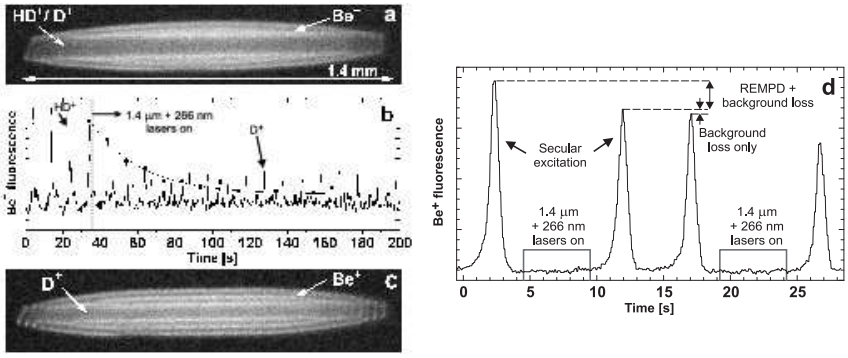


**Fig. 12.** (a) Initial ion crystal: ≈1100 $Be^+$, ≈100 $HD^+$, and ≈20 $D^+$ ions at ≈20 mK (the presence of cold $HD^+$ ions is obvious from the dark crystal core). (b) Repeated secular excitation of the crystal in (a) at 3 V amplitude. The excitation frequency was swept between 500 kHz and 1500 kHz. The IR laser is tuned to the maximum of the $(v = 0, L = 2) \rightarrow (v' = 4, L' = 1)$ line. The curve is an exponential fit with a decay constant of 0.04 $s^{-1}$. (c) Ion crystal after dissociation of all $HD^+$ ions: ≈1100 $Be^+$ and ≈50 $D^+$ ions at ≈20 mK. (d) Measurement cycle consisting of repeated probing of the number of $HD^+$ ions before and after exposure to the spectroscopy lasers [69].

was ∼5 MHz, and its frequency was calibrated with an accuracy of 40 MHz by absorption spectroscopy in a water vapor cell.

Due to the weak coupling between external and internal (rotational) degrees of freedom, the internal temperature of the $HD^+$ ions is close to room temperature, in thermal equilibrium with the vacuum chamber [70,10]. There is significant (>5%) population for rotational levels up to $L=6$. Indeed, we have observed 12 transitions between 1391 nm and 1471 nm, from lower rotational levels $L=0$ to $L=6$.

The loss of $HD^+$ ions not only depends on the REMPD process, but also on transitions induced by blackbody radiation (BBR). We modeled the loss of $HD^+$ by solving the rate equations for the populations of all $(v, L)$ levels interacting with the IR and UV lasers, as well as with the BBR radiation at 300 K. The theoretically obtained excitation spectrum (see Fig. 13 and text below) of the levels probed by the IR laser is included, but for the remainder of the calculation hyperfine structure, due to electron, nuclear and rotational spins, is ignored. The rovibrational transition moments involved are taken from [71]. The rate of dissociation by UV light is obtained using cross sections from [68]. For typical UV intensities, dissociation rates of $10^2$–$10^3$ $s^{-1}$ are found. The rate equation model reveals two different timescales at which the $HD^+$ number declines during a typical experiment. A first, fast (<1 s) decay occurs when the IR laser selectively promotes $HD^+$ ions from a specific $(v=0, L)$ level to a rotational level in $v'=4$, from which they are efficiently photodissociated. This process rapidly dissociates those $(v = 0, L)$ $HD^+$ ions which are in the hyperfine states probed by the IR laser. The remaining molecular ions (a significant fraction of the total initial

number) are dissociated significantly slower, essentially at the rate at which the hyperfine levels of $(v = 0, L)$ are repopulated by BBR and spontaneous emission. For example, for the $(v = 0, L = 2) \rightarrow (v' = 4, L' = 1)$ transition, and for typical intensities of 6 W/cm$^2$ for the IR and 10 W/cm$^2$ for the UV laser, the fast $HD^+$ decay takes place at a rate $\sim$10 s$^{-1}$ (which is not resolved experimentally), whereas the decay due to BBR–induced repopulation occurs at a rate of $\sim$0.04 s$^{-1}$. The latter rate is fairly consistent with the measured decay depicted in Fig.12(b), but observed decay rates depend strongly on which part of the hyperfine spectrum is interrogated. This points at a shortcoming of the simple rate equation model used here, and our observations can probably be explained precisely only by a rate equation model which takes the full hyperfine structure of all involved $(v, L)$ levels into account.

As an example, Fig. 12(b) shows the time evolution of the $HD^+$ secular excitation resonance while the $HD^+$ ions are excited on the maximum of the rovibrational line $(v = 0, L = 2) \rightarrow (v' = 4, L' = 1)$ at 1430.3883 nm. The decrease of the $HD^+$ resonance in the secular excitation spectrum, induced by the REMPD process, is accompanied by a decrease of the dark crystal core containing the MHIs. The secular excitation spectrum also shows an increase of the number of $D^+$ ions, which result from the dissociation of excited $HD^+$ ions. These ions are sympathetically cooled and remain in the crystal core. Fig. 12(c) shows the mixed-species ion crystal after all $HD^+$ was dissociated. The dark crystal core has shrunk significantly, and the crystal now contains $\approx$1100 $Be^+$ and $\approx$50 $D^+$ ions. Assuming equal probability for photodissociation to $D^+$ and $H^+$, this number indicates that most generated $D^+$ ions are sympathetically cooled and trapped. Loss rates are obtained by exponential fitting to the maxima of the $HD^+$ resonances in the secular excitation spectrum (solid line in Fig. 12(b)). In this way, a 0.01 s$^{-1}$ background loss rate of $HD^+$ ions from the trap is obtained when both the IR and UV lasers are turned off. This loss is due to chemical reactions between $HD^+$ ions and background gases. The observed background loss rate is fitted well by a single exponential decay, which rules out strong nonlinear dependence of the $Be^+$ fluorescence during secular excitation on the number of $HD^+$ ions.

The spectroscopic signal used to produce the spectra in Fig. 13 is the molecular ion dissociation probability, obtained as the relative change of the heights of the $HD^+$ secular resonances in the $Be^+$ fluorescence before and after the REMPD excitation (Fig. 12(d)). For each transition, the $HD^+$ dissociation probability was measured as a function of the frequency of the IR laser, in steps of 15 MHz. Each data point was obtained by averaging over several individual measurements of the $HD^+$ dissociation probability occurring over $\sim$5 s. Each data point requires a new loading of $HD^+$ ions in the $Be^+$ crystal. For all measurements, comparable $HD^+$ ion numbers were used, as deduced from the size of the crystal core after loading. However, during each $HD^+$ loading cycle a small fraction of the $Be^+$ is lost from the trap, due to chemical reactions with neutral HD gas [63]. The same $Be^+$ ion crystal can be used for up to 40 $HD^+$ loadings, sufficient for obtaining the spectra in Fig. 13. A typical spectrum is taken within 1-2 hours.

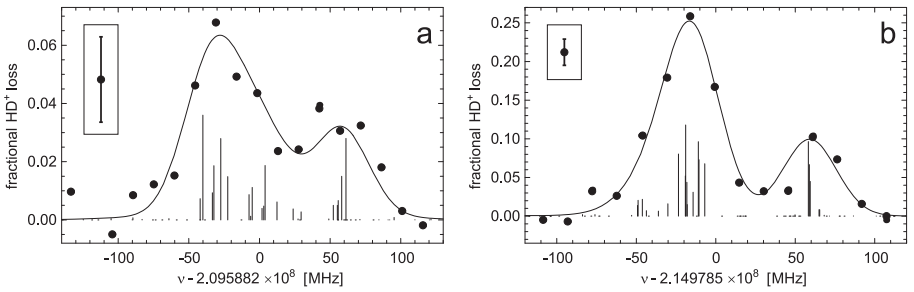


**Fig. 13.** Rovibrational transition spectra with partially resolved hyperfine splitting: (a) $(v=0, L=2) \rightarrow (v'=4, L'=1)$ at 1430 nm, (b) $(v=0, L=2) \rightarrow (v'=4, L'=3)$ at 1394 nm. The curves are fits to the data (•), where the theoretical stick spectra were broadened by ≈40 MHz. The theoretical spectrum exhibits a large number of very weak transitions, due to weak mixing of pure coupled angular momentum states. The ordinate values are the molecular ion dissociation probability for a 5 s irradiation of 0.65 W/cm$^2$ IR and 10 W/cm$^2$ UV light. The insets show typical error bars [69].

Detailed measurements for two transitions $(v=0, L=2) \rightarrow (v'=4, L'=1,3)$ are shown in Figs. 13(a,b). Both spectra reveal a partly resolved hyperfine structure, which can be compared with the prediction from an effective spin Hamiltonian, written as $H_{\rm eff} = b_1 \mathbf{I}_p \cdot \mathbf{S} + c_1 I_{pz} S_z + b_2 \mathbf{I}_d \cdot \mathbf{S} + c_2 I_{dz} S_z + \gamma \mathbf{S} \cdot \mathbf{J}$ [72,73]. Here, $\mathbf{I}_p$, $\mathbf{I}_d$, and $\mathbf{S}$ denote the spin of the proton, deuteron, and electron, respectively; the subscript $z$ indicates the projection on the internuclear axis. The hyperfine coefficients $b_1$, $b_2$, $c_1$, $c_2$, and $\gamma$ have been recently calculated to high accuracy [43], see Sec. 2.4. The hyperfine level energies and eigenfunctions are found by diagonalization of the matrix representation of $H_{\rm eff}$ in a suitable angular momentum coupling scheme. Terms arising from the nuclear spin-rotation and deuteron quadrupole interactions are neglected as they contribute $\ll$1 MHz to the hyperfine level energies [43]. The results of the diagonalization were subsequently used to calculate line strengths (Eq. 11) of the individual hyperfine components within a given rovibrational transition, leading to "stick spectra", as shown in Fig. 13. Inhomogeneous broadening of the spectra may be accounted for by convolving each line with a Gaussian lineshape of a given width.

The broadened stick spectra are fitted to the experimental spectra using the linewidth, the vertical scale and the frequency offset as fit parameters (Fig. 13). The frequency offset corresponds to the deperturbed ro-vibrational transition frequency, which is thus determined to within the accuracy of the wavelength calibration of the IR laser (40 MHz) and the fit uncertainty (3 MHz). The measured deperturbed ro-vibrational transition frequency is in good agreement with the *ab initio* results from [21], see Fig. 13. The partly resolved hyperfine structure in the measured spectra agrees well with the theoretical results obtained from [72,43]. We find both theoretically and experimentally that the hyperfine structure for other transitions in the P and R branches is similar to that in Figs. 13(a,b).

We observe a typical line broadening of 40 MHz, which corresponds to $k_B \times (0.2\,\mathrm{K})$ of energy in the axial motion. The kinetic energy in the secular motion (as inferred from molecular dynamics simulations) of the $HD^+$ ions can give rise to broadening of about 10 MHz only [61]. Saturation broadening also does not play a significant role, as confirmed by comparing spectra taken at different IR and UV intensities. Using the polarization-dependent 313 nm fluorescence of the $Be^+$ ions as a magnetic field probe, the magnetic field (which is along the direction of propagation of the 313 nm laser beam) has been adjusted and verified to be 50 mT and to vary by no more than 40 mT over the extent of the crystal, which implies Zeeman broadening <1 MHz. This leaves Doppler broadening due to micromotion as the most probable cause for the observed line broadening. This micromotion could arise from phase shifts in the rf potentials applied to the various electrodes, and from coupling between axial (IR laser beam direction) and radial ion motion. For our trap, in which the $HD^+$ ions are located at least 10 $\mu$m away from the trap axis, the (radial) micromotion energy exceeds $k_B(0.5\,\mathrm{K})$.

The results described are of significance in several respects. They demonstrate, for the first time, the possibility of high-resolution spectroscopy of small, trapped molecular ion samples, sympathetically cooled well into the millikelvin range. We have achieved a spectral resolution 10 times higher than with any previous cold molecular ion method, and the same enhancement was obtained for the excitation rate. The observed population dynamics demonstrated the weakness of collisions. The methods used for trapping, cooling and detection are quite general, and are applicable to a host of other molecular ion species. This includes other ions of astrophysical and cosmological interest such as $H_3^+$ and its isotopomers, which have been trapped in our setup [61,62]. Also, the spectral resolution achieved here may be further improved: for instance, first-order Doppler broadening may be circumvented by use of a tightly confining trap which holds the ions in the Lamb-Dicke regime, or by two-photon spectroscopy. Furthermore, the presence of the atomic coolant ions offers an in situ tool to detect possible perturbing fields.

## 5 Conclusion and Outlook

In summary, the development of high-accuracy laser spectroscopy of trapped MHIs has made significant progress. On the theory side, the energies have been calculated with a relative accuracy of the order of 1 ppb. Detailed predictions of the line strengths of one- and two-photon transitions have been given, which are important guides for the experiments. Certain systematic shifts (dc and ac Stark shifts [15,22]) have also been calculated, but are not described here. On the experimental side, several important techniques have been demonstrated: cooling of MHIs to tens of mK, vibrational-state selective photodissociation, one-photon vibrational spectroscopy with spectral resolution at the level of $2{\cdot}10^{-7}$, rotational population measurement, in-situ ion detection, tunable, high-power, continuous-wave narrow-linewidth laser for two-photon spectroscopy. Based on the present

results, it is expected that the two-photon $H_2^+$ spectroscopy experiment will ultimately allow a spectral resolution at the level of $3 \cdot 10^{-10}$, while the one-photon $1.4\,\mu$m $HD^+$ spectroscopy in the current apparatus will be limited by Doppler broadening to several parts in $10^8$. One-photon spectroscopy of $HD^+$ vibrational transitions having longer wavelength or the use of a trap with stronger confinement should allow reaching the Lamb-Dicke regime, with a strong increase in spectral resolution. As described above, two-photon spectroscopy is another alternative.

For both ion species, the investigation of systematic shifts will become an important task. It is expected that Zeeman shifts and Stark shifts can be reduced or measured to a level below one part in $10^{10}$ in a cold ion ensemble. This should enable comparisons of experimental and theoretical transition frequencies at levels below 1 ppb, and, in the longer term, the development of a novel approach to the measurement of mass ratios of electron and hydrogen isotopes.

In the future, it may become attractive to use the method of quantum-logic-enabled spectroscopy [74,75]. Some of the experimental limitations (broad state population distribution, need for destructive detection of molecular excitation, systematic effects) encountered with the approaches described here could be substantially alleviated.

## Acknowledgements

We thank P. Blythe and H. Daerr for their contributions and M. Okhapkin, A. Nevsky, I. Ernsting and A. Wicht for discussions and assistance. This work was supported by the German Science Foundation, the EC Network HPRN-CT-2002-00290 "Cold Molecules". We also thank S. Kilic, F. Bielsa, A. Douillet, T. Valenzuela and O. Acef for their contributions, as well as the LNE-SYRTE (Paris Observatory) and LPL (Université Paris 13) laboratories for lending IR optical components and their absolute frequency measurement setup. (J.K.) thanks the Alexander-von-Humboldt-Foundation for support. (V.K.) acknowledges support of RFBR, grant No. 05-02-16618.

## References

1. C.A. Leach and R.E. Moss, *Annu. Rev. Phys. Chem.* **46**, 55 (1995).
2. see e.g. the DIREF database, http://diref.uwaterloo.ca; P.F. Bernath and S. McLeod, J. Mol. Spectrosc. **207**, 287 (2001).
3. K.B. Jefferts, Phys. Rev. Lett. **23**, 1476 (1969).
4. W.H. Wing, G.A. Ruff, W.E. Lamb, J.J. Spezeski, Phys. Rev. Lett. **36**, 1488 (1976).
5. A. Carrington, Science **274**, 1327 (1996), and references therein.
6. A.D.J. Critchley, A.N. Hughes, I.R. McNab, Phys. Rev. Lett. **86**, 1725 (2001).
7. J.J. Spezeski, Ph.D. thesis, Yale University (1977).
8. Y.P. Zhang, C.H. Cheng, J.T. Kim, J. Stanojevic, and E.E. Eyler, Phys. Rev. Lett. **92**, 203003 (2004), and references therein.
9. H. Schnitzler, Ph.D. dissertation, Univ. Konstanz (2001).
10. J.C.J. Koelemeij, B. Roth, and S. Schiller, in preparation (2006).

11. H. Müller, S. Herrmann, A. Saenz, A. Peters, C. Lämmerzahl, Phys. Rev. D **70**, 076004 (2004).
12. S. Schiller and V. Korobov, Phys. Rev. A **71**, 032505 (2005).
13. J.P. Uzan, Rev. Mod. Phys. **75**, 403 (2003).
14. D. DeMille, Phys. Rev. Lett. **88**, 067901 (2002).
15. L. Hilico, N. Billy, B. Grémaud, and D. Delande, Eur. Phys. J. D **12**, 449 (2000).
16. J.-Ph. Karr and L. Hilico, J. Phys. B **39**, 2095 (2006).
17. P.J. Mohr and B.N. Taylor, Rev. Mod. Phys. **77**, 1 (2005).
18. J. Verdu, S. Djekic, S. Stahl, T. Valenzuela, M. Vogel, G. Werth, T. Beier, H.J. Kluge, W. Quint, Phys. Rev. Lett. **92**, 093002 (2004).
19. S.G. Karshenboim, Phys. Reports **422**, 1 (2005).
20. R.E. Moss, Molecular Physics **80**, 1541 (1993).
21. R.E. Moss, Molecular Physics **78**, 371 (1993).
22. J.-Ph. Karr, S. Kilic, and L. Hilico, J. Phys. B **38**, 853 (2005).
23. V.I. Korobov, Phys. Rev. A **61**, 064503 (2000).
24. D.H. Bailey and A.M. Frolov, J. Phys. B **35**, 4287 (2002).
25. Zong-Chao Yan, Jun-Yi Zhang, and Yue Li, Phys. Rev. A **67**, 062504 (2003).
26. M.M. Cassar and G.W.F. Drake, J. Phys. B **37**, 2485 (2004).
27. A.M. Frolov and V.H. Smith, Jr. J. Phys. B **28**, L449 (1995).
28. V.I. Korobov, J. Phys. B **35**, 1959 (2002); F.E. Harris A.M. Frolov, and V.H. Smith, Jr., J. Chem. Phys. **121**, 6323 (2004).
29. H.A. Bethe and E.E. Salpeter, *Quantum mechanics of one– and two–electron atoms*, Plenum Publishing Co., New York, 1977.
30. V.B. Berestetsky, E.M. Lifshitz and L.P. Pitaevsky, *Relativistic Quantum Theory*, Pergamon, Oxford, 1982.
31. V.I. Korobov, Phys. Rev. A **74**, 052506 (2006).
32. K. Pachucki, J. Phys. B **31**, 3547 (1998).
33. A. Yelkhovsky, Phys. Rev. A **64**, 062104 (2001).
34. V.I. Korobov, Phys. Rev. A **70**, 012505 (2004).
35. V.I. Korobov, Phys. Rev. A **73**, 024502 (2006).
36. H. Araki, Prog. Theor. Phys. **17**, 619 (1957); J. Sucher, Phys.Rev. **109**, 1010 (1958).
37. V.I. Korobov and Ts. Tsogbayar, in preparation.
38. J.R. Sapirstein, D.R. Yennie, in: T. Kinoshita (Ed.), *Quantum Electrodynamics*, World Scientific, Singapore, 1990.
39. M.I. Eides, H. Grotch, and V.A.Shelyuto, Phys. Reports **342**, 63 (2001).
40. A.J. Layzer, Phys. Rev. Lett. **4**, 580 (1960).
41. K. Pachucki, Ann. Phys. (N.Y.) **226**, 1 (1993).
42. K. Pachucki, Phys. Rev. Lett. **72**, 3154 (1994); M.I. Eides and V.A. Shelyuto, Phys. Rev. A **52**, 954 (1995).
43. D. Bakalov, V.I. Korobov, and S. Schiller, Phys. Rev. Lett. (to be published).
44. V.I. Korobov, L. Hilico, and J.-Ph. Karr, Phys. Rev. A **74**, 040502(R) (2006).
45. D. Bakalov, V.I. Korobov, S. Schiller, In *Proceedings of the International Conference on exotic atoms "EXA 2005"*, February 21-25, 2005, Vienna, Austria.
46. B. Cagnac, G. Grynberg and F. Biraben, J. Physique **34**, 845 (1973); J.C. Garreau, M. Allegrini, L. Julien and F. Biraben, J. Physique **51**, 2275 (1990).
47. L. Hilico, N. Billy, B. Grémaud and D. Delande, J. Phys. B **34**, 491 (2001).
48. A.V. Matvijenko and L.I. Ponomarev, J. Phys. B **5**, 27 (1972); J. Carbonel, R. Lazauskas, D. Delande, L. Hilico, S. Kilic, Europhysics Letter **64**, 316 (2003).
49. A. Carrington *et al.*, J. Chem. Soc. Faraday Trans. **89**, 603 (1993); A. Carrington, C.A. Leach, and M.R. Viant, Chem. Phys. Lett. **206**, 77 (1993).

50. G.H. Dunn, Phys. Rev. **172**, 1 (1968). JILA report **92** (1968).
51. Senem Kilic, thèse de l'université Pierre et Marie Curie (Paris 6), 2005.
52. Y. Weijun, R. Alheit, G. Werth, Z Physik D **28**, 87 (1993).
53. L.S. Rothman *et al.*, J. Quant. Spec. Rad. Tr **96**, 139 (2005).
54. R.M. Williams *et al.*, Optics Letters **24**, 1844 (1999).
55. M.S. Taubman *et al.*, Optics letters **27**, 2164 (2002).
56. F. Bielsa, T. Valenzuela, A. Douillet, J.-Ph. Karr, and L. Hilico, submitted to Optics Letters.
57. F. Bielsa, K. Djerroud, A. Goncharov, T. Valenzuela, A. Douillet, C. Daussy, A. Amy-Klein, L. Hilico, submitted to J. Mol. Spec.
58. A. Amy-Klein *et al.*,Optics Letters **30**, 3320 (2005).
59. D.J. Larson *et al.*, Phys. Rev. Lett. **57**, 70 (1986).
60. K. Molhave and M. Drewsen, Phys. Rev. A **62**, 0011401(R) (2000).
61. P. Blythe *et al.*, Phys. Rev. Lett. **95**, 183002 (2005).
62. B. Roth *et al.*, J. Phys. B **39**, S1241 (2006).
63. B. Roth *et al.*, Phys. Rev. **A 73**, 042712 (2006).
64. A. Ostendorf *et al.*, to appear in Phys. Rev. Lett. (2006).
65. H. Schnitzler *et al.*, Applied Optics **41**, 7000 (2002).
66. B. Roth, A. Ostendorf, H. Wenz, and S. Schiller, J. Phys. B **38**, 3673 (2005).
67. B. Roth, P. Blythe, and S. Schiller, submitted to Phys. Rev. A (2006).
68. M. Tadjeddine and G. Parlant, Mol. Phys. **33**, 1797 (1977); A. Kondorskiy, private communications (2006).
69. B. Roth, J.C.J. Koelemeij, H. Daerr, and S. Schiller, Phys. Rev. A **74**, 040501(R) (2006).
70. A. Bertelsen, S. Jorgensen, and M. Drewsen, J. Phys. B **39**, 83 (2006).
71. E.A. Colbourn and P.R. Bunker, J. Mol. Spect. **63**, 155 (1976).
72. R.D. Ray and P.R. Certain, Phys. Rev. Lett. **38**, 824 (1977).
73. A. Carrington, I. McNab, and C. Montgomerie, J. Phys. B **22**, 3551 (1989).
74. D.J. Wineland *et al.*, in *Proceedings of the 6th Symposium on Frequency Standards and Metrology*, edited by P. Gill, World Scientific, Singapore, p. 361 (2002).
75. P.O. Schmidt *et al.*, Science **309**, 749 (2005).

# Danksagung

Herrn Prof. Stephan Schiller möchte ich danken, dass er mich in seinem Institut aufgenommen und mir die Leitung der Ionenfallen-Projekte anvertraut hat. Seine fortwährende Unterstützung in allen Belangen hat entscheidend zum Fortgang und zum Erfolg meiner Arbeit beigetragen. Weiterhin möchte ich mich für das hohe Maß an Eigenverantwortung und wissenschaftlicher Selbstängigkeit bedanken, die mir Prof. Schiller ermöglicht hat. Das Arbeiten in seinem Institut hat stets Freude bereitet.

Den aktuellen und ehemaligen Mitarbeitern der Ionenfallen-Projekte möchte ich einen besonderen Dank aussprechen.
Dr. Jeroen Koelemeij, Dipl. Phys. David Offenberg sowie Chaobo Zhang, Msc, danke ich für die exzellente Zusammenarbeit und die zahlreichen Diskusionen, die wesentlich zum Gelingen der Arbeit beigetragen haben. In diesem Zusammenhang seien auch Dr. Alexander Ostendorf, Dr. Mark Alexander Wilson, Dr. Peter Blythe, Dipl. Phys. Ulf Fröhlich, Dipl. Phys. Heiner Daerr, Dipl. Phys. Hartmut Borwaski, sowie Dipl. Phys. Thomas Fritsch erwähnt, denen ich herzlich für Ihre wichtigen Beiträge zu den einzelnen Projekten, die vielen Diskussionen in der Aufbauphase der Projekte sowie für zahllose Messnächte danke. Durch ihre Hilfsbereitschaft bei der Durchführung der Messungen sowie ihr Interesse am Vorankommen der Projekte hatten sie einen unschätzbaren Anteil an der stets angenehmen Atmosphäre im Labor. Prof. Andreas Wicht und Dipl. Phys. Ingo Ernsting möchte ich herzlich für die sehr gute Zusammenarbeit bei den Frequenzmessungen und für ihre Unterstützung bei vielen Problemen und Fragen danken.

Bei allen Mitarbeitern des Instituts bedanke ich mich für die stets angenehme Arbeistatmosphäre. Besonders möchte ich dabei Dr. Alexander Nevsky, Dr. Maxim Okhapkin, Dipl. Phys. Christian Eisele, Dipl. Phys. Ulf Bressel sowie die ehemaligen Kollegen Dr. Piergiorgio Antonini, Dr. Luca Haiberger und Dr. Frank Müller erwähnen. Herrn Dr. Helmut Wenz danke ich für seinen Beitrag zu den numerischen Simulationen und für viele hilfreiche Diskussionen.

Bei Frau Rita Gusek und Herrn Peter Dutkiewicz möchte ich mich für die vielfältige und tatkräftige Unterstützung bei der Entwicklung der Elektronik sowie den auftretenden technischen Problemen im Labor bedanken. Die gute Zusammenarbeit mit den Mitarbeitern der mechanischen Werkstätten, Herrn Jens Bremer und Herrn Heinrich Hoffmann, sowie mit den Mitarbeitern der mechanischen Zentralwerkstatt der WE

Physik war ebenso essentiell für den Fortschritt an den Projekten.

Ich möchte mich ebenfalls bei Dr. Claus Lämmerzahl bedanken, der in der Anfangszeit meiner Arbeit zum Gelingen der numerischen Simulationen beigetragen hat. Des Weiteren habe ich viel aus den Diskussionen mit Dr. Dimitar Bakalov und Dr. Vladimir Korobov über die präzise Berechnungen der Übergangsfrequenzen in Wasserstoffmolekülionen gelernt. Weiterhin gilt mein Dank Stefan Förster für zahlreiche wertvolle Diskussionen.

Ein besonderer Dank gilt meiner Familie für die vorbehaltlose und fortwährende Unterstützung in allen Bereichen. Natascha Roth danke ich für jegliche Unterstützung, Rücksichtnahme und für ihr Verständnis.